NOTE TO USERS

This reproduction is the best copy available.

UMI

DISSERTATION

PIER MOMENT-ROTATION BEHAVIOR OF HIGH PERFORMANCE STEEL HPS70W I-GIRDERS

Submitted by

An Vinh Tran

Department of Civil Engineering

In partial fulfillment of the requirements

For the Degree of Doctor of Philosophy

Colorado State University

Fort Collins, Colorado

Fall 2002

COLORADO STATE UNIVERSITY

November 11, 2002

WE HEREBY RECOMMEND THAT THE DISSERTATION PREPARED UNDER OUR SUPERVISION BY *AN VINH TRAN* ENTITLED ***PIER MOMENT-ROTATION BEHAVIOR OF HIGH PERFORMANCE STEEL HPS70W I-GIRDERS*** BE ACCEPTED AS FULFILLING IN PART REQUIREMENTS FOR THE DEGREE OF DOCTOR OF PHILOSOPHY.

Committee on Graduate Work

Marvin E. Criswell

Paul R. Heyliger

Frederick W. Smith

Erik G. Thompson

Bryan A. Hartnagel, Adviser

Department Head

ABSTRACT OF DISSERTATION

PIER MOMENT-ROTATION BEHAVIOR OF HIGH PERFORMANCE STEEL HPS70W I-GIRDERS

This dissertation presents a study of the pier moment-rotation behavior of compact and noncompact high performance steel HPS70W I-shape girders in the context of examining two restrictions for inelastic design of steel bridge girders in the current edition of the AASHTO LRFD bridge code (AASHTO, 1998 and interim 2001). The first restriction is that inelastic design involving the moment-rotation relationship of steel girders with a yield strength exceeding 50 ksi is prohibited. Though, bridge designers are currently allowed to go to plastic moment for I-shape girders having a yield strength of 70 ksi. The second restriction is that the AASHTO LRFD inelastic design methods cannot be used on girders that do not meet the compactness requirements stated in the provisions.

To determine whether or not these restrictions should be modified, examination of the pier moment-rotation behavior of HPS70W I-shape girders was undertaken through experimental testing and numerical modeling. Large-scale laboratory experiments were

performed for noncomposite girders. Finite element models of the tested specimens were then analyzed based on the material inputs obtained from experimental examination of the stress-strain relationships for HPS70W. The inelastic moment-rotation behavior of HPS70W girders was determined both experimentally and numerically.

The experimental and numerical responses agree well and thus validate the numerical model. These results also show that compact/noncompact and composite/noncomposite HPS70W I-girders have the strength and ductility suitable for the application of inelastic analysis and design. This research suggests that the two restrictions for inelastic design of steel bridge girders in the current AASHTO LRFD bridge code (AASHTO, 1998 and interim 2001) should be modified for such girders. This work also demonstrates that the proposed improved simplified inelastic design (ISID) procedures (Barth, Hartnagel, White, and Barker, 2001) are suitable for high performance steel, HPS70W, compact and noncompact I-girders. In addition, from the noncomposite numerical models, which were validated by experiment, finite element models were developed for composite girders and were examined. The numerical results confirm that the pier moment-rotation behavior is similar for composite and noncomposite cross sections.

An Vinh Tran
Department of Civil Engineering
Colorado State University
Fort Collins, CO 80523
Fall 2002

ACKNOWLEDGEMENTS

The author gratefully acknowledges the sponsors of the project and Colorado State University. The project would not have been a success without generous funding from Mountain Plains Consortium, plate donations from Bethlehem Lukens Plate, a division of Bethlehem Steel Corporation, Burns Harbor, Indiana, and girder fabrication from Zimmerman Metals, Inc., Denver, CO. The author would like to sincerely thank the faculty and staff of Colorado State University (CSU), College of Engineering, and Department of Civil Engineering for their support and guidance through both his undergraduate and graduate studies.

The author wishes to express his thanks to the Graduate School and the professors in his Doctoral Committee. A special thanks is expressed to Dr. Bryan A. Hartnagel, the dissertation supervisor, for his support, encouragement, patience, guidance and useful comments throughout the long process. The author gratefully thanks Dr. Marvin E. Criswell, Dr. Paul R. Heyliger, and Dr. Erik G. Thompson not only for being in the Doctoral Committee but also for the valuable teaching in the graduate school courses. The author also owes thanks to Dr. Frederick W. Smith for being in the Doctoral Committee and for his interest in the dissertation.

Sincere thanks are expressed to Dr. Daniel K. Sunada who has had an immeasurable impact on the author's learning and teaching process. The author also extends his gratitude to Dr. Thomas J. Siller, the freshman advisor of the author, Dr.

Johannes Gessler, the undergraduate program advisor, and Dr. Richard M. Gutkowski, the masters program advisor, for their teaching and guidance.

The author also expresses his appreciation to all students and technical staff working at the Structures Lab of the Engineering Research Center - CSU, especially Michael Griffeth, Dr. Abdalla Shigidi, and Brian Valentine, for their assistance in the experiments of the project. The author also owes thanks to Hibbitt, Karlsson & Sorensen, Inc., the Academic Computing and Networking Services - CSU, and the Engineering Network Services - CSU for providing the ABAQUS finite element program useful in the numerical analysis of the project.

Finally, the author wishes to sincerely thank all of his English tutors and instructors, especially Dr. & Mrs. Stephen Paranka (Fort Collins, 1991), Dr. & Mrs. Richard Walsh (Fort Collins, 1991), Dr. Cannon (Houston Community College, 1993), and Dr. Charles Brainer (Intensive English Program - CSU, 1993) for their generous support, teaching, and encouragement.

An Vinh Tran
Department of Civil Engineering
Colorado State University
Fort Collins, CO 80523
Fall 2002

DEDICATION

In tribute to their generous support, I dedicate this work to my family: to preceding generations and to my extended family. I am especially grateful to my parents, Loc Vinh Tran and Trinh Thi Le, my uncle, Loi Van Le, and my sister, Tam-Trang Vinh Tran, who made this possible.

An Vinh Tran
Department of Civil Engineering
Colorado State University
Fort Collins, CO 80523
Fall 2002

TABLE OF CONTENTS

LIST OF TABLES

LIST OF FIGURES

CHAPTER 1

INTRODUCTION

1.1 Introduction

Inelastic design of steel bridge girders offers the potential for significant cost savings because it accounts for the true strength of a bridge, which is often considerably above the strength predicted by elastic or pseudo-plastic procedures used in present bridge specifications (Hartnagel, 1997). On the other hand, the 1998 version of the Load and Resistance Factor Design (LRFD) specifications of the American Association of State Highway and Transportation Officials (AASHTO) forbid inelastic design procedures for steel plate girders having a specified minimum nominal yield stress of steel, F_y, exceeding 50 ksi. The 1998 version of AASHTO LRFD 2nd Edition also limited the nominal flexural strength, M_n, of steel plate girders having F_y exceeding 50 ksi to the yield moment capacity, M_y, rather than the plastic moment capacity, M_p (AASHTO, 1998). Nonetheless, evidence from current research on high performance steel (HPS) initiated the consideration to account inelastic strength with the limitation of plastic moment capacity, M_p. Additionally, the interim 2001 specifications of AASHTO LRFD 2nd Edition now allow steel plate girders having $F_y \leq 70$ ksi to reach M_p (AASHTO, interims 2000 and 2001) provided certain restrictions are met. In an effort to determine whether or not bridge designers can take advantage of the inherent properties of HPS, this

research will specially focus on I-shape plate girders fabricated from ASTM A709 HPS70W steel, a HPS with a nominal yield stress of 70 ksi.

In brief, high performance steel (HPS) contains less carbon than conventional steel, leading to an increase in its weld-ability and toughness. Additional alloying ingredients contribute to its superior weathering characteristics. A thermo-mechanical controlled process of essentially quenching and tempering provides the gain of additional strength. HPS weathering steel is suitable for use in the unpainted condition, and this gives designers the option to reduce painting and associated maintenance in many bridge locations.

1.2 Purpose and Objectives

The purpose of this research is to study the pier moment-rotation behavior of compact and noncompact I-shape bridge girders fabricated from high performance steel (HPS). To accomplish the purpose, the research consists of two main objectives.

The first objective of this research is to compare experimental laboratory moment-rotation tests and corresponding numerical moment-rotation finite element analysis of HPS70W steel components to current AASHTO LRFD moment-rotation equations. The second objective is to compare inelastic moment-rotation post peak behavior of numerical noncomposite models to corresponding numerical composite models.

The tasks necessary to complete the objectives of the research are:

1. Experimental tasks: Four various length and size HPS70W I-shape steel girders are tested in the common simply supported configuration, which models upside

down the interior support regions of continuous girders (see Chapter 2, Figure 2.3.1.2). The first two girders meet compact section slenderness requirements for flange and web elements as presented in AASHTO LRFD (AASHTO, 1998 and interims 1999, 2000, & 2001). Details of the two compact-girder tests discussed herein are also documented in Griffeth's Master-of-Science thesis (Griffeth, 2001) supervised by the author's adviser. The other two girders are samples of noncompact sections; specifically, the web is noncompact.

2. Numerical tasks: Establish finite element models corresponding to the four tested HPS70W I-shape steel girders. Develop the finite element composite models from finite element noncomposite models that are verified by experimental results.

3. Analysis and synthesis task: Compare the results obtained from experimental works and numerical works to determine the pier moment-rotation behavior of HPS70W I-shape steel girders. Compare the results to current and proposed AASHTO LRFD moment-rotation specifications to provide conclusions and suggestions.

1.3 Significance of the Study

Inelastic analysis and design procedures permit more economical I-shape girders to be used. Inelastic procedures allow for the yielding of entire steel cross sections to occur at interior supports of continuous span I-shape bridge girders. Plastic hinges that form at piers though must have adequate ductility so that the plastic hinges don't unload before the theoretical plastic strength of the bridge girder is reached. As a result, inelastic rotation at the piers permits moment-redistribution from negative pier moments to positive moment regions. Since the moment-redistribution causes slight inelastic rotation

at the pier regions, small permanent deflection, and some residual moments, the bridge is still serviceable. After an initial overload, deformations stabilize, the structure achieves shakedown, and future loads will be resisted elastically.

However, according to AASHTO inelastic design procedures for the Service Limit State Control of Permanent Deflection (AASHTO, 1998 and interim 2001), the moment-rotation behavior of I-shape girders constructed of steel having F_y greater than 50 ksi has not been sufficiently documented to permit the use of inelastic analysis procedures. In other words, for I-shape girders having a specified minimum nominal yield stress of steel, F_y, of 70 ksi, bridge designers can allow cross sections to reach the plastic moment capacity, M_p, but they still cannot use inelastic analysis. To determine whether or not the current restriction should apply to bridge girders fabricated from HPS70W steel plates, it is necessary to clarify the pier moment-rotation behavior of HPS70W I-girders. Consequently, the pier moment-rotation behavior will document whether geometric failure or material failure occurs first in compact HPS girders.

The inelastic pier moment-rotation post peak behavior for noncomposite and composite I-girder sections are thought to be nearly the same. A composite beam or girder is a steel beam or girder connected to a concrete slab so that the steel element and the slab, and/or the longitudinal rebars within the slab, respond to the bending loads as a unit. In positive-bending region, both the slab and rebars participate in this unit, but in negative-bending regions only the rebars participate. To be simplified and unified, a current focus is to have only one procedure that encompasses compact and noncompact cross-sectional girders as well as composite and noncomposite cross-sectional girders. The study will determine inelastic pier moment-rotation post peak behaviors of

noncomposite and composite I-girder sections. Comparisons will be made to confirm that behavior is similar for composite and noncomposite cross sections. The need for a unified procedure is evident because some states allow composite construction over the interior support regions while others do not.

1.4 Report Organization

This research report consists of five chapters. Chapter 1 provides a description of the purpose of the study and a rationale for its significance. Chapter 2 presents a review and background of the relevant previous studies for pier moment-rotation behavior of I-shape steel girders. Current AASHTO LRFD moment-rotation specifications and inelastic behavior for steel bridge girders will be discussed. Existing experimental moment-rotation curves of conventional steel and HPS of compact and noncompact sections in noncomposite (and composite for conventional steel) will be presented. Research relating to numerical moment-rotation behavior of conventional steel and HPS of compact and noncompact noncomposite sections will be discussed. A recently proposed inelastic design of steel I-girder bridges is also introduced.

Chapter 3 describes the laboratory tests for HPS70W compact and noncompact noncomposite sections and details the finite element models for HPS70W compact/noncompact noncomposite/composite sections. In Chapter 4, experimental and numerical findings of moment-rotation of HPS70W will be synthesized to develop the moment-rotation behavior compared to current AASHTO LRFD moment-rotation specifications and the proposed inelastic design provision. Chapter 5 then summarizes the important results and presents conclusions of this research.

In addition, References provides relevant publications, and Glossary and Notation define the main terminologies and symbols used in this research. Finally, Appendix presents some useful information for experimental and numerical work in this study, including some relevant figures of test setup of previous authors and flexural-capacity-equation sets in the proposed inelastic design provisions.

CHAPTER 2

BACKGROUND AND LITERATURE REVIEW

2.1 Introduction

The purpose of this research is to study the pier moment-rotation behavior of compact and noncompact I-shape HPS bridge girders, examining two restrictions for inelastic design of steel bridge girders in the current edition of the AASHTO LRFD bridge specifications. First, inelastic design involving the moment-rotation relationship of steel girders is prohibited if the steel has a minimum specified yield strength, F_y, exceeding 50 ksi (AASHTO, 1998 and interims 1999, 2000, & 2001). Second, the available AASHTO LRFD inelastic design methods cannot be used on girders that do not meet the compactness requirements stated in the provisions.

2.2 Current ASSHTO LRFD Specifications

2.2.1 AASHTO requirements of compact section slenderness, bearing stiffener, and lateral bracing locations

First, as specified by AASHTO, the compact section requirements for the web and the flange, respectively, are:

$$\frac{2D_{cp}}{t_w} \le 3.76\sqrt{\frac{E}{F_{yc}}} \qquad \text{(AASHTO 6.10.4.1.2)}$$

$$\frac{b_f}{2t_f} \le 0.382\sqrt{\frac{E}{F_{yc}}} \qquad \text{(AASHTO 6.10.4.1.3)}$$

where:

D_{cp} = depth of web in compression at plastic moment (in.),

t_w = web thickness (in.),

b_f = width of compression flange (in.),

t_f = thickness of compression flange (in.),

E = modulus of elasticity of steel, and

F_{yc} = specified minimum yield strength of the compression flange.

Second, bearing stiffeners shall be placed on the webs of plate girders at all bearing locations and at all locations supporting concentrated loads, and the stiffeners shall extend the full depth of the web and, as closely as practical, to the outer edges of the flanges (AASHTO 6.10.8.2). AASHTO recommends the width, b_t (in.), of each projecting stiffener element shall satisfy:

$$b_t \le 0.48t_p\sqrt{\frac{E}{F_{ys}}} \qquad \text{(AASHTO 6.10.8.2.2)}$$

where:

t_p = thickness of stiffener (in.),

F_{ys} = yield strength of stiffener (ksi).

Third, lateral bracing along the compression flange prevents lateral torsional buckling, and thus, insures that a girder meeting compact section requirements can reach its inherent plastic moment capacity. In three-point loading, the midspan (at the load point) is the most critical region of a girder for lateral torsional buckling. As a result,

lateral bracing is first provided at the midspan of the test girders, and the compression flange bracing from the load point to the next compression flange brace is checked against the maximum unbraced length permitted by AASHTO. The maximum unbraced length, L_b, is equal to

$$L_b \le \left(0.124 - 0.0759\left(\frac{M_l}{M_p}\right)\right)\left(\frac{r_y E}{F_{yc}}\right) \qquad \text{(AASHTO 6.10.4.1.7)}$$

where:

L_b = unbraced length (in.),

r_y = radius of gyration about the weak bending axis (in.),

M_l = lower factored moment at either end of the unbraced length (kip-in),

M_p = plastic moment (kip-in),

F_{yc} = compression flange yield strength (ksi), and

E = modulus of elasticity (ksi).

2.2.2 Current AASHTO LRFD moment-inelastic rotation provision

Figure 2.2.1 shows the current AASHTO LRFD moment-rotation provision, which plots the applied moment normalized to the plastic moment versus plastic rotation, where:

θ_{inel} = total inelastic rotation = sum of end inelastic rotations, $\theta_{inel\text{-}left}$ and $\theta_{inel\text{-}right}$

M_p = plastic moment,

M_{pc} = effective plastic moment (a common value of plastic rotation, θ_p, where M_{pc} occurs is $\theta_p = 0.063$ radian (Schilling & Morcos, 1988)), and from AASHTO 6.10.10.1.2d, Strength limit state (AASHTO, interim 2001):

$M_{pc} = R_f M_{pf} + R_w M_{pw}$ to account for local buckling during plastic rotation,

M_{pf} = flange plastic moment capacity component,

M_{pw} = web plastic moment capacity component,

R_f = flange local buckling reduction factor = $\frac{0.0845E(2t_f / b_f)^2}{F_{yf}} \leq 1.0$,

R_w = web local buckling reduction factor = $\frac{1.32E(t_w / D_{cp})^2}{F_{yw}} \leq 1.0$.

E = modulus of elasticity of steel,

t_f = flange thickness,

b_f = flange width,

F_{yf} = nominal yield stress of steel in flange,

t_w = web thickness,

D_{cp} = depth of web in compression, taken at the plastic moment, and

F_{yw} = nominal yield stress of steel in web.

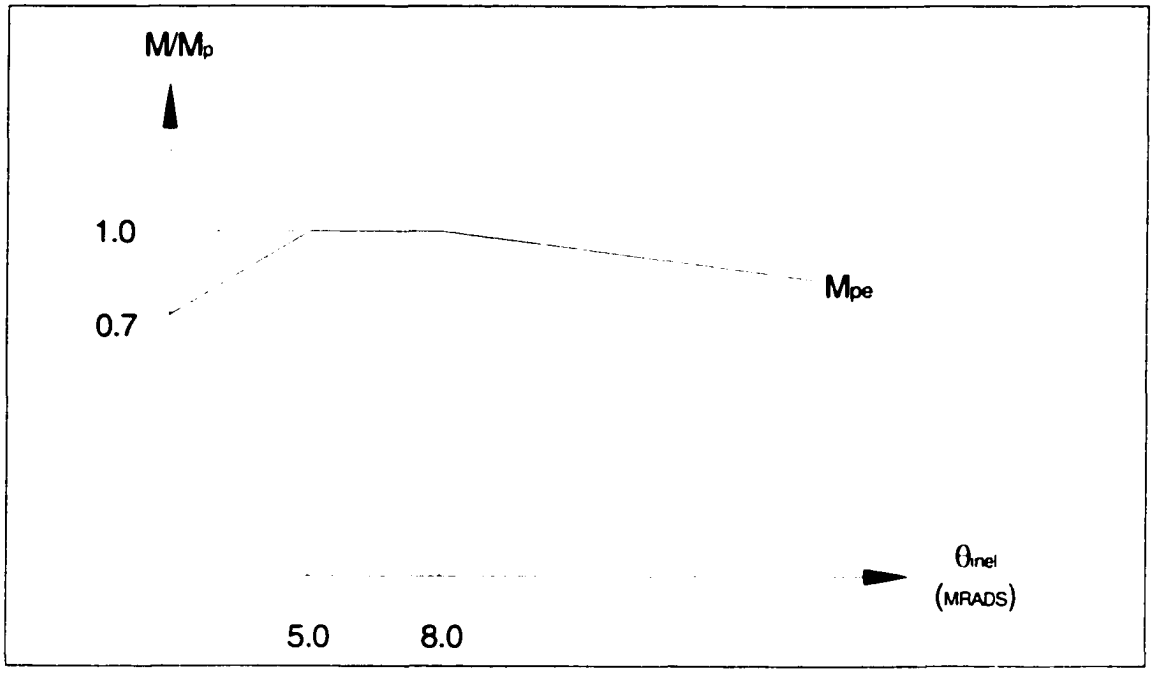

Figure 2.2.1 AASHTO 6.10.10.2.4d

2.3 Inelastic Moment-Rotation Behavior

2.3.1 Single girders

2.3.1.1 Noncomposite sections

In inelastic analysis, a member's ability to resist rotation is characterized by its moment-rotation relationship. Figure 2.3.1.1 presents a typical moment-rotation relationship for a simply supported steel girder. One common measure of the ductility of a girder is the rotation capacity, R, defined as:

$$R = \frac{\theta_u}{\theta_p} - 1$$

where:

θ_p = the hypothetical total (or one end) rotation when M_p is reached, assuming the girder remains completely elastic up to M_p, and

θ_u = the total (or one end) rotation at which the moment capacity returns to M_p after exceeding M_p and deforming past θ_p.

The expected rotation capacity, R, is three for a compact girder (AISC LRFD specification, 2nd edition, page 6-39, footnote [c] (American Institute of Steel Construction, 1998)). However, for bridges it is now thought that the maximum rotation necessary for redistribution of moments is 30 mrads = 0.030 radian (Schilling, 1986).

The moment-rotation behavior is affected by a number of factors. The spread of yielding throughout the cross section and along the length of the member, the initial pattern of residual stresses, and the girder proportions (ratio of the flange area to web area) mainly govern the shape of the ascending portion. The spacing of the compression flange bracing, the compression flange slenderness, the web slenderness, and initial imperfection (out-of-flatness) primarily affect the shape of the descending portion.

Additionally, the behavior of a simply supported member under a distributed load is similar to that under a concentrated load, but the inelastic rotation is spread over a longer yield region (Hartnagel, 1997).

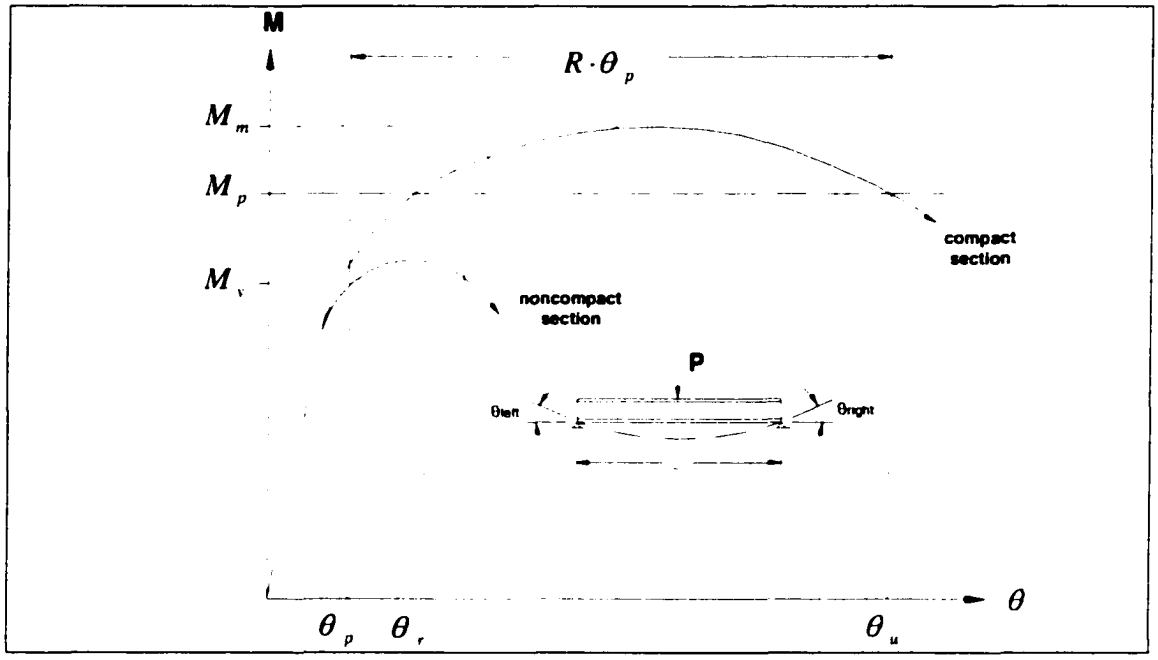

Figure 2.3.1.1 A typical moment-rotation curve for a simple span girder with adequate lateral bracing provided

As the loading increases in Figure 2.3.1.1, yielding starts below the yield moment, M_y, due to initial residual stresses. Plastic rotation, caused by this yielding, thus adds to the theoretical elastic rotation to produce a total actual rotation. As the loading continues to increase, the moment M approaches a maximum value, M_m, which may be larger or smaller than the plastic moment, M_p. For compact sections, M_m typically exceeds M_p because of strain hardening, and the moment-rotation curve remains above M_p over a significant range of rotation. For noncompact sections, M_m usually remains below M_p throughout the loading and may or may not reach M_y.

Additionally, the slope of the descending portion of the curve depends on not only the spacing of lateral supports for the compression flange but also the slenderness of the flange and the web. Compact and noncompact width to thickness ratios of the flange and the web are limited to prevent local buckling before the material reaches its yield strength. While local buckling is causing major distortions of the cross section and/or lateral buckling is causing large permanent lateral deflections, the descending curve continues indefinitely (Hartnagel, 1997).

When the load is fully removed after yielding has started, the unloading curve is usually parallel to the elastic loading curve. As a result, a residual permanent rotation, θ_r, remains while no permanent moment remains after the load is fully removed. If the same load is applied again one or more times, no additional yielding occurs, and thus any additional loading will follow up and down the original unloading curve (dashed line Figure 2.3.1.1) as long as the original maximum applied moment is not exceeded (solid line Figure 2.3.1.1). However, when the original load corresponding to that moment is surpassed, the additional load follows a continuation of the original curve. Consequently, the unloading from this higher load again follows a line still parallel with the original elastic loading curve but further apart.

The previous discussion of a typical moment-rotation curve shown in Figure 2.3.1.1 is based on the assumption that the loading is applied at a very slow rate in the inelastic range. In other words, the load and deflection (moment and rotation) are allowed to stabilize after each load or deflection (moment or rotation) increment in the inelastic range. If a deflection (or rotation) increment is rapidly applied and then held constant in the inelastic range, the load (or moment) will first exceed the theoretical value

indicated by the curve in the figure, but will gradually decrease to the theoretical value as it stabilizes after a few minutes. This behavior occurs because time is required to cause yielding (inelastic straining) of steel elements (Hartnagel, 1997).

Figure 2.3.1.2 illustrates the correlation between the negative moment region near a pier in a continuous span girder and a simple-span experimental specimen loaded in negative bending by a concentrated load at midspan, in which the midspan load simulates the pier reaction and the simple supports simulate the adjacent inflection points. For the simply supported span, the total girder rotation, composed of elastic and inelastic components, is equal to the sum of the end rotations, θ_{left}, and θ_{right}. For a prismatic member, the theoretical total elastic rotation, θ_e, is equal to:

$$\theta_e = \frac{ML}{2EI} = \frac{PL^2}{8EI}$$

where:

P = midspan load,

M = midspan moment of simply supported span, $M = \frac{PL}{4}$,

L = span length,

I = moment of inertia, and

E = modulus of elasticity.

While elastic rotation occurs over the entire length of the simply supported span, inelastic rotation intensively appears in a finite yield region at midspan and is calculated by subtracting the calculated elastic portion from the measured total rotation. Since the unloading portion follows a path with the same slope as the elastic loading portion, the plastic rotation caused by a given load is equal to the permanent rotation that remains

after the load has fully been removed. No additional plastic rotation occurs as long as no higher load is applied again.

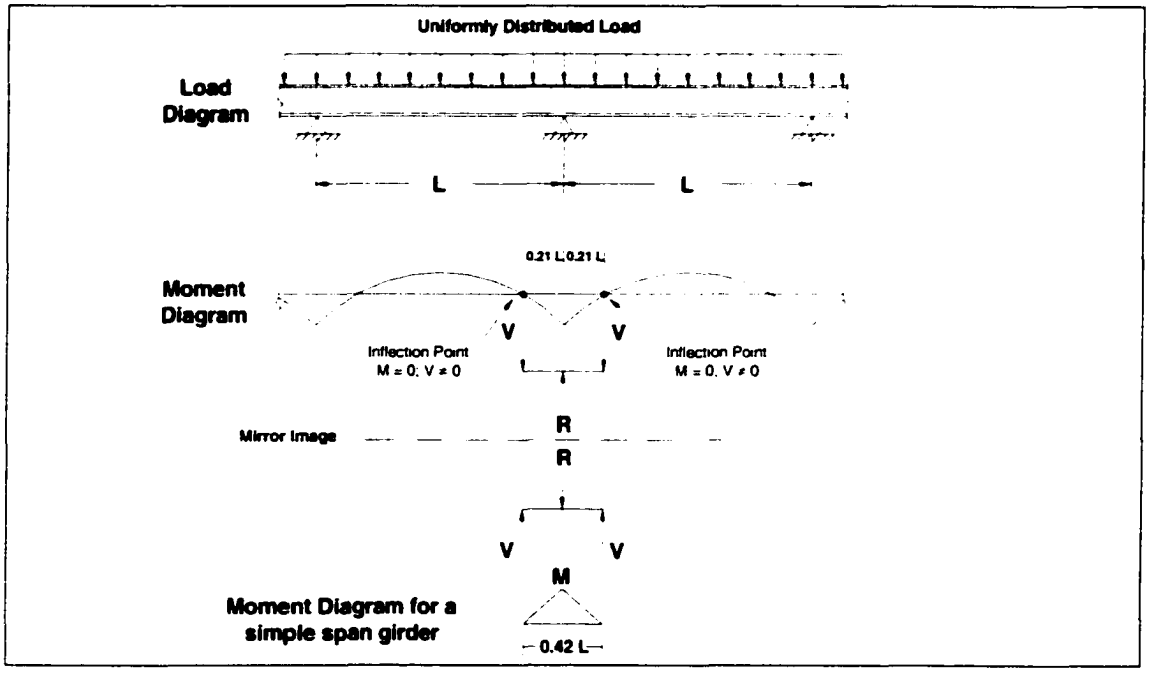

Figure 2.3.1.2 Correlation between the negative moment region near a pier in a continuous span girder and the experimental test girder

Moreover, although inelastic rotation actually occurs within a finite yield length, it is usually assumed to occur at a single cross section (infinitesimal length) for calculation simplicity in inelastic analysis and design procedures. Hence, the simply supported member is assumed to respond elastically over its entire length and plastically at a single, angular discontinuity (see Figure 2.3.1.3). The angular discontinuity is equivalent to cutting the member into two halves slightly off-square (more cut off in tensile yielding zone) and then welding the cut ends together. Thus, the inelastic rotation from yielding has the same effect on subsequent structural behavior as an angular discontinuity that can be built in to the member (Hartnagel, 1997). The resulting positive

moment at the interior support region, which only occurs when member is held down on the pier (usually by dead load), is useful in bridge design, since it reduces the overstressed negative moments and slightly increases the positive under stressed composite moment regions.

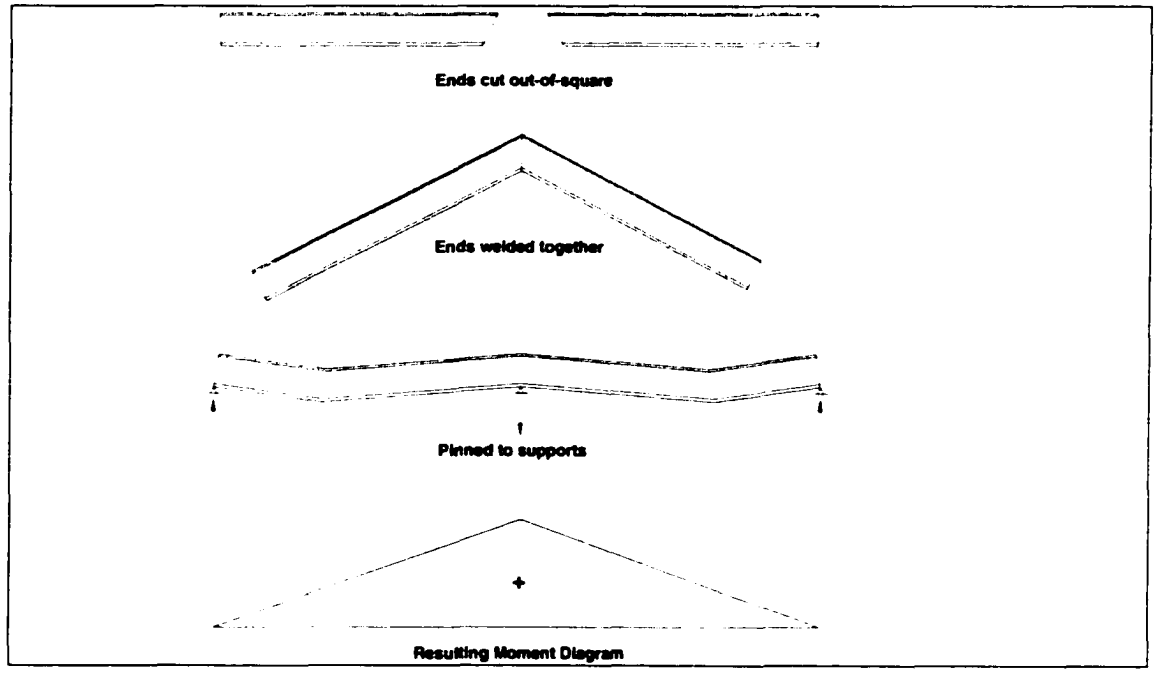

Figure 2.3.1.3 Plastic rotation analogy

2.3.1.2 Composite sections

- *Positive bending*

There are several considerable differences although the inelastic behavior of composite girders in positive bending is similar to that discussed earlier for noncomposite members. For composite sections, yielding first starts in the tension flange (bottom flange in positive bending) at a load below that corresponding to the yielding moment, M_y, because of residual stresses. As the loading continues, yielding then progresses

through the bottom flange, web, and top flange and eventually causes tension cracking of the concrete slab's lower portion. During this stage, the moment-rotation curve continues to rise until a failure load is ultimately reached when the concrete in the top portion of the slab suddenly crushes.

The descending portion of the moment-rotation curve is not similar to that for noncomposite sections since local buckling and lateral buckling do not occur when most of the steel section is in tension. Consequently, the failure moment, M_m, usually exceeds the plastic moment, M_p, due to the strain hardening. Depending on the proportions of the cross section, the difference between M_m and M_p can be high as 35 percent (Ansourian, 1982; Rotter and Ansourian, 1979). In addition, the shape factor, M_p/M_y, for composite sections in positive bending, which ranges up to 1.50, is usually considerably larger than that of noncomposite I-sections, which is usually less than 1.15. As a result, yielding usually starts at a much lower percentage of M_p, and there is a large rounded portion of the moment-rotation curve between M_y and M_p.

The unloading behavior is basically the same as that for noncomposite sections. Unloading in the inelastic range follows a line parallel with the original elastic loading curve on the moment-rotation plot unless the applied load exceeds that required to cause tension cracking in the slab. After all load is removed, a permanent deflection and rotation, but no moment, remains.

If the load is applied to the steel section before the slab has hardened, this section will behave as a noncomposite section. Any yielding that occurs during this stage will cause a permanent angular discontinuity that remains in the composite member after the slab has hardened, but the composite section is not otherwise affected (Hartnagel, 1997).

The dynamic yield effects also apply to composite sections as discussed for noncomposite sections (see Section 2.3.1.1).

- *Negative bending*

Simply supported composite girders are not normally loaded in negative bending. However, inelastic behavior under such loading is discussed here because it simulates behavior in negative-bending regions of continuous spans (see Figure 2.3.1.2). A typical moment-rotation curve for a simple-span composite member loaded in negative bending by a concentrated load at midspan is illustrated in Figure 2.3.1.4.

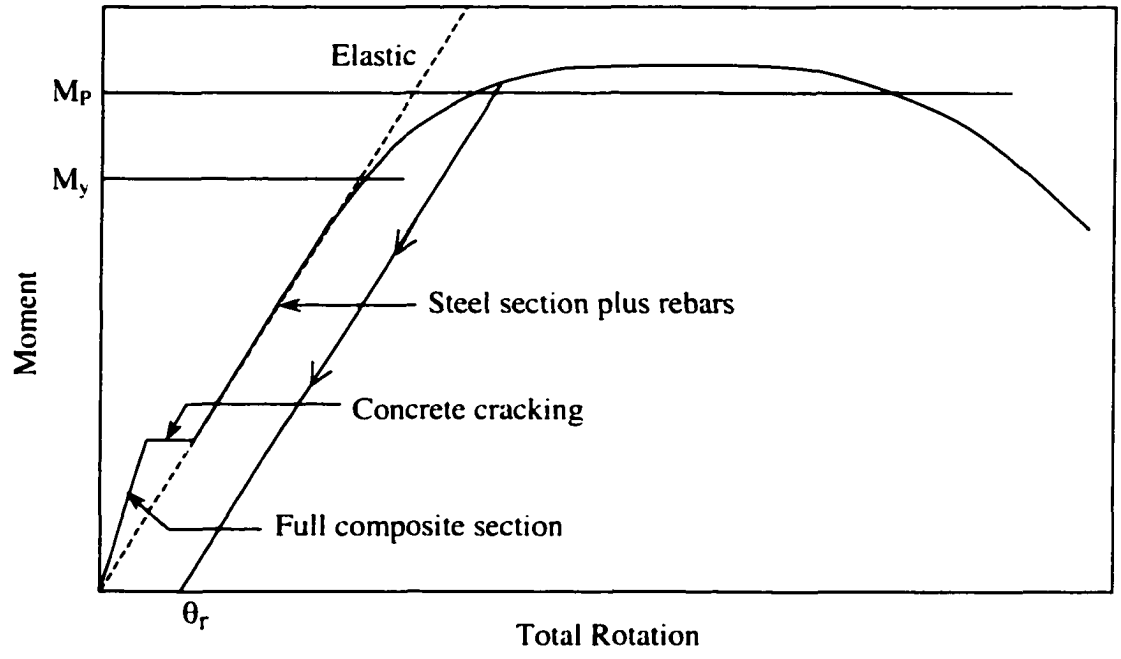

Figure 2.3.1.4 Typical moment-rotation curve for composite section in negative bending.

The initial slope of the ascending portion of the curve is defined by the stiffness of the uncracked composite section. When cracking of the concrete slab occurs, the

ascending portion shifts to a new position as shown in the figure (Carskaddan, 1991). A horizontal shift will occur if the moment is held constant during concrete cracking. If the rotation is held constant, a vertical shift will occur. In either case, the new position falls on the curve for the cracked section that consists of the steel section plus the rebars. Like the uncracked-section curve, the cracked section curve passes through the origin.

The composite member behaves afterward as a noncomposite member as previously discussed, and the unloading curve is parallel with the ascending elastic line for the steel section plus the deck reinforcement. As shown in the Figure 2.3.1.4, the permanent rotation, θ_r, which remains after fully unloading for a moment above the cracking moment, is the plastic rotation for that moment. Hence, cracking of the slab does not contribute to the plastic rotation (Carskaddan, 1991).

In addition, the effect of loads applied to the steel section before the slab has hardened is the same as previously discussed. Any yielding that occurs during this stage will cause a permanent angular discontinuity that remains in the composite member after the slab has hardened, but the composite section is not otherwise affected.

2.3.2 Redistribution moments in continuous span girders

Positive- and negative-bending regions between inflection points in continuous spans behave like simple spans in developing plastic rotations as discussed previously. However, when simple spans are joined together into a continuous span, permanent moments and also permanent deflections automatically develop as a result of yielding at any cross section. Hence, these permanent moments are often called automoments

(Grubb, 1985; Haaijer et. al., 1970, 1987, and 1993) or redistribution moments since they are caused by a redistribution of the elastic moments (AASHTO, 1998 and interim 2001).

As a continuous-span girder is progressively loaded, no redistribution of moments occurs along the span until yielding starts at any location. Thereafter, the distribution of moments change because of the resulting plastic rotation (angular discontinuity) at the yield location as the loading continues to increase. Specifically, a shifting of moment from the yield location to other adjacent locations occurs because the moment at the yield location increases at a slower rate than it did in the elastic range. In continuous-span bridge girders, yielding usually starts first at piers and shifts moment from negative- to positive-bending regions (Hartnagel, 1997).

2.3.2.1 Due to yielding at pier in continuous spans

For a two-span girder, the development of redistribution moments due to yielding at the pier that causes a permanent angular discontinuity can be simulated by cutting the ends of two girders slightly off square and then welding them together end to end (see Figure 2.3.1.3). As discussed previously in Section 2.3.1, when the spliced girder is placed on the abutments and held down against the pier (usually by dead load or by a downward reaction at the pier), redistribution moments occur along the girder as illustrated in an exaggerated manner in the figure (Hartnagel, 1997).

For a three-span girder, Figure 2.3.2.1 conceptually illustrates how to determine the magnitude of the redistribution moments and permanent deflections by classical methods of indeterminate analysis if the amount of the plastic rotation at Pier 1 is known. In these methods, the continuous span is treated as a series of simple spans. Depending

on the known pier plastic-rotation and the stiffness of the adjacent spans, the end moments necessary to restore continuity and thus the magnitude of the redistribution moments are determined.

Redistribution moments must peak at pier locations and vary linearly between reactions because the redistribution moments are held in equilibrium by the reactions at the piers and abutments. In addition, if yielding and plastic rotations occur at more than one pier, the total redistribution moments will be the summation of the redistribution moments that are caused by the plastic rotation at each pier and can be separately calculated. Subsequent loading may cause additional yielding and thus modify the redistribution moments.

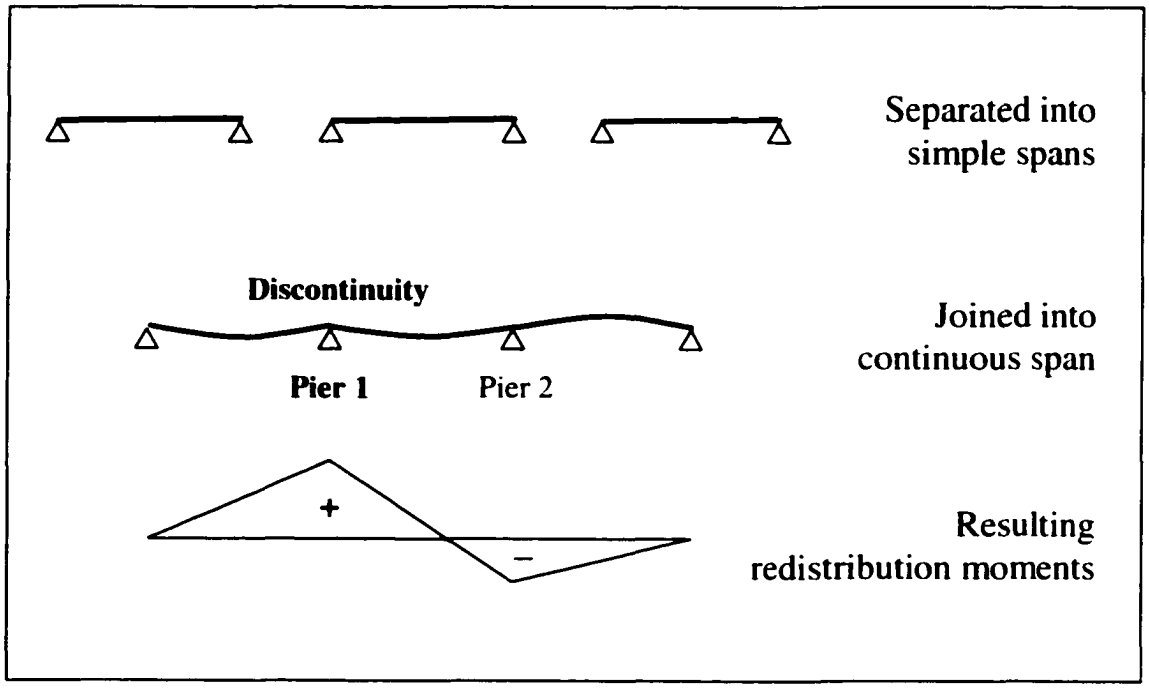

Figure 2.3.2.1 Redistribution moments due to discontinuity at Pier 1

2.3.2.2 Due to yielding within a span

Plastic rotations and thus redistribution moments are also caused by yielding at peak-moment and splice locations within a span. Figure 2.3.2.2 illustrates the development of such redistribution moments for yielding at midspan of Span 1 of a three- span girder. Again, the plastic rotation is assumed concentrated in an angular discontinuity and the continuous span is conceptually separated into three simple spans. The end slopes caused by the angular discontinuity are defined by:

$$S = \frac{aR}{L}$$

where:

S = the slope at one end of the span,

R = the plastic rotation assumed at the angular discontinuity

a = the distance from the angular discontinuity to the opposite end, and

L = the span length.

As previously discussed, the ends moments necessary to restore continuity and thus the redistribution moment as well as permanent deflections caused by the known plastic rotation can be determined with classical methods of indeterminate analysis.

Held in equilibrium by the reactions, these redistribution moments must again peak at pier locations and vary linearly between reactions. The total redistribution moments for the girder will be the combination of the redistribution moments caused by yielding at other locations within the span, within other spans, and redistribution moments due to yielding at piers that can be calculated individually. Additionally, yielding at any span or pier location causes redistribution moments throughout the girder (Hartnagel, 1997).

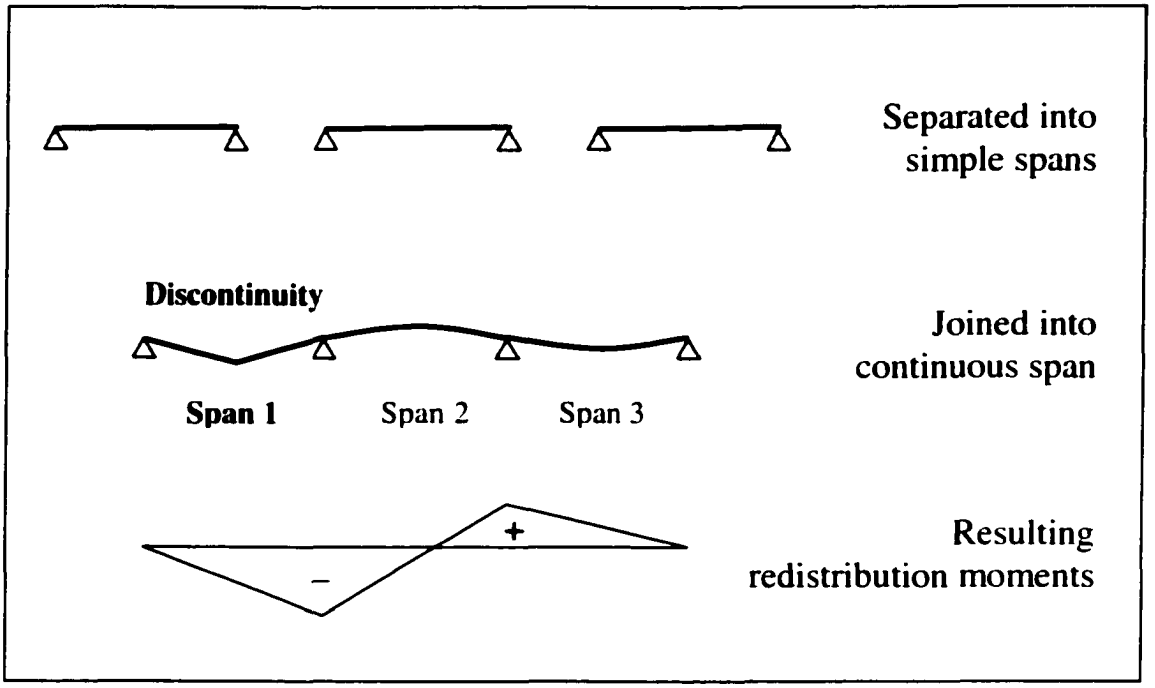

Figure 2.3.2.2 Redistribution moments due to discontinuity in Span 1

2.3.2.3 Relationships defining moments and deflections

The correct moments for any loading are equal to the algebraic sum of elastic moments caused by the applied loads and the redistribution moments due to yielding during this loading (or some previous loading). If the same loading is repeated, no additional yielding and thus no changes in redistribution moments and permanent deflections occur. However, a higher loading will cause additional yielding and hence change the redistribution moments and permanent deflections. In addition, a different distribution of loads may or may not cause additional yielding and variation in redistribution moments.

In order to uniquely define the redistribution moments and permanent deflections and thus fully characterize the inelastic behavior of the girder, it is necessary to determine the plastic rotations caused at all yield locations by a given loading as discussed earlier.

All plastic rotations, as mentioned previously, are assumed concentrated in angular discontinuities and the rest of the girder is assumed elastic. Two relationships are available to define these plastic rotations: a continuity relationship and a rotation relationship. These two relationships provide simultaneous equations to uniquely determine the moments and plastic rotations throughout the girder.

The continuity relationship interrelates the plastic rotations and total moments, which are elastic moments due to applied loads plus redistribution moments, along the girder. The continuity relationship depends on the distribution of stiffness along the girder and provides one equation at each pier location. The rotation relationship is the plastic-rotation curve as discussed previously. The ascending portion of this curve depends primarily on the spread of yielding throughout the cross section and along the length of the member, the initial pattern of residual stresses, and the girder proportions (ratio of the flange area to web area). The descending portion depends primarily on the compression-flange slenderness, web slenderness, and compression-flange bracing spacing. The rotation relationship provides one equation at each yielding location (Hartnagel, 1997).

2.3.2.4 Ultimate strength

When the moment at a critical location can no longer be shifted to other locations, the theoretical ultimate strength is reached. For an interior span, this occurs when the effective-plastic-moment capacity is reached at three locations defining a mechanism (ASCE, 1971; Beedle, 1958). If strain hardening is ignored, the theoretical ultimate strength corresponds to the maximum loading that can theoretically be applied to the

girder. However, the actual ultimate strength (maximum loading) may be higher due to the strain hardening when the critical sections are sufficiently compact.

As the loading is increased, large plastic rotations may occur at some yield locations, and thus the moment is shifted to other locations as discussed previously. While these plastic rotations are occurring, the corresponding moments vary as defined by the appropriate moment-plastic-rotation curves mentioned earlier (see Figure 2.2.1). In the continuous-span bridge girders, pier sections are usually required to sustain such large plastic rotations to reach ultimate strength. If the sections are noncompact, the moment-plastic-rotation relationship may be into the descending portions of the curves so that the effective-plastic-moment capacities at those locations may be properly below the full theoretical plastic moments. In addition, peak positive-bending moment locations may also sustain significant plastic rotations. If such sections are composite, however, those locations sustain the plastic rotations without a decrease in moment capacity as discussed earlier (Hartnagel, 1997).

2.3.3 Multigirder systems

The inelastic redistribution of moments discussed above arises longitudinally within a single continuous-span steel girder. In multigirder bridges, inelastic redistribution of moments can also occur laterally among the individual steel girders. The inelastic lateral redistribution of moments can develop in both simple-span and continuous-span bridges and provides a reserve strength that is not normally accounted for in design or rating (Barker and Galambos, 1992).

The development of inelastic lateral redistribution of moments can be demonstrated by considering a four-lane simple-span bridge that consists of six identical girders and is loaded by a single vehicle in an outer lane. Caused by this type of loading, the elastic moments in the individual girders vary from a maximum in the exterior girder under the load to a much smaller moment in the other exterior girder. The actual distribution of the elastic moments among the girders depends on the ratio of the longitudinal stiffness of the girders over the lateral stiffness of diaphragms or cross frames and the slab.

As the loading continues to increase, no lateral redistribution of moments among the girders occurs until yielding initiates in the exterior girder under the load. Afterward, the loaded exterior girder reduces its stiffness and thus takes a smaller fraction of any additional loading. Once the moment in the exterior girder reaches its maximum-moment capacity, additional loading must be carried by other girders of the multigirder bridge. Consequently, the lateral distribution of moments becomes uniform.

Additionally, if the exterior girder is compact, the post-peak moment it carries will remain constant for a while as the other girders continue to take additional moment. However, if the exterior girder is noncompact, the moment it carries may decrease in conformance with its rotation curve as the other girders continue to take additional moment. When plastic hinges form in all girders, the ultimate strength of the bridge is reached.

Furthermore, inelastic redistribution of moments usually occurs in both the longitudinal and lateral directions for continuous-span multigirders. Continuity and rotation relationships apply at all yield locations in the girders, as well as redistribution

moments, plastic rotations, and permanent deflections develop as previously discussed. However, the deflections of the individual girders are now interrelated by elastic bending of the slab and diaphragms or cross frames in the lateral direction. Consequently, the loading carried by each girder, which is a given in the analysis of an individual girder, changes with respect to both total magnitude and distribution along the length as plastic hinges develop in the girders (Hartnagel, 1997).

Finally, the importance of inelastic lateral distribution of moments depends primarily on the lateral position of the loading. For loading with a large lateral eccentricity (i.e. loading only in the outside lane of a multilane bridge), considerable additional load can be applied after a mechanism forms in the first girder. However, there is no reserve strength for loading distributed laterally in such a way that the elastic moments are the same in all girders since all girders form mechanisms at the same loading.

2.3.4 Incremental collapse and shakedown

In a continuous-span girder, incremental collapse occurs when a sequence of loads causes progressive increases in permanent deflections without limit. On the other hand, shakedown, also called deflection stability, occurs when permanent deflections stabilize after a finite number of loading cycles and all subsequent behavior is fully elastic. Studies of incremental collapse and shakedown in continuous-span girders have been extensively conducted by Eyre and Galambos (1970 and 1973), Grundy (1976 and 1983), Gurley (1981 and 1982), Fukomoto and Yoshida (1969), Toridis and Wen (1966),

and others (Eyre and Galambos, 1969), especially in connection with plastic-design requirements for buildings (ASCE, 1971 and Beedle, 1958).

In a structure that satisfies classical plastic-design assumptions, shakedown occurs if a pattern of redistribution moments can be found such that the algebraic sum of these moments and the elastic moments due to a loading in the sequence is not numerically larger than the plastic-moment capacity at any location (ASCE, 1971). The main plastic-design assumption related to shakedown is that all sections must have moment-rotation curves that can be satisfactorily approximated by an ascending straight line to the plastic moment preceding a horizontal line extending sufficiently to allow the development of the required redistribution moments (see Figure 2.2.1). Compact noncomposite sections of conventional steel satisfy this requirement (Hartnagel, 1997).

Actual compact structures always reach shakedown at higher loads than predicted by the classical theory (ASCE, 1971) since the strain hardening is ignored in the assumed moment-rotation curve mentioned above. In addition, because redistribution moments cannot develop in simple spans, incremental collapse does not occur in such spans. Consequently, the spans behave elastically, according to the assumed moment-rotation curve, until the applied moment exceeds the plastic-moment capacity at some location due to a particular loading in the sequence. The spans then theoretically collapse under that loading.

Experimental determinations of shakedown for a sequence of loadings are usually performed in the following way (ASCE, 1971 and Beedle, 1958). Each loading in the sequence consists of a set of concentrated and/or distributed loads applied in specified directions at specified locations. The magnitude of a sequence is defined by a single

factor that applied to all individual loads in the sequence, and all individual loads in all sets in the sequence are interrelated by specified ratios. In the test, a sequence of loadings with a low factor is applied first and repeated. The permanent deflections generally increase by a successively smaller amount each loading cycle. If the permanent deflections finally stabilize, shakedown has been achieved for that factor. Then the process is repeated with progressively higher factors until a critical factor, for which the permanent deflections do not stabilize, is reached.

2.3.4.1 Due to sequential loading for compact bridge girders

Recently, studies of incremental collapse and shakedown in continuous-span girders have been extensively conducted by Barker (1990 and 1995), Barker and Galambos (1992), Weber (1994), and others (Galambos et. al., 1993). The incremental collapse and shakedown behavior will be discussed first for compact noncompopsite girders, which satisfy the classical plastic-design assumptions, and later for noncompact girders, which present somewhat more complex behavior.

Figure 2.3.4.1 shows how incremental collapse or shakedown can happen in a symmetrical three-span compact noncompopsite girder due to repeated passages of heavy trucks across the bridge. To symbolize the passage of two trucks with a constant spacing, a set of two concentrated loads is consecutively placed at different critical locations on the bridge in the figure.

For any particular position of the live loads, the resulting elastic moments that occur throughout the girder do not change. However, redistribution moments develop due to yielding and are modified by repeated passages of these loads. Additionally,

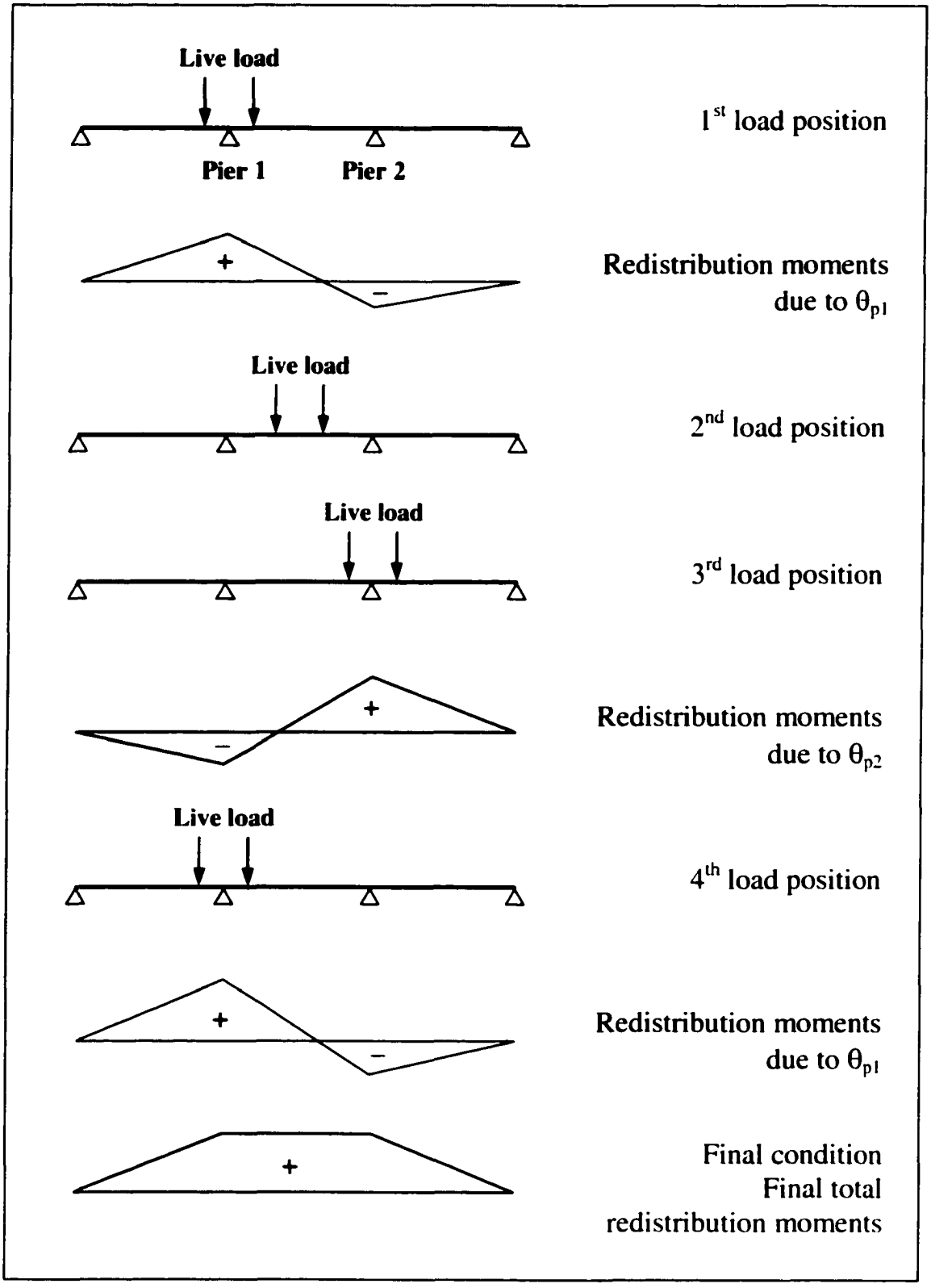

Figure 2.3.4.1 Redistribution moments for sequential loading

yielding is assumed to occur only when the elastic moment combined with the redistribution moment at any section exceeds the plastic-moment capacity. Hence, the small amount of yielding that occurs between the yield moment and the plastic moment is neglected corresponding to classical-design plastic assumptions (Hartnagel, 1997).

First, the live loads stand astride Pier 1. Combined with the dead load, the loads are assumed to cause a negative-elastic-moment exceeding the negative-plastic-moment capacity at that pier. The resulting plastic rotation at Pier 1, θ_{p1}, thus causes the shown redistribution moments. At the pier, the algebraic sum of the negative-elastic-moment and the positive-redistribution-moment equals the negative-plastic-moment capacity.

Second, the live loads are placed midway between the two piers to cause the maximum possible positive moments in Span 2. It is assumed that the resulting positive-elastic-moment combined with the existing positive-redistribution-moment due to θ_{p1} does not exceed the positive-plastic-moment capacity at critical locations so that no change in plastic rotation and no redistribution moment occur.

Third, the live loads are then advanced to straddle Pier 2. Due to symmetry, they cause the same negative-elastic-moment at that piers as was originally caused at Pier 1. The combination of the negative-elastic-moment caused by the dead and live loads and the negative-redistribution-moment due to θ_{p1} is assumed to exceed the negative-plastic-moment capacity of the section so that a plastic rotation, θ_{p2}, occurs at that pier. As shown, the resulting positive-redistribution-moment at Pier 2 due to θ_{p2} is higher than the original positive-redistribution-moment at Pier 1 due to θ_{p1} by an amount equal the negative-redistribution-moment at Pier 2 due to θ_{p1}. The total redistribution moment at

that stage, and at subsequent stages, is equal to the sum of the redistribution moments due to plastic rotations, θ_{p1} and θ_{p2}, at Piers 1 and 2.

Fourth, the live loads are now returned to straddle Pier 1 and cause an additional plastic rotation and thus a higher positive-redistribution-moment at that pier. The new positive-redistribution-moment at Pier 1 due to the additional plastic rotation at Pier 1 must increase because it is now equal to the negative-elastic-moment combined with the negative-redistribution-moment at Pier 1 due to θ_{p2}, which was zero when the live loads first straddled Pier 1, minus the negative-plastic-moment capacity.

As this loading sequence proceeds, the plastic rotations at the two piers and thus the resulting redistribution-moments continue to increase, but at slower rate, until they stabilize at the final redistribution-moments shown. If the final positive-redistribution-moment combined with the maximum positive-elastic-moment (when the live loads are placed between the piers) does not exceed the positive-plastic-moment capacity at that location, shakedown has occurred. Otherwise, incremental collapse will occur since the positive-bending section cannot sustain any more moment shifted from negative-bending regions through the formation of the redistribution moments (Hartnagel, 1997).

2.3.4.2 Due to sequential loading for noncompact bridge girders

For typical composite noncompact bridge girders, the simple bilinear plastic-rotation curve previously assumed in the classical plastic-design theory is not appropriate. In negative-bending regions at piers, the maximum moment for such girders is usually limited to the yield-moment, rather than the plastic-moment capacity. In addition, the amount of plastic rotation at the pier that occurs before unloading is much smaller than

for noncomposite compact sections. In positive-bending regions between the piers, however, the composite sections are usually compact since the location of the neutral axis is shifted so that less web is in compression. Such sections hence sustain considerable plastic-rotations between the yield and plastic moments as described previously. As a result, it is not appropriate to assume that the rotation curve for such sections is elastic to the plastic moment as is done in classical plastic-design theory.

Although those differences in the rotation curves exist, incremental collapse or shake down develops in much the same way for noncompact bridge girders as was discussed for compact bridge girders. As a sequence of loadings is applied, the actual development of the permanent deflection and redistribution moments can be mathematically traced by the unified autostress method (Schilling, 1989, 1991, and 1993) or the residual-deformation method (Dishongh, 1990 and 1992; Dishongh and Galambos, 1992). Again, shakedown will occur if all positive-bending sections can accept more moment shifted from negative-bending regions through the formation of redistribution moments under a sequence of loadings. Otherwise, incremental collapse will happen when a positive-bending section cannot sustain any more moment shifted.

Nonetheless, the following differences in shakedown behavior exist for noncompact girders compared to compact girders. At each pier in noncompact girders, the algebraic sum of the negative-elastic-moment and the positive-redistribution-moments due to plastic rotations at all yield locations cannot exceed the yield-moment capacity (instead of the plastic-moment capacity for compact section) of the cracked section. In addition, the algebraic sum may need to be limited to an even lower value if the plastic rotation at the pier is large enough to be on the descending portion of the

moment-rotation curve. Besides, yielding will usually occur in positive-bending regions and influence the development of redistribution moments and permanent deflections. Particularly, each plastic rotation in a positive-bending region causes redistribution moments (throughout the girder) that thus adds to or subtracts from the maximum elastic moment at each pier (Hartnagel, 1997).

In a composite noncompact girder, shakedown will occur if the algebraic sum of the elastic moment and all redistribution moment does not exceed (1) the plastic-moment capacity at each positive-bending section and (2) the effective-plastic-moment capacity at each negative-bending section. For the conventional steels, this effective-plastic-moment capacity does not exceed the yield-moment capacity and depends on the plastic rotation expected to occur after the permanent deflections due to a sequence of loadings have stabilized (i.e. at shakedown). The elastic moment mentioned above is the maximum that can occur at the section, which is checked for any position of live loads, and thus can be obtained from the elastic-moment envelope (Hartnagel, 1997).

2.3.4.3 Due to dynamic yielding

Time is required to cause yielding (inelastic straining) of steel elements as discussed in Section 2.3.1.1, and this dynamic yielding effect can cause progressive increases in permanent deflections that are similar to those for continuous-span girders under sequential loadings as discussed previously. In simply supported girders, the progressive increases in permanent deflections can occur due to dynamic yielding, but not due to sequential loadings. In continuous spans, however, progressive increases in permanent deflections can occur due to dynamic yielding and/or sequential loading (Ho,

1972). Hence, in continuous spans under sequential loadings, dynamic yielding effects can increase the number of loading cycles required to achieve shakedown or cause incremental collapse.

Dynamic yielding affects the development of permanent deflections in the following way. If a stationary heavy truck on a simple-span girder bridge causes a midspan moment above the yield-moment capacity, but below the plastic-moment capacity, the resulting permanent deflection can be theoretically predicted. To isolate the effect of dynamic yielding, consider a number of fast passages of a similar, but lighter, truck that causes the same elastic stresses, which is possible due to impact load, as the stationary truck. Since the full permanent deflection does not have time to develop before the truck has left the bridge, the first passage will cause significantly smaller permanent deflections than the stationary truck. Each subsequent passage of the lighter truck at the same speed will cause an additional increment of permanent deflection until the total reaches the value theoretically predicted for the stationary truck. Experimental observations show that the permanent-deflection increment, which depends on the speed and weight of the truck, is usually largest for the first passage and decreases progressively for subsequent passages. Apparently, this is because the differences between the actual and full permanent deflection decreases with each passage and asymptotically approaches zero (Hartnagel, 1997).

If a stationary heavy truck on a simple-span girder bridge cause a moment above the plastic-moment capacity (or maximum-moment capacity when this capacity is considerably above the plastic-moment capacity due to the strain hardening), the girder will collapse. If the similar lighter truck, which causes the same elastic stresses as the

stationary truck, travels across the bridge at a fast speed, the bridge probably will undergo significant permanent deflection instead of collapse. Subsequent passages of this truck will cause additional increments of permanent deflection and eventual collapse of the bridge. Hence, permanent-deflection increases due to dynamic yielding, as well as sequential loading, can result in either shakedown or incremental collapse.

The AASHTO road tests by Highway Research Board (HRB, 1962a and 1962b) provided experimental evidence of the effects of dynamic yielding consistent with the theoretical behavior described above. Ten composite and noncomposite steel beam bridges with simple spans of 50 feet were subjected to many passages of trucks traveling at speeds between 20 and 50 mph. The bridges were one lane wide and utilized three parallel beams. Most of the bridges (bridges 1A, 2B, 3B, 9A, and 9B) were subjected to about 500,000 truck passages and illustrated shakedown behavior, in which the permanent defections increased rapidly during the initial phases of the regular test traffic, but then the bridges turned into almost stable after a few hundred passages (HBR, 1962b). However, tests of some (bridges 1B, 2A, 4A, and 4B) terminated earlier when excessive permanent deflections occurred within a few hundred passages and illustrated incremental collapse, in which the permanent deflections did not stabilize and were expected to continue without limit. The mean measured dynamic strains developed in the beams of a particular bridge by a particular truck remained approximately constant over the life of the test. However, the stresses caused by individual passages varied considerably about this mean.

2.3.4.4 Alternating plasticity

Alternating plasticity, which occurs when a section is subjected to repeated reversals of moments large enough to cause yielding in both directions (American Society of Civil Engineers (ASCE), 1971), is another type of deflection instability that has been studied in connection with plastic-design requirements. A stable hysteretic loop forms if such yielding occurs, but repeated load applications will eventually cause failure by low-cycle fatigue (Hartnagel, 1997).

However, significant alternating plasticity does not occur if the range of alternating moments does not exceed twice the yielding-moment capacity of the section (ASCE, 1971). The behavior will instead remain basically elastic if this limit is not exceeded. If ever, the limit is rarely exceeded in highway bridges. Consequently, alternating plasticity need not be considered in the inelastic design of such bridges although it is of concern mainly in earthquake design of buildings.

2.3.5 Fatigue

It is occasionally questioned whether or not yielding permitted in the inelastic design of bridges unfavorably affects fatigue life. As previously discussed, the yielding permitted at piers (and other locations) eventually causes redistribution moments that assure elastic behavior during subsequent loadings being the same or lesser in magnitude. Additionally, the amount of yielding that can occur at these locations is restricted by the elastic behavior of the remaining structure. In this respect, the yielding is similar to that occurring in the web, due to residual stresses or moment above the yield moment for compact sections, of hybrid beams (ASCE-AASHO, 1968) or even in bridges designed

by elastic procedures. In all of these cases, the elastic portions of the structure restrict local yielding so that elastic behavior eventually develops.

Such yielding usually lowers the peak residual stresses and thus modifies the original residual-stress distribution that occurs in most steel members (Schilling, 1984). However, the yielding does not change the stress range caused at a point by a truck passage across the bridge, but simply shifts the stress range by changing the magnitude of the constant superimposed-residual-stress. Such a shift does not generally change the fatigue life significantly because stress range is the main stress parameter controlling fatigue life. Tests have confirmed that the fatigue lives of hybrid beams are not reduced by restricted local yielding of the web (Frost and Schilling, 1964) although there are exceptions that rarely apply to the cases under discussion (Schilling, 1984).

Consequently, the effects on fatigue behavior of restricted local yielding, in the webs of hybrid beams and in elastically designed homogenous beams, are not considered in the bridge specifications (AASHTO, 1998 and interim 2001; ASCE-AASHO, 1968). It is reasonable to also neglect the effects on fatigue behavior of the same kind of restricted local yielding in inelastically designed beams and girders (Hartnagel, 1997).

2.4 Experimental Moment-Rotation Behavior Of Compact And Noncompact Conventional Steel Girders

2.4.1 University of Missouri-Columbia, Hartnagel, 1997 (noncomposite and composite)

Bryan Hartnagel, while at the University of Missouri-Columbia, experimentally studied inelastic procedures to determine the true strength of continuous, composite bridge girders constructed from conventional steel (F_y = 50 ksi) (Hartnagel, 1997). The

research emphasized three objectives: (1) proposing new comprehensive and practical inelastic procedures that allow compact and noncompact sections, (2) experimentally verifying inelastic limit state behavior with large scale continuous span tests of composite girders, and (3) examining the moment rotation behavior of compact and noncompact pier sections.

Experimental modeling and testing of compact and noncompact continuous girders, which were fabricated from steel having specified minimum nominal yield stress, F_y, not exceeding 50 ksi, were conducted to verify inelastic design limits and investigate inelastic behavior. The tests for the three-span composite compact girder consisted of one three-continuous-span-girder test and four component tests, which were three composite and one noncomposite similar to the compact bridge girder section (see Appendix, Section A.1, Hartnagel's dissertation, Figures 3.7, 3.8, 3.17 and 3.18). In addition, one two-continuous-span-girder test and two component tests, one composite and one noncomposite similar to the noncompact bridge girder section, were also conducted for the two-span composite noncompact girder (see Appendix, Section A.1, Hartnagel, 1997, Figures 4.11 and 4.12). All component tests were set up in double cantilever manner to simulate the pier region of a bridge girder.

For these tests, lateral bracing satisfying the AASHTO requirements (see Section 2.2.1) were provided. In addition, measurement instruments utilized were: (1) load cells to measure loads, (2) Linear Variable Displacement Transducers (LVDT), deflection dial gages, and string-potentiometers attached to the underside of the girders to directly obtain deflections, (3) LVDTs, deflection dial gages, and string-potentiometers attached to the

underside of the girders, at known distances within the spans, to indirectly acquire rotations, and (4) quarter-bridge-configuration strain gages to measure strains.

Results from experimental testing girders subjected to simulated moving truckloads were then compared to design limit states of AASHTO LRFD inelastic design bridge specifications (see Appendix, Section A.1, Hartnagel, 1997, Figures 3.12, 3.19 to 3.22, and 4.14, 4.20 to 4.21). New simplified procedures are proposed to satisfy the two limit states, the Service Limit State Control of Permanent Deflection and the Strength Limit State, applicable to both compact and noncompact sections. The proposed procedures utilize elastic moment envelopes and do not require successive loadings, iterative procedures, or simultaneous equations.

In brief, inelastic steel bridge design procedures allow the redistribution of negative pier region elastic moments to adjacent positive moment regions and hence account for the reserve strength inherent in multiple span steel girder bridges. The moment redistribution causes slight inelastic rotation at the intermediate support regions, residual moments in the beam, and some permanent deflection. After the redistribution, the structure achieves shakedown, and thus deformations stabilize as future loads are resisted elastically.

2.5 Experimental Moment-Rotation Behavior Of Compact And Noncompact HPS Girders

2.5.1 Lehigh University, Fahnestock and Sause, 1998 (noncomposite only)

Experimental testing by Fahnestock and Sause at Lehigh University investigated the use of HPS100W steel in highway bridges and the flexural strength as well as the ductility anticipated by current design specifications (Fahnestock & Sause, 1998). Two

girders, one fully compact (Specimen 1) and one fully noncompact (Specimen 2), were formulated consistent with the AASHTO LRFD specifications. The specimens were loaded to failure under three-point-loading which replicated the condition of negative flexure at an interior pier of a continuous span bridge.

For these tests at Lehigh University, lateral bracing satisfying the AASHTO requirements (see Section 2.2.1) were applied. In addition, measurement instrumentation employed were: (1) load cells to measure loads, (2) strain gages to measure strains, (3) LVDTs and dial gages to directly obtain deflections, and (4) rotation meters attached along the length of the girders to acquire rotations (see Appendix, Section A.2, Fahnestock & Sause, 1998, Figures 3.10 and 3.11).

In brief, Specimen 1 (the compact girder) exhibited an ultimate flexural strength three percent greater than the plastic strength anticipated by the AASHTO LRFD specifications, but revealed a rotation capacity, R, of 0.28, less than the anticipated rotation capacity of three (common value considered necessary for redistribution of moments of a compact girder in buildings (AISC LRFD, 2nd edition, 1998)). As a result, the flexural ductility of Specimen 1 may be sufficient for bridge I-girders, although further investigation of this is needed. In addition, Specimen 2 (the noncompact girder) displayed an ultimate flexural strength three percent less than the plastic strength expected by the AASHTO LRFD specifications, and did not have a rotation capacity, R, as defined in Section 2.3.1 (see Appendix, Section A.2, Fahnestock & Sause, 1998, Figures 4.18 to 4.21 and 5.19 to 5.22). It was thus concluded that the inelastic analysis procedures of the AASHTO LRFD specifications should not be permitted for HPS100W

steel I-girders, both compact and noncompact cross sections, until evidence is provided that these I-girders offer sufficient flexural ductility.

2.5.2 University of Nebraska-Lincoln, Yakel, Mans, and Azizinamini, 1999 (noncomposite only)

Researchers at the University of Nebraska-Lincoln experimentally tested the flexural capacity of HPS70W I-shape girders fabricated of mainly HPS70W steel as well as 50W steel (Yakel, Mans, & Azizinamini, 1999). Their report discussed two tests for compact and noncompact sections and compared the experimental results to the corresponding numerical estimates using finite element method (see Section 2.6.4). A primary objective of the testing was to investigate the validity of current AASHTO limitations related to the maximum allowed yield strength. Another intention was to develop sets of experimental data that could be used to verify numerical finite element models reproducing the flexural behavior of steel plate girders. Besides, moment capacity as well as the interaction of unbraced lengths and local buckling of the flange and web were also of primary concern.

In these studies at the University of Nebraska, two girders of similar dimensions were designed, constructed, and tested in the conventional simply supported configuration (see Table 2.5.2.1). In proportion to AASHTO specifications, Girder A was formulated to be noncompact (web noncompact, flanges compact) while girder D was compact (flanges compact, web compact). A feature of the two girders was that HPS70W steel was utilized in the midspan region of both the flanges and web while 50W steel was employed in the flanges and web in the end regions. To join both the flange and the web plates in both girders, a number of butt welds were applied, precipitated by

the span length. As opposed to girders consisting of only HPS70W steel, the choice to fabricate girders composed to two types of steel was a direct result of the availability (or lack thereof) of HPS at the time of fabrication. The appropriate design was established based on the assumption that the end regions of the girders would respond elastically to the loading.

Table 2.5.2.1 University of Nebraska girder dimensions

Property	Girder A (noncompact)	Girder D (compact)
Test span, L (ft)	62	53
Web depth inside flanges, D (in.)	34	28 ¾
Web thickness, t_w (in.)	3/8	3/8
Flange width, b_f (in.)	16 ¼	16 ¼
Flange thickness, t_f (in.)	1 ¼	1 ¼
Ratio of web depth in compression, D_{cp}/D	0.5	0.5
Nominal flange slenderness, $b_f/2t_f$	5.4	5.4
Nominal web slenderness, $2D_{cp}/t_w$	90.7	76.7
a_r	0.52	0.44

where:

D_{cp} = depth of web in compression, taken at the plastic moment (in.), and

a_r = ratio of web compression area to flange compression area, taken at the plastic moment.

For these tests, lateral bracing satisfying the AASHTO requirements (see Section 2.2.1) were applied. Measurement instrumentation consisted of: (1) load cells to measure loads, (2) strain gages to measure strains, (3) string-potentiometers (string-pots) to directly obtain deflections, and (4) digital dial gages as well as string-pots attached to steel bars extended from girder ends to indirectly acquire rotations (see Appendix, Section A.3, Yakel, Mans, & Azzinamini, 1999, Figures 2.13 to 2.16).

The girders were predicted by AASHTO to develop the yield moment capacity. The resulting moment-rotation responses of both compact and noncompact girders actually developed a moment resistance greater than their plastic moment capacities until their inelastic rotations approximately reached 47 mrads and 85 mrads, respectively. These values are much greater than the maximum rotation considered necessary for redistribution of moments of 30 mrads (Schilling, 1986). The plastic moment capacity of each girder was calculated based on the actual material properties and the measured specimen dimensions. In addition, the inelastic rotational ductility, R, of Girder A (the noncompact girder) was found to be about 1.2, as opposed to the current AASHTO provisions that underestimate the capacity of noncompact sections. For noncompact sections, AASHTO provisions require only a minimum yield moment capacity but not any inelastic rotational capacity. Girder D (the compact girder) displayed an inelastic rotational ductility, R, estimated at R = 1.9, less than the expected rotation value of three (AISC LRFD specification, 2nd edition, 1998) for a compact girder (see Appendix, Section A.3, Azzinamini, Yakel, & Mans, 1999, Figures 2.24, 2.25, 2.37, 2.38, 2.46, and 2.47).

2.5.3 Colorado State University, Griffeth, 2001 (Hartnagel's group) (noncomposite only)

Michael Griffeth at the Colorado State University (CSU) experimentally tested the flexural capacity of HPS70W I-shape girders constructed of HPS70W steel (Griffeth, 2001). The primary objective of the testing was to compare experimental laboratory moment-rotation tests of HPS70W steel to current AASHTO LRFD moment-rotation equation. Two compact girders, one nonsymmetric (Specimen #1) and one symmetric

(Specimen #2), were tested in the conventional simply supported configuration. Specimens #1 and #2 (see Table 2.5.3.1) were classified as compact girders, nominally, according to AASHTO specifications of compact section requirements for the web and flange (see Section 2.2.1). In the table, the nominal or [average of tested values] values are based on the nominal yielding strength, $F_{yf} = F_{yw} = 70.0$ ksi for all the flanges and web, or the average material tested data, $F_{yf} = 83.35$ ksi for the flanges and $F_{yw} = 69.83$ ksi for the web (see Sections 3.2.2 and 3.3.2), respectively.

Table 2.5.3.1 CSU compact girder dimensions

Property	Specimen #1 (nominal compact)	Specimen #2 (nominal compact)
Test span, L (ft)	19.5	22
Web depth inside flanges, D (in.)	16	19
Web thickness, t_w (in.)	1/4	1/4
Compression flange width, b_{fc} (in.)	9	9
Tension flange width, b_{ft} (in.)	10	9
Flange thickness, t_f (in.)	3/4	3/4
Ratio of web depth in compression, D_{cp}/D, nominal [avg. of tested values]	0.594 [0.612]	0.5 [0.5]
Nominal flange slenderness, $b_f/2t_f$	6.0	6.0
Web slenderness, $2D_{cp}/t_w$, nominal [avg.]	76.0 [78.3]	76.0 [76.0]
a_r, nominal [average of tested values]	0.352 [0.363]	0.352 [0.352]

where:

D_{cp} = depth of web in compression, taken at the plastic moment (in.), and

a_r = ratio of web compression area to flange compression area, taken at the plastic moment.

A feature of the two girders was that a varied D_{cp}/D ratio of 0.5 and 0.6 was applied to account for concrete deck and rebar forces near intermediate supports in composite girders (0.5 models noncomposite, and 0.6 models composite). Furthermore, test girder dimensions were constrained by the actuator loading capacity, about 200 kips,

available at CSU and plate thickness sizes donated from Bethlehem Lukens Plate, a division of Bethlehem Steel Corporation, Burns Harbor, Indiana. The girders were fabricated by Zimmerman Metals, Inc., Denver, Colorado.

Figure 2.5.3.1 shows a photograph of the CSU overall final testing apparatus. Predominately a testing facility for timber structures, testing steel at CSU Structural Engineering Lab, initially required the overhaul and strengthening of a pre-existing test apparatus. Four components are utilized for the final design of the entire steel testing apparatus (see Table 2.5.3.2): (1) a stiffened distributor beam linking two 100 kip capacity actuators, (2) interchangeable column posts for adjustment of the loading level, (3) compression-flange lateral bracing system, and (4) girder reaction supports.

Figure 2.5.3.1 Overall testing apparatus at CSU structural engineering lab

Table 2.5.3.2 CSU testing apparatus summary

Description and Specification	AISC Member Size
Distributor Beam. ASTM A572, Grade 50.	W10x68
Vertical Column Lateral Bracing and Support System. ASTM A572, Grade 50.	W8x40
Back-to-Back Angles for Lateral Bracing. ASTM A36, Grade 36.	L3x3x1/2
Various Length Column Posts. ASTM A500, Grade B.	6x6 structural tubing, ½" thick
Various Plate Sizes and Thickness. ASTM A36, Grade 36.	---------
High Strength Bolts. ASTM A325 (Type 1)	---------

At first, a linear variable displacement transducer (LVDT) was mounted on an aluminum plate and connected to each actuator allowing displacement-control actuator movement, as opposed to load-control actuator movement (see Figure 2.5.3.2). This renovation ultimately permitted a thorough, careful examination of post-peak behavior.

Additionally, loading the test girders demands to use two 100 kip capacity actuators in conjunction for sufficiently applying a midspan, concentrated force corresponding to the plastic moment capacity of the stiffest girder. As a result, two separate load frames, each supporting an actuator, were joined and reinforced with eight, bolted bracing angles. A stiffened distributor beam is employed to link the fixed-height actuators, which are spaced about 5 ft. apart. Furthermore, the actuator maximum vertical travel distance of 6 in. inherently requires manufacture of various length interchangeable column posts, which are added as needed to provide the vertical travel distance beyond 6 in., to ultimately examine the post-peak behavior of the girders. In detail, the column posts are bolted to the bottom of the distributor beam and comprised of 1/2 in. thick square structural tubing welded to end plates. For load bearing, a 3 in.

diameter half-round is connected to the bottom end plate of the column post (see Figure 2.5.3.3).

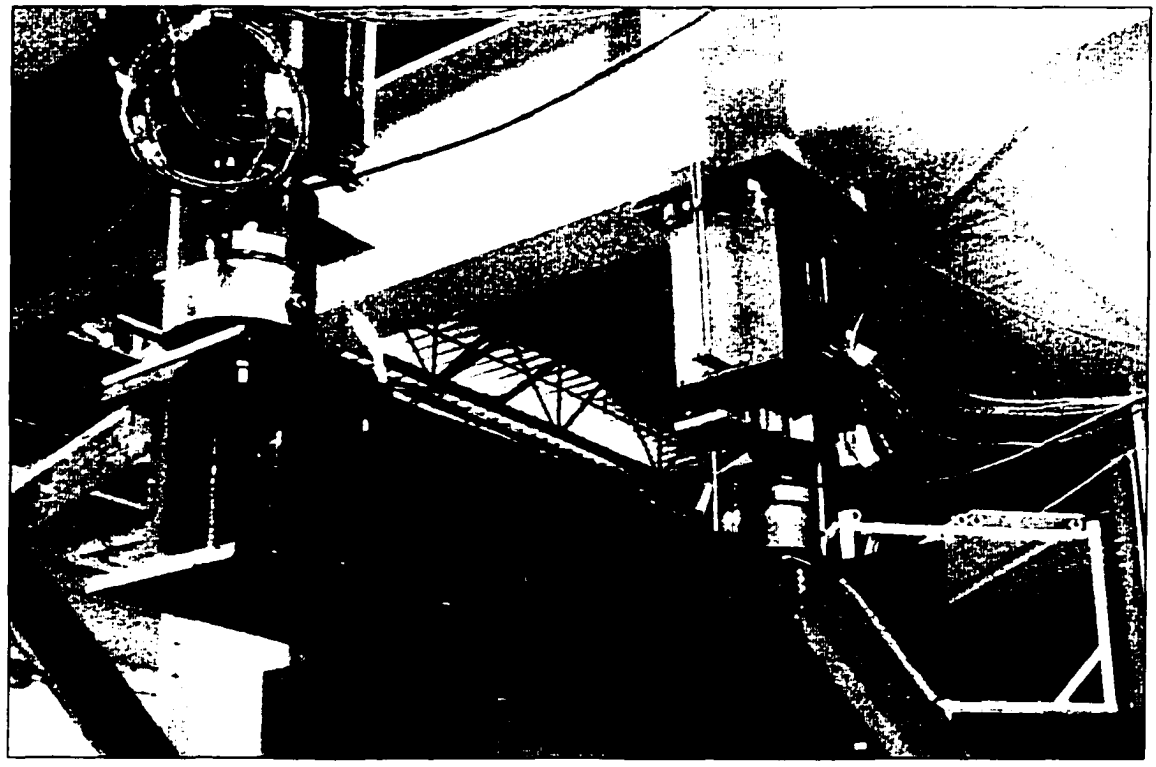

Figure 2.5.3.2 LVDTs, actuators, distributor beam, and the load frame bracing

The CSU experimental testing facility imitates a universal testing machine. The girder reactions are resisted by the concrete floor (see Figures 2.5.3.4 & 2.5.3.5). The compressive actuator uplift force is counterbalanced by a system of two parallel connecting frames made of wide flange steel girders, which pull up against a massive 46 kip-concrete pad tied down to the strong floor. The length of the concrete tie down pad is shorter than the test girder lengths, and thus, the reaction loads of the girder are directly on the strong floor.

Figure 2.5.3.3 Load bearing point

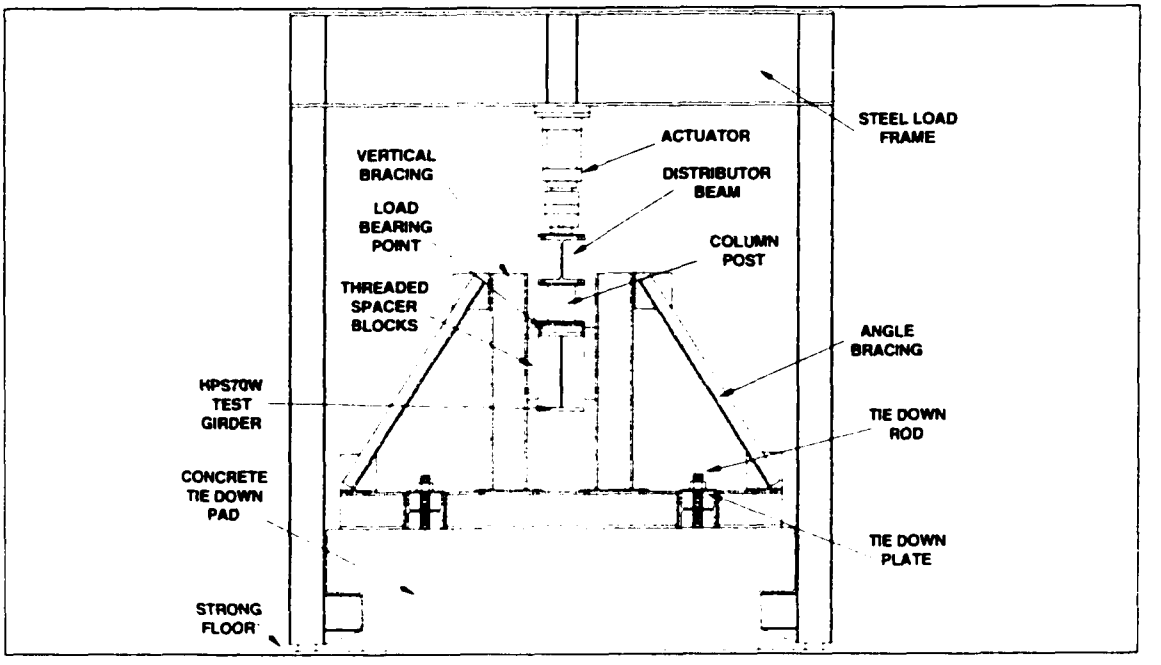

Figure 2.5.3.4 Testing apparatus and bracing cross-view configuration (Beam reaction supports omitted for clarity)

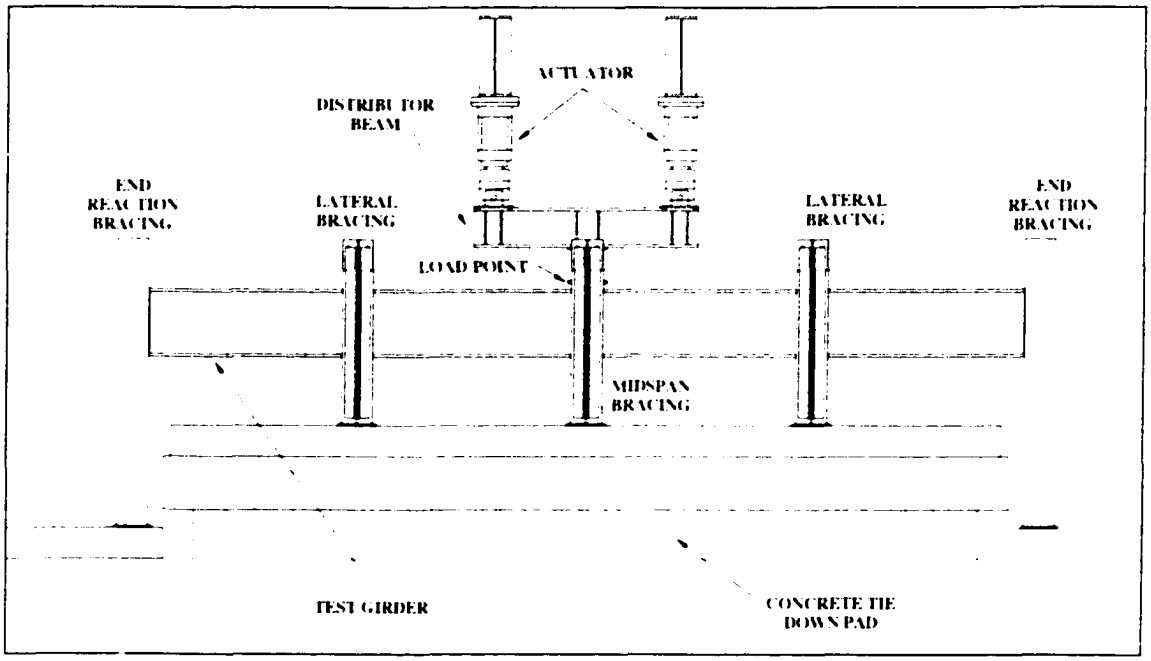

Figure 2.5.3.5 Testing apparatus and girder bracing longitudinal configuration (Load frame columns omitted)

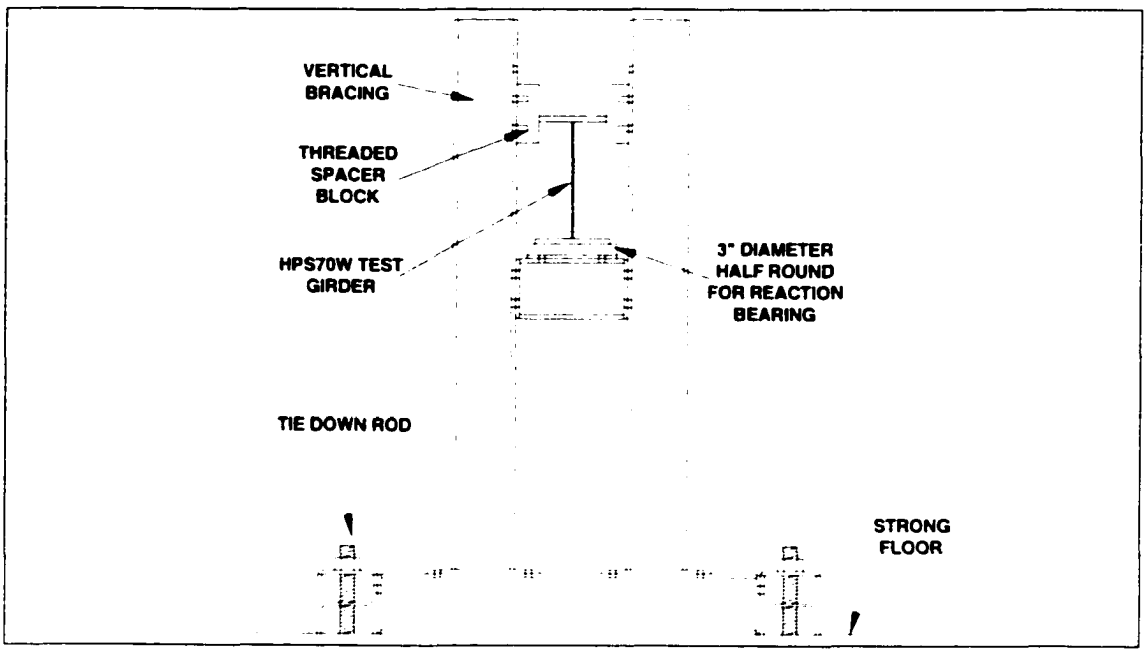

Figure 2.5.3.6 Reaction bracing and supports

Moreover, AISC-LRFD-specified slip-critical, bolted connections are assigned for both lateral bracing and reaction supports. These types of connections prevent movement or slip, which would have an unfavorable effect on the test results, and also promise a changeable test setup to be compatible with a broad range of possible future experiments. In addition, the lateral bracing, whose locations are specified by AASHTO 6.10.4.1.7 (see Section 2.2.1), consists of vertical, wide flange columns top-braced by double angles, and thin threaded spacer blocks were greased and bolted to the vertical columns to allow for smooth vertical movement of the test specimen within the bracing (see Figure 2.5.3.4). The height of the reaction supports must assure enough clearance to allow for sufficient midspan deflection and rotation of the deepest test girder (see Figure 2.5.3.6). Finally, the member sizes of the vertical column bracing and the lateral bracing were determined based on the maximum lateral force located at midspan, which was conservatively anticipated to be 10% of the compression flange force. The entire system was modeled in the SAP2000 structural analysis computer program, in which case it exhibited minimal, acceptable displacements and deformations.

For the laboratory testing of the two noncompact HPS70W girders, electrical instrumentation employed were: (1) master-slave MTS 407 controllers with LVDTs to operate hydraulic actuators in a displacement-control manner, (2) load cells in actuators to measure loads, (2) string-potentiometers attached to the underside of the girders to obtain deflections, directly, and rotations, indirectly, and (4) quarter-bridge-configuration strain gages to measure strains.

The moment-rotation responses of both compact girders, Specimen #1 and Specimen #2, predicted by AASHTO at a minimum to develop the yield moment

capacity, actually developed a moment resistance greater than their plastic moment capacities until their inelastic rotations approximately reached 60 mrads and 45 mrads, respectively. These values are much greater than the maximum rotation considered necessary for redistribution of moments of 30 mrads (Schilling, 1986). Similar to the results of Yakel, Mans, & Azizinamini, 1999, both girders here did not exhibit the anticipated rotational capacity of three as for compact girders (AISC LRFD, 2nd edition, 1998).

2.5.4 Experimental HPS composite tests

There are no documented cases of experimental tests involving composite girders fabricated from HPS.

2.6 Numerical Moment-Rotation Behavior Of Compact And Noncompact Conventional Steel And HPS Girders

2.6.1 Physical attributes and behavioral phenomena affecting the strength and stability of structures

The physical attributes and behavior phenomena affecting the strength and stability of a structure are defined (Zubeck, 2000) below:

Geometric nonlinearity

- P-Δ effect – effect of axial force acting through displacements associated with member chord rotation.
- P-δ effect – effect of axial force acting through displacements associated with member curvature.

- Wagner effect – effect of bending moment and axial forces acting through displacements associated with member twisting.
- Curvature shortening – effect of curvature on longitudinal displacements at member ends.
- Sway shorting – effect of large chord rotation on longitudinal displacements at member ends.
- Lateral torsional buckling.
- Local buckling and local distortion.
- Interaction of local and member instability.

Material nonlinearity

- Strain hardening.
- Elastic unloading.
- Yielding – concentrated or spread yielding.
- Multi-dimensional plasticity effect.
- Influence of loading sequence on path dependent plasticity.
- Cyclic plasticity effect – Bauschinger, cyclic hardening, elastic shakedown.
- Strain-aging.

Physical attributes

- Initial geometric imperfections – out-of-plumpness, out-of-straightness, cross-sectional distortion, and connection eccentricities.
- Initial residual stresses.
- Positive and negative member end restraint.
- Cross-section symmetry/nonsymmetry.

- Prismatic/nonprismatic member profile.
- Location of stiffeners and bracing.
- Composite interconnection with concrete slabs.

The finite element method of analysis cannot be extended to encompass all the aspects listed above, and not all of these aspects apply to bridges. However, the attributes of geometric nonlinearity, material nonlinearity, initial geometric imperfection, and initial residual stresses used in the numerical moment-rotation analysis are discussed below.

2.6.2 Elsevier Science Ltd, Engineering Structures, 1998, Barth and White (noncomposite only)

As published in Engineering Structures, 1998, Barth and White's paper presented the implementation and execution of a reasonable comprehensive set of finite element models to evaluate the pier moment-rotation characteristics of continuous-span steel I girders (Barth and White, 1998). The paper summarized the key requirements and important results of the numerical parametric studies and thus developed simple moment-rotation relationships for use in design and rating of bridge girders (see Figure 2.6.2.1 and Section 2.7 for details of M_n and θ_{RL}). The parametric studies are conducted using STARS finite element code and full nonlinear shell finite element models of the hypothetical physical noncomposite girders fabricated from steel with a minimum specified yield strength of 50 ksi. The displacement-base 9-node Lagrangian shell elements were employed for half-length models, densely spaced at the midspan and gradually increased spacing to the end support (see Figure 2.6.2.2).

For a typical finite element mesh, the shell elements were assigned as 8 across the upper flange (in compression), 10 across the web, and 4 across the lower flange (in tension). Three-node Lagrange eccentric beam elements were utilized for transverse stiffeners. In addition, Figure 2.6.2.2 also presents the inputs of stress-strain relationship, residual stresses, and initial imperfection applied in the parametric studies. From the presented values of modulus of elasticity, E = 29000 ksi, and the specified minimum nominal yield stress, F_y = 50 ksi, the yield strain, $\varepsilon_y = \frac{F_y}{E}$, was 0.00172, and thus the corresponding ratio of yield strains, $\frac{\varepsilon_u}{\varepsilon_y} = \frac{0.011}{0.00172} = 6.4$, was employed.

Furthermore, the self-equilibrating Gauss point residual stresses were assigned differently for the compression and tension flanges although the maximum positive and negative values were same, +0.95 F_y and -0.5 F_y, respectively, for both flanges. For the web, the maximum positive residual stress was F_y while the constant negative residual stress, depended on the D/t_w ratio, which varied from 0.03 to 0.15 F_y.

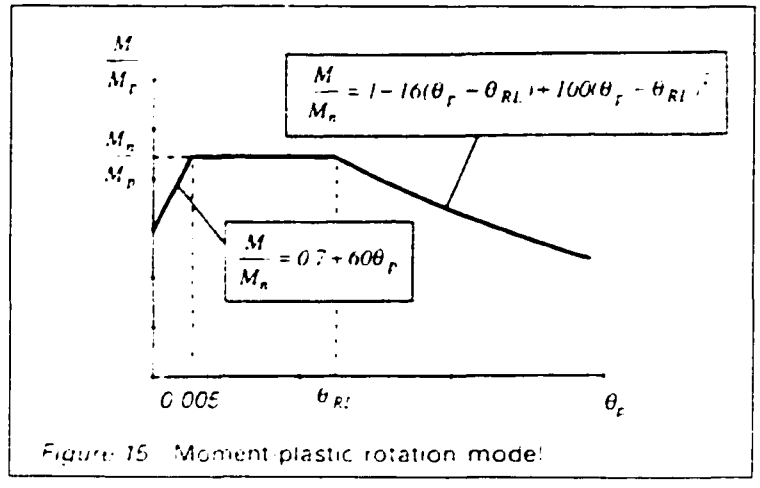

Figure 15 Moment plastic rotation model

Figure 2.6.2.1 Model of moment-plastic rotation behavior (Source: Figure 15, Barth & White, 1998)

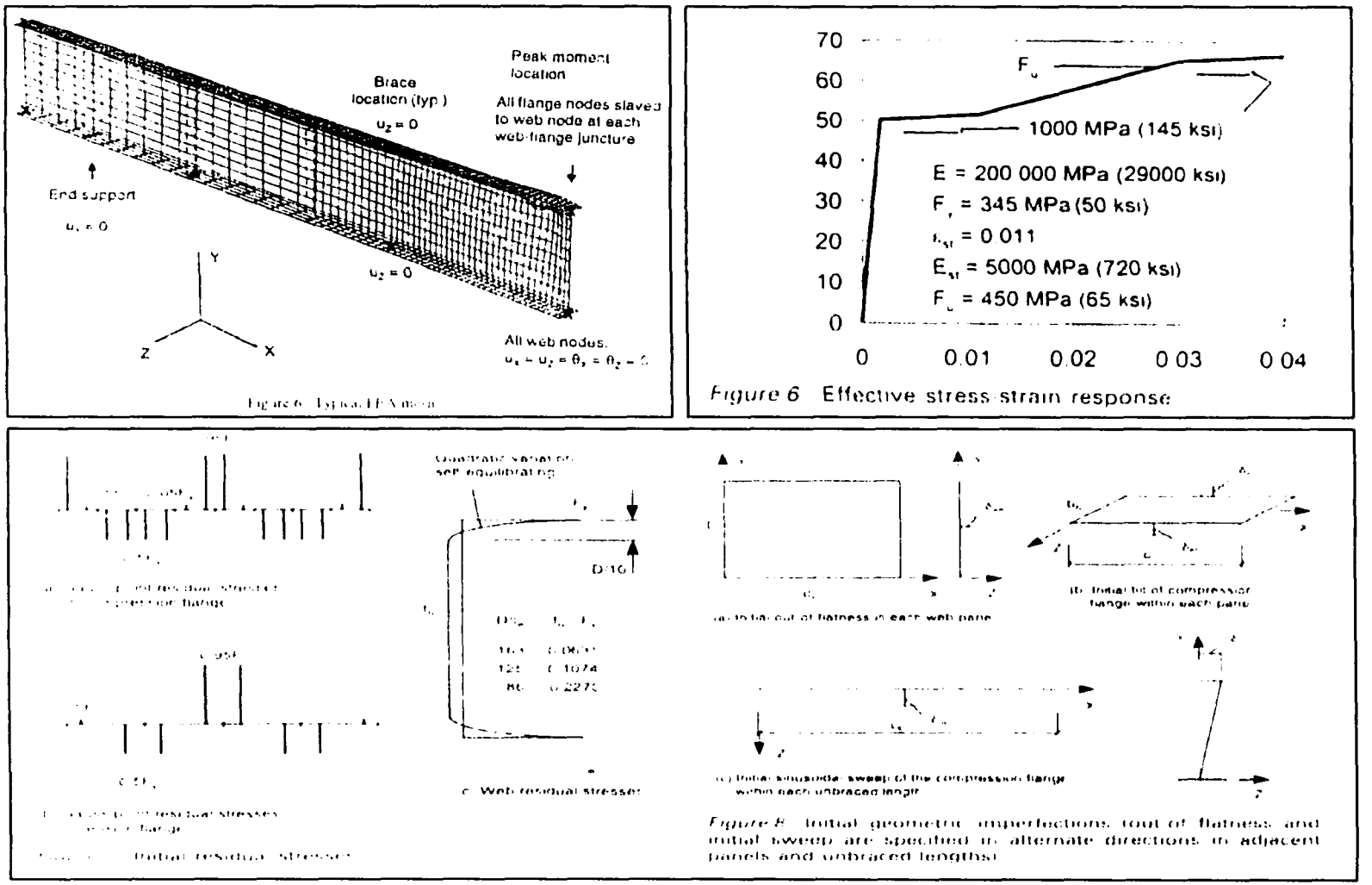

Figure 2.6.2.2 Typical FEM mesh, stress-strain relationship, residual stresses, and initial imperfections (Source: Figures 5 to 8, Barth & White, 1998)

Moreover, the initial out-of flatness of the web, δ_{ow}, and the maximum tilt of the flanges, δ_{of}, were specified similar to the maximum values permitted by the American Welding Society (AWS) Code. For the web, the AWS maximum values range from d/67 for panels of interior girders with one-sided stiffeners (where d is the least panel dimension) to D/150 for unstiffened girders (where D is the web panel depth measured using a straight edge whose length is no less than d). For the flange, the maximum value is 1/100 of the total flange width or ¼ in., whichever is greater. In this work, the initial imperfection were specified as:

If $d_o < D$, then $\delta_{ow} = d_o/100$; otherwise $\delta_{ow} = D/100$, and

if $b_{fc} < 0.3\ d_o$, then $\delta_{of} = b_f/150$; otherwise $\delta_{of} = 0.3d_o/150 = d_o/500$ (see Figure 2.6.2.2).

2.6.3 Georgia Institute of Technology, White, Barth, and Bobb, 1998 (noncomposite only)

In conjunction with the Georgia Institute of Technology, White, Barth, and Bobb numerically investigated the strength and ductility of HPS70W girders (White, Barth, and Bobb, 1998). Using finite element modeling, the researchers studied the influence of geometric and material parameters on the flexural behavior of I-girders fabricated from high performance steel (HPS) of Grade 70W. Three cross-section geometric parameters are examined: the compression flange slenderness, $b_{fc}/2t_{fc}$, the web slenderness, $2D_{cp}/t_w$, and the cross-section aspect ratio of the web depth to the compression flange width, D/b_{fc}. Three material parameters are considered: the yield ratio, $YR = F_y/F_u$, the ratio of the strain hardening and yield strains, $\varepsilon_{st}/\varepsilon_y$, and the strain hardening modulus, E_{st}. The numerical moment-rotation curves obtained from these parametric studies are compared

with simplified plastic moment-rotation equations that have been developed in previous research and with current AASHTO specifications.

In the HPS70W parametric studies, half-length models of the displacement-base 9-node Lagrangian shell elements using STARS finite element code and the inputs of residual stresses and initial imperfection were same as for steel with a minimum specified yield strength of 50 ksi in Section 2.6.2 above. For the stress-strain relationships, Figure 2.6.3.1 following presents the combinations of the yield ratio, F_y/F_u = 0.8 or 0.9, the strain hardening strain, $\varepsilon_{st} = 1\varepsilon_y$ or $10\varepsilon_y$, and the strain hardening modulus, E_{st} = 400 ksi or 800 ksi.

Overall, the researchers concluded that the HPS70W girders satisfactorily achieved the yielding capacity although none would meet the traditional requirement of rotational capacity, R, of three (AISC LRFD, 2nd edition, 1998). In fact, it was examined that even though HPS70W steels typically have a higher yield ratio, F_y/F_u, than conventional steels, such as 0.77 for A572 Grade 50, all girders reach the yield moment capacity, M_y, and a number of girders exceed the plastic moment capacity M_p.

In the HPS70W parametric studies, the combined effects of the yield ratio, F_y/F_u = 0.8 or 0.9, the strain-hardening strain, $\varepsilon_{st} = 1\varepsilon_y$ or $10\varepsilon_y$, and the strain hardening modulus, E_{st} = 400 ksi or 800 ksi, are not large enough to merit the use of these parameters as variables in equations for prediction of flexural strength or general moment rotation response. However, there was some benefit associated with a decrease in the yield ratio from 0.9 to 0.8 although the benefit is small in the case of $\varepsilon_{st} = 10\varepsilon_y$ when the material has a yield plateau. Slightly improved behavior is observed for girders constructed from

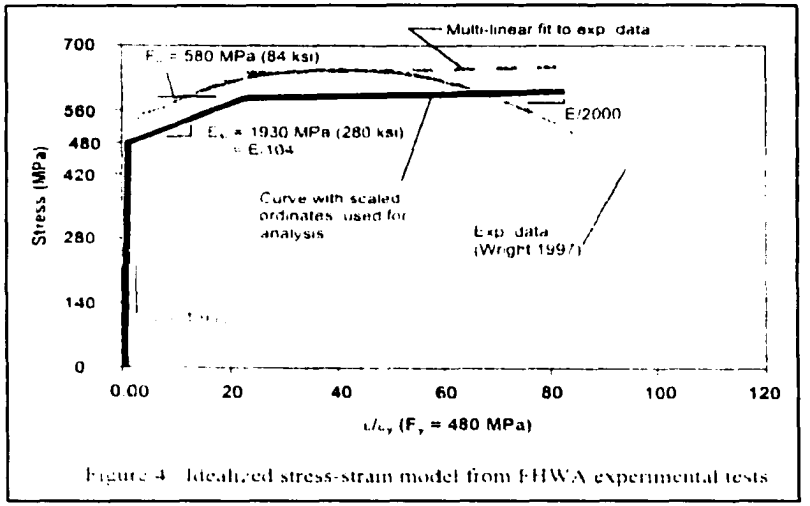

Figure 4 Idealized stress-strain model from FHWA experimental tests

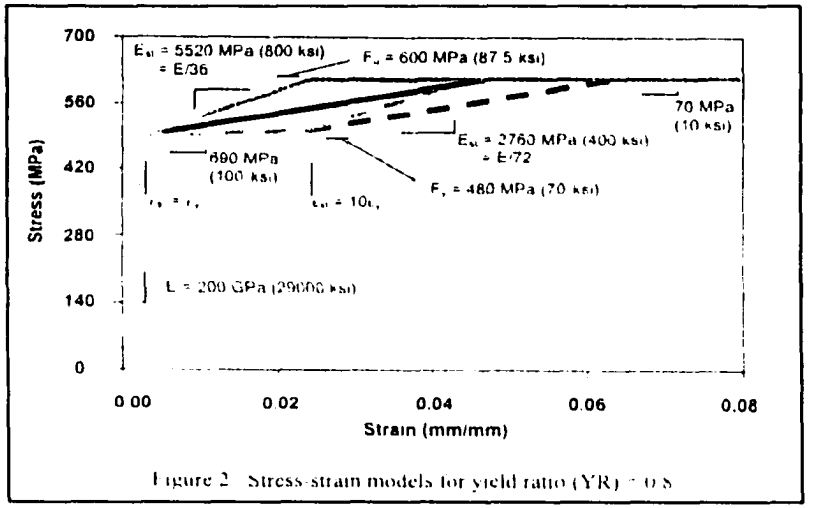

Figure 2 Stress-strain models for yield ratio (YR) = 0.8

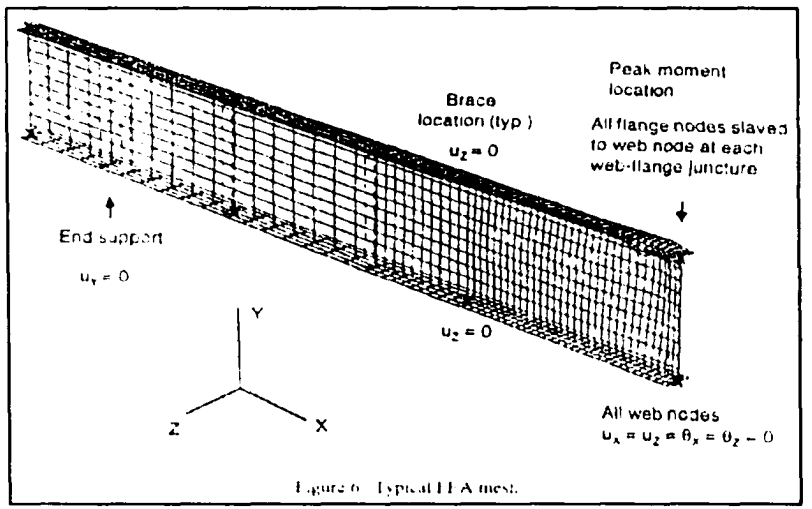

Figure 6 Typical FEA mesh

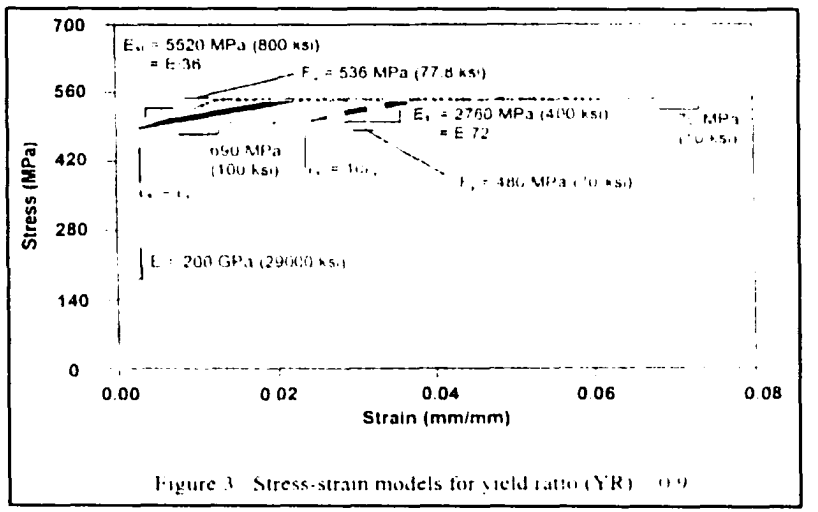

Figure 3 Stress-strain models for yield ratio (YR) = 0.9

Figure 2.6.3.1 Typical FEM mesh and variations of stress-strain relationship (Source: Figures 2, 3, 4, and 6, White, Barth, & Bobb, 1998)

material having $\varepsilon_{st} = 1\varepsilon_y$ when the material immediately strain-hardens upon reaching the yield limit without having an extended yield plateau.

Additionally, the effect of varying the flange slenderness, $b_{fc}/2t_{fc}$, between the ultra compact and compact limits, $b_{fc}/2t_{fc} = 5.86$ and $b_{fc}/2t_{fc} = 7.77$, respectively, on the moment capacity is negligible. However, changing the flange slenderness from ultra compact to compact has a significant influence on the shape of the moment plastic rotation curves, increasing in magnitude the slope of the descending curve. Changing the web slenderness, $2D_{cp}/t_w$, from the compact limit to the maximum AASHTO limit for transversely stiffened girders had a small effect on the maximum strength. This is expected when either compact or ultra compact flanges provided most of the flexural capacity for the studies. Hence, within the prediction equations, the effect of the web slenderness on the shape of the inelastic moment-rotation curves is assumed to be negligible. Surprisingly, the cross section aspect ratio, D/b_{fc}, was found to be the most significant of the geometric parameters studied in this numerical work. This parameter has a considerable influence on both the moment capacity and the shape of the inelastic moment-rotation curve. An increase in D/b_{fc} from 3.00 to 4.25, while holding the flange slenderness, the web slenderness, and the girder L_b/r_y constant, reduced the moment capacity by an amount as large as 12%.

Finally, further studies are recommended to understand the behavior of HPS70W girders more completely. Future research should be extended to include a number of cases involving unsymmetrical girders with $D_{cp}/D > 0.5$. Finite element studies similar to those reported here should be conducted using the maximum brace spacing permitted by the traditional AASHTO equations for flexural strength. In here, a constant normalized

L_b/r_y was employed within the critical unbraced segment based on the required brace spacing for the AASHTO Q formula. Nonetheless, braces can generally be spaced at larger intervals when the traditional AASHTO equations using the plate girder strength reduction factor, R_b, are applied for the flexural strength (AASHTO, 1997).

2.6.4 University of Nebraska-Lincoln, Yakel, Mans, and Azizinamini, 1999 (noncomposite only)

Researchers at the University of Nebraska-Lincoln developed sets of experimental data that could be used to verify numerical finite element models reproducing the flexural behavior HPS70W I-shape girders fabricated of mainly HPS70W steel as well as 50W steel (Yakel, Mans, & Azizinamini, 1999). Their report discussed two tests for compact and noncompact sections and compared the experimental results (see Section 2.5.2) to the corresponding numerical estimates using finite element methods (FEM). Stating that the FEM modeling was still an ongoing task, the researchers showed several preliminary steps taken in developing finite element model using ANSYS version 5.5 finite element analysis program.

For a typical finite element mesh of the noncomposite girders, elements of ANSYS's SHELL181, a 4-node shell with 6 degrees of freedom per node, were utilized, densely spaced at the midspan and gradually increased spacing to the end support. Eight shell elements were defined across each of the compression and tension flanges and 12 (not equal but smaller elements in compression zone and larger elements in tension zone) shell elements across the web (see Figure 2.6.4.2). Figure 2.6.4.1B) illustrates the web-flange connectivity used in the FEM model, showing that the web connects to the centroid of the flanges. The error caused by this connection is an artificial increase in the

height of the plate representing the web. Since the increased unbraced length of the web will make it more receptive to buckling resulting in lower predicted loads, the assumption is considered as conservative.

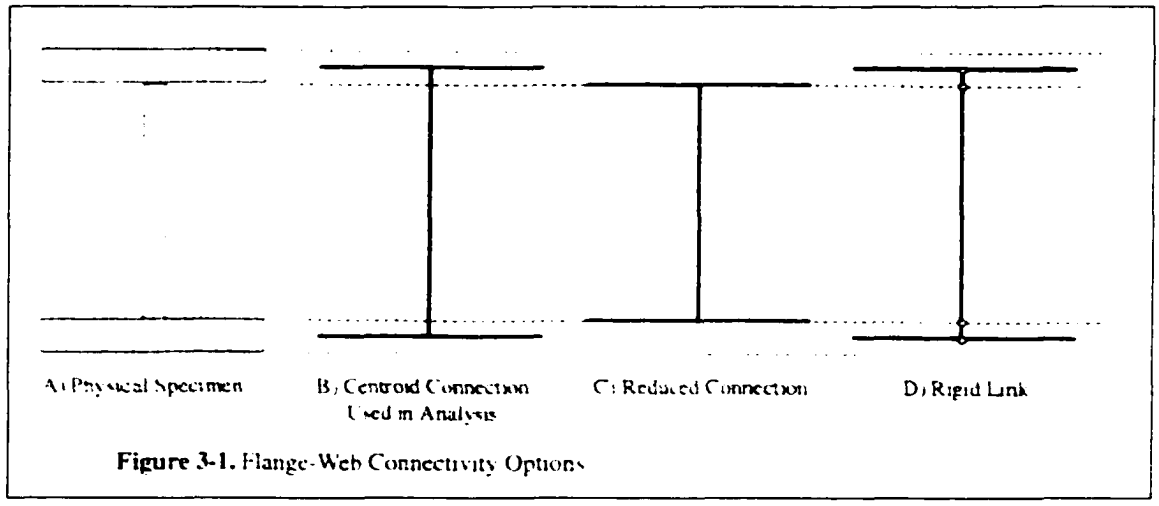

Figure 3-1. Flange-Web Connectivity Options

Figure 2.6.4.1 Flange-web connectivity options.
(Source: Yakel, Mans, and Azizinamini, 1999)

Additionally, the uni-axial tension test was employed to obtain stress-strain data. During the necking portion of the tension test, the true stress-strain can be approximated based on data of area reduction and the assumption of a uniform stress distribution prior to necking. However, after necking the stress distribution over the cross-section is far from uniform. Therefore, the "true stress-true strain" curve, which is needed for the finite element analysis, is converted from the engineering stress-strain curve, which is experimentally obtained, following an iterative procedure until the engineering stress-strain curves determined numerically agreed with that obtained experimentally.

Figure 2.6.4.2 presents residual stresses assigned for the web and the flanges. For both flanges, the maximum positive and negative residual stresses are +0.98 F_y and -0.98/3 F_y, respectively. For the web, the maximum positive residual stress was 0.98 F_y

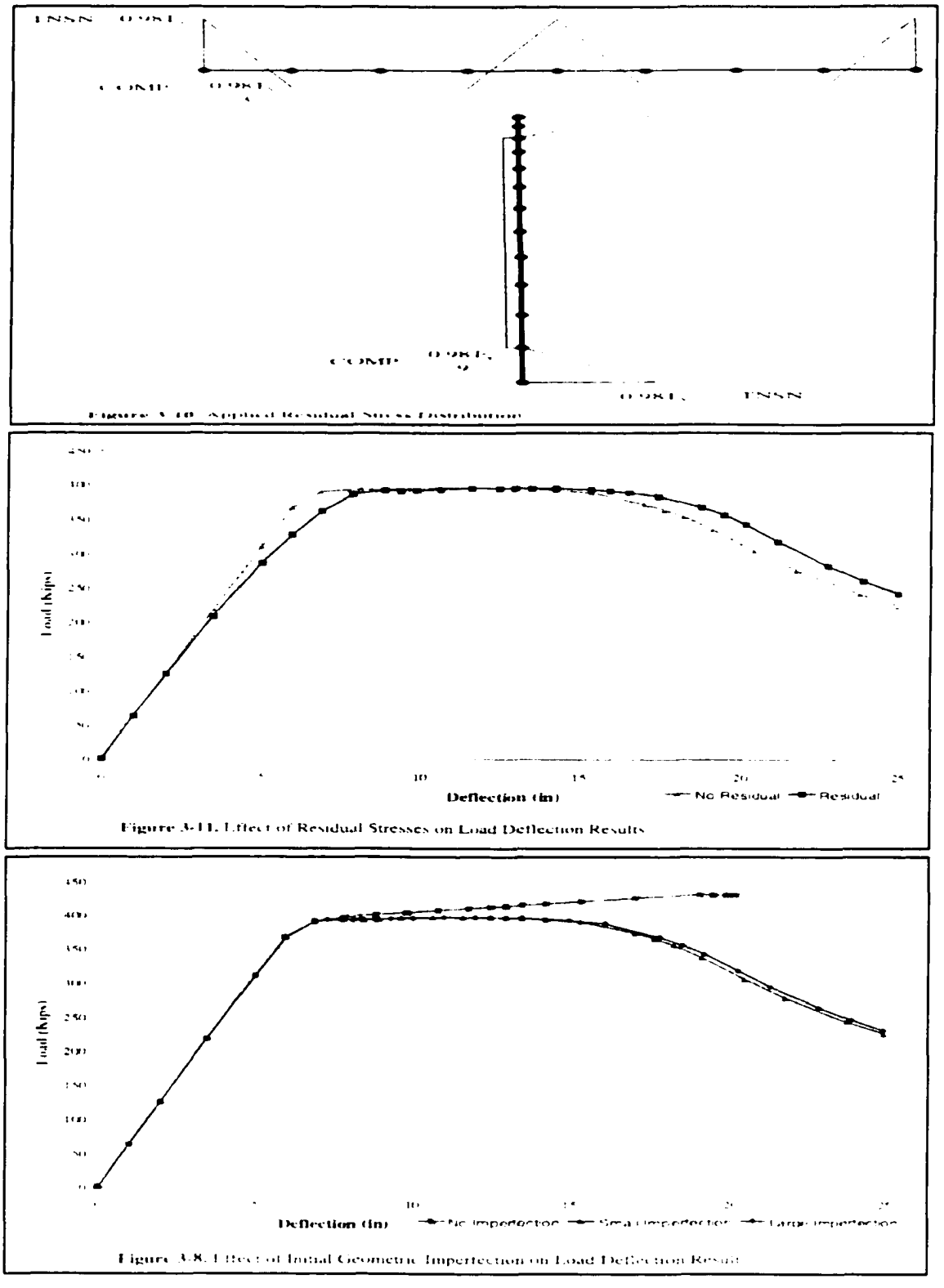

Figure 2.6.4.2 Residual stress distribution and effects of residual stresses and imperfection. (Source: Yakel, Mans, and Azizinamini, 1999)

while the constant negative residual stress was specified as 0.98/9 F_y. In addition, the effect of residual stresses in the moment-rotation (or load-deflection) diagram was "rounding off" of the curve as the girder yields even though the magnitude of residual stresses has no effect on the ultimate moment (or load) capacity. Moreover, the results from running a number of analyses concluded that what type or how much imperfection introduced into the model does not influence the results significantly, and thus one does not have to exactly recreate the imperfections found in the real girder (see Figure 2.6.4.2). Hence, the imperfection input for numerical analysis was modeled as the following. An eigenvalue buckling analysis was applied on the simply supported girder loaded at midspan. The resulting first eigenvector from the analysis was scaled down such that the maximum displacement was 0.1 inch, and these scaled displacements were superimposed on the original geometry thus generating a distorted mesh.

2.6.5 University of Missouri-Columbia, Zubeck, 2000 (noncomposite only)

Michael Zubeck, while at University of Missouri-Columbia, numerically developed inelastic moment-rotation curves for nonlinear analysis of intermediate support regions of continuous span steel girders produced of high-strength steel up to 70 ksi yield strength (Zubeck, 2000). The analysis of noncomposite girders, which were compact (compact flange and web) and noncompact (compact flange and noncompact web), was performed using MSC/NASTRAN finite element code with nonlinear solutions.

For the numerical models, the QUAD4 elements, a 4-node plate element with 5 degrees of freedom per node, were employed densely spaced at the midspan and

gradually increased spacing to the end support. Eight QUAD4 flexure elements were defined across each of the compression and tension flanges, and 15 QUAD membrane elements comprised the web. In addition, Figure 2.6.5.1 shows the rate of convergence of displacement vs. number of web elements through depth (at fixed 25 elements along the length) and displacement vs. number of flange element along the length (at fixed 4 elements across the flange width). As the number of the web membrane elements increases, the deflection converges quickly while the deflection with respect to the increasing number of bending elements of flanges converges slowly. The imperfection input for numerical analyses was modeled similar to the method of Yakel, Mans, and Azizinamini, 1999, in which the resulting first-eigenvector from the buckling analysis was scaled down such that the maximum displacement was 0.1 inch, and these scaled displacements were superimposed on the original geometry thus generating a distorted mesh (see Section 2.6.4).

However, here in Zubeck's dissertation, two different first-eigenvectors were obtained from two types of buckling analyses. One was a linear elastic eigenvalue buckling analysis, Imperfection A, performed using the simple beam loading while the other was a normal modes analysis, Imperfection B, performed using the simply supported beam boundary conditions (see Figure 2.6.5.1). For the University of Missouri test beam, the maximum moment capacities (in ft-kips) resulted from the two different types of imperfection were very close, as 142.7 for Imperfection A and 143.2 for Imperfection B, compared to 147.8 for no imperfection.

Furthermore, the residual stresses were assigned for the web and the flanges as the same as in Yakel, Mans, and Azizinamini, 1999 (see Section 2.6.4). For both flanges, the

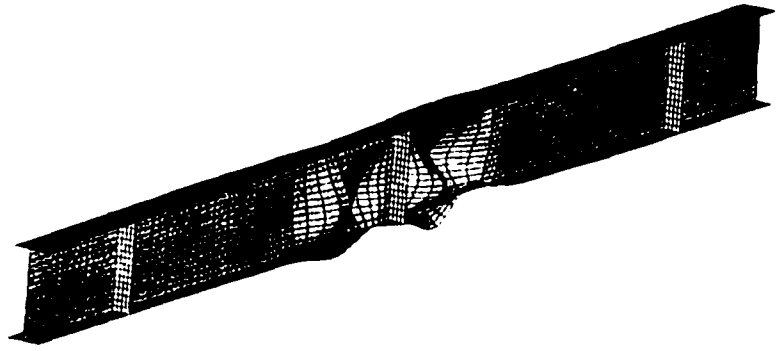

Figure 6.4 Linear elastic eigenvalue buckling analysis deformed shape (Imperfection A)

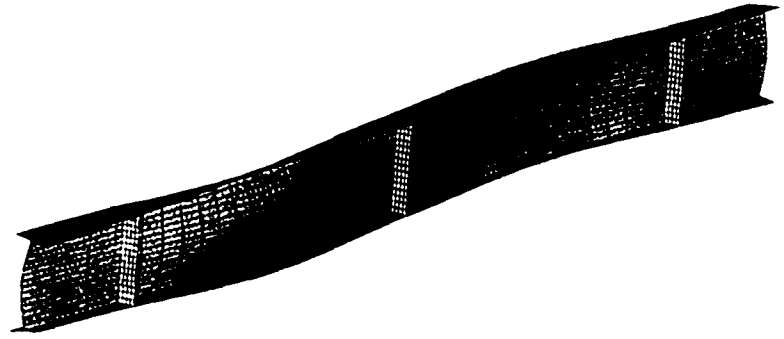

Figure 6.5 Normal modes analysis deformed shape (Imperfection B)

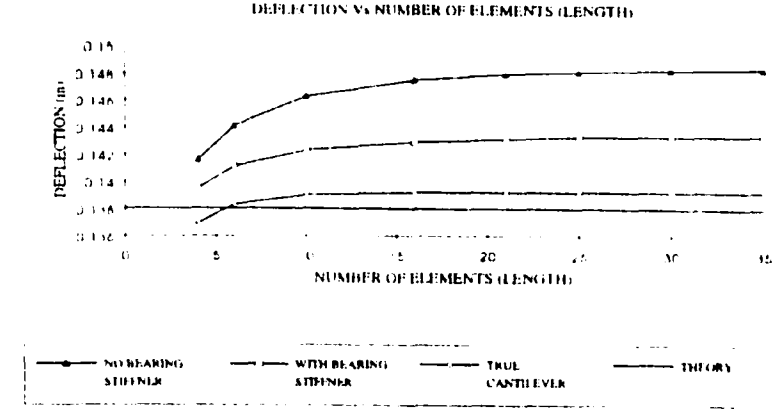

Figure 5.9 Displacement vs. number of flange elements along length.

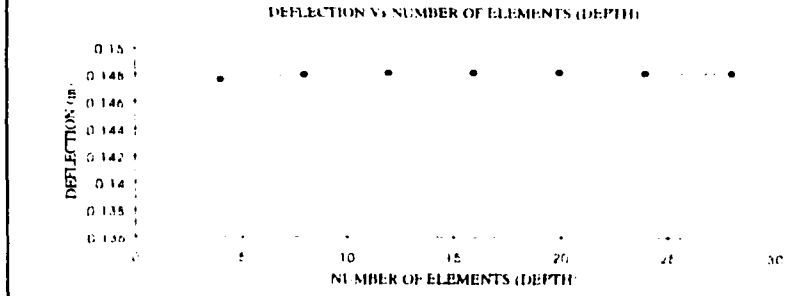

Figure 5.10 Deflection vs. number of web elements through depth (no bearing stiffener)

Figure 2.6.5.1 Left: Deformed shapes to be scaled for initial imperfections - Right: Convergence of deflections vs. numbers of flange and web elements. (Source: Figures 5.10 and 6.5, Zubeck, 2000)

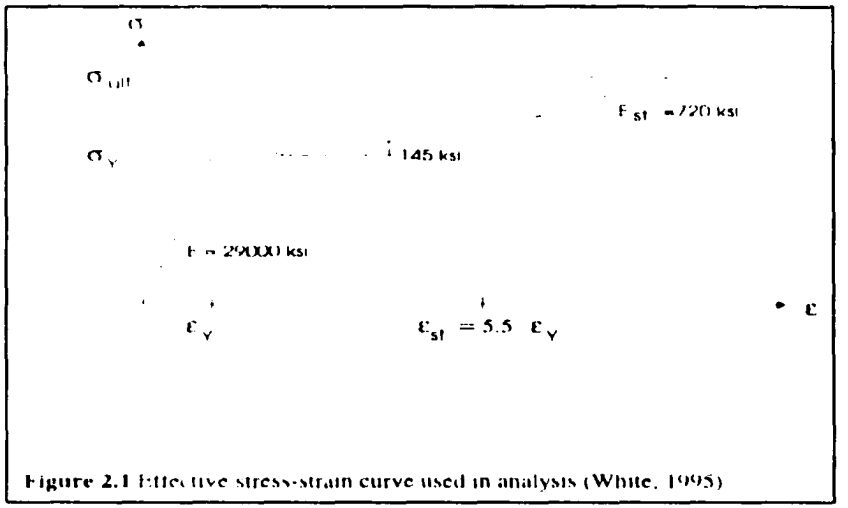

Figure 2.1 Effective stress-strain curve used in analysis (White, 1995)

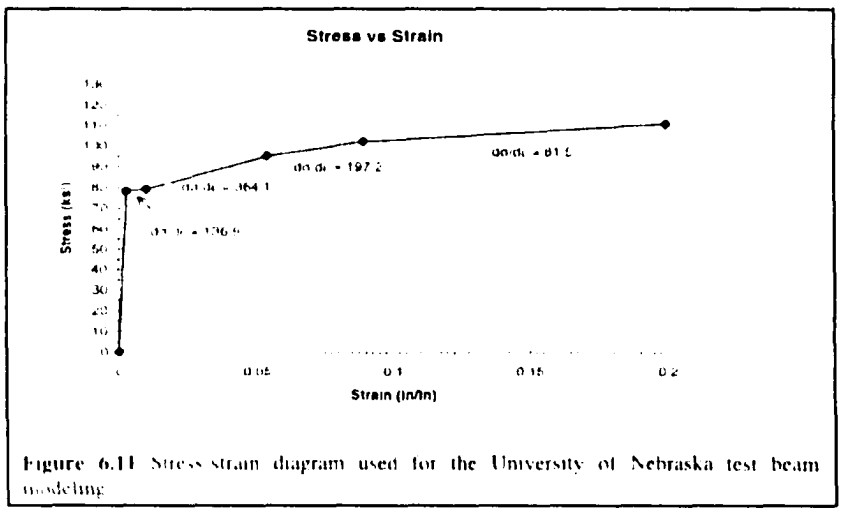

Figure 6.11 Stress-strain diagram used for the University of Nebraska test beam modeling

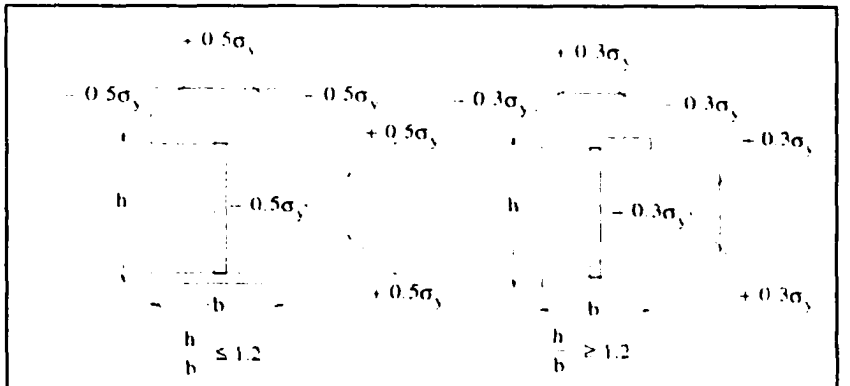

Figure 2.3a Residual stress pattern for rolled I-sections (Toma and Chen, 1994)

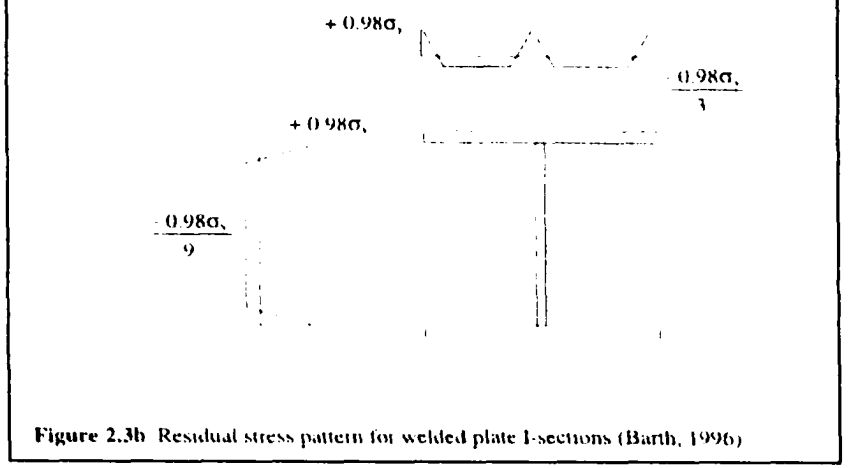

Figure 2.3b Residual stress pattern for welded plate I-sections (Barth, 1996)

Figure 2.6.5.2 Stress-strain relationship and initial residual stresses used in FEM analysis. (Source: Figures 2.1, 2.3, and 6.1, Zubeck, 2000)

maximum positive and negative residual stresses are +0.98 F_y and -0.98/3 F_y, respectively. For the web, the maximum positive residual stress was 0.98 F_y while the constant negative residual stress was specified as 0.98/9 F_y. Moreover, Figure 2.6.5.2 presents the inputs of stress-strain relationship applied in the analyses. The value of modulus of elasticity, E, is presented as 29,000 ksi although "the actual elastic modulus of the material is most likely less than the common tabular listing used in the theoretical calculations (Zubeck, 2000, pg.136)" was stated. Similarly to Barth and White's paper, 1998 (see Section 2.6.2), the initial hardening/plastic flow region slope of E = 145 ksi preceding the strain hardening slope of E = 720 ksi were employed for the analysis of conventional steel. However, the ratio of yield strains, $\frac{\varepsilon_{st}}{\varepsilon_y} = 5.5$, was utilized instead of the value of 6.4 as in Section 2.6.2. In addition, a different stress-strain multilinear curve was chosen for the analysis of high performance steel, in which a "yield plateau slope" of 136.9 ksi preceded a first strain-hardening slope, E_{st} = 364.1 ksi, that was followed by a second and a third strain hardening slope of 197.2 ksi and 81.5 ksi, respectively (Zubeck, 2000).

The numerical models, which are ultra-compact flange with compact web, compact flange with compact web, and compact flange with noncompact web constructed of high performance steel up to 70 ksi yield strength, all exceeded maximum moment capacity and the unloading curve was above the limits determined by the current AASHTO LRFD code provisions (AASHTO, 1998 & interim 2001). On the other hand, the noncompact web model of high performance steel did not reach the moment capacity predicted by the inelastic moment-rotation model proposed by Barth and White, 1998.

2.6.6 Analytical models for HPS composite girders

There are no documented cases of analytical models involving composite girders fabricated from HPS.

2.7 The Improved Simplified Inelastic Design proposed by Barth, Hartnagel, White, and Barker (December 2001)

As under review to be published in Journal of Bridge Engineering, ASCE, the paper of "Improved Simplified Inelastic Design of Steel I Girder Bridges" (Barth, Hartnagel, White, and Barker, 2001) presented an extension to a recently proposed inelastic design (Barker, Hartnagel, Schilling, and Dishongh, 2000) of steel I girder bridges. The proposed inelastic design procedures encompass provisions for compact and noncompact cross sectional I girders.

First, basic developments that lead to the proposed inelastic design approach were summarized. The paper then outlined an equation set that provide an improved characterization of the inelastic moment-rotation response for a wide range of I beams and plate girders. Next, the paper presented the development of improved expressions for the effective-plastic-moment, M_{pe}, capacity of continuous-span steel I girder bridges. These expressions were compared with the results from 68 experimental tests involving various loading conditions, girder geometries, girder types, and steel grades.

Thereafter, the effective-plastic-moment predictions that are based on these equations in combination with the recently proposed design method produce results in greater accuracy and simplicity of the proposed approach. In detail, Barker et al. (2000) provided a summary of the experimental verification of these design methods, showing

that girders designed using effective-plastic-moment approaches satisfy all AASHTO limit-state design levels and provide overall good performance.

Finally, the extraordinary ease of use of the resulting procedure was demonstrated by a design example using the procedure proposed by Schilling et al. (1997) combined with the new M_{pc} expressions. The calculation of the maximum flexural strength in the example were based on a potential-unified-set of equations for general unstiffened and transversely stiffened bridge I beams and plate girders.

Although similar results are achieved with significantly less effort by using the proposed simplified procedure, the engineer may perform a more rigorous inelastic-design-analysis by making direct use of the moment-plastic rotation relationship shown in Figure 2.7.1. The reader is referred to (Barth and White, 2000) for a discussion of this direct approach, in which the pier plastic rotations are calculated rather than being assumed as estimated upper-bound values for the rotation demand.

In Figure 2.7.1, the model shown for the moment-inelastic rotation response, M-θ_p, of pier sections was initially proposed Barth and White (1998) and White and Barth (1998). In this model, the M-θ_p behavior is divided into three regions:

(1) a linear pre-peak curve from zero plastic rotation of $\theta_p = 0$ at $M = 0.7M_n$ to a plastic rotation of $\theta_p = 0.005$ radian at M_n, where M_n is the nominal flexural capacity,

(2) a plateau at the nominal resistance, M_n, from $\theta_p = 0.005$ radian to a value denoted by the parameter plastic rotation at the onset of unloading, θ_{RL} (where θ_{RL} can be as small as 0.005 radian, in which case the girder unloads immediately upon reaching its peak moment capacity), and

(3) a quadratic unloading curve given by the equation

$$\frac{M}{M_n} = 1 - 16(\theta_p - \theta_{RL}) + 100(\theta_p - \theta_{RL})^2 \qquad (1)$$

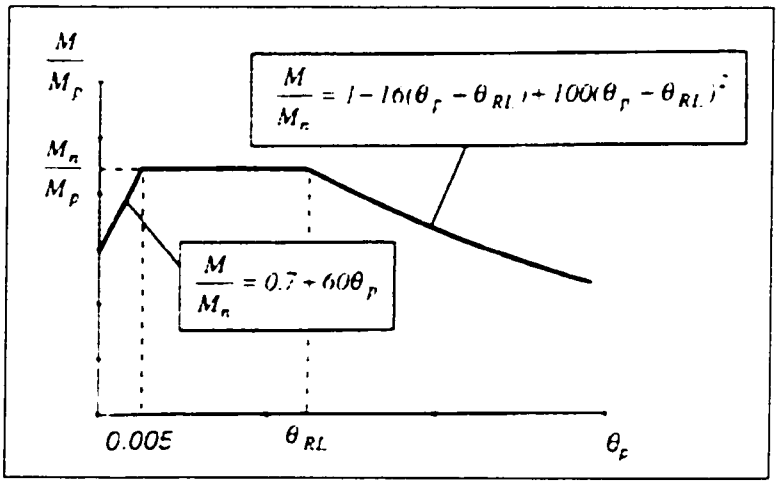

Figure 2.7.1 Moment-plastic rotation relationship (Source: Barth, Hartnagel, White, and Barker, 2001)

The linear pre-peak curve is the same as that specified for autostress design of compact I shapes in the current AASHTO LRFD specifications (AASHTO, interim 2001). Barth and White (1998) also developed an equation for the nominal moment resistance. However, any valid equation for the flexural capacity may be used for M_n.

The calculation of the nominal moment resistance, M_n, based on a potential-unified-set of flexural strength equations is outlined in the Appendix (see Appendix, Section A.4). Potential-resistance equations would predict strengths greater than the yield moment capacity, M_y, for several geometries, and would provide a continuous definition of the strength between that of braced compact sections, which have a nominal capacity of plastic moment, M_p, and other sections, which have smaller maximum strengths due to instability.

The plastic rotation at the onset of unloading, θ_{RL}, in the suggested M-θ_p model is expressed as

$$\theta_{RL} = 0.128 - 0.287\frac{b_{fc}}{2t_{fc}}\sqrt{\frac{F_{yc}}{E}} - 0.0216\frac{D}{b_{fc}} + 0.0482\frac{b_{fc}}{2t_{fc}}\sqrt{\frac{F_{yc}}{E}}\frac{D}{b_{fc}} \geq 0.005 \qquad (2)$$

where:

b_{fc} = compression flange width,

D = total web depth,

E = modulus of elasticity,

F_{yc} = yield stress of compression flange,

t_{fc} = compression flange thickness, and

θ_{RL} = plastic rotation at which pier-section flexural resistance theoretically will start to decrease with increasing rotations,

The above M-θ_p equations were obtained based on statistical regression analysis of the results from a large finite element parametric study (Barth and White, 1998), followed by verification against experimental test data (White and Barth, 1998). Several investigators (e.g., Earls, 2000; Yakel et al., 1999; and Fahnestock and Sause, 1998) have showed that the model in Fig. 2.7.1 is conservative relative to specific experimental and finite element results (which have design parameters that tend to enhance the moment-rotation response).

However, a number of attributes of the Barth and White (1998) research account for realistic aspects that prevent the proposed equations from being excessively conservative. For instance, in all the finite element studies in (Barth and White, 1998) and (Barth et al., 2000), at least two unsupported segments are considered on each side of

the maximum moment location. The additional segments outside of the critical one provide continuity effects that tend to enhance the pier moment-rotation response. The reader is referred to (Barth and White, 1998) and (Barth et al., 2000) for detailed discussions of the finite element parametric studies.

Based on the limits of the supporting experimental and finite element studies, the suggested M-θ_p equations are limited to transversely-stiffened I girders with $L_b \leq L_{pd}$,

$$\frac{b_{fc}}{2t_{fc}} \leq \left[\lambda_{pf} = 0.38\sqrt{\frac{E}{F_{yc}}} \right] \tag{3}$$

$D/b_{fc} \leq 4.25$, and $D_{cp}/D \leq 0.75$ (White and Barth, 1998), where:

D_{cp} = depth of web in compression at theoretical plastic-moment capacity;

L_b = laterally unsupported length between brace points;

L_{pd} = maximum laterally unsupported length permitted for inelastic design;

λ_{pf} = the current AASHTO (2001) flange compactness limit[1].

Furthermore, the equations are applicable only to constant depth members and to yield strengths, F_y, up to 480 MPa (70 ksi). Also, White and Barth (1998) suggest that the shear, V, should be limited to $V \leq 0.6\ V_n$, where V_n is the nominal web shear capacity, within the unsupported segments adjacent to the piers, including tension field action if applicable. This restriction was employed within their finite element studies; however, the equations appear to predict the results of experimental tests accurately for V up to $0.8V_n$.

---

[1] White and Barth (1998) considered girders with $b_{fc}/2t_{fc}$ values up to $0.41\sqrt{E/F_{yc}}$; the (AASHTO, interim 2001) flange compactness limit (Eq. (3)) is adopted here as a simplification.

CHAPTER 3

LABORATORY TESTS AND NUMERICAL MODELS

3.1 Introduction

In order to achieve the pier moment-rotation behavior of high performance steel HPS70W I-shape girders, a program of both experimental and numerical works was conducted. First, large-scale laboratory simple-span testing was performed similarly to previous research presented in Chapter 2. The testing consisted of four experiments of noncomposite compact/noncompact sections of HPS70W I-shape girders fabricated by Zimmerman Metals, Inc., Denver, Colorado. The test girder dimensions were constrained by the actuator loading capacity, about 200 kips, available at CSU and plate thickness sizes donated from Bethlehem Lukens Plate, a division of Bethlehem Steel Corporation, Burns Harbor, Indiana. Second, experimental examination of the stress-strain relationships for HPS70W is necessary for the material inputs of numerical analyses. The laboratory experiments followed ASTM E-8, Standard Tests Methods for Tension Testing of Metallic Materials, published by the American Society for Testing and Materials (ASTM). Third, numerical works were conducted on both noncomposite and composite sections, using ABAQUS finite element code. Post peak procedures, modified Rik's method for load and displacement control, nonlinear option, and the

accounting of initial imperfections and residual stresses will be employed in the ABAQUS finite element models.

3.2 Experimental Works For Moment-Rotation Of Noncomposite HPS70W Girders

3.2.1 Testing of four noncomposite compact/noncompact HPS70W specimens

Large-scale laboratory testing for four noncomposite HPS70W specimens, two "nominal" compact and two noncompact sections, were completed in 2001. The noncomposite girders were tested in the conventional simply supported configuration, and lateral compression-flange bracing satisfying the AASHTO requirements (see Section 2.2.1) was applied (see Section 2.3.3, Figure 2.3.3.5). For the laboratory testing of the four noncomposite HPS70W girders, electrical instrumentation employed were: (1) master-slave MTS 407 controllers with linear variable displacement transducers (LVDTs) to operate hydraulic actuators in a displacement-control manner, (2) load cells in actuators to measure loads, (2) string-potentiometers attached to the underside of the girders to obtain deflections, directly, and rotations, indirectly, and (4) quarter-bridge-configuration strain gages (inside the Hewlett Packard (HP) Data Acquisition and Control Unit) to measure strains. For the two noncompact girders, a deflection dial gage was also employed to measure midspan deflection of the bottom flange.

Figure 3.2.1.1 displays the dimensions of the four girders. In proportion to AASHTO specifications (AASHTO, interim 2001), Table 3.2.1.1 presents the dimensions of the two "nominal" compact girders. Specimens #1 and #2 (see Section 3.2.3 for "nominal/actual" considerations). Specimen #1 (span of 19.5 ft) had a larger lower flange, which lowered the elastic neutral axis to put more girder web into compression

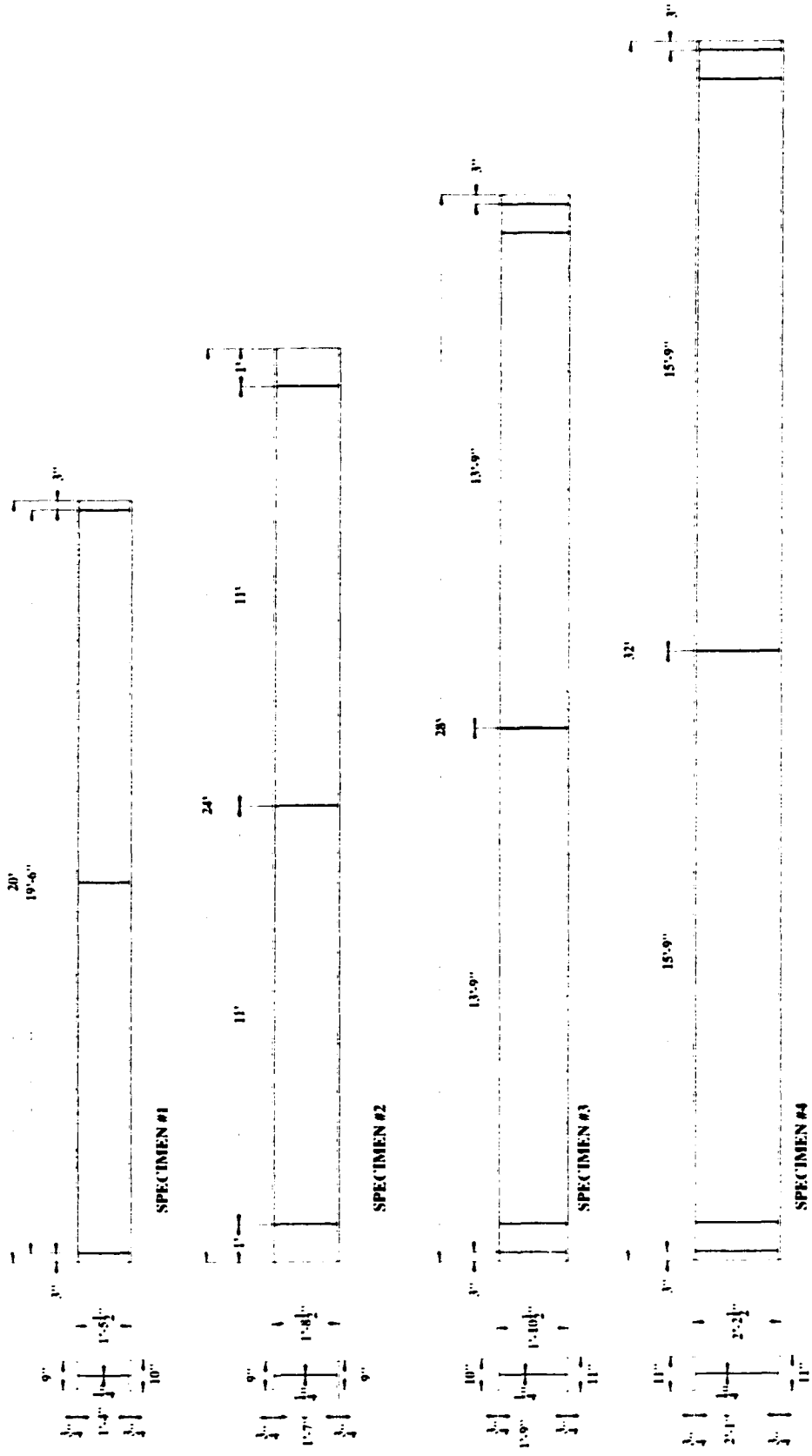

Figure 3.2.1.1 CSU compact and noncompact girder dimensions

Table 3.2.1.1 CSU compact girder dimensions

Property	Specimen #1 (nominal compact)	Specimen #2 (nominal compact)
Test span, L (ft)	19.5	22
Web depth inside flanges, D (in.)	16	19
Web thickness, t_w (in.)	1/4	1/4
Compression flange width, b_{fc} (in.)	9	9
Tension flange width, b_{ft} (in.)	10	9
Flange thickness, t_f (in.)	3/4	3/4
Ratio of web depth in compression, D_{cp}/D, nominal [avg. of tested values]	0.594 [0.612]	0.5 [0.5]
Nominal flange slenderness, $b_f/2t_f$	6.0	6.0
Web slenderness, $2D_{cp}/t_w$, nominal [avg.]	76.0 [78.3]	76.0 [76.0]
a_r, nominal [average of tested values]	0.352 [0.363]	0.352 [0.352]

Table 3.2.1.2 CSU noncompact girder dimensions

Property	Specimen #3 (noncompact)	Specimen #4 (noncompact)
Test span, L (ft)	27.5	31.5
Web depth inside flanges, D (in.)	21	25
Web thickness, t_w (in.)	1/4	1/4
Compression flange width, b_{fc} (in.)	10	11
Tension flange width, b_{ft} (in.)	11	11
Flange thickness, t_f (in.)	3/4	3/4
Ratio of web depth in compression, D_{cp}/D, nominal [avg. of tested values]	0.571 [0.585]	0.5 [0.5]
Nominal flange slenderness, $b_f/2t_f$	6.67	7.33
Web slenderness, $2D_{cp}/t_w$, nominal [avg.]	96.0 [98.3]	100.0 [100.0]
a_r, nominal [average of tested values]	0.400 [0.410]	0.379 [0.379]

where:

D_{cp} = depth of web in compression, taken at the plastic moment (in.), and

a_r = ratio of web compression area to flange compression area, taken at the plastic moment.

($D_{cp}/D = 0.6$). This was to account for the concrete deck and rebars near interior supports in composite girders. However, Specimen #2 was a symmetric I-girder ($D_{cp}/D = 0.5$)

with larger cross-section and span of 22 ft. Table 3.2.1.2 displays the dimensions of the two noncompact girders. In proportion to AASHTO specifications, Specimens #3 and #4 were designed with compact flanges and a noncompact web. Specimen #3 (span of 27.5 ft) had a larger lower flange, which lowered the elastic neutral axis to put more girder web into compression ($D_{cp}/D = 0.6$), to account for the concrete deck and rebars near interior supports in composite girders. On the other hand, Specimen #4 was a symmetric I-girder ($D_{cp}/D = 0.5$) with larger cross-section and span of 31.5 ft. In the tables, the nominal or [average of tested values] values are based on the nominal yielding strength, $F_{yf} = F_{yw} = 70.0$ ksi for all the flanges and web, or the average material tested data, $F_{yf} = 83.35$ ksi for the flanges and $F_{yw} = 69.83$ ksi for the web (see Sections 3.2.2 and 3.3.2), respectively.

- Testing apparatus design and overhaul

The four noncomposite girders were tested in the conventional simply supported configuration. The overhaul and strengthening of a pre-existing test apparatus consisted of joining and reinforcing two separate load frames, each supporting a 100 kip-capacity actuator for sufficiently applying a midspan, concentrated force and establishing the lateral bracing system, whose unbraced length are specified by AASHTO 6.10.4.1.7 (see Section 2.2.1). In addition, a linear variable displacement transducer (LVDT) was connected to each actuator to allow displacement-control actuator movement that ultimately permitted a thorough, careful examination of post-peak behavior. All details of testing apparatus design and overhaul are credited to Griffeth's Master-of-Science thesis (Griffeth, 2001) supervised by the author's advisor (see Section 2.5.3).

- Specimen instrumentation and measurement

A data acquisition system, which consists of HP 3852A Data Acquisition and Control Unit operated by LabVIEW 5.0 installed on a personal computer, reads electronic signals from the LVDTs, load cells, strain gages, and string-potentiometers (string-pots) through electronic channels. For each channel, the data acquisition system receives 20 data points per reading and averages them to obtain one value per reading. In addition, the total applied midspan load was determined as the summation of actuator load cell forces, which were obtained from electronic readings through MTS 407 controllers (a master and a slave) connected to the data acquisition system. Since load cells were not located at the two end reactions, the support reactions are assumed to be each equal to one half of the applied load.

Figures 3.2.1.2, 3.2.1.3, 3.2.1.4 & 3.2.1.5 present the instrumentation locations of Specimen #1, #2, #3, and #4, respectively. At midspan, ten strain gages on each girder measured longitudinal strains at two cross sections, five gages each respectively 8 in. north and south of midspan. The strain gages were calibrated at 1000 μ strain with a shunt resistor. Additionally, a string-pot was attached to the underside of each girder to directly measure the vertical deflections at midspan. For the two noncompact girders, Specimens #3 and #4, a deflection dial gage was also employed to measure midspan deflection of the bottom flange (see Figure 3.2.1.6). For the two compact girders, Specimens #1 and #2, two additional string-pots were attached to an aluminum cantilever bar glued to the web at north and south near midspan to check the very small point rotations around the neutral axis (see Figure 3.2.1.7).

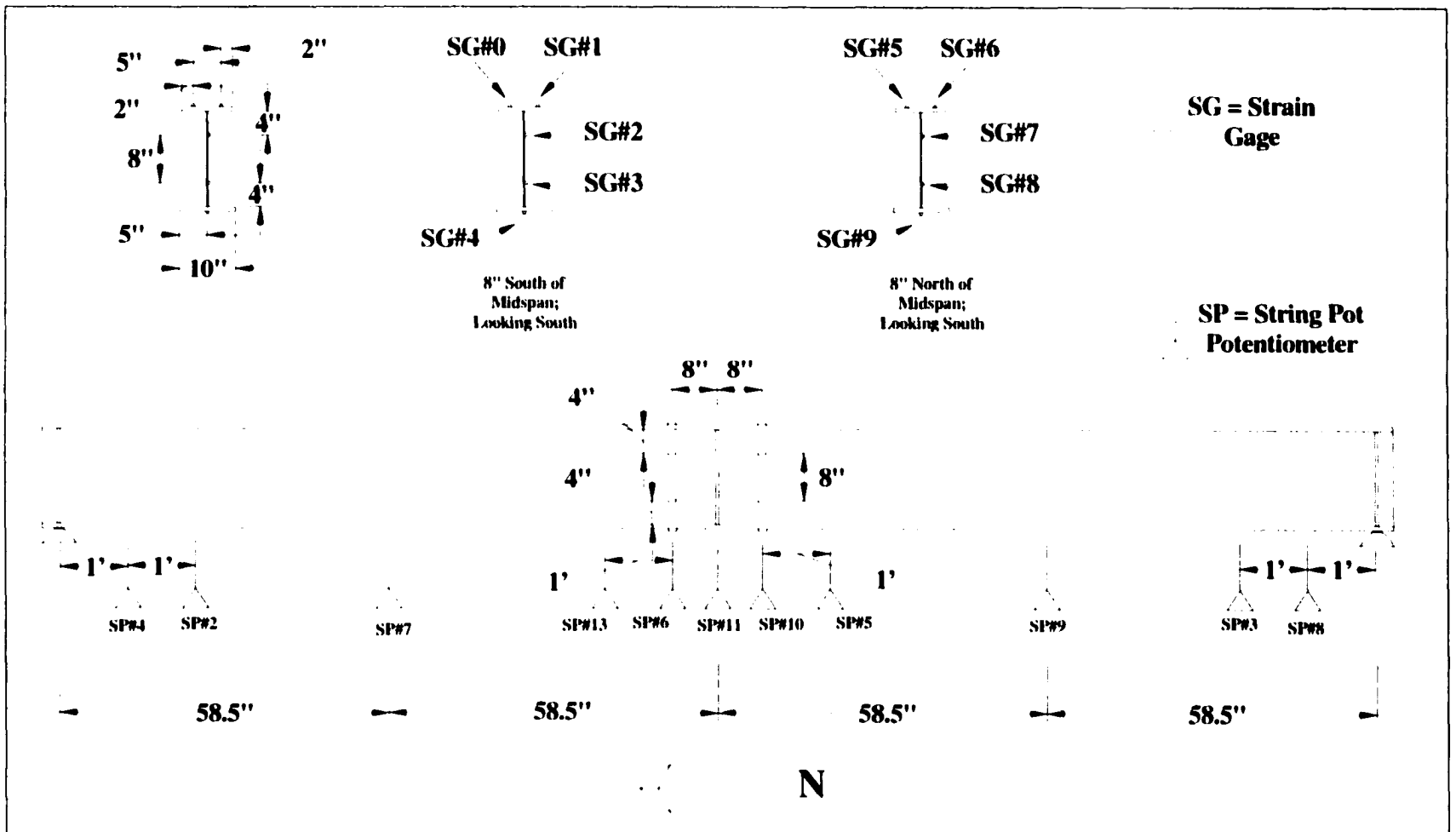

Figure 3.2.1.2 Specimen #1 - Instrumentation locations

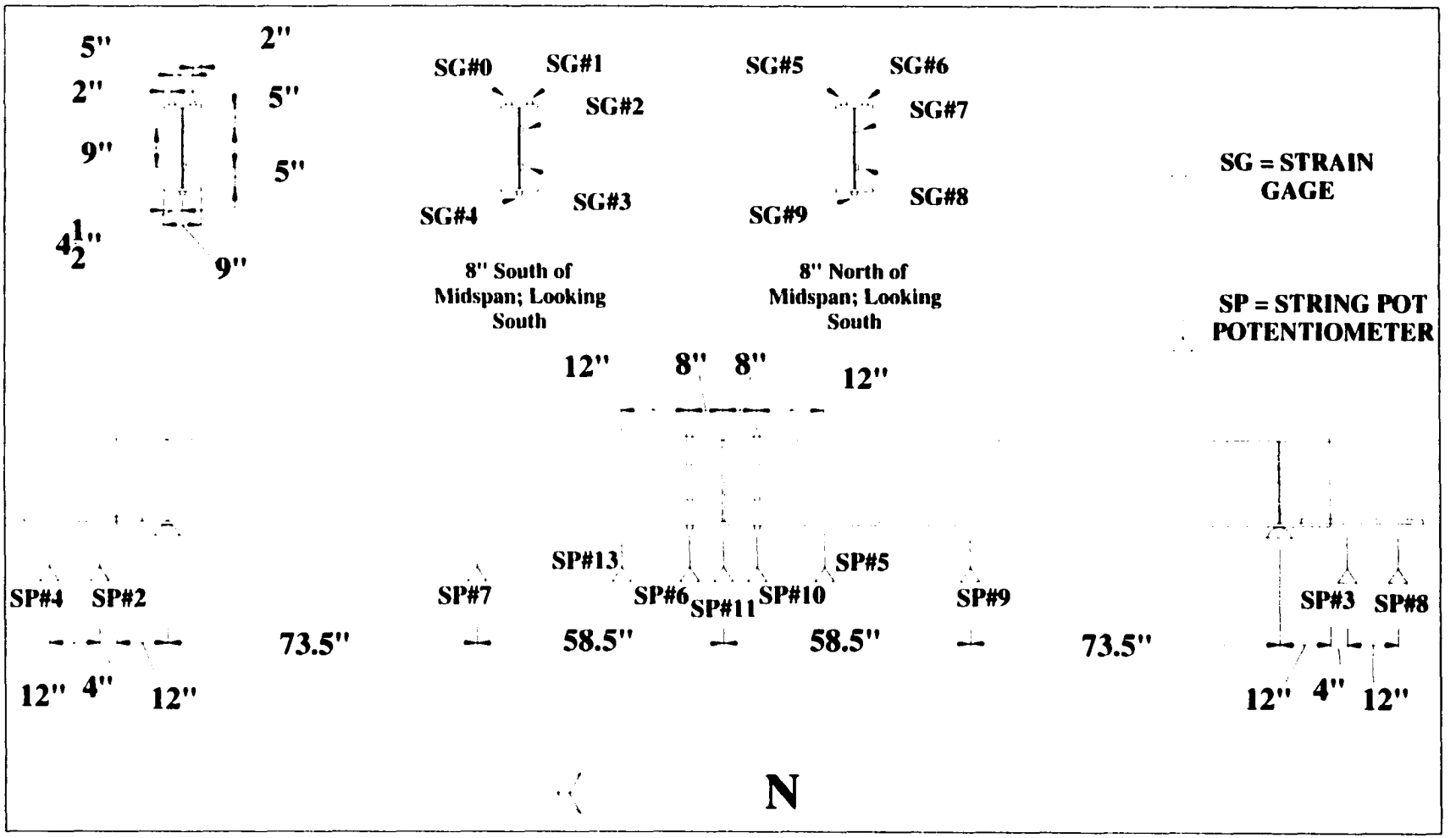

Figure 3.2.1.3 Specimen #2 - Instrumentation locations

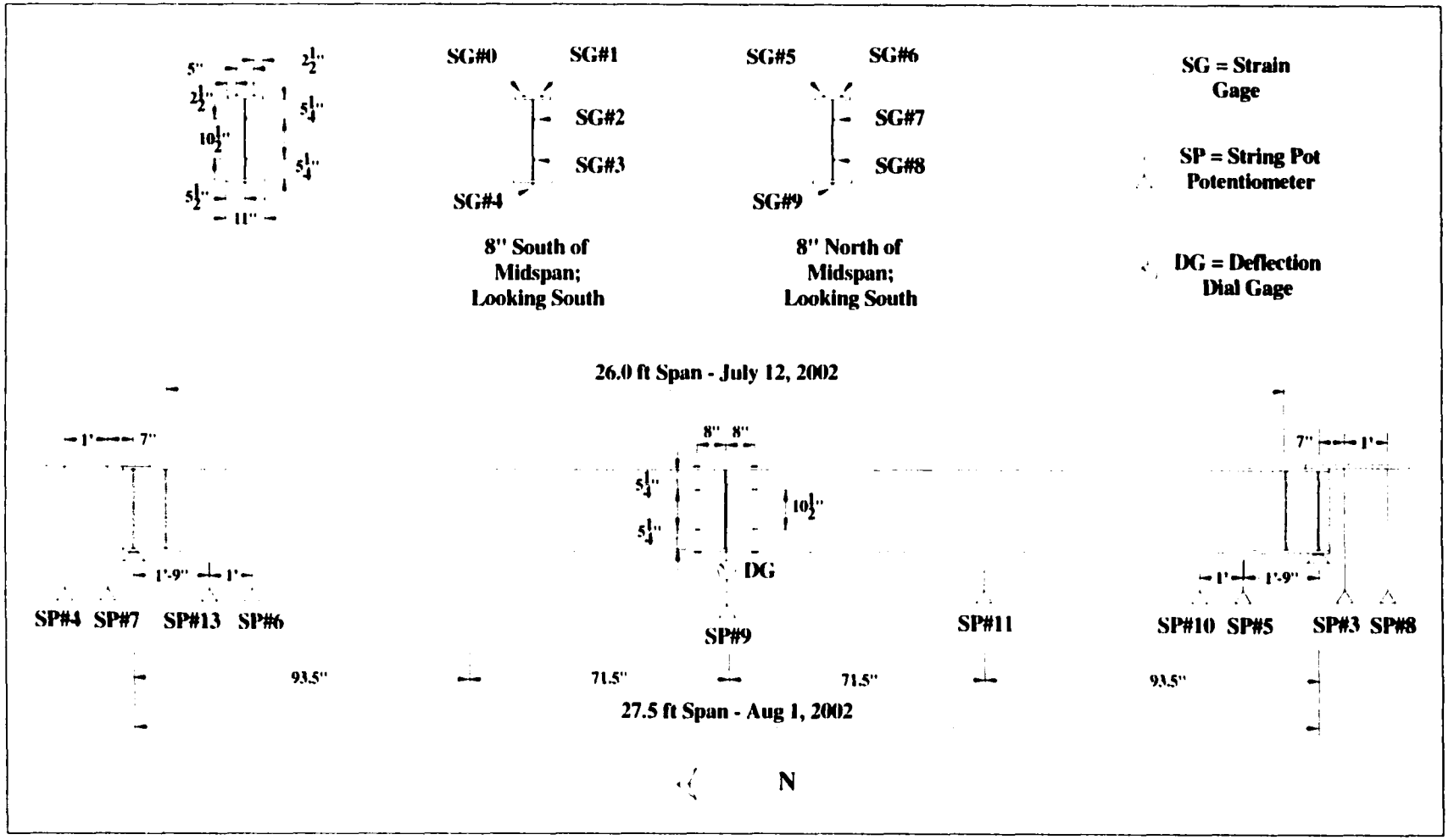

Figure 3.2.1.4 Specimen #3 - Instrumentation locations

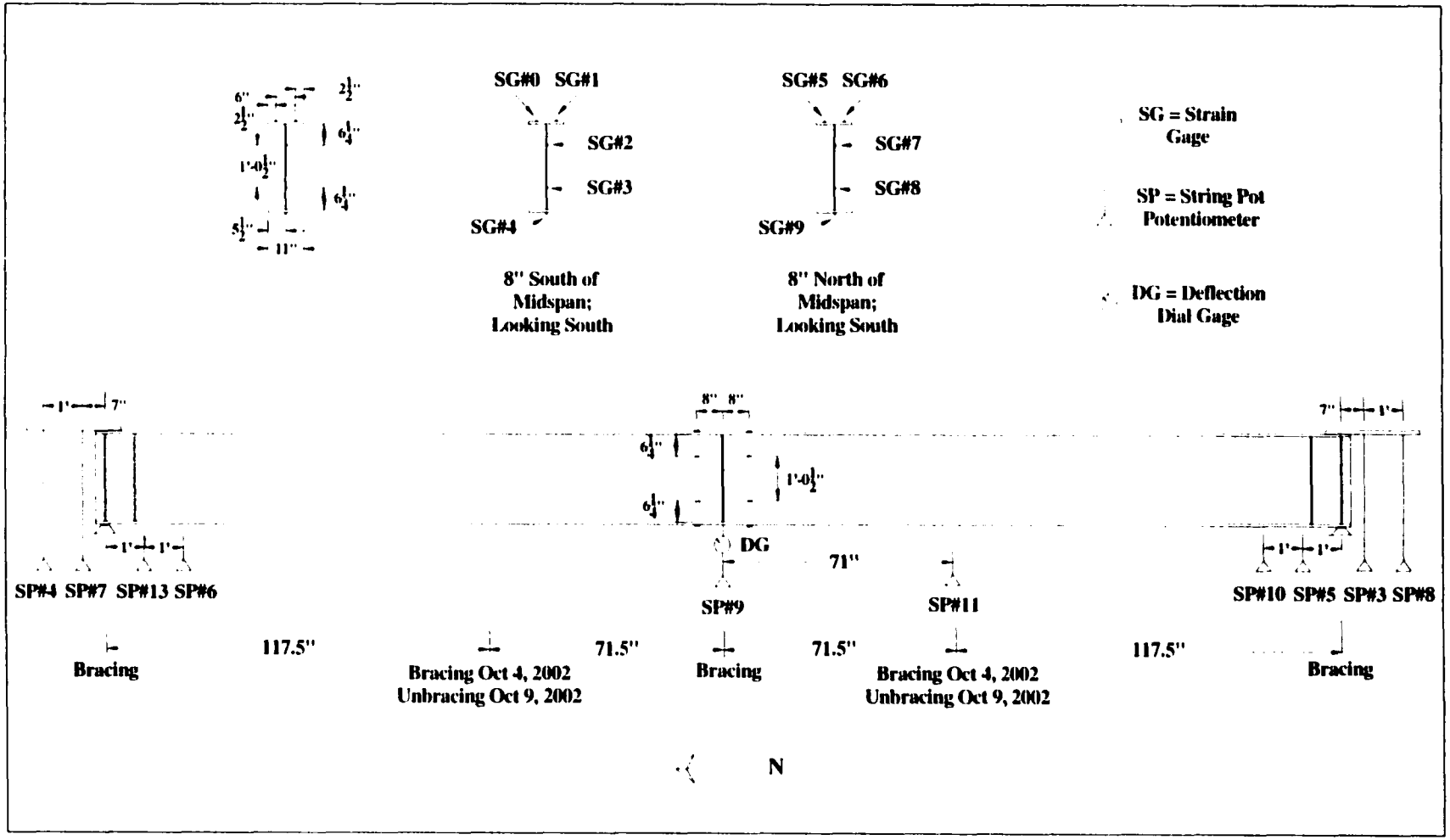

Figure 3.2.1.5 Specimen #4 - Instrumentation locations

Figure 3.2.1.6 Left: Midspan arrangement for Specimens #3 and #4
Right: Typical end rotation measurement instrumentation

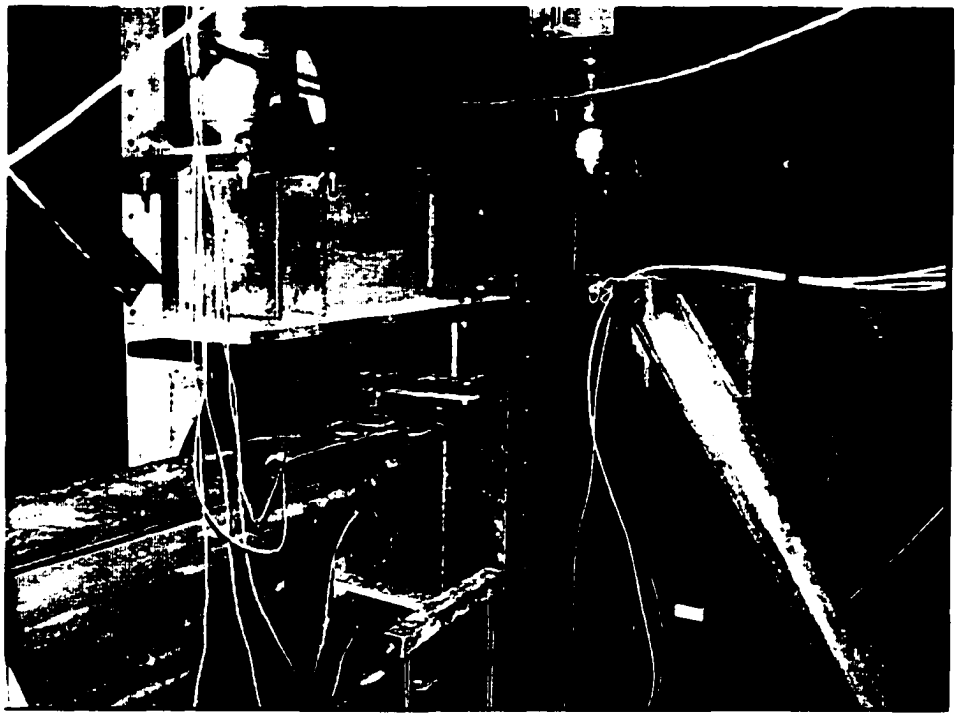

Figure 3.2.1.7 Midspan arrangement for Specimens #1 and #2

At the support regions, four to eight additional string-pots, spaced at known distances, were attached to the under and/or top side of each girder to indirectly obtain two near-end rotations that were averaged over 12 in. (see Figure 3.2.1.6). Additionally, one (or two) string-pots were attached to the underside of each girder to directly measure the vertical deflection(s) at intermediate point(s) in span.

- Test procedures

Under displacement control rates, the girders were tested in a simply supported configuration and deflected vertically downward. First, the test for Specimen #1 was performed on February 1, 2001. Specimen #1 was deflected vertically downward to 1.85 in. at a rate of 4 in./hr, and the load was removed at the same displacement rate. Each time when the testing was paused at various displacement and load intervals, the

computer data acquisition system acquired LVDT, load cell, strain gage, and string-pot readings. Then, the load was totally removed. A new displacement rate of 8 in./hr was applied until the specimen was deflected vertically downward 4.38 in. During this period, incremental data readings were taken, and the load was again removed at 8 in./hr. At this time, after the load was totally removed, a longer column post was installed since the girder's permanent midspan vertical displacement was approximate 2.2 in. Thereafter, at a reloading rate of 10 in./hr, a maximum load of 196.5 kips (maximum moment of 957.9 ft-kips) was reached at a midspan deflection of 4.44 in. ("total rotation" of 0.0899 rad measured near the supports as shown in Figure 3.2.1.2). When a significant change in load resistance and large scale local deformations were observed, at which Specimen #1 was deflected downward totally 7.04 in. ("total rotation" of 0.1332 rad) corresponding to a total load of 170 kips (moment of 828.9 ft-kips), the load was removed. Finally, Specimen #1 bounced back due to the elastic recovery to a permanent midspan deflection of 5.24 in. ("total rotation" of 0.0937 rad at near supports) corresponding to zero load and moment. There were 119 total readings for Specimen #1.

Second, Specimen #2 was tested on February 15, 2001. It was deflected vertically downward to 2.11 in. at a rate of 3 in./hr, and then the load was totally removed at 6 in./hr. During this period, the testing was halted at various displacement and load intervals for the computer data acquisition system to acquire LVDT, load cell, strain gage, and string-pot readings. Then, the reloading progressed at a new displacement rate of 6 in./hr. A maximum load of 203.9 kips (maximum moment of 1121.6 ft-kips) was reached at a midspan downward deflection of 3.60 in. ("total rotation" of 0.0594 rad measured near the supports as shown in Figure 3.2.1.3). When the specimen was

deflected vertically downward 4.93 in., the load was removed at 10 in./hr. As before, periodic data readings were taken. After the load was totally removed this time, a longer column post was utilized since the girder's permanent midspan vertical deflection was approximately 2.82 in. Thereafter, a reloading rate of 10 in./hr was applied. When a significant change in load resistance and large scale local deformations were observed, at which Specimen #2 was deflected downward totally 6.81 in. ("total rotation" of 0.1076 rad) corresponding to a total load of 155.2 kips (moment of 853.5 ft-kips), the load was removed. Finally, Specimen #2 bounced back to a permanent midspan deflection of about 4.94 in. ("total rotation" of 0.0593 rad at near supports) corresponding to zero load and moment. There were 145 total readings for Specimen #2.

Third, test for Specimen #3 was first performed on July 12, 2001 with its original span of 26.0 ft (see Figure 3.2.1.4). Initially, Specimen #3 was deflected vertically downward to 0.846 in. at a rate of 4 in./hr, and then the load was removed at 4 in./hr. Again, the testing was halted at various displacement and load intervals for taking periodic data. After the load was totally removed, the displacement rate was increased to 6 in./hr for reloading. With yielding on the compression flange and web in compression (strain gages #0, #1, #2, #5, and #6) at a total load of 192.4 kips (moment of 1250.9 ft-kips), the specimen was deflected vertically downward 2.545 in. ("total rotation" of 0.0411 rad measured inside and near the supports). The total load then reached and was maintained exceeding the nominally available load capacity of 200 kips. Suddenly, the hydraulic pump shutdown because of over-temperature when the total load was about 209.1 kips (moment of 1359.2 ft-kips). From a vertical deflection of 2.904 in. ("total rotation" of 0.0465 rad) at this stage, the specimen bounced back to a deflection of 0.428

in. ("total rotation" of 0.0054 rad) at a corresponding load of 3.5 kips (moment of 22.6 ft-kips) due to elastic recovery. Afterward, the reloading was continued for a rate of 10 in./hr. As before, periodic data readings were taken until hydraulic pump shutdown again because of over-temperature at a total load of 215.2 kips (moment of 1398.8 ft-kips) corresponding to a vertical deflection of 3.131 in. ("total rotation" of 0.0508 rad). From that stage, the specimen bounced back to permanent a defection of 0.507 in. (permanent "total-rotation" of 0.0057 rad) at zero load and moment. There were 111 total readings for Specimen #3 on the July 12-test.

Thereafter, the span of Specimen #3 was increased to 27.5 ft in order to have a larger available moment with the same available load. Test for Specimen #3 was continued with the longer span on August 1, 2001 (see Figure 3.2.1.4) at a rate of 10 in./hr. North-web buckled to West at a total load of 208.5 kips (moment of 1433.4 ft-kips). At a maximum total load of 208.6 kips (moment of 1434.4 ft-kips) in the yielding plateau stage, Specimen #3 was deflected vertically 3.609 in. beyond the permanent deflection of 0.507 in.. After the load was totally removed at 10 in./hr, a longer column post was utilized as the girder's permanent midspan vertical deflection totally increased to 1.00 in. Then, at a reloading rate of 20 in./hr until a significant flange buckle was noticed at a maximum load of 209.8 kips (moment of 1442.4 ft-kips), Specimen #3 was deflected downward totally 4.07 in. ("total rotation" of 0.0619 rad). When the distributor beam connecting the two actuators was considerably uneven, the load was removed for safety. At that unloading starting point, Specimen #3 was deflected downward totally 4.56 in. ("total rotation" of 0.0623 rad) corresponding to a total load of 202.9 kips (moment of 1395.2 ft-kips). Finally, Specimen #3 bounced back to a final permanent

midspan deflection of 1.58 in. ("total rotation" of 0.0215 rad inside and near supports) corresponding to an approximate zero load and moment. There were 60 total readings for Specimen #3 on the August 1-test.

Fourth, Specimen #4 was experimentally tested with two variations of lateral compression-flange bracing. Test on Specimen #4 was first performed on October 4, 2001 with bracing at midspan load point, end reactions, and in between middle and end satisfying AASHTO specifications (AASHTO, 1998 interim 2001) for both compact and noncompact section (see Figure 3.2.1.5 and calculations in Section 3.3.1). At a loading rate of 6 in./hr and unloading rate of 10 in./hr, the testing was halted at various displacement and load intervals for taking periodic data. With yielding on the compression flange at a total load of 204.6 kips (moment of 1610.8 ft-kips), the specimen was deflected downward 3.14 in. ("total rotation" of 0.0438 rad measured inside and near the supports). The midspan deflection then increased to 3.40 in. ("total rotation" of 0.0465 rad) at a maximum load of 215.2 kips (moment of 1694.8 ft-kips). The specimen was unloaded when the midspan deflection was 3.41 in. ("total rotation" of 0.0466 rad) at a total load of 214.9 kips (moment of 1692.7 ft-kips). When the load was totally removed, the permanent midspan defection was 0.39 in. corresponding to a permanent "total-rotation" of 0.0045 rad. There were 39 total readings for Specimen #4 on the October 4-test.

Finally, test on Specimen #4 was continued on October 9, 2001 with bracing only at midspan and at supports, for which the unbraced length did not dissatisfy AASHTO specifications (see Figure 3.2.1.5 and calculations in Section 3.3.1). A loading rate of 6 in./hr and unloading rate of 10 in./hr were applied. At a total load of 164.2 kips (moment

of 1292.7 ft-kips), the specimen's North side displaced to West slightly. At a maximum load of 215.9 kips (moment of 1700.2 ft-kips), the midspan deflection increased to 3.08 in. beyond the permanent deflection of 0.39 in. ("total rotation" of 0.0433 rad in addition to the permanent "total-rotation" of 0.0045 rad). The specimen was unloaded when the midspan deflection totally reached 3.51 in. ("total rotation" of 0.0479 rad) at a total load of 215.2 kips (moment of 1694.5 ft-kips). When the load was totally removed, the final permanent midspan deflection was 0.46 in. (final permanent "total-rotation" of 0.0048 rad inside and near supports). There were 37 total readings for Specimen #4 on the October 9-test.

Results of the large-scale laboratory testing for the four noncomposite HPS70W specimens are performed on plots of moment-rotation relationships in Section 4.2. In addition, Figures 3.2.1.8 and 3.2.1.9 below present the states of midspan deformed shapes and final deformed shapes of Specimen #1, respectively. Figure 3.2.1.10 displays final deformed shapes of Specimen #2 while Figure 3.2.1.11 show the midspan deformed shape of Specimen #3 and a photo of Specimen #4 after its October 4-test.

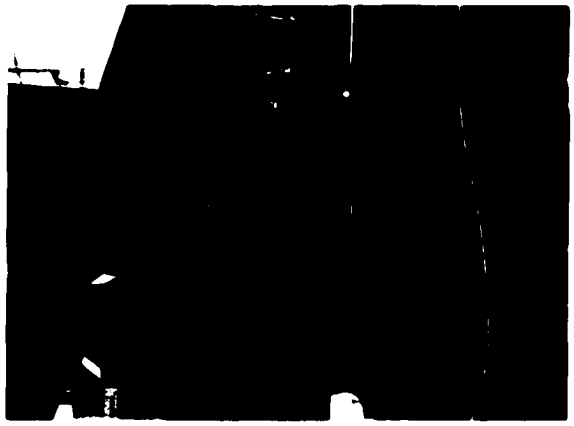

Local web buckle. This is just below the local flange buckle that is depicted in each of the other three photos.	Beginning of a local flange buckle.

This is the same flange and web local buckle at an advanced state.	This is the beam after unloading. Note that the loading half round is lifted off the beam. The beam was simply supported and loaded in the middle.

Figure 3.2.1.8 States of midspan deformed shape of Specimen #1 (February 1, 2001)

Figure 3.2.1.9 Final deformed shapes of Specimen #1 (February 1, 2001)
Above: Local web and flange buckle at midspan
Below: Lateral torsional buckle of compression flange

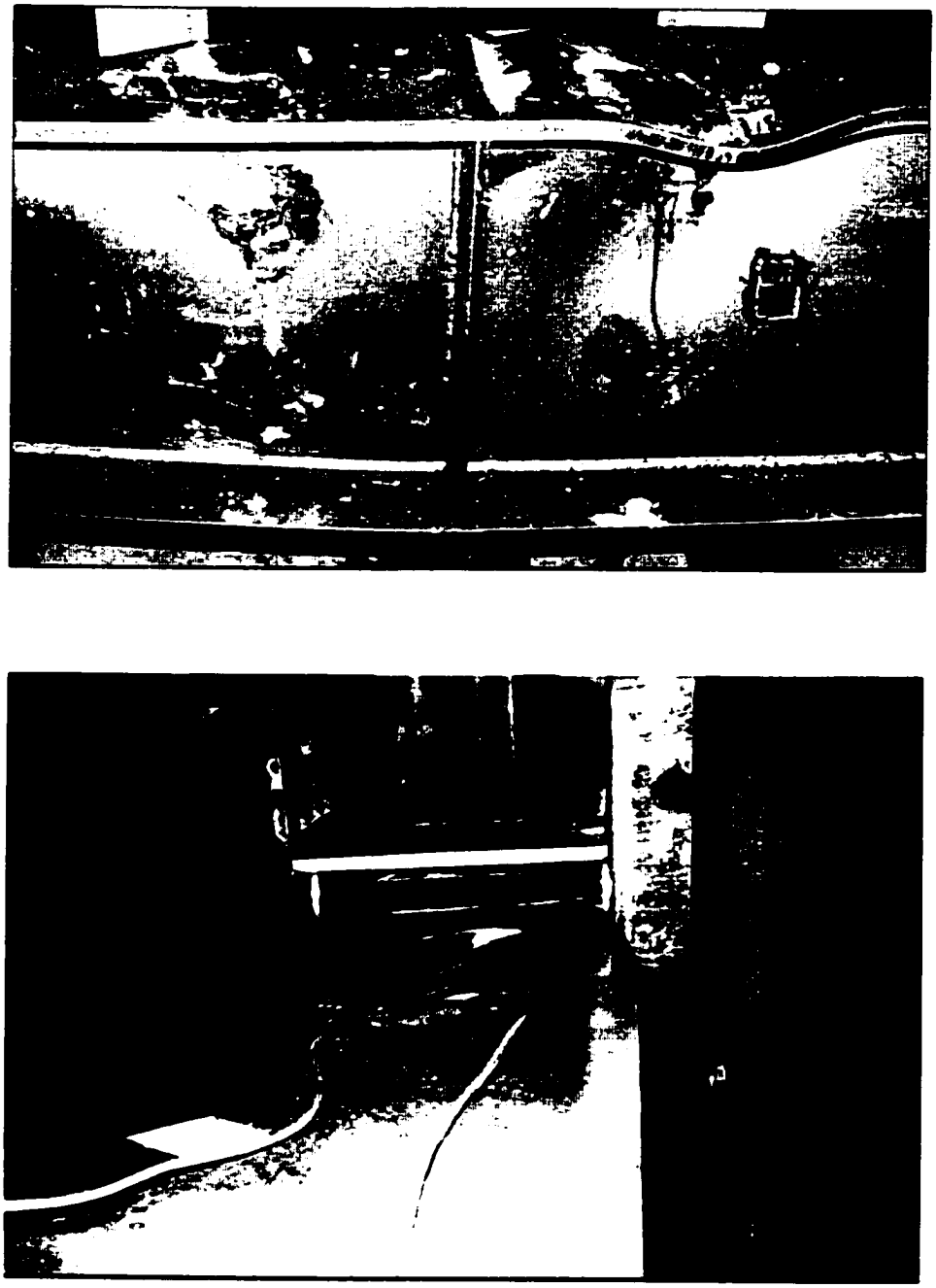

Figure 3.2.1.10 Final deformed shapes of Specimen #2 (February 15, 2001)
Above: Local web and flange buckle at midspan
Below: Lateral torsional buckle of compression flange

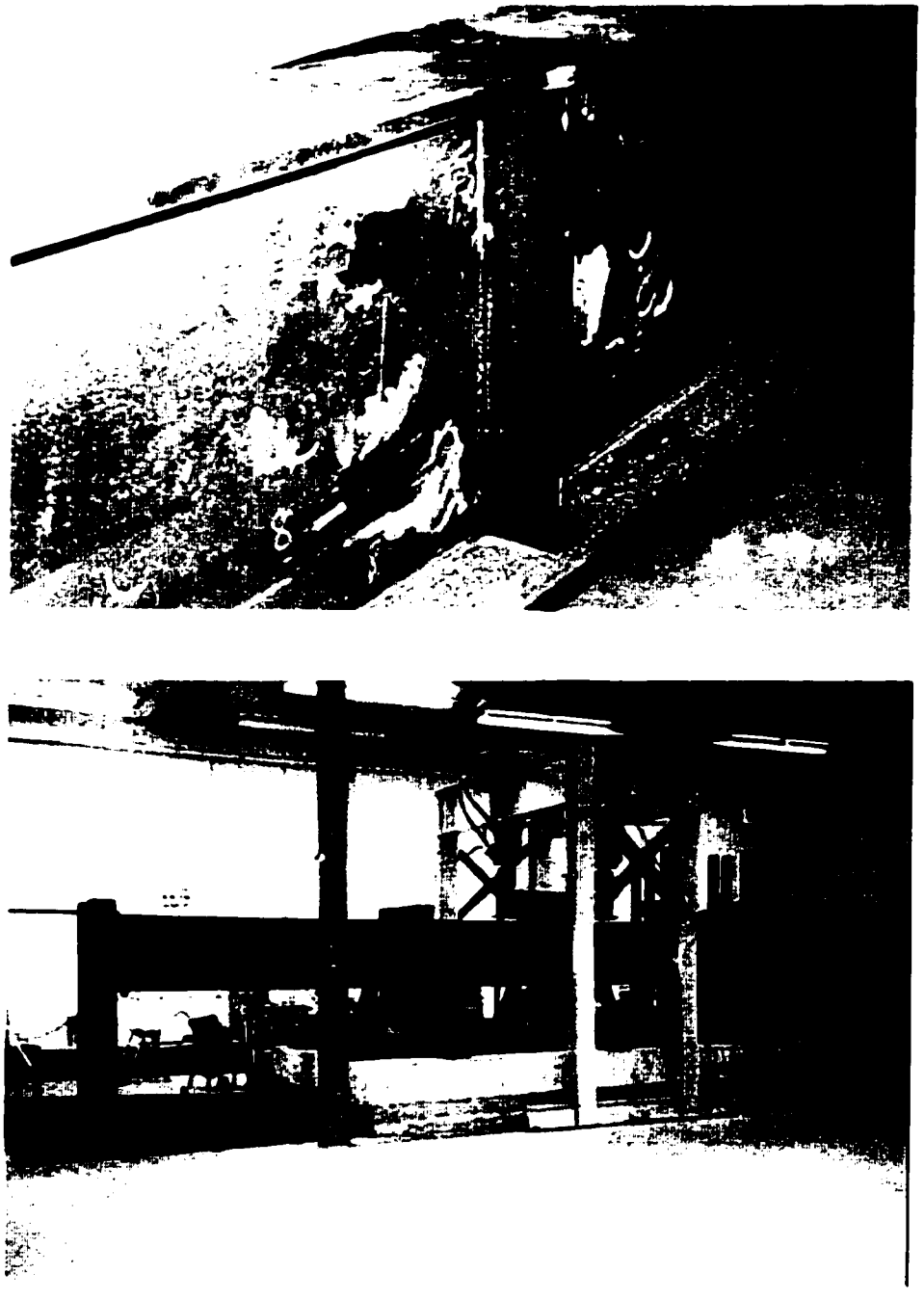

Figure 3.2.1.11 Above: Midspan deformed shape of Specimen #3 (August 1, 2001)
Below: Specimen #4 after first tested (October 4, 2001)

3.2.2 Experimental examining the stress-strain relationship for HPS70W as inputs for numerical analyses of HPS70W girders

Experimental examination of the stress-strain relationships for HPS70W is necessary for the material inputs of numerical analyses. Beside the inputs of residual stresses and imperfection, several parametrical variations in the material stress-strain relationship can result in changes in pier moment-rotation response of the numerical models of HPS70W I-shape girders. In previous studies, different authors used different typical options of proper material inputs for numerical models of HPS70W girders. For instance, the ratio of yield strains, $\varepsilon_{st}/\varepsilon_y$, was employed as 10 (White, Barth, & Bobb, 1998), or 6.4 (Barth & White, 1998), or 5.5 (Zubeck, 2000). In addition, a "yield plateau slope" was applied as 100 ksi preceding a first strain-hardening slope, E_{st} = 800 ksi (or 400 ksi), (White, Barth, & Bobb, 1998), or another "yield plateau slope" could be chosen as 136.9 ksi corresponding to a first strain-hardening slope, E_{st} = 364.1 ksi, that was followed by a second and a third strain-hardening slope of 197.2 ksi and 81.5 ksi, respectively (Zubeck, 2000). Furthermore, there were various values for the modulus of elasticity of the flange steel and web steel, E_{flange} and E_{web}, in Appendices B1 and B2 of the Yakel, Mans, and Azizinamini's report (Yakel, Mans, and Azizinamini, 1999).

Hence, to decide proper material inputs for numerical models of HPS70W girders at CSU, tensile tests on a number of flange and web samples were performed to determine the values of the modulus of elasticity, E, and the stress-strain relationships of HPS70W. The photos of the samples, parallel and perpendicular to the rolling direction, for the uniaxial tensile tests are displayed in Figures 3.2.2.1, 3.2.2.2, 3.2.2.3, and 3.2.2.4. The laboratory experiments followed ASTM E-8, Standard Tests Methods for Tension Testing of Metallic Materials, published by the American Society for Testing and

Materials (ASTM). The results of the uniaxial tensile tests for flange and web samples as material inputs for numerical models are presented in Section 3.3.2.

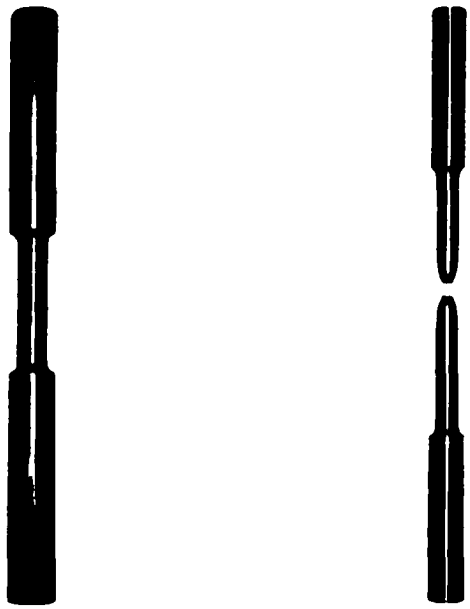

Figure 3.2.2.1 Flange samples of HPS70W for uniaxial tensile tests - Parallel to rolling direction

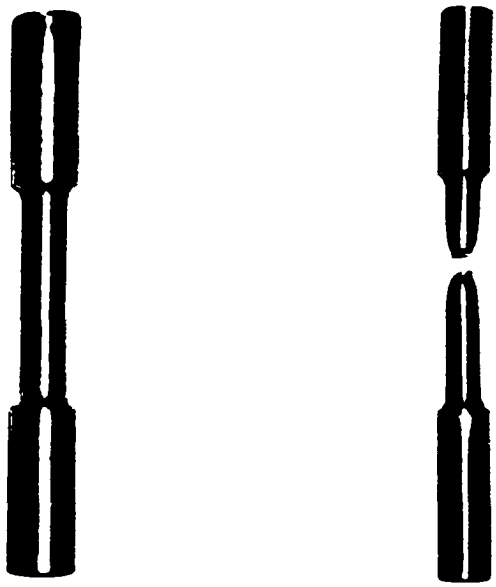

Figure 3.2.2.2 Flange samples of HPS70W for uniaxial tensile tests - Perpendicular to rolling direction

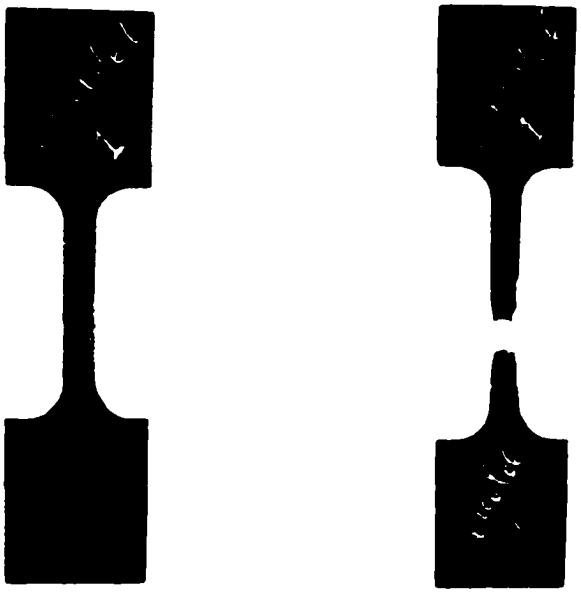

Figure 3.2.2.3 Web samples of HPS70W for uniaxial tensile tests - Parallel to rolling direction

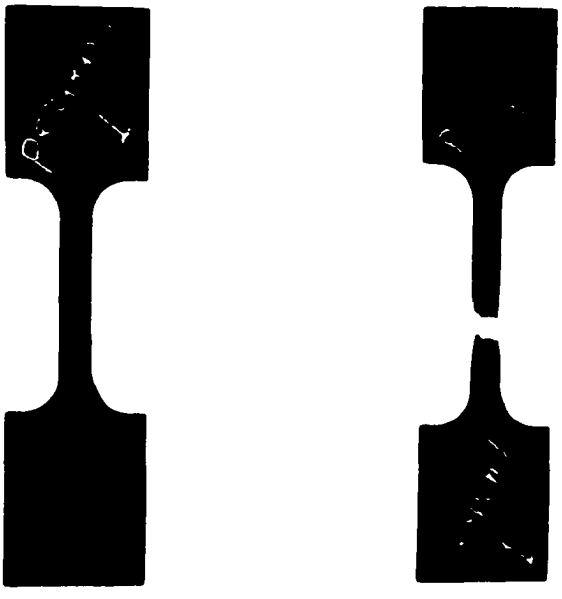

Figure 3.2.2.4 Web samples of HPS70W for uniaxial tensile tests - Perpendicular to rolling direction

3.2.3 Material tested data of HPS70W plates: a query for "nominal compact" classification and calculation for plastic moments

HPS70W Specimens #1 and Specimen #2 at Colorado State University (CSU) were classified as compact girders, nominally. The classification at CSU was based on the two compact section requirements AASHTO 6.10.4.1.2 and AASHTO 6.10.4.1.3 for web and flange, respectively (AASHTO, interim 2001). Particularly for the web, the limit value of $\frac{2D_{cp}}{t_w} \le 3.76\sqrt{\frac{E}{F_{yc}}}$, as 76.5 for CSU, was calculated by substituting the conventional modulus of elasticity of steel, E = 29,000 ksi, and the specified minimum yield strength of the compression flange, F_{yc} = 70 ksi for HPS70W, nominally. However, the limit value, $3.76\sqrt{\frac{E}{F_{yc}}}$, becomes 71.5 when substituting F_{yc} = 83.35 ksi and E = 30,113 ksi, averaged from material tested data. At this stage, the web slenderness ratio, $\frac{2D_{cp}}{t_w}$, as 76.0, nominally [or 78.3, actually], for Specimen #1 and 76.0 for Specimen #2, is greater the limit value of 71.5. As a result, both HPS70W "nominal" compact girders at CSU would be questioned to be classified as noncompact.

Tables 3.2.1.1 and 3.2.1.2 in Section 3.2.1 present the dimensions of CSU's HPS70W girders, Specimens #1 to #4. Based on the dimensions and the nominal yielding strength, $F_{yf} = F_{yw}$ = 70.0 ksi for all the flanges and web, or the average material tested data, F_{yf} = 83.35 ksi for the flanges and F_{yw} = 69.83 ksi for the web, the plastic moments, M_p, for Specimens #1, #2, #3, and #4 are calculated in the Appendix (see Appendix, Section A.5).

3.3 Numerical Moment-Rotation Of Noncomposite HPS70W Girders

3.3.1 Implementation of ABAQUS finite element code

The numerical moment–rotation analyses of HPS70W noncomposite girders at CSU are performed using ABAQUS finite element code with nonlinear solutions. ABAQUS buckling analysis, post-peak analysis procedures, modified Rik's method for load and displacement control, nonlinear option, and accounting for initial imperfections and residual stresses will be employed for all ABAQUS finite element models (Hibbitt, Karlsson & Sorensen, Inc., 1997 and 1999).

For the half-length models of the noncomposite girders, the S4R elements, an ABAQUS 4-node, thick shell element with 6 degrees of freedom per node, are employed densely spaced at the midspan and gradually increased spacing to the end support. Sixteen shell elements are assigned across each flange and 16 elements through the web to provide for reasonable/economical convergence and input for residual stress distribution as in previous studies (see Section 2.4). In addition, the number, which must be odd number, of integration points through thickness of a shell section is chosen as 5 (default), 15, and 11 for 0.25 inch-web, 0.75 inch-flange, and 0.50 inch-bearing stiffener, respectively.

Figures 3.3.1.1, 3.3.1.2, 3.3.1.3, and 3.3.1.4 illustrate the FEM meshes in initial and deformed shapes of Specimens #1, #2, #3, and #4, respectively. For the half-length numerical model of each specimen, Table 3.3.1.1 presents the total numbers of elements, nodes, and variables are utilized in an ABAQUS nonlinear analysis and the time consumed for a numerical analysis.

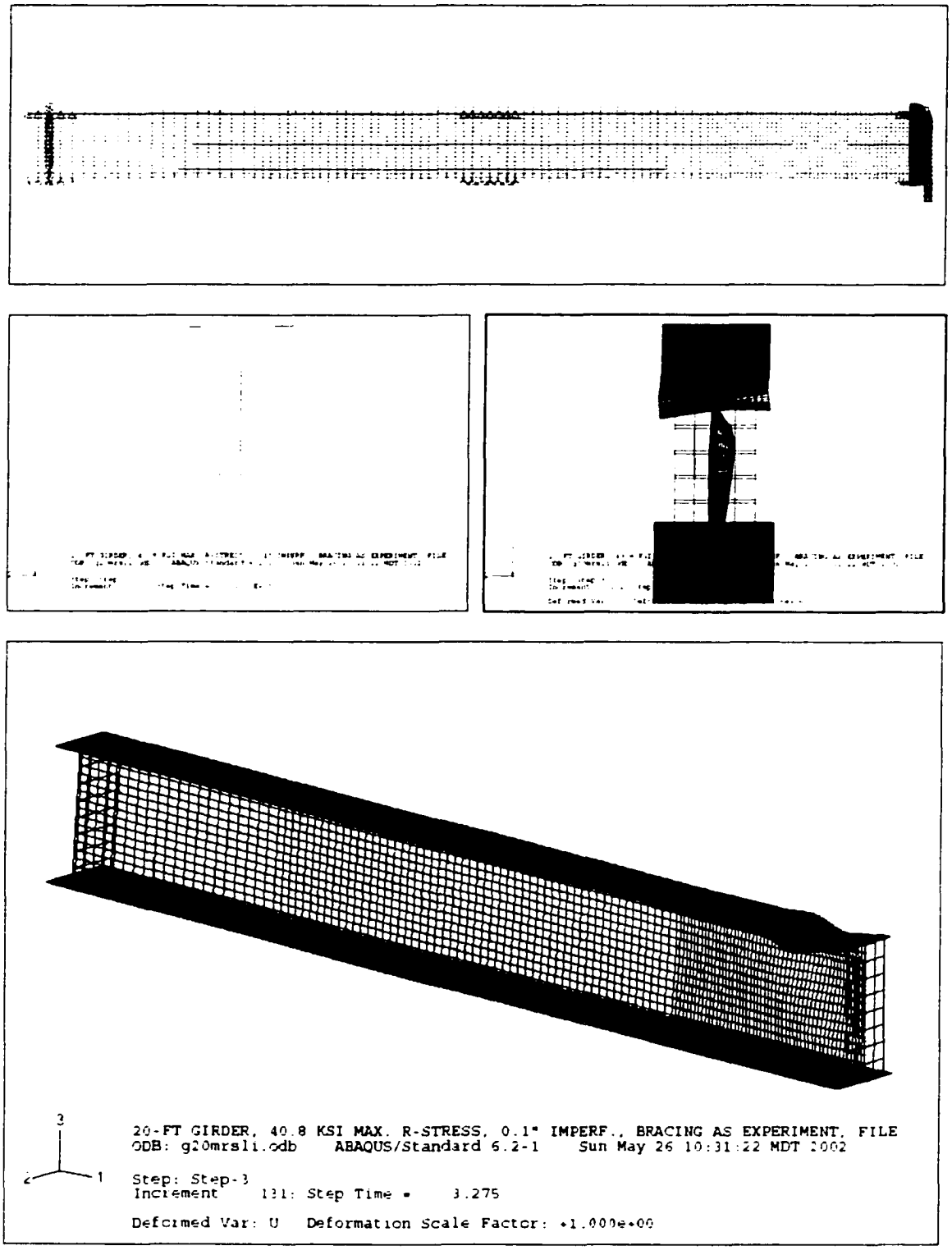

Figure 3.3.1.1 Initial and deformed shapes of FEM model for CSU Specimen #1

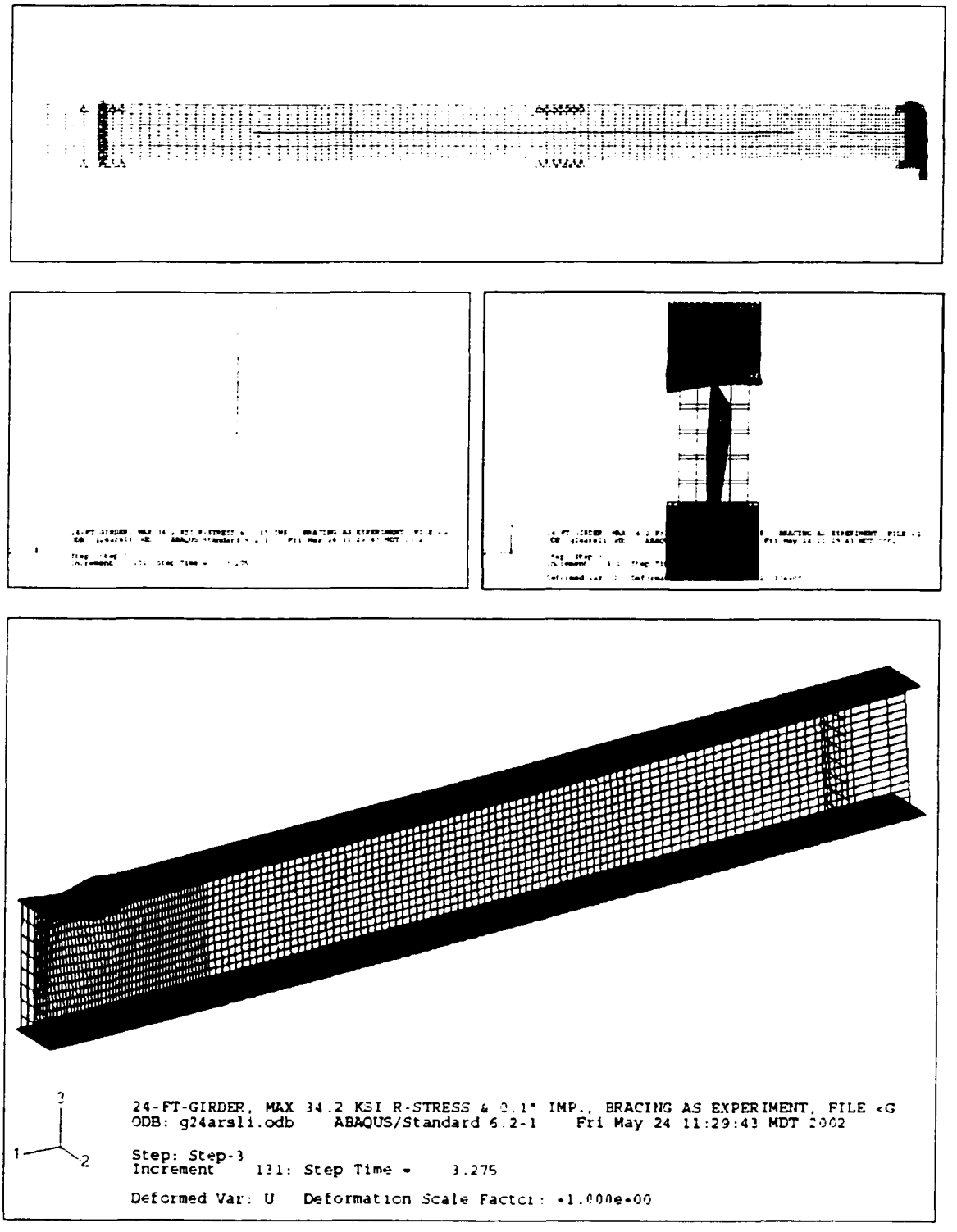

Figure 3.3.1.2 Initial and deformed shapes of FEM model for CSU Specimen #2

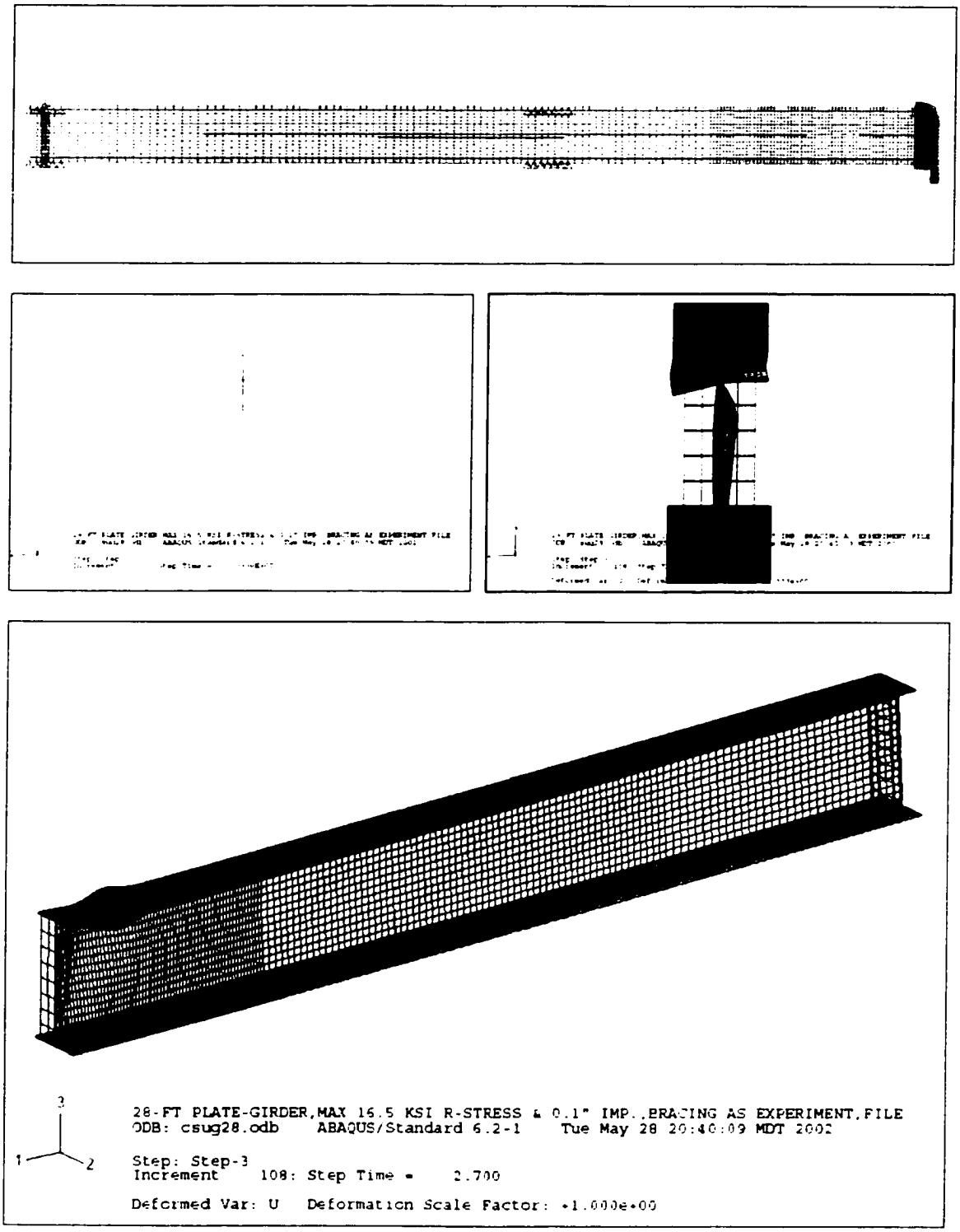

Figure 3.3.1.3 Initial and deformed shapes of FEM model for CSU Specimen #3

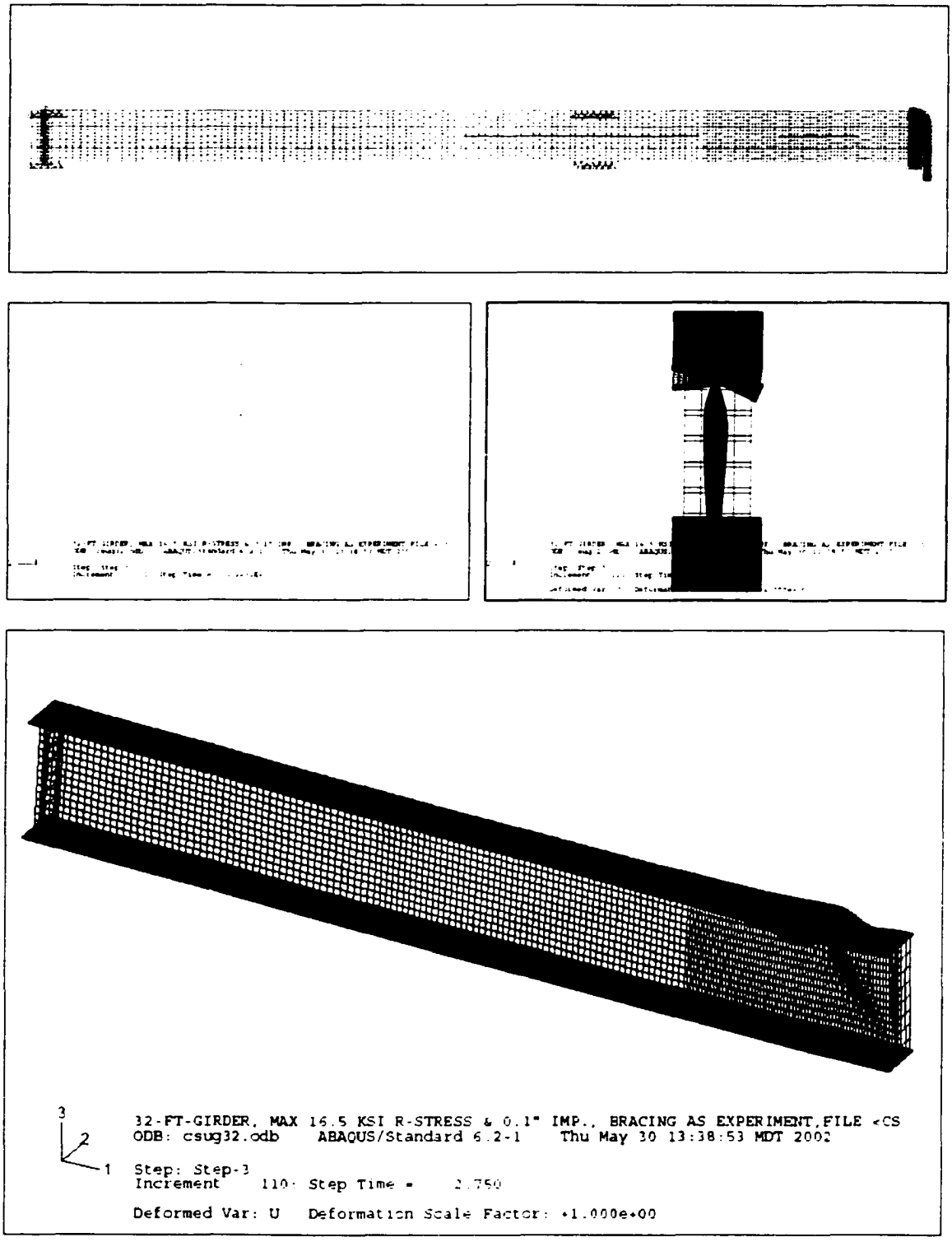

Figure 3.3.1.4 Initial and deformed shapes of FEM model for CSU Specimen #4

Table 3.3.1.1 Half-length numerical model properties

Property	Model for Specimen #1	Model for Specimen #2	Model for Specimen #3	Model for Specimen #4
Number of elements	6112	6784	7792	8560
Number of nodes	6279	6965	7994	8778
Number of variables	37674	41790	47964	52668
Time consumed	24 hours	34 hours	38 hours	38 hours

3.3.2 Materials inputs for numerical models

The moment-rotation behavior, obtained from numerical models, of HPS70W I-shape girders at intermediate support regions is complex and surprising. Beside the inputs of residual stresses and imperfection, several parametrical variations in the material stress-strain relationship can result in changes in moment-rotation response of the numerical models. In previous studies, different authors used different typical options of proper material inputs for numerical models of HPS70W girders. For instance, the ratio of yield strains, $\varepsilon_{st}/\varepsilon_y$, was employed as 10 (White, Barth, & Bobb, 1998), or 6.4 (Barth & White, 1998), or 5.5 (Zubeck, 2000). In addition, a "yield plateau slope" was applied as 100 ksi preceding a first strain-hardening slope, E_{st} = 800 ksi (or 400 ksi), (White, Barth, & Bobb, 1998), or another "yield plateau slope" could be chosen as 136.9 ksi corresponding to a first strain-hardening slope, E_{st} = 364.1 ksi, that was followed by a second and a third strain-hardening slope of 197.2 ksi and 81.5 ksi, respectively (Zubeck, 2000). Furthermore, there were various values for the modulus of elasticity of the flange steel and web steel, E_{flange} and E_{web}, in Appendices B1 and B2 of the Yakel, Mans, and Azizinamini's report (Yakel, Mans, and Azizinamini, 1999).

In addition, according to "High Performance Steels for Bridges: HPS70W - A Technical Overview" by Bethlehem Lukens Plate, (Bethlehem Lukens Plate, 1999), the average value of the yield strength, F_y, and the yield ratio, $YR = F_y/F_u$, is approximate 82 ksi and 0.86, respectively. Figure 3.3.2.1 below displays statistical data for 240 plates of HPS70W in thickness ranging from 0.5 to 3.1 in.

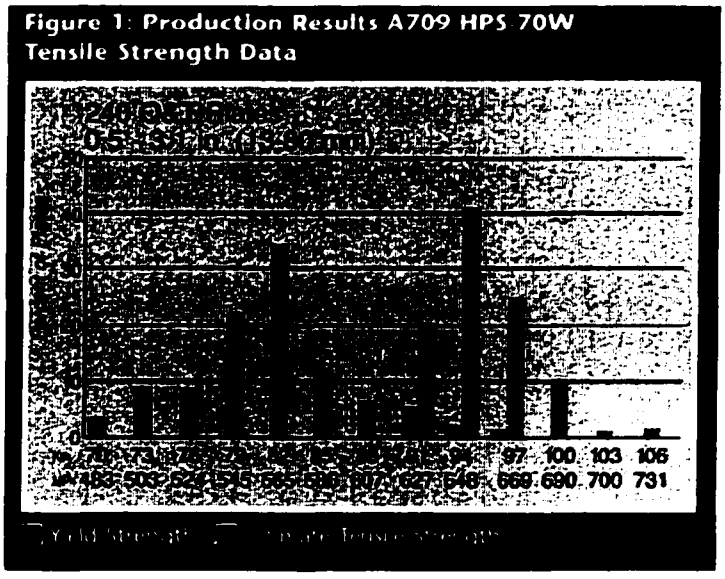

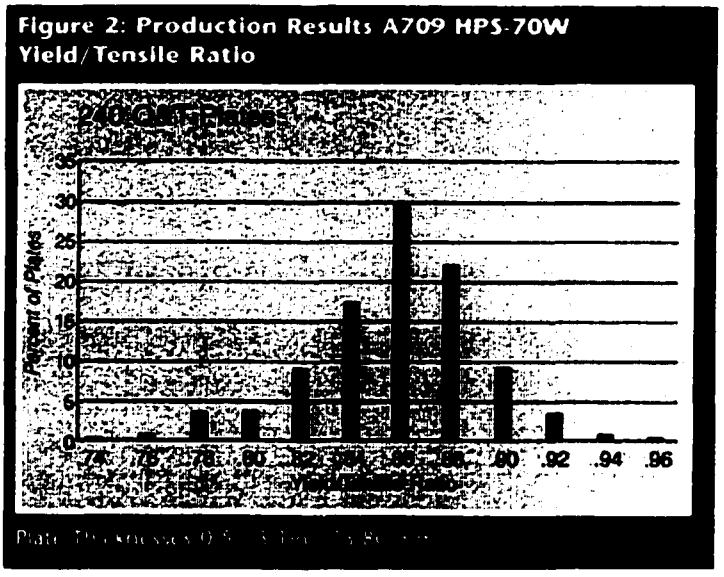

Figure 3.3.2.1 Statistical data of the yield strength, ultimate strength, and yield ratio for HPS70 plates. (Source: Bethlehem Lukens Plate, 1999, 008-HPS-70W Brochure, Figures 1 and 2)

Hence, to decide proper material inputs for numerical models of HPS70W girders at CSU, tensile tests on a number of flange coupons and web coupons (see Section 3.2.2) were performed to determine the values of the modulus of elasticity, E, and the stress-strain relationships of HPS70W, which are displayed in Figures 3.3.2.2 and 3.3.2.3. Section A.7 of Appendix also presents the stress-strain curves until failure of the flange and web coupons. For the moment-rotation analyses, the CSU numerical outcomes are thus calculated from the combination of the material inputs in Table 3.3.2.1 below and the artificial inputs of initial imperfection and residual stresses as discussed in Section 3.3.3 following.

Table 3.3.2.1 HPS70W material inputs for numerical moment-rotation analyses

Material properties	HPS70W flanges	HPS70W web
Modulus of elasticity, E	30,113.1 ksi	23,354.3 ksi
2^{nd} slope approaching the 0.2% offset yield strength	NA	6,500 ksi
Yield plateau slope	4.4 ksi	No yield plateau
Yield strength, F_y	83.35 ksi	69.83 ksi (0.2% offset F_y)
Ratio of strain-hardening and yield strains, $\varepsilon_{st}/\varepsilon_y$	6.4	NA
1^{st} strain-hardening slope, E_{st}	290 ksi	1,200 ksi
2^{nd} strain-hardening slope	110 ksi	450 ksi
3^{rd} strain-hardening slope	NA	140 ksi
Ultimate strength, F_u (flat plateau)	93.82 ksi	103.5 ksi
Yield ratio, $YR = F_y/F_u$	0.89	0.67
Poisson's ratio, ν	0.3	0.3

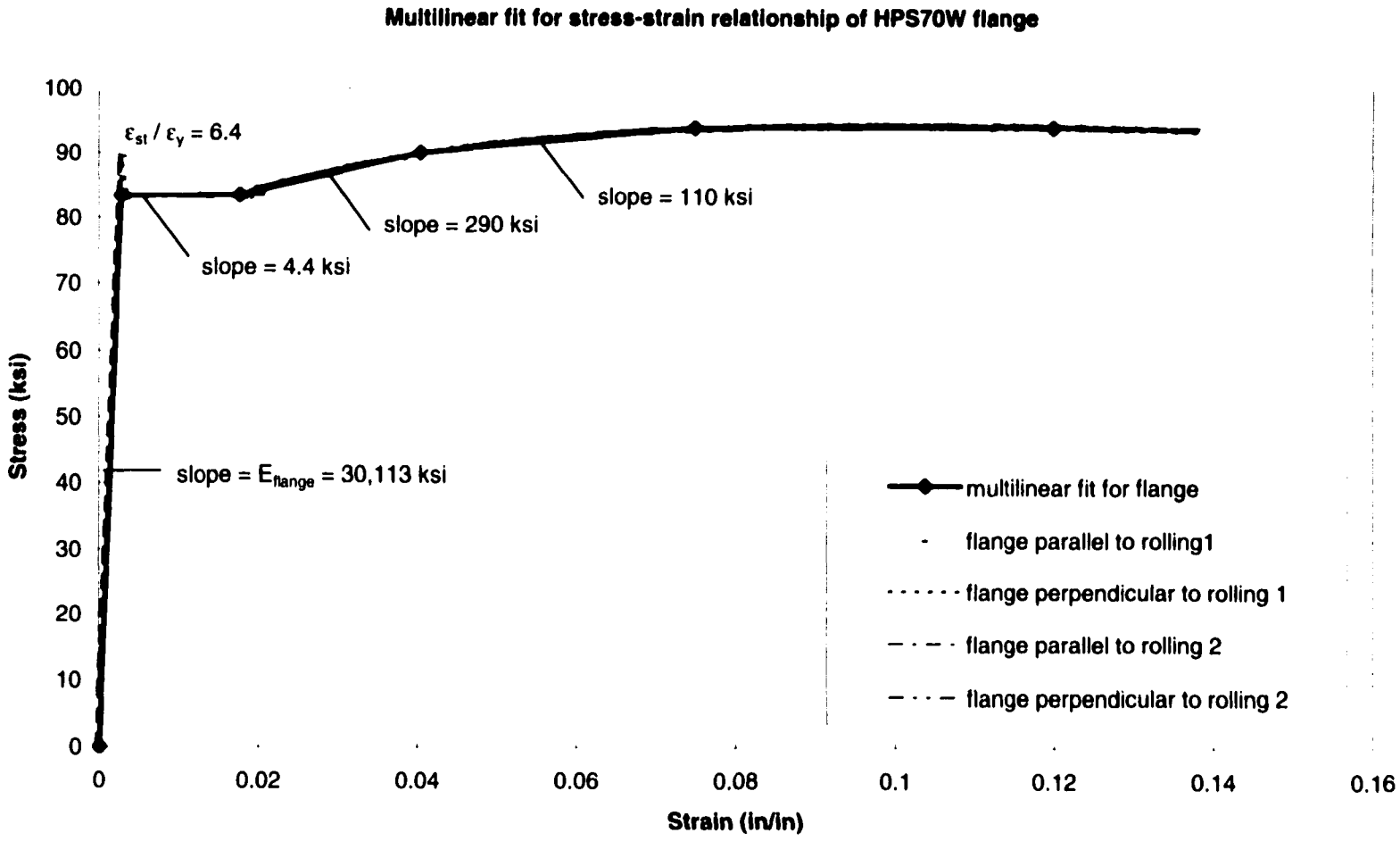

Figure 3.3.2.2 Experimental engineering stress-strain relationship for the flanges as material inputs for numerical analyses of HPS70W girders

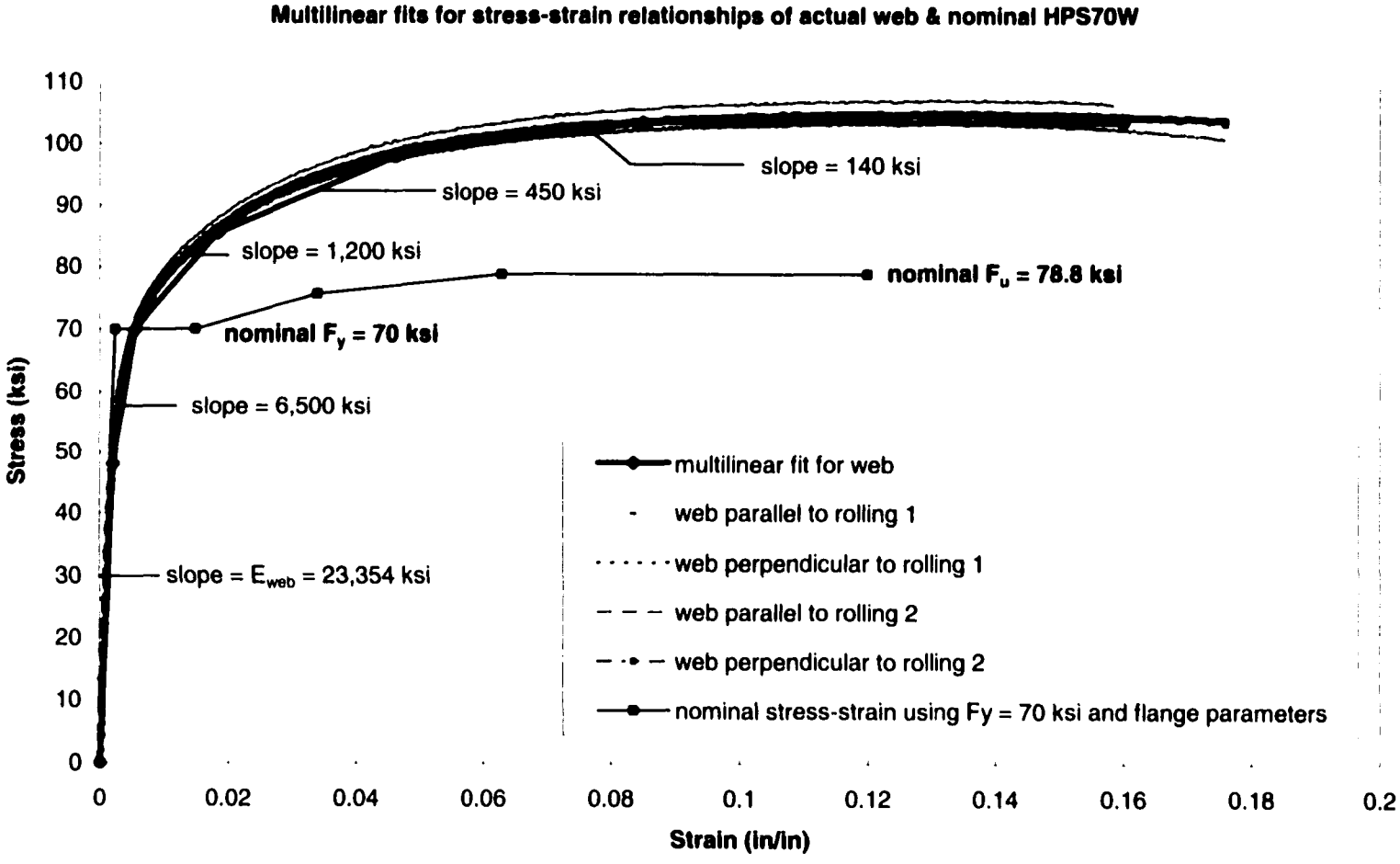

Figure 3.3.2.3 Experimental engineering stress-strain relationship for the web as material inputs for numerical analyses of HPS70W girders

3.3.3 Inputs of initial imperfections and residual stresses for numerical models

In this research, the residual stresses are introduced as a constant value over each element. For instance, following the values suggested previously (Yakel, Mans, and Azizinamini, 1999; Zubeck, 2000), the maximum positive residual stress is assigned as $+\frac{0.98}{2} F_{yf} = \frac{0.98}{2}(83.35\ ksi) \approx +40.8\ ksi$ (the peak value is divided by two for going from ramp distribution to block distribution) for the flanges of Specimen #1 (web depth of 16 in.), and the maximum negative residual stress is applied as $-\frac{0.98}{3} F_{yf} = -\frac{0.98}{3}(83.35\ ksi) \approx -27.2\ ksi$. For the web of Specimen #1, the maximum positive residual stress is employed again as +40.8 ksi for the elements at the flange-web connectivity while the constant negative residual stress is specified as $-\frac{0.98}{9} F_{yw} = -\frac{0.98}{9}(69.83\ ksi) \approx -7.6\ ksi$ (see Table 3.3.3.1).

To account for the tendency of a deeper web that has lower residual stresses at the web-flange junction, the piecewise residual stress distributions for the flanges and the web were adjusted to be applied to Specimens #2, #3, and #4. Based on F_{yw} = 69.83 ksi, Table 3.3.3.2 presents the distribution of initial residual stresses for Specimen #2 (web depth of 19 in.) with a maximum positive value of +34.2 ksi and a maximum negative value of –22.8 ksi, which are lower in magnitude than those of Specimen #1 (web depth of 16 in.). In addition, if the maximum residual stress of +16.5 ksi for welded shape is applied, according to AISC LRFD design (AISC, 1998), the entire distribution over web and flanges will be proportioned from the maximum value of +40.8 ksi to the corresponding peak of +16.5 ksi. Table 3.3.3.3 presents the distribution of initial residual stresses for Specimen #3 (web depth of 21 in.) and Specimen #4 (web depth of 25 in.).

Table 3.3.3.1 Distribution of initial residual stresses for Specimen #1

Residual stresses (ksi) in Specimen #1 (nonsymmetric)									
Element	1	2	3	4	5	6	7	8	9 to 16
Upper flange	+40.8	+13.6	-27.2	-27.2	-27.2	-27.2	+13.6	+40.8	symmetric of 1 to 8
Web	+40.8	+4.8	-7.6	-7.6	-7.6	-7.6	-7.6	-7.6	
Lower flange	+28.2	+9.4	-27.2	-27.2	-27.2	-27.2	+13.6	+40.8	

Table 3.3.3.2 Distribution of initial residual stresses for Specimen #2

Residual stresses (ksi) in Specimen #2 (symmetric)									
Element	1	2	3	4	5	6	7	8	9 to 16
Flanges	+34.2	+11.4	-22.8	-22.8	-22.8	-22.8	+11.4	+34.2	symmetric of 1 to 8
Web	+34.2	+11.4	-7.6	-7.6	-7.6	-7.6	-7.6	-7.6	

Table 3.3.3.3 Distribution of initial residual stresses for Specimens #3 and #4

Residual stresses (ksi) in Specimen #3 (nonsymmetric)									
Element	1	2	3	4	5	6	7	8	9 to 16
Upper flange	+16.5	+5.5	-11.0	-11.0	-11.0	-11.0	+5.5	+16.5	symmetric of 1 to 8
Web	+16.5	+1.9	-3.1	-3.1	-3.1	-3.1	-3.1	-3.1	
Lower flange	+11.8	+3.9	-11.0	-11.0	-11.0	-11.0	+5.5	+16.5	
Residual stresses (ksi) in Specimen #4 (symmetric)									
Element	1	2	3	4	5	6	7	8	9 to 16
Flanges	+16.5	+5.5	-11.0	-11.0	-11.0	-11.0	+5.5	+16.5	symmetric of 1 to 8
Web	+16.5	+1.9	-3.1	-3.1	-3.1	-3.1	-3.1	-3.1	

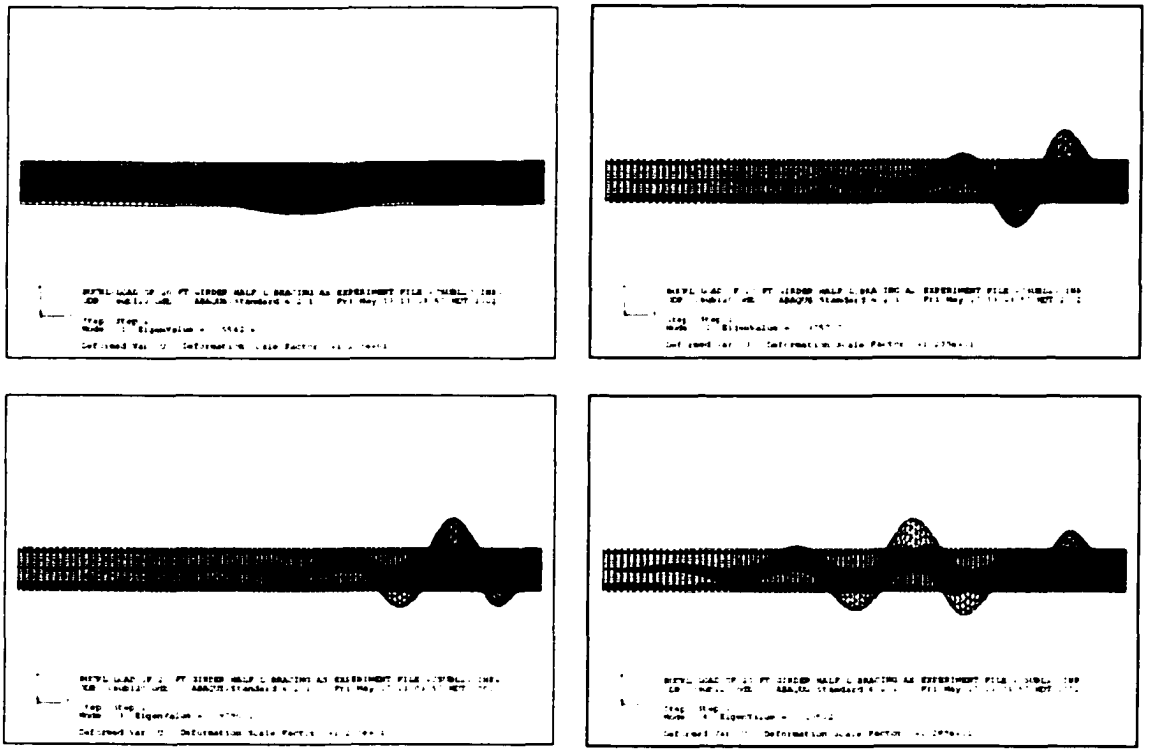

Figure 3.3.3.1 The first four eigenmodes of buckling analysis for Specimen #1

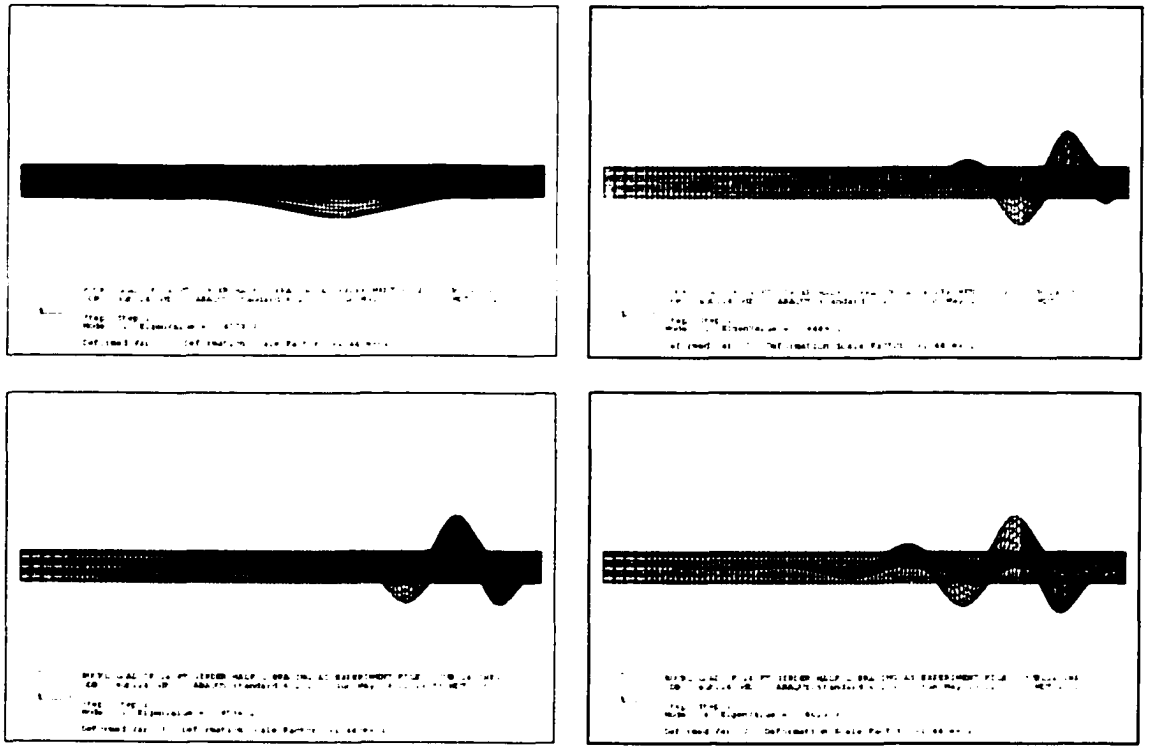

Figure 3.3.3.2 The first four eigenmodes of buckling analysis for Specimen #2

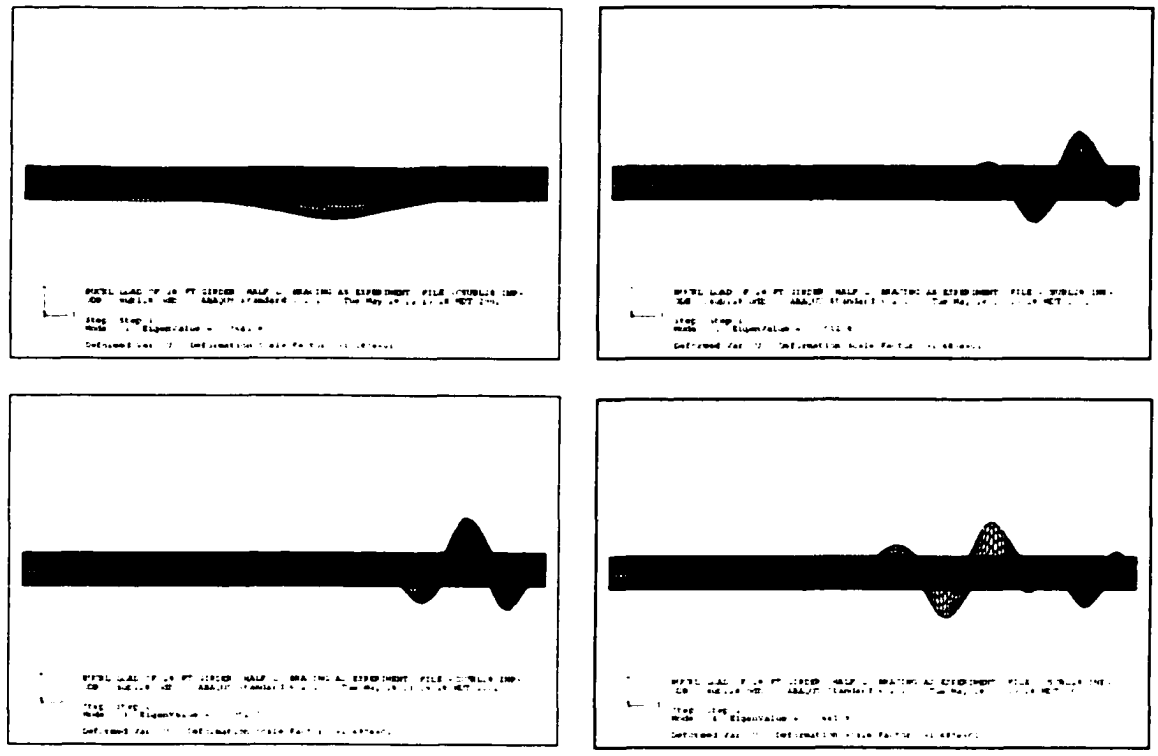

Figure 3.3.3.3 The first four eigenmodes of buckling analysis for Specimen #3

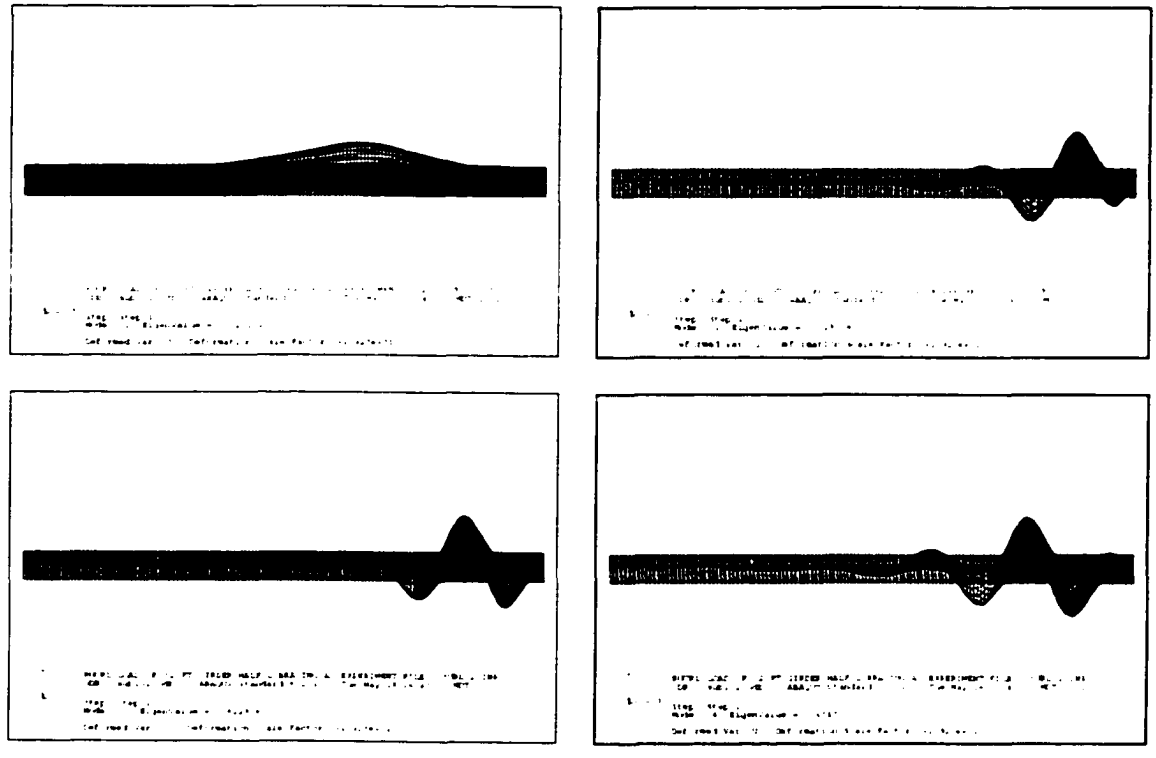

Figure 3.3.3.4 The first four eigenmodes of buckling analysis for Specimen #4

The imperfection input for numerical analyses was modeled similarly to the method of Yakel, Mans, and Azizinamini, 1999, in which the resulting first-eigenvector from the buckling analysis was scaled down such that the maximum displacement was 0.1 inch, and these scaled displacements were superimposed on the original geometry thus generating a distorted mesh (see Section 2.4.3). However, in this research, an arbitrary combination of eigenvectors, which are weighted descending from the first-eigenvector down to the fourth (as noted in ABAQUS post-peak analysis procedures (Hibbitt, Karlsson & Sorensen, Inc., 1999)), can be scaled down such that the maximum combined displacement is from 0.1 to 0.2 inch and then applied as an initial imperfection. Figures 3.3.3.1, 3.3.3.2, 3.3.3.3, and 3.3.3.4 in the previous pages present the first four eigenmodes of the buckling analyses for Specimens #1, #2, #3, and #4, respectively.

3.3.4 Bracing lengths: numerical studies for Specimens #3 and experimental and numerical studies for Specimen #4

Lateral bracing along the compression flange prevents lateral torsional buckling, and thus, insures that a girder meeting compact section requirements can reach its inherent plastic moment capacity. The effects of lateral bracing lengths on pier moment-rotation behavior of CSU's HPS70W I-shape noncompact girders, Specimen #3 and Specimen #4, will be studied from the response of the specimens with lateral compression-flange bracing classified in satisfying/dissatisfying the AASHTO requirements (AASHTO, 1998 and interim 2001) categories. The maximum unbraced length, L_b, for compact section is:

$$L_b \le \left(0.124 - 0.0759\left(\frac{M_1}{M_p}\right) \right) \left(\frac{r_t E}{F_y} \right) \qquad \text{(AASHTO 6.10.4.1.7)}$$

where:

L_b = unbraced length (in.),

r_y = radius of gyration about the weak bending axis (in.),

M_l = lower factored moment at either end of the unbraced length (kip-in),

M_p = plastic moment (kip-in),

F_{yc} = compression flange yield strength (ksi), and

E = modulus of elasticity (ksi).

In addition, the maximum unbraced length, L_b, for noncompact section is:

$$L_b \le L_p = 1.76\, r_t \sqrt{\frac{E}{F_{yc}}} \qquad \text{(AASHTO 6.10.4.1.8)}$$

where:

L_b = unbraced length (in.),

L_p = maximum unbraced length (in.),

r_t = radius of gyration about the weak bending axis of the area of the compression flange plus 1/3 area of the web in compression (in.),

F_{yc} = compression flange yield strength (ksi), and

E = modulus of elasticity (ksi).

In three-point loading, the midspan (at the load point) is the most critical region of a girder for lateral torsional buckling. As a result, lateral bracing is first assigned at the midspan of the test girders, and the compression flange bracing from the load point to the next compression flange brace is checked against the maximum unbraced length permitted by AASHTO.

- Specimen #3 (half span L/2 = 330 in / 2 =165 in, triangular moment diagram):

If AASHTO 6.10.4.1.7 specification is applied for compact section, the maximum unbraced length, L_p, is:

$$L_p = \left(0.124 - 0.0759\left(\frac{M_1}{M_p}\right)\right)\left(\frac{r_y E}{F_{yc}}\right) = \left\{0.124 - 0.0759\left[\frac{\frac{(165in - L_p)}{165in} M_p}{M_p}\right]\right\}\left(\frac{(2.634in)(29000ksi)}{70ksi}\right)$$

$L_p = 105.4$ in

If AASHTO 6.10.4.1.8 specification is applied for noncompact section, the maximum unbraced length, L_p, is:

$$L_p = 1.76\, r_t \sqrt{\frac{E}{F_{yc}}} = 1.76\,(2.727in)\sqrt{\frac{29000ksi}{70ksi}} = 97.7in$$

- Specimen #4 (half span L/2 = 378 in / 2 = 189 in, triangular moment diagram):

If AASHTO 6.10.4.1.7 specification is applied for compact section, the maximum unbraced length, L_p, is:

$$L_p = \left(0.124 - 0.0759\left(\frac{M_1}{M_p}\right)\right)\left(\frac{r_y E}{F_{yc}}\right) = \left\{0.124 - 0.0759\left[\frac{\frac{(189in - L_p)}{189in} M_p}{M_p}\right]\right\}\left(\frac{(2.705in)(29000ksi)}{70ksi}\right)$$

$L_p = 98.0$ in

If AASHTO 6.10.4.1.8 specification is applied for noncompact section, the maximum unbraced length, L_p, is:

$$L_p = 1.76\, r_t \sqrt{\frac{E}{F_{yc}}} = 1.76\,(2.992in)\sqrt{\frac{29000ksi}{70ksi}} = 107.1in$$

Specimen #3 was experimentally tested with lateral compression-flange bracing configuration, at midspan, 71.5 in. North and South from midspan, and at supports, which satisfies the AASHTO specifications (AASHTO, 1998 and interim 2001) for both categories of compact and noncompact sections. Numerically, the finite element model for Specimen #3 was analyzed with four variations of lateral compression-flange bracing:

(1) bracing at midspan, 71.5 in. North and South from midspan, and at supports as experiment (unbraced length, L_b, satisfies AASHTO specifications for both compact and noncompact sections),

(2) bracing at midspan, 97.75 in. North and South from midspan (at limited unbraced length for noncompact section from AASHTO 6.10.4.1.8 specification), and at supports,

(3) bracing at midspan, 105.25 in. North and South from midspan (at limited unbraced length for compact section from AASHTO 6.10.4.1.7 specification), and at supports, and

(4) bracing only at midspan and at supports (L_b dissatisfies AASHTO specifications).

The effects of the various unbraced lengths on the inelastic moment-rotation relationship for Specimen #3, which were resulted from the analysis of the four numerical models satisfying/dissatisfying the AASHTO specifications of lateral compression-flange bracing, are presented in Section 4.3.

Specimen #4 was experimentally tested with two variations of lateral compression-flange bracing:

(1) bracing at midspan, 71.5 in. North and South from midspan (unbraced length, L_b, satisfies AASHTO specifications (AASHTO, 1998 interim 2001) for compact section (at 98 in) and noncompact section (at 107.1 in)), and at supports, and

(2) bracing only at midspan and at supports (L_b dissatisfies AASHTO specifications).

The corresponding numerical model of Specimen #4 was analyzed with two bracing configurations as experiments.

3.4 Numerical Moment-Rotation Of HPS70W Steel Composite Specimen

For the I-shape steel portion, the same ABAQUS S4R elements, 4-node, thick shell elements with 6 degrees of freedom per node, were employed densely spaced at the midspan and gradually decreased spacing to the end support. Sixteen shell elements are assigned across each flange and 16 elements through the web as used for the noncomposite models discussed in Section 3.3. In addition, a tensile concrete deck with steel rebars inside will be appended to the tensile flange. Several options to model the concrete deck were attempted, consisting of: (1) concrete elements as shell or membrane elements linked to tensile flange, (2) steel rebars in the tensile concrete deck as truss elements linked to tensile flange, and (3) concrete deck as continuum (solid) elements.

3.4.1 Antithesis for modeling concrete deck by shell elements linked to I-shape steel portion

One option to model the tensile concrete deck is using shell elements for the deck and linking the deck shell elements to the shell elements of the tensile flange. ABAQUS analysis runs still reveal the numerical moment-rotation behavior. However, the resulted

strain distribution over entire cross-section showed an incorrect elastic composite strain behavior. Instead of a tensile strain distribution for the I-component under tension and tensile concrete deck, the elastic strain distribution was piecewise linear with a kink at the interface of the outer edge of the tensile flange. The reason was that ABAQUS found the neutral surface, corresponding to zero strain, of the concrete shell elements under bending. ABAQUS thus automatically interpolated the existing tensile strain at the outer edge of the tensile flange back to zero at the neutral surface of the concrete shell, and the false strain continued on the opposite way of that being supposed (see Figure 3.4.1.1).

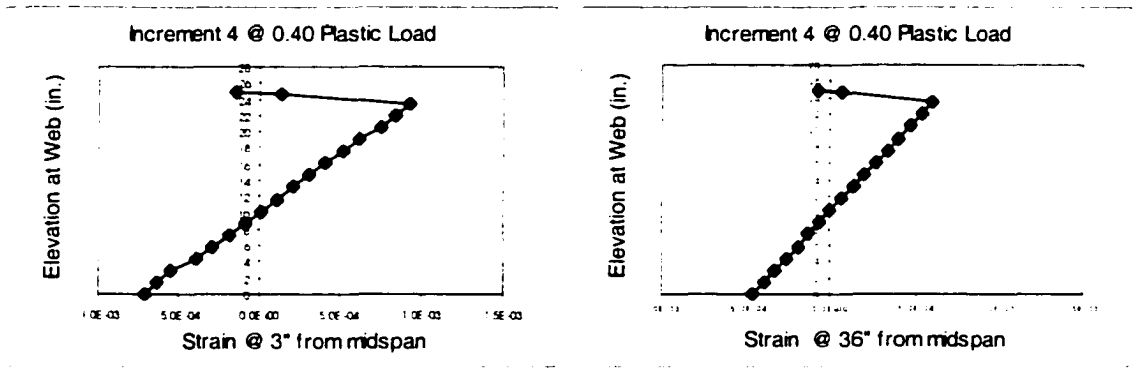

Figure 3.4.1.1 False elastic strain distribution over FEM composite cross-section

3.4.2 Continuum solid element option for concrete deck and pseudo-transformed section properties

A promising option for numerical modeling for the concrete deck is to use ABAQUS C3D8 solid (continuum) element, an 8-node linear brick element with three degrees of freedom (u_x, u_y, u_z) per node. At the interface of the concrete deck and the I-shape steel, continuum elements and shell elements will be assigned to have same nodes since AASHTO requires fully composite action if the composite action is used in bridge

girders. For each numerical run of composite girder analysis, the same ABAQUS post peak procedures, modified Rik's method for displacement-control, and nonlinear option and accounting for initial imperfections and residual stresses are applied. Unsurprisingly, when concrete considerably cracks and thus leads to the lack of compatibility (see Figure 2.3.1.4 in Section 2.3.1), the ABAQUS run automatically stops. In order to continue the numerical solution to the post-peak analysis, the option of the equivalent transformed Young's modulus, E_{trans}, for corresponding transformed area from steel rebars to concrete area, assuming all concrete cracks and fully plastic action of entire composite section, will be discussed on the following pages.

Recall from the transformation of section properties in elastic bending of a straight beam, the flexural rigidity equality must be held, regardless to any location of the neutral axis (NA):

$$E_1 I_{NA1} = E_2 I_{NA2}$$

where:

E_1 = modulus of elasticity of material in cross-section (1),

E_2 = modulus of elasticity of material in cross-section (2),

I_{NA1} = moment of inertia of cross-section (1) with respect to the neutral axis, and

I_{NA2} = moment of inertia of cross-section (2) with respect to the neutral axis.

The modular ratio thus is determined as:

$$n = \frac{E_1}{E_2} = \frac{I_{NA2}}{I_{NA1}}.$$

Consider:

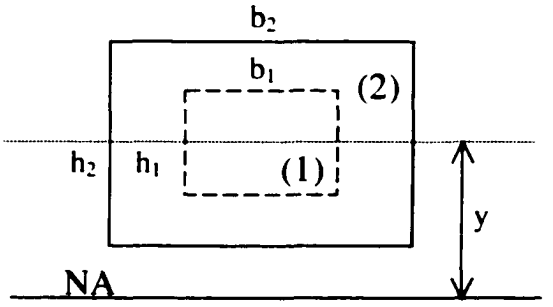

The moment of inertias of the two rectangular sections (1) and (2) are:

$$I_{NA1} = I_{c1} + y^2 A_1 = \frac{b_1 h_1^3}{12} + y^2 (b_1 h_1) \quad \text{and} \quad I_{NA2} = I_{c2} + y^2 A_2 = \frac{b_2 h_2^3}{12} + y^2 (b_2 h_2).$$

The modular ratio becomes: $n = \dfrac{I_{NA2}}{I_{NA1}} = \dfrac{I_{c2} + y^2 A_2}{I_{c1} + y^2 A_1}$.

For the modular ratio, n, to be independent of the distance, y, from the neutral axis to the centroids of the sections (1) and (2), the derivative $\dfrac{dn}{dy}$ must vanish for any y:

$$\frac{dn}{dy} = \frac{2yA_2(I_{c1} + y^2 A_1) - 2yA_1(I_{c2} + y^2 A_2)}{(I_{c1} + y^2 A_1)^2} = 0$$

$$A_2(I_{c1} + y^2 A_1) - A_1(I_{c2} + y^2 A_2) = 0$$

$$\frac{A_2}{A_1} = \frac{I_{c2}}{I_{c1}} \quad \text{for any } y$$

Hence, at y = 0, the equality above becomes $\dfrac{A_2}{A_1} = \dfrac{I_{c2}}{I_{c1}}$. Substituting A = bh and $I_c = \dfrac{bh^3}{12}$ for the two rectangular sections (1) and (2), the equality leads to $h_1 = h_2$ required. As a result, the modular ratio is established as $n = \dfrac{E_1}{E_2} = \dfrac{I_{NA2}}{I_{NA1}} = \dfrac{A_2}{A_1}$, corresponding to the geometry of transformed cross-sections below:

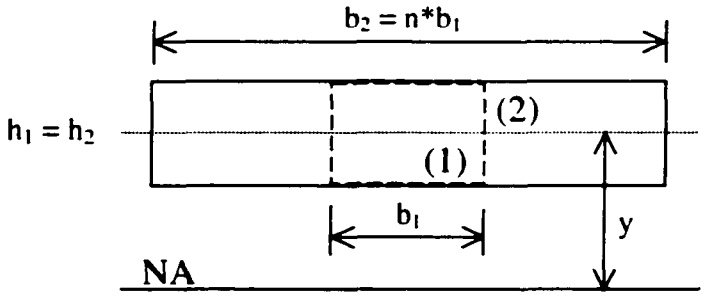

Now, for the case of the longitudinal rebars inside the concrete deck, consider the rebar layer as a thin rectangle (1). The rectangle's width is assigned the same as the concrete deck width, and rectangle's thickness is equal to the quotient of the cross-section area of longitudinal rebars divided by the concrete deck width, as shown below:

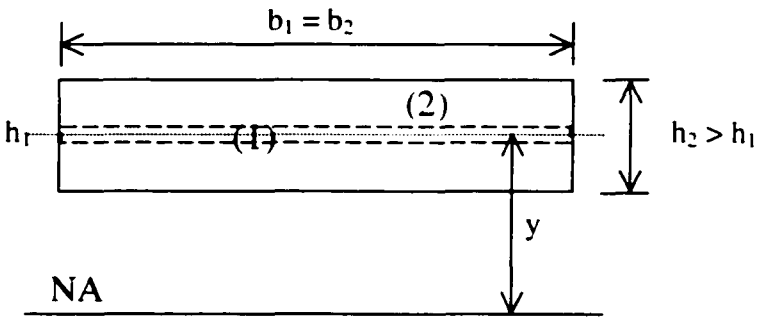

Obviously, since h_2 is greater than h_1, the ratio of $\frac{I_{NA2}}{I_{NA1}}$ depends on y, and thus the transformation of section properties cannot be applied, theoretically. However, in the cases of composite girders when y is large enough, the term y^2 will dominate in the expression of moment of inertia, $I_{NA} = I_x + y^2 A$. Hence, the ratio of $\frac{I_{NA2}}{I_{NA1}}$ could be approximated as $\frac{A_2}{A_1}$ again, and a pseudo-transformation of section properties would be applied with the modular ratio $n = \frac{E_1}{E_2} \approx \frac{A_2}{A_1}$.

As a result, this pseudo-modular ratio, $n = \frac{A_2}{A_1}$, will be utilized in ABAQUS runs to surpass the lack of compatibility of the numerical models when concrete deck cracks are large. Eventually, the pseudo-transformed area of the steel rebars, not the unknown modulus of elasticity of the cracked reinforced concrete deck, will contribute to the plastic moment in inelastic behavior (see Section 2.3.1.2).

Figure 3.4.2.1 presents several promising results from the approach of using the pseudo-modular ratio with pseudo-transformed area. Using the ABAQUS code, a sample composite model that corresponds to a composite girder tested in a double-cantilever configuration reveals reasonable elastic strain distributions over the composite cross-section and an expected post-peak deformed shape.

3.4.3 FEM models for composite HPS70W girders

For each numerical run of composite girder analysis, the same ABAQUS post peak procedures, modified Rik's method for displacement-control, and nonlinear option are applied. For the I-shape steel portion, the same ABAQUS-S4R-shell elements are assigned across each flange and through the web, using the same material inputs (see Section 3.3.2) and accounting for initial imperfections and residual stresses (see Section 3.3.3) as for the noncomposite models. In addition, a tensile concrete deck with steel rebars inside is appended to the tensile flange, using ABAQUS C3D8 solid (continuum) elements. At the interface of the concrete deck and the I-shape steel, continuum elements and shell elements will be assigned to have same nodes since AASHTO requires fully composite action if the composite action is used in bridge girders. Assuming all concrete cracks and fully plastic action of entire composite section, the equivalent transformed

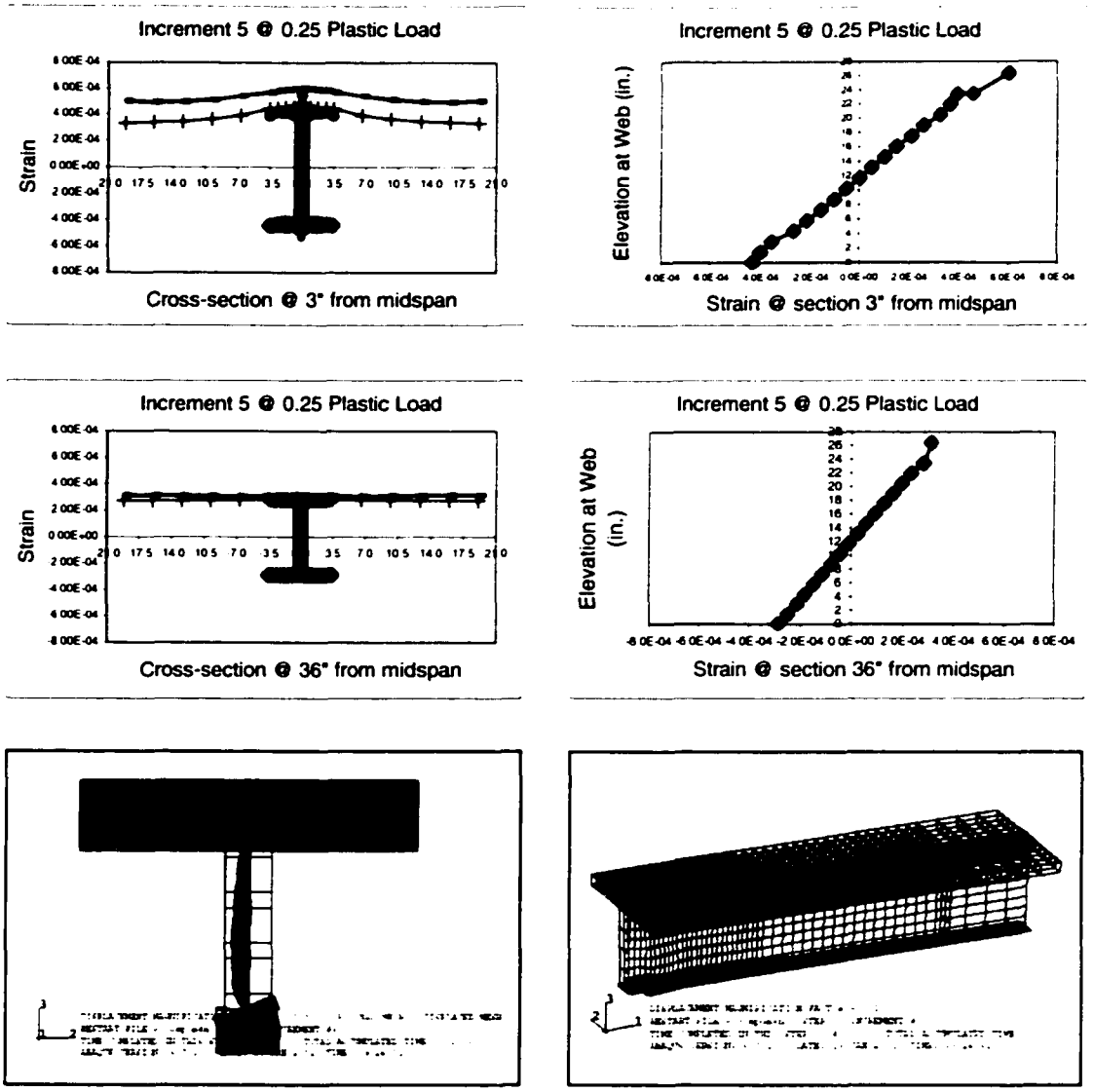

Figure 3.4.2.1 Reasonable strain distributions and post-peak deformed shape of numerical composite model using pseudo-transformation of area

modulus of elasticity, E_{trans}, based on the pseudo-transformed area from steel rebars to concrete area with the pseudo-modular ratio, $n = \frac{E_{rebars}}{E_{concrete}} \approx \frac{A_{concrete}}{A_{rebars}}$, is employed in ABAQUS runs as previously discussed. In this research, the area ratio of secondary rebars (in direction parallel to the girders) over concrete is taken as one percent as common design for bridge concrete decks.

The effects of composite/noncomposite on the moment-rotation behavior of CSU's HPS70W girders were studied from the FEM-model responses of the steel girders with and without the concrete deck in the tension zone. Corresponding to the symmetric girders, Specimens #2 and #4, the composite sections were developed by appending a concrete deck as 1/3 scale to the tensile flange of the actual symmetric steel portion. On the other hand, fictitious symmetric-I steel portions based on the dimensions of the actual compression flange and web are assumed for models associated to the nonsymmetric girders, Specimens #1 and #3. Then, a concrete deck as 1/3 scale is appended to the tensile flange of the fictitious symmetric-I for these models.

Tables 3.4.3.1 and 3.4.3.2 present the dimensions of the composite sections corresponding to Specimens #1 to #4, based on AASHTO 4.6.2.6.1 specifications for interior girders (AASHTO, interim 2001). Figures 3.4.3.1, 3.4.3.2, 3.4.3.3, and 3.4.3.4 illustrate the half-length FEM meshes deformed shapes of the composite models corresponding to Specimens #1, #2, #3, and #4, respectively. Table 3.4.3.3 presents the total numbers of elements, nodes, and variables are utilized in an ABAQUS nonlinear analysis and a typical time consumed for each composite-model analysis.

For the comparisons of FEM models corresponding to the symmetric girders, Specimens #2 and #4, the calculated plastic moments, M_p, based on the average material tested data are employed (see Appendix, Section A.5). For the comparisons of FEM models corresponding to the nonsymmetric girders, Specimens #1 and #3, the fictitious plastic moments, M_p, are calculated based on the dimensions of the fictitious symmetric steel portion and the average material tested data, F_{yf} = 83.35 ksi for the flanges and F_{yw} = 69.83 ksi for the web (see Appendix, Section A.6).

Table 3.4.3.1 Composite section dimensions corresponding to experimental nonsymmetric-I, Specimen #1 and Specimen #3

Property	Specimen #1 (nominal compact)	Specimen #3 (noncompact)
Test span, L = 0.42 L_c(ft)	19.5	27.5
Web depth inside flanges, D (in.)	16	21
Web thickness, t_w (in.)	1/4	1/4
Compression flange width, b_{fc} (in.)	9	10
Fictitious tension flange width, b_{ft} (in.)	9	10
Flange thickness, t_f (in.)	3/4	3/4
1/3-scale-model slab thickness, t_s (in.)	3	3
Based on girder span, L_c/4 (in.)	139	196
Based on section, $12t_s + b_f/2$ (in.)	40.5	41
Based on spacing, 1/3-scale spacing (in.)	48	48
Effective concrete flange width, b_E (in.)	40.5	41

Table 3.4.3.2 Composite section dimensions corresponding to experimental symmetric-I, Specimen #2 and Specimen #4

Property	Specimen #2 (nominal compact)	Specimen #4 (noncompact)
Test span, L = 0.42 L_c(ft)	22	31.5
Web depth inside flanges, D (in.)	19	25
Web thickness, t_w (in.)	1/4	1/4
Compression flange width, b_{fc} (in.)	9	11
Actual tension flange width, b_{ft} (in.)	9	11
Flange thickness, t_f (in.)	3/4	3/4
1/3-scale-model slab thickness, t_s (in.)	3	3
Based on girder span, L_c/4 (in.)	157	225
Based on section, $12t_s + b_f/2$ (in.)	40.5	41.5
Based on spacing, 1/3-scale spacing (in.)	48	48
Effective concrete flange width, b_E (in.)	40.5	41.5

where:

L_c = bridge girder span (in.), for which the test span, L = 0.42 L_c, and

b_E = effective concrete flange width (in.), as the least of L_c/4, $12t_s + b_f/2$, and the average spacing between girders, according to AASHTO 4.6.2.6.1 specifications for interior girders (AASHTO, interim 2001).

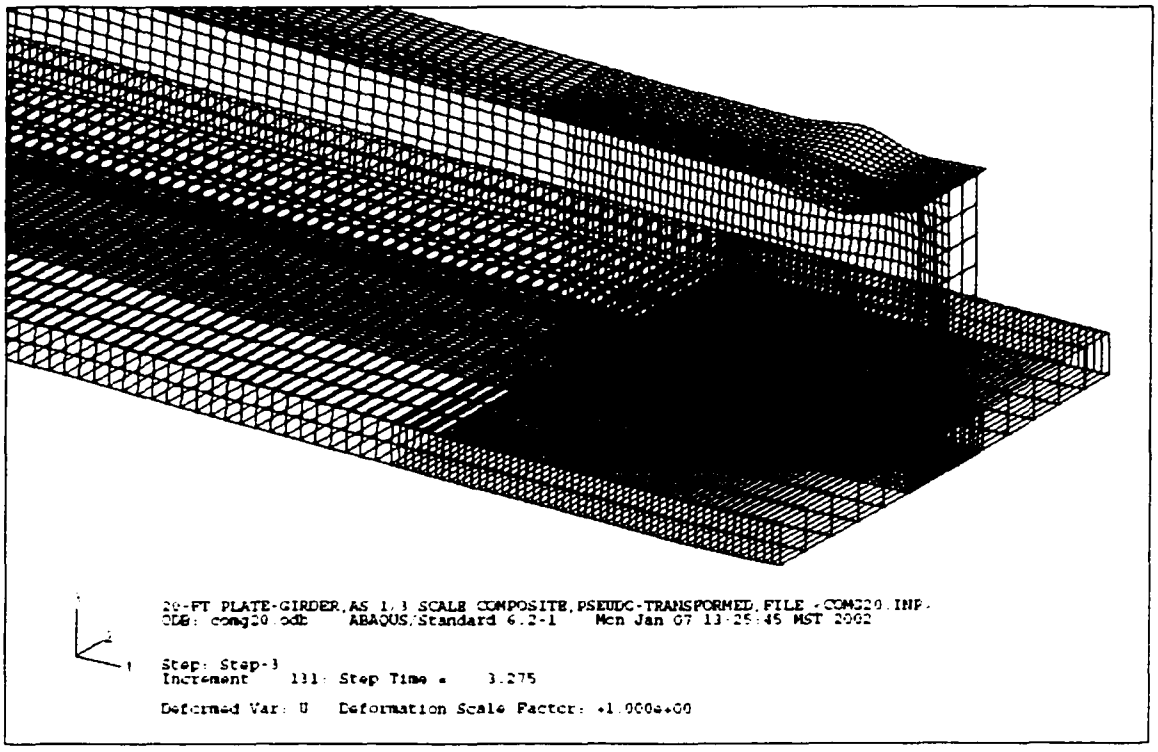

Figure 3.4.3.1 Deformed shape of composite model corresponding to Specimen #1

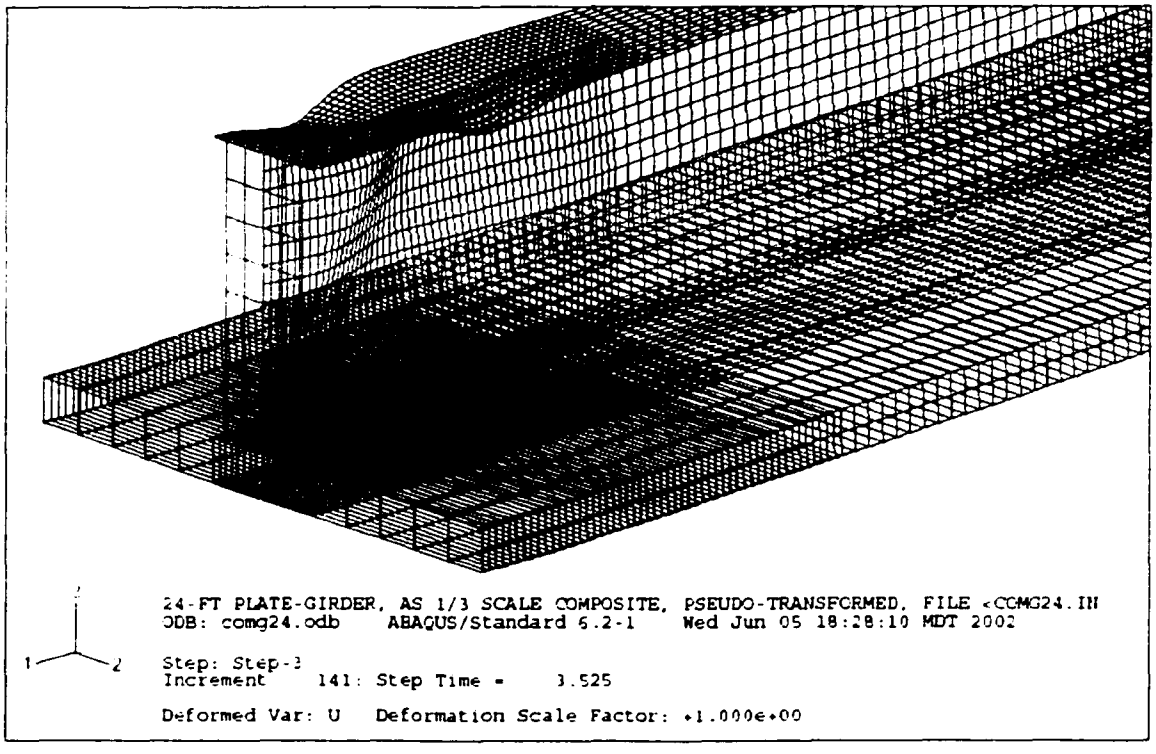

Figure 3.4.3.2 Deformed shape of composite model corresponding to Specimen #2

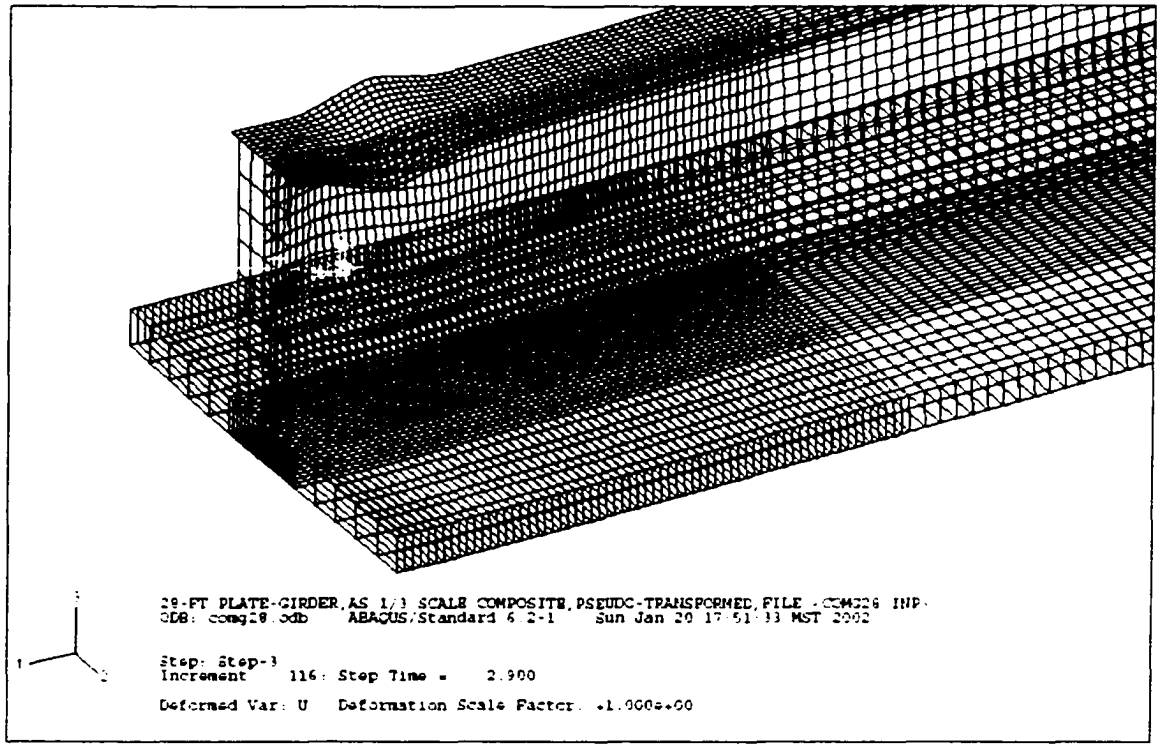

Figure 3.4.3.3 Deformed shape of composite model corresponding to Specimen #3

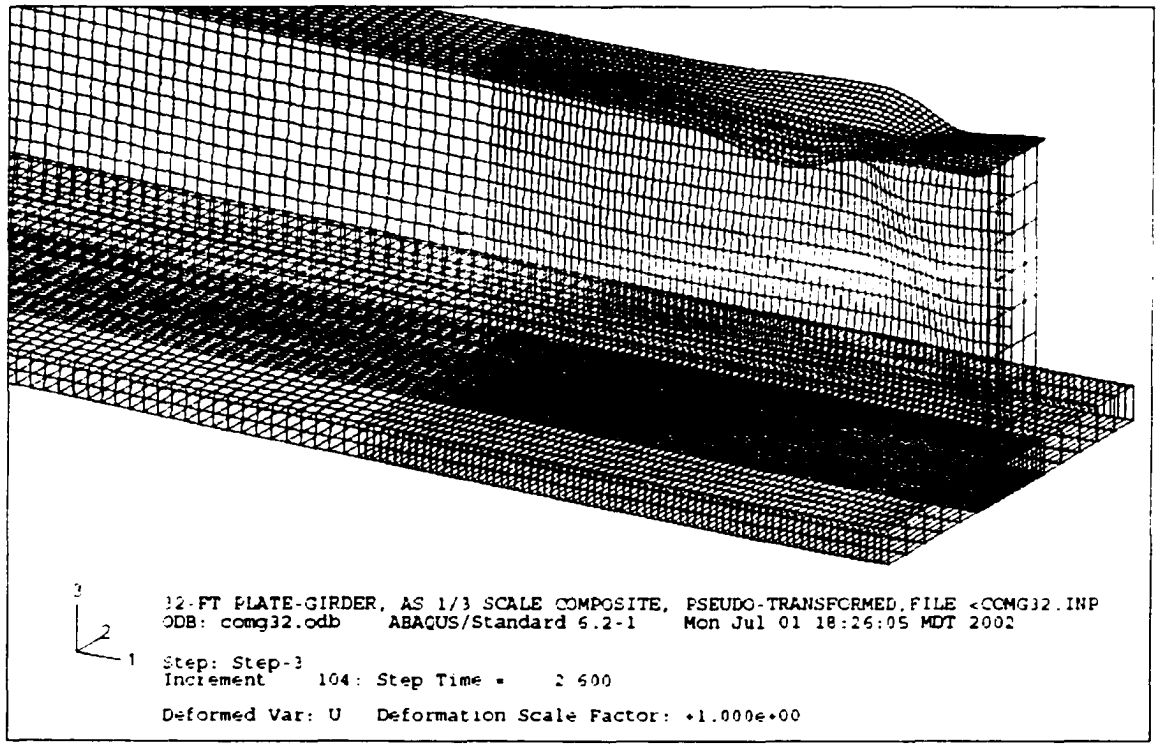

Figure 3.4.3.4 Deformed shape of composite model corresponding to Specimen #4

Table 3.4.3.3 Half-length composite FEM model properties

Property	Composite Model #1	Composite Model #2	Composite Model #3	Composite Model #4
Number of elements	9388	10424	11978	13162
Number of nodes	10978	12182	13988	15364
Number of variables	51771	57441	65946	72426
Time consumed	35 hours	44 hours	61 hours	52 hours

CHAPTER 4

PIER MOMENT-ROTATION BEHAVIOR OF HPS70W I-GIRDERS

4.1 Introduction

The pier moment-rotation behavior of HPS70W I-shape girders were synthetically developed from the experimental and numerical responses of specimens classified in compact/noncompact and composite/noncomposite categories. In addition, the effects of lateral bracing lengths on pier moment-rotation behavior of CSU's HPS70W I-shape noncompact girders, Specimen #3 and Specimen #4, were studied from the response of the specimens with lateral compression-flange bracing classified in satisfying/dissatisfying the AASHTO requirements (AASHTO, 1998 and interim 2001) categories.

Before detailing the experimental moment-rotation results, linear strain distribution was first checked against the elastic neutral axis for each of the noncomposite HPS70W specimens, Specimens #1 to #4. Second, the similarity and difference between some numerical moment-total rotations and corresponding moment-inelastic rotations were noticed. Third, the effects of residual stresses and initial imperfection on numerical models were verified.

Figure 4.1.1 illustrates the linear strain measurements, which vary with loads, through the I-section and the corresponding locations of the elastic neutral axis by intercepting the best-fit lines of linear strain distributions with the vertical axis of the web for Specimen #1. The elastic neutral axis, which is supposed to be at the centroid of the cross section as 8.406 in. from bottom of the lower flange, is shifted upward a little bit, about 0.2 in. to 0.5 in. Similarly, the linear strain distributions through the I-section and the corresponding locations of the elastic neutral axis for Specimens #2, #3, and #4 are demonstrated in Figures 4.1.2, 4.1.3, and 4.1.4, respectively. The locations of the elastic neutral axis, which are 10.25 in., 10.862 in., and 13.25 in. from bottom of the lower flange for Specimens #2, #3, and #4, respectively, are all shifted a little bit from the I-section's centroids upward into the compression zone about 0.2 in. to 0.5 in., which are tolerated.

Figures 4.1.5 and 4.1.6 display the experimental curves and a number of numerical moment-total rotation and moment-inelastic rotation relationships at different locations for the 19.5 ft-span girder (Specimen #1) and the 22 ft-span girder (Specimen #2), respectively. At different locations near the supports as shown in Figures 4.1.5 and 4.1.6 for Specimens #1 and #2, the moment-inelastic rotation relationships are numerically almost identical although the moment-total rotation relationships are different. In the figures, the ascending (elastic) portion of the moment-rotation curves shows that the experimental girders are little bit stiffer than the numerical models. The reason was attributed to the actual modulus of elasticity, E, of HPS70W that is somewhat greater than the numerical inputs for E as in Chapter 3.

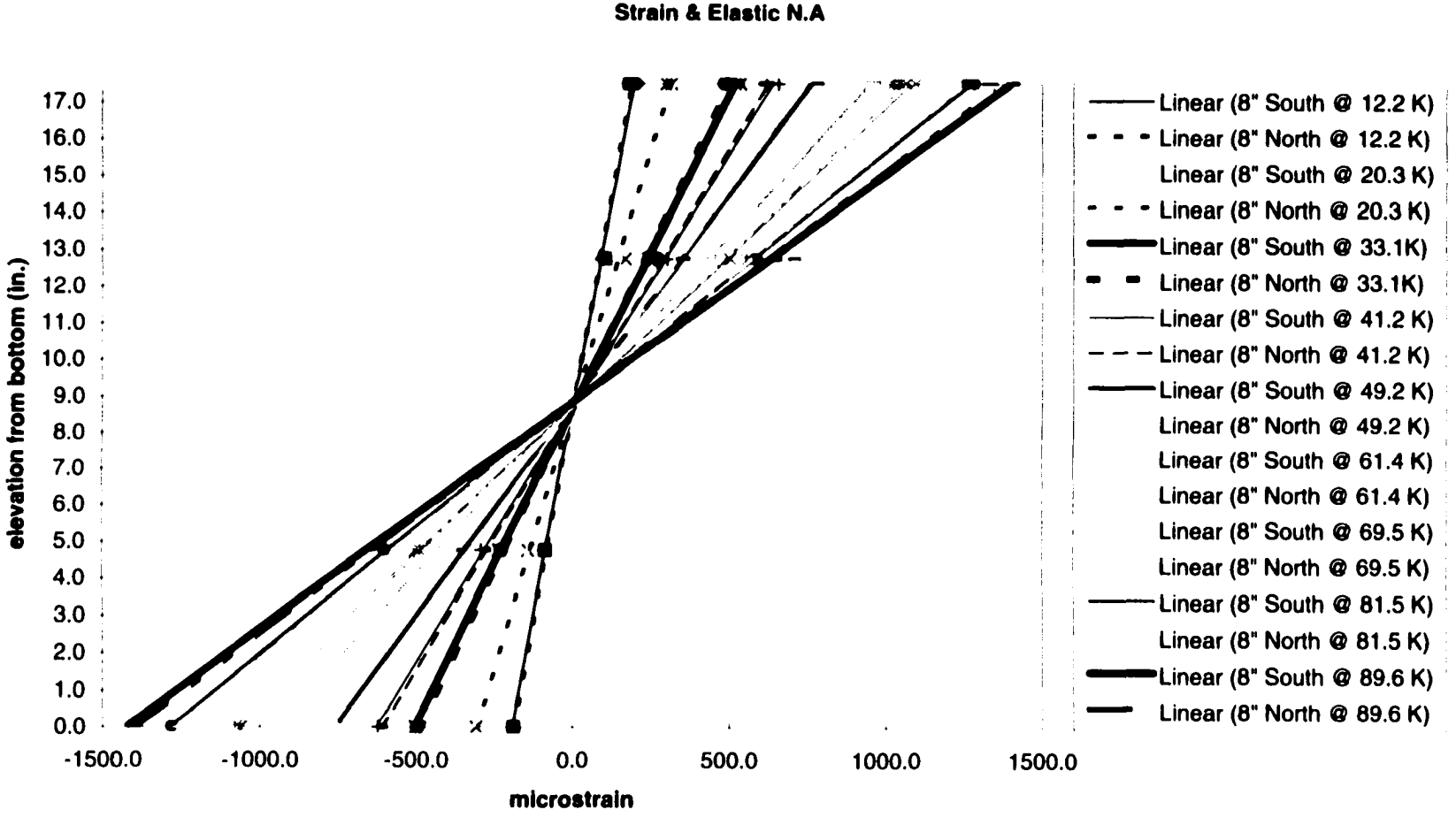

Figure 4.1.1 Linear strain distributions through cross-section and elastic neutral axis for Specimen #1

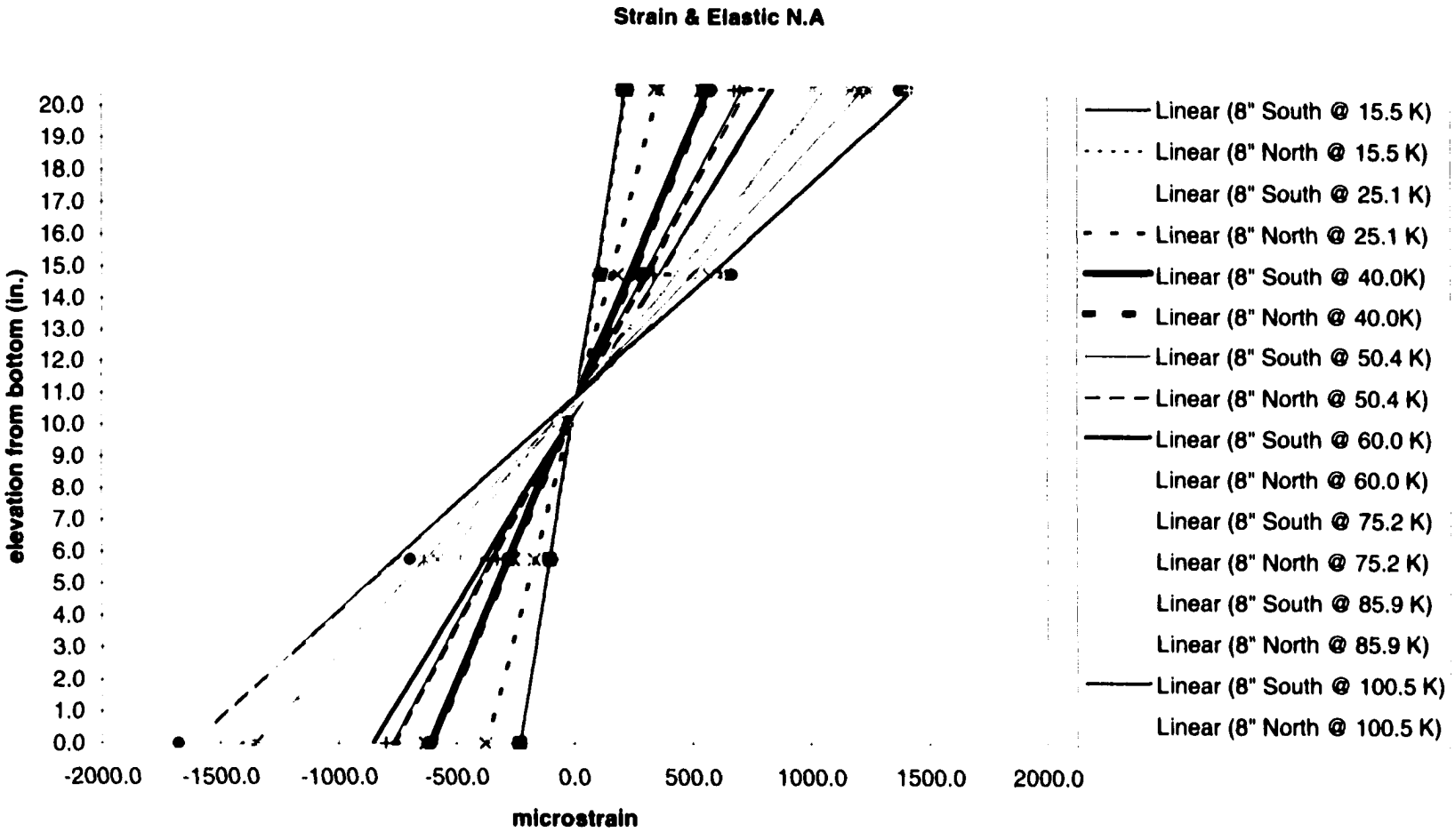

Figure 4.1.2 Linear strain distributions through cross-section and elastic neutral axis for Specimen #2

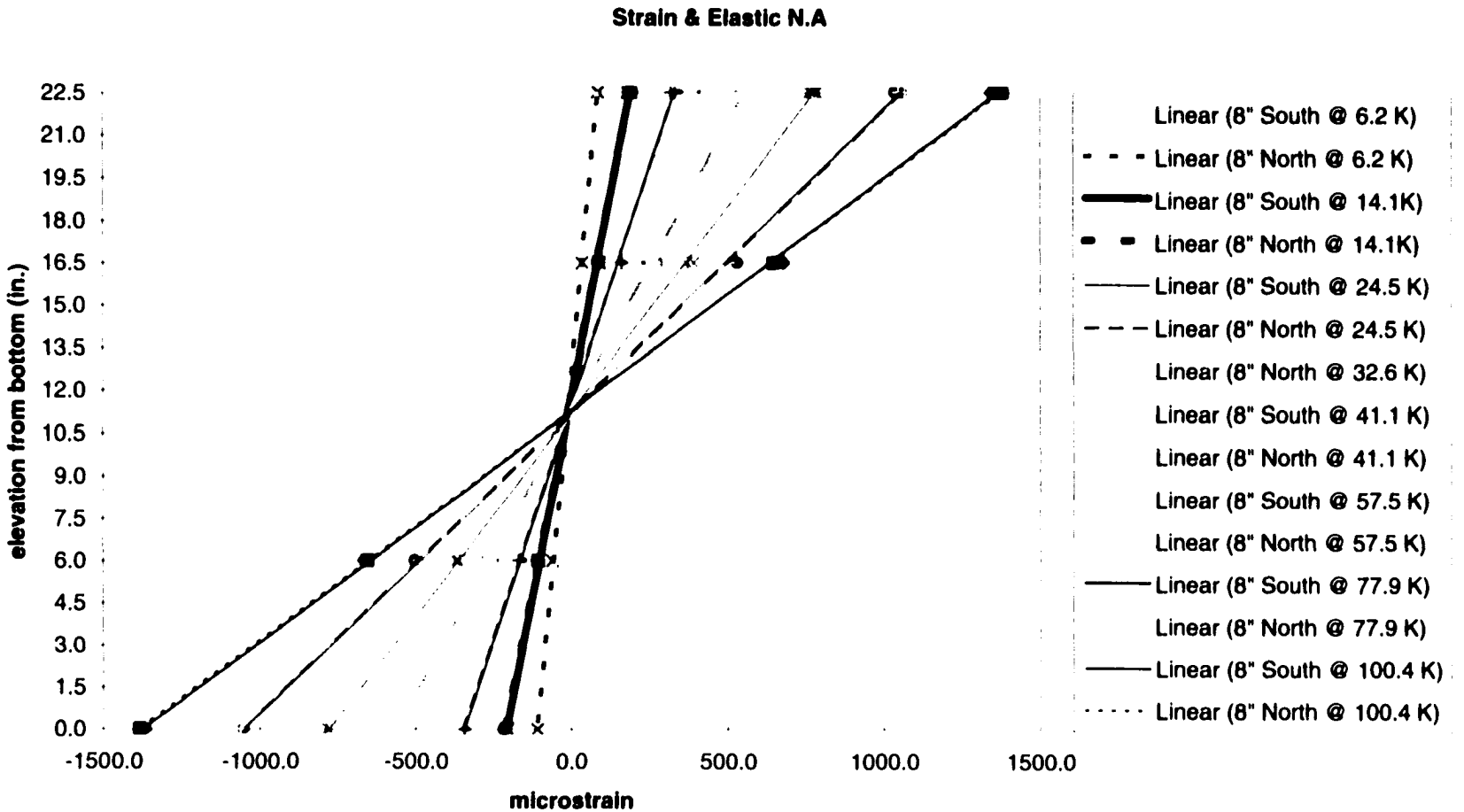

Figure 4.1.3 Linear strain distributions through cross-section and elastic neutral axis for Specimen #3

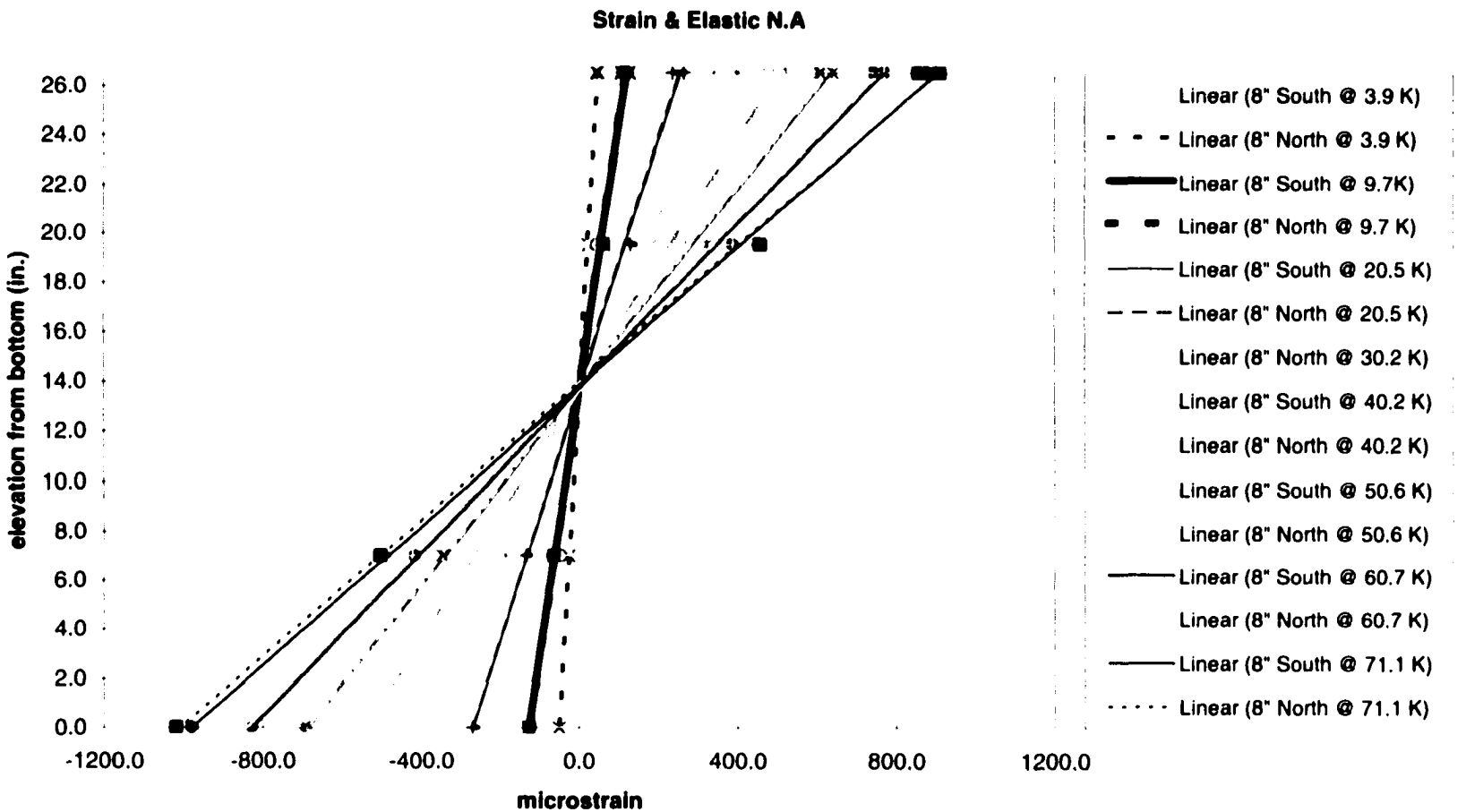

Figure 4.1.4 Linear strain distributions through cross-section and elastic neutral axis for Specimen #4

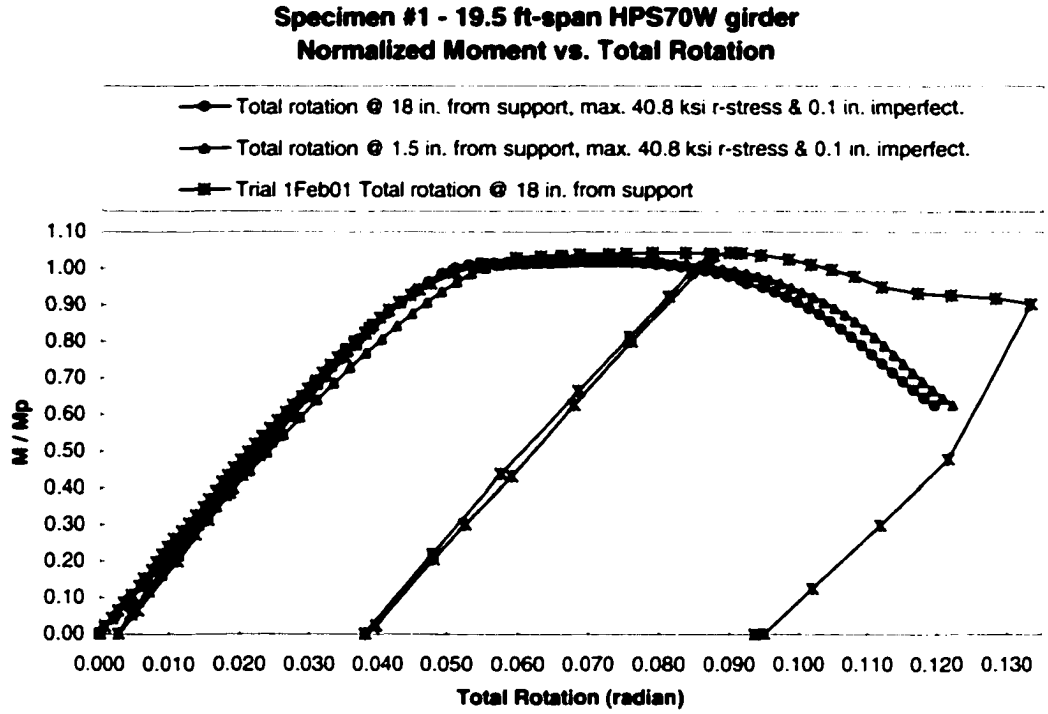

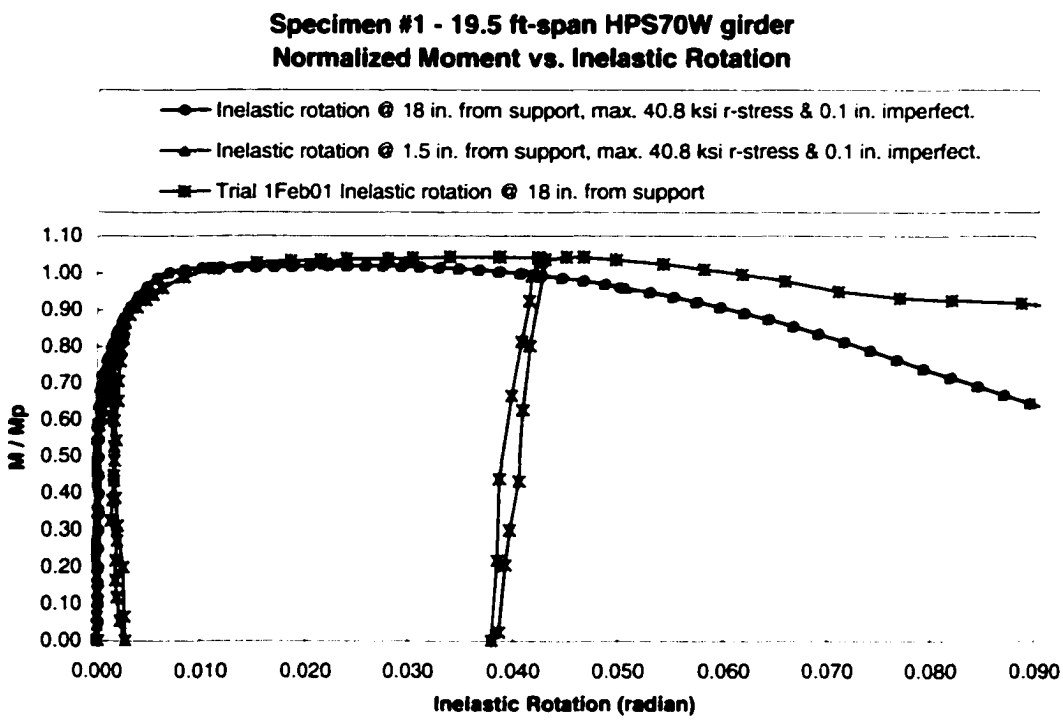

Figure 4.1.5 Specimen #1 - Numerical moment-total rotation and moment-inelastic rotation at different locations near the supports

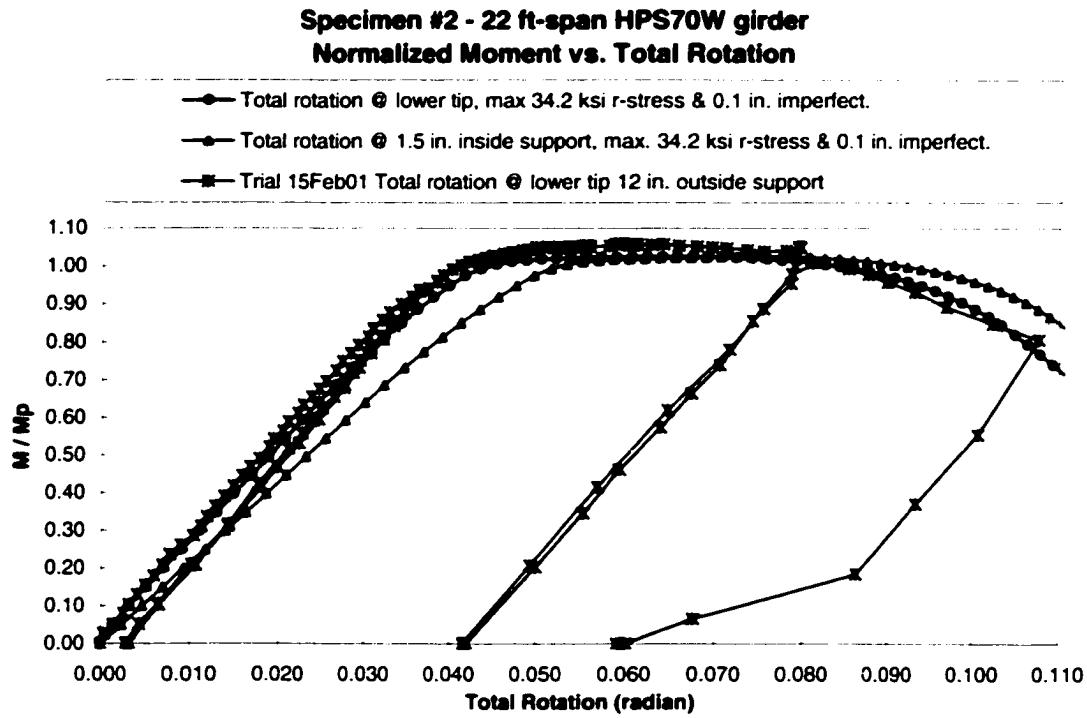

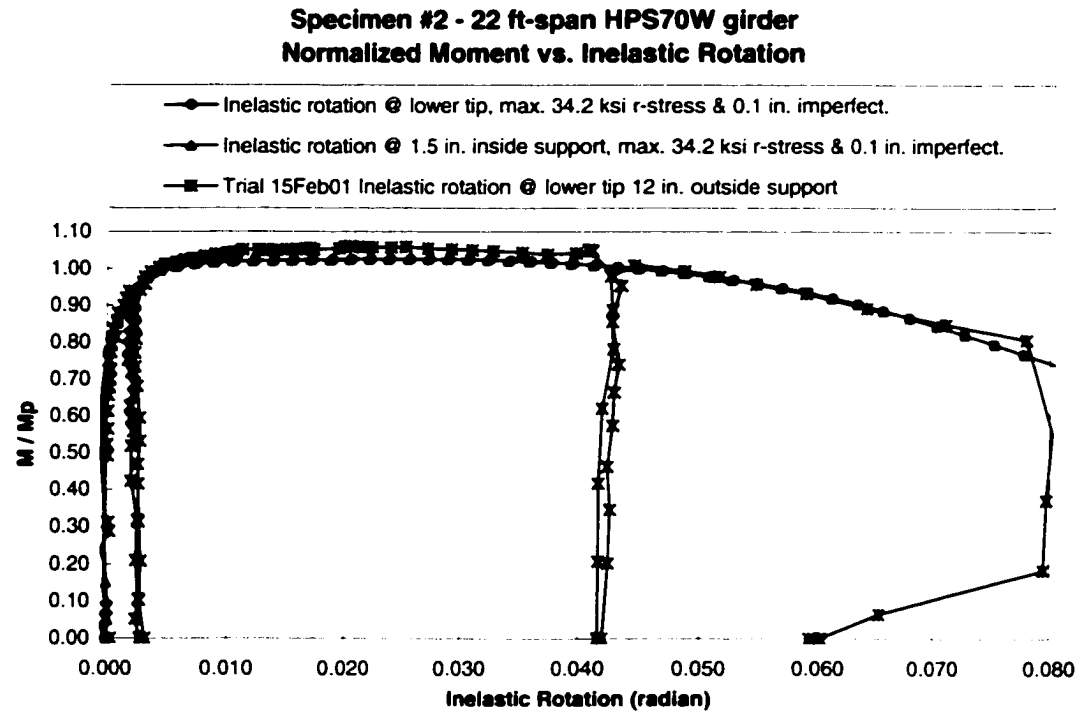

Figure 4.1.6 Specimen #2 - Numerical moment-total rotation and moment-inelastic rotation at different locations near the supports

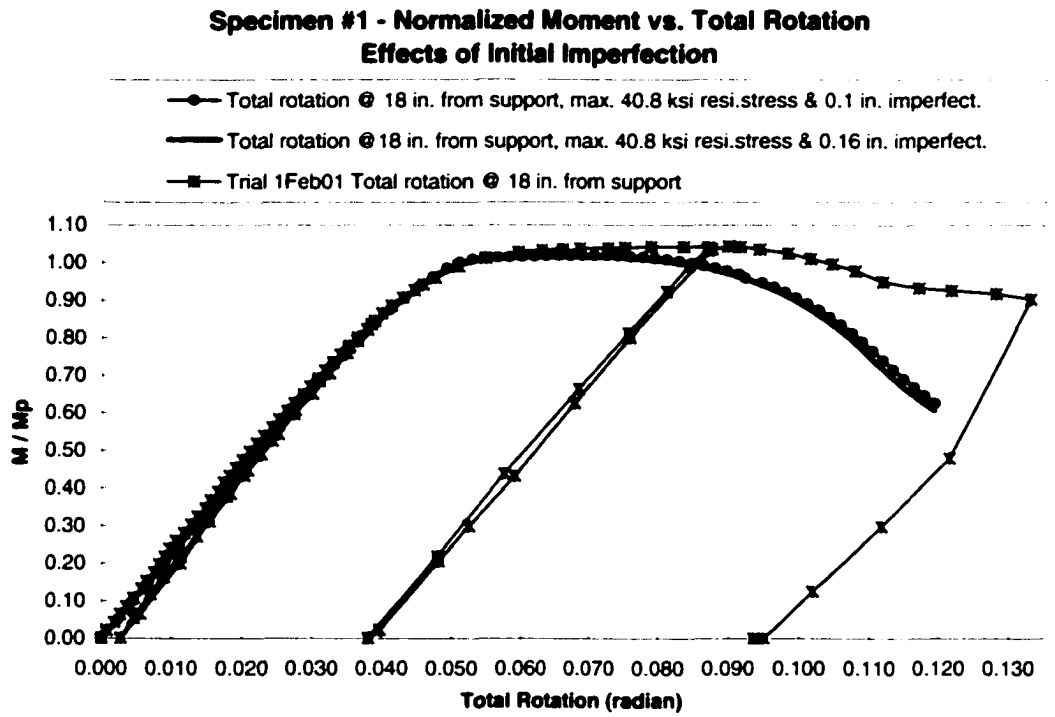

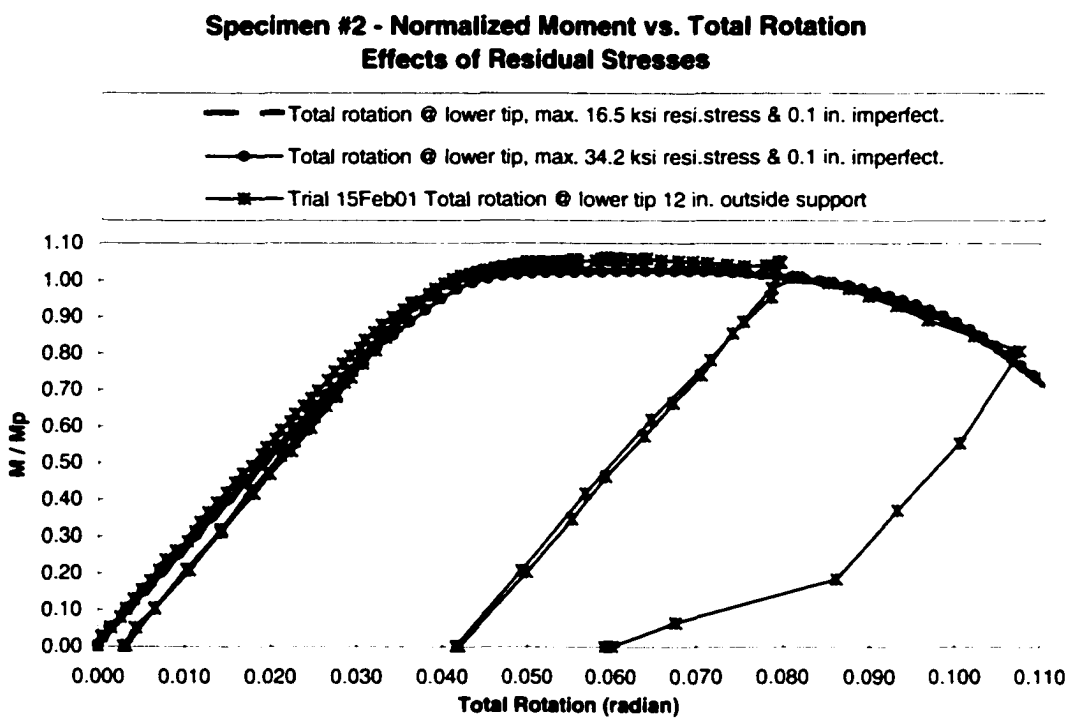

Figure 4.1.7 Effects of residual stresses and initial imperfection on numerical models of Specimen #1 (above) and Specimen #2 (below)

Figures 4.1.7 illustrates the effects of initial residual stresses and imperfections on the numerical outcomes of the 19.5 ft-span girder (Specimen #1) and the 22 ft-span girder (Specimen #2). The results are in agreement with previous studies of Yakel, Mans, and Azizinamini, 1999 and Zubeck, 2000. The effect of residual stresses in the moment-rotation diagram was "rounding off" the curve as the girder yields even though the magnitude of residual stresses has no effect on the ultimate moment capacity. In addition, more imperfection introduced into the model made the post-plateau portion of the moment-rotation curve to descend with steeper slopes although the influence was not significant.

4.2 Inelastic Moment-Rotation Relationships of the CSU's HPS70W Noncomposite Specimens

The pier moment-rotation behavior of HPS70W I-shape girders were synthetically developed from the response of specimens classified in compact/noncompact and composite/noncomposite categories. For the CSU "nominal compact/noncompact" noncomposite HPS70W girders, the experimental results obtained from girder testing and the numerical outcomes acquired from ABAQUS analyses are very close. For each of the four CSU's HPS70W girders, the comparisons with AASHTO specifications (AASHTO, interim 2001) consist of a division for "nominal compact/noncompact", in which the nominal yield stress, F_y = 70 ksi, is applied in the AASHTO specifications, and another portion for "actual noncompact" (see Section 3.2), in which average tested yield strengths, F_{yw} = 69.83 ksi for the web and F_{yf} = 83.35 ksi for the flanges, are utilized in the predicted equations.

In detail, Figures 4.2.1, 4.2.2, and 4.2.3 display the moment-rotation capacity, R, and the AASHTO predicted comparison (6.10.10.2.4d (for M/M_p) & 6.10.10.1.2d (for M_{pc})) in both portions of "nominal compact" and "actual noncompact" for Specimen #1. Likewise, the comparisons for Specimen #2 are presented in Figures 4.2.4, 4.2.5, and 4.2.6. Similar to the results of Yakel, Mans, and Azizinamini, 1999, both girders here do not exhibit the anticipated rotational capacity of three as for compact girders (AISC LRFD specification, 2nd edition, 1998). However, the rotation capacity, R, of Specimen #1 can be seen probably greater than three, nominally, while it is actually estimated as 1.44. Besides, Specimen #2 exhibits its inelastic rotational ductility, R, of 2.29, nominally, and 1.34, actually. The results of inelastic moment-rotation relationship for both compact girders, Specimen #1 and Specimen #2, exceed the current AASHTO specifications and the proposed improved simplified inelastic design predictions, nominally and actually. Their moment-rotation responses actually developed a moment resistance greater than their plastic moment capacities until their inelastic rotations approximately reached 40 mrads and 44 mrads, respectively. These values are much greater than the maximum rotation of 30 mrads now thought necessary for redistribution of moments in bridges (Schilling, 1986; Barth, Hartnagel, White, and Barker, 2001).

Figures 4.2.7 and 4.2.8 display the AASHTO predicted comparison (6.10.10.2.4d (for M/M_p) & 6.10.10.1.2d (for M_{pc})) for Specimen #3 in both portions of "nominal noncompact", in which the nominal yield stress, F_y = 70 ksi, is applied in the AASHTO specifications, and "actual noncompact", in which average tested yield strengths, F_{yw} = 69.83 ksi for the web and F_{yf} = 83.35 ksi for the flanges, are utilized in the predicted equations. The comparisons for Specimen #4 are presented in Figures 4.2.9 and 4.2.10.

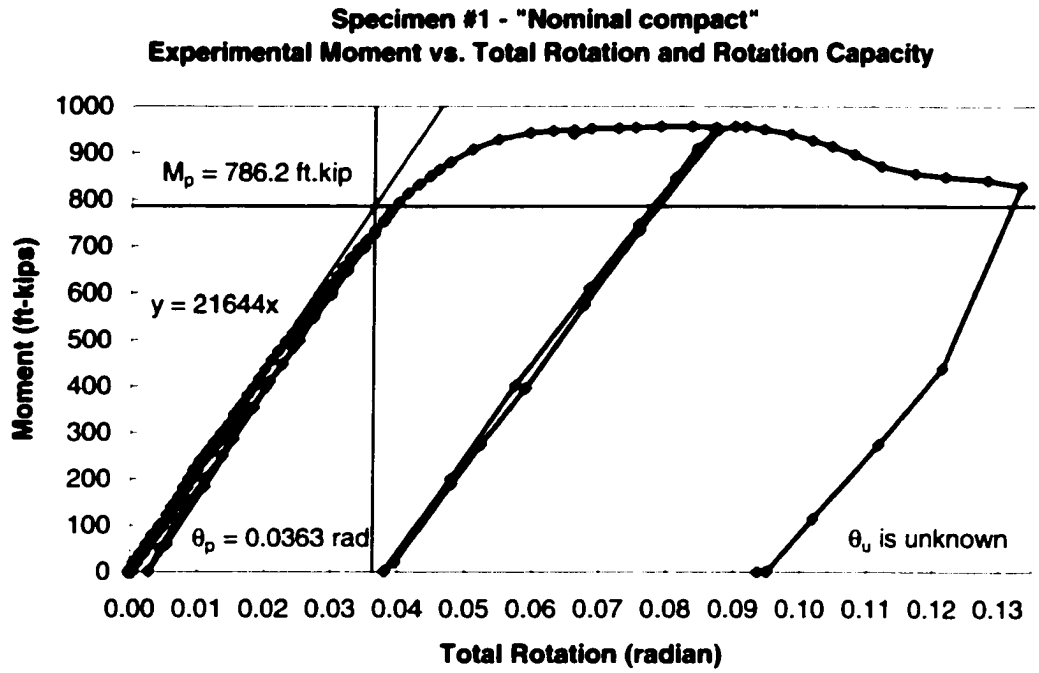

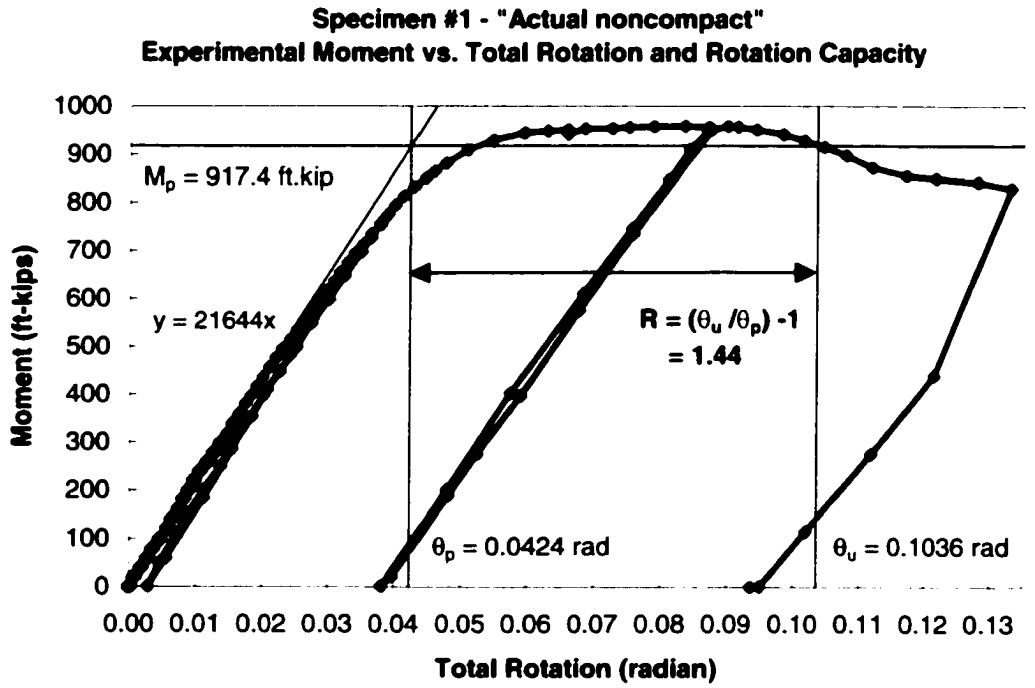

Figure 4.2.1 Nominal and actual rotational capacity, R, of Specimen #1

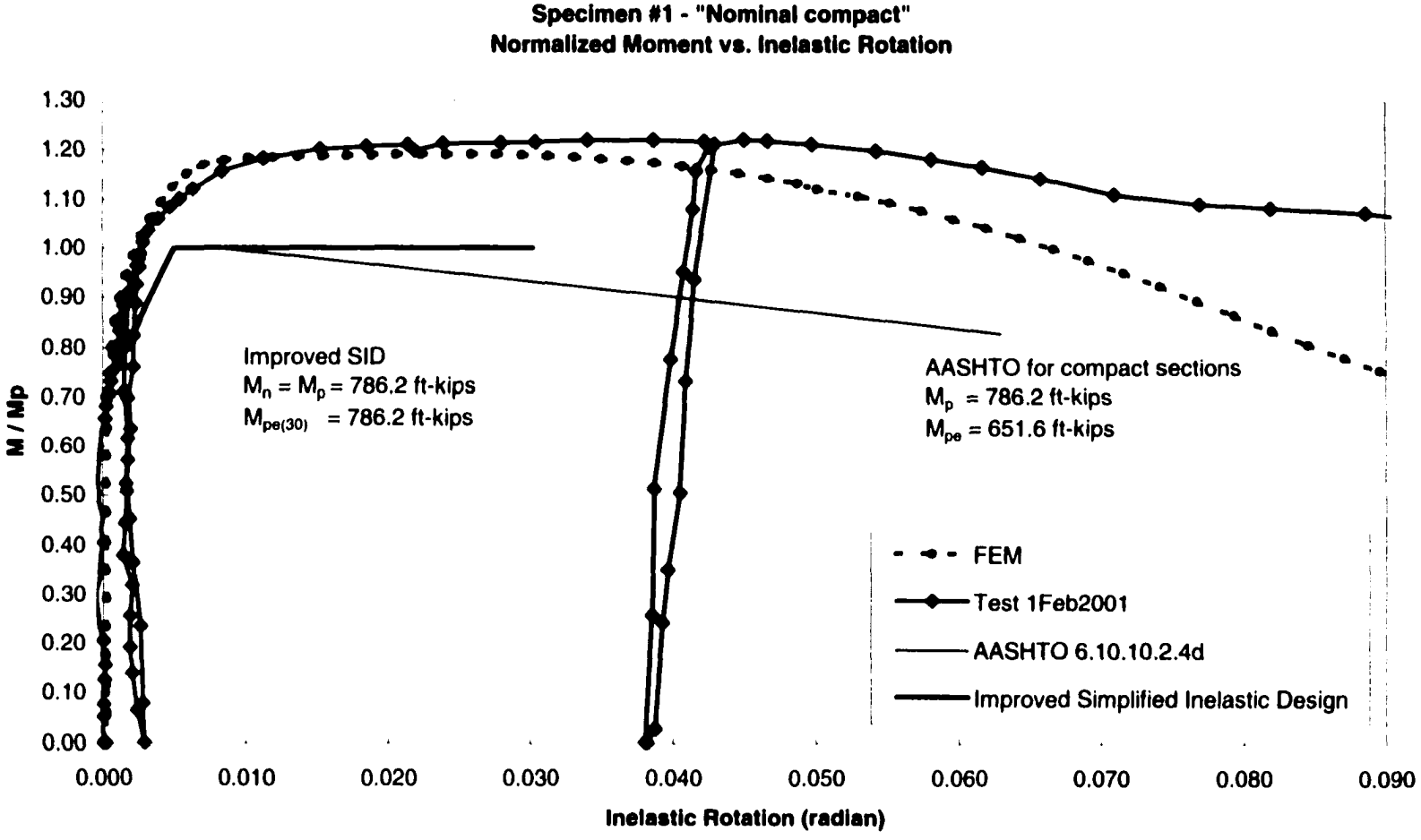

Figure 4.2.2 AASHTO predicted comparison for Specimen #1, nominally

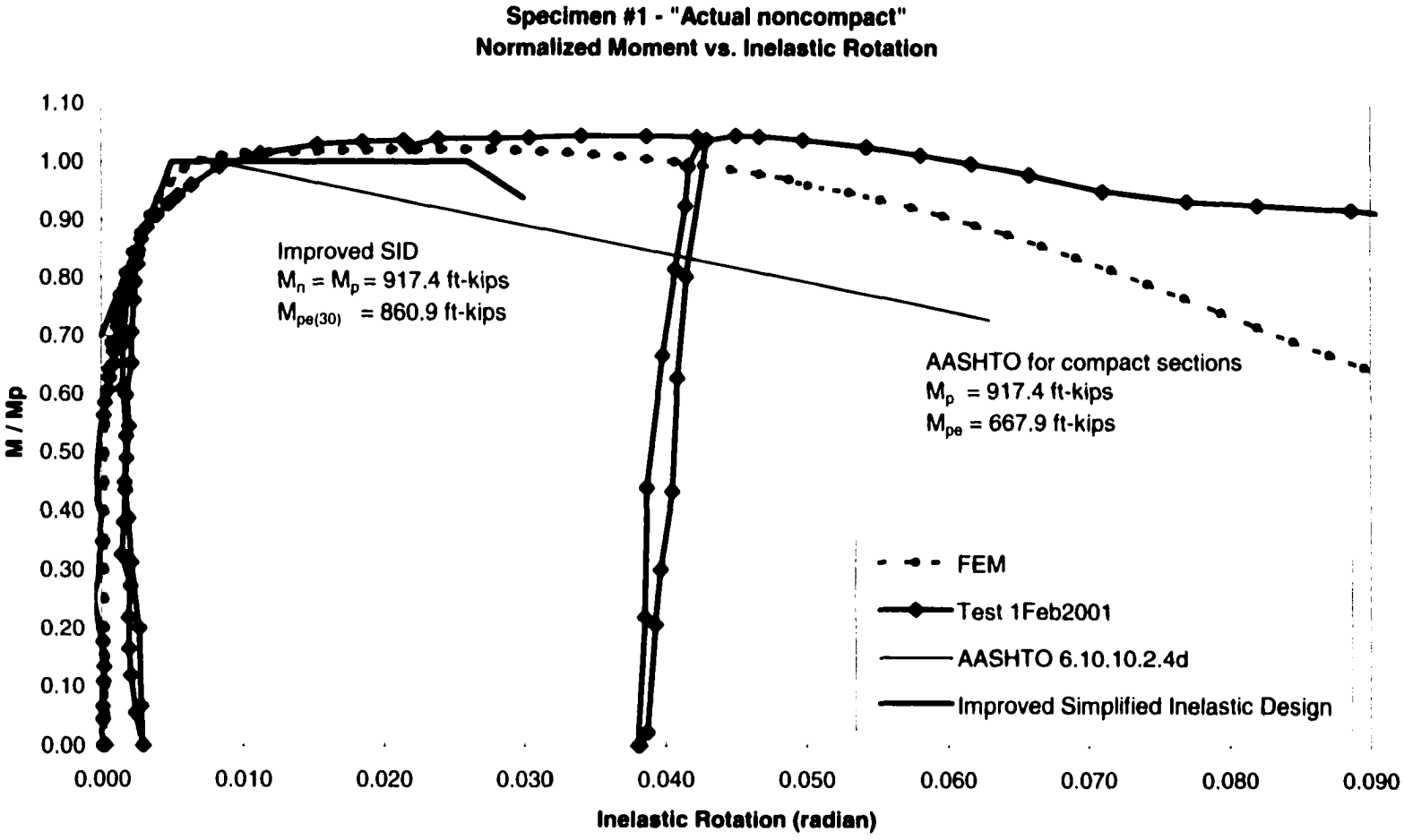

Figure 4.2.3 AASHTO predicted comparison for Specimen #1, actually

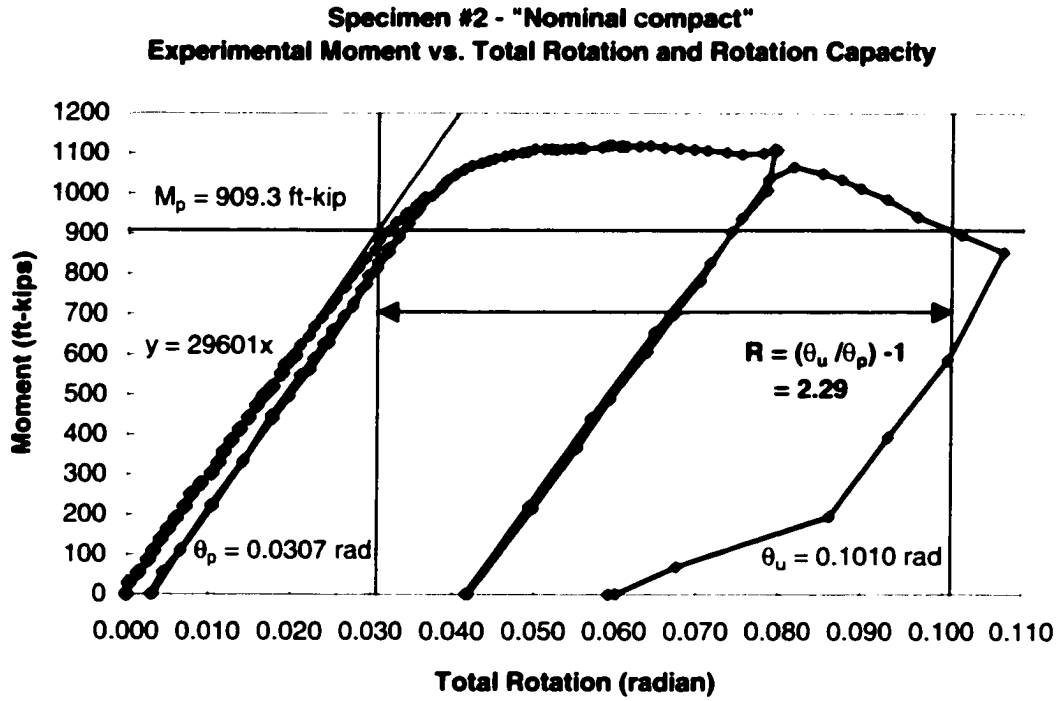

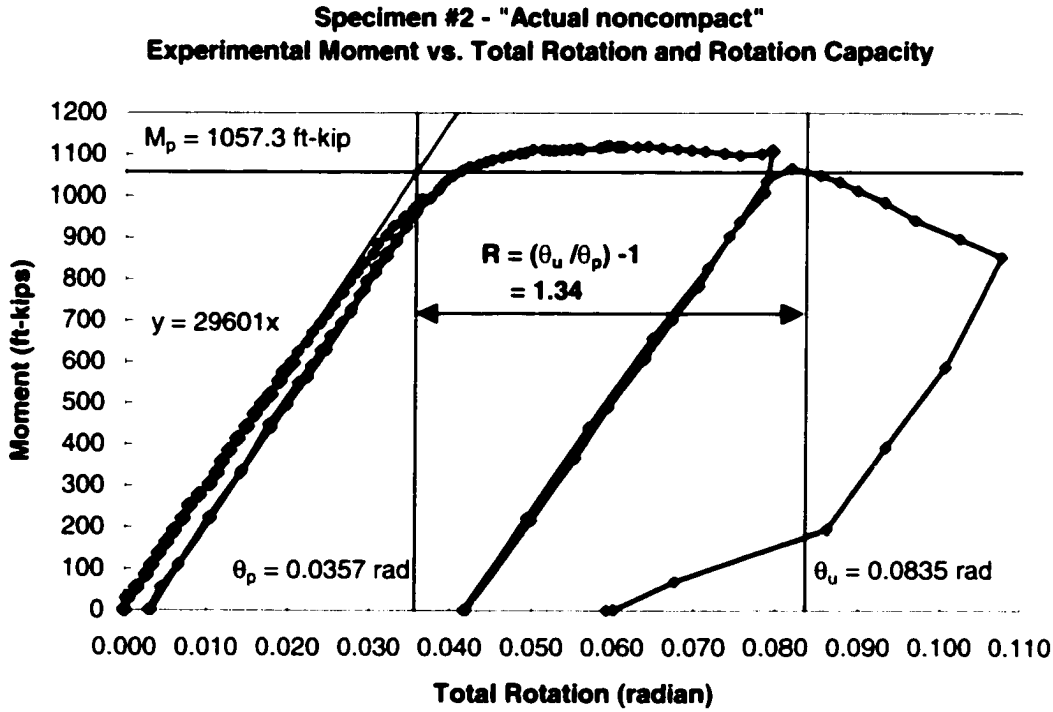

Figure 4.2.4 Nominal and actual rotational capacity, R, of Specimen #2

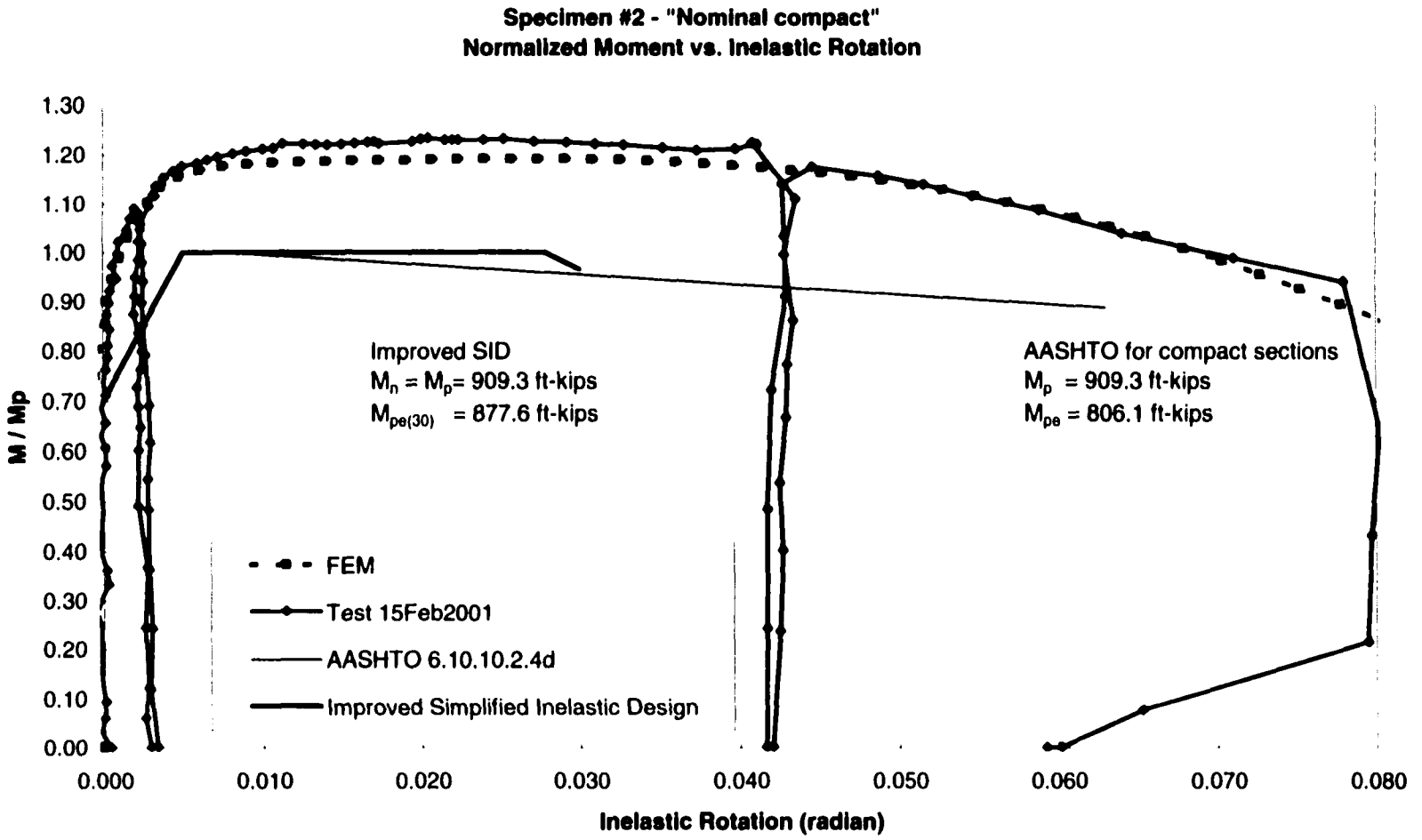

Figure 4.2.5 AASHTO predicted comparison for Specimen #2, nominally

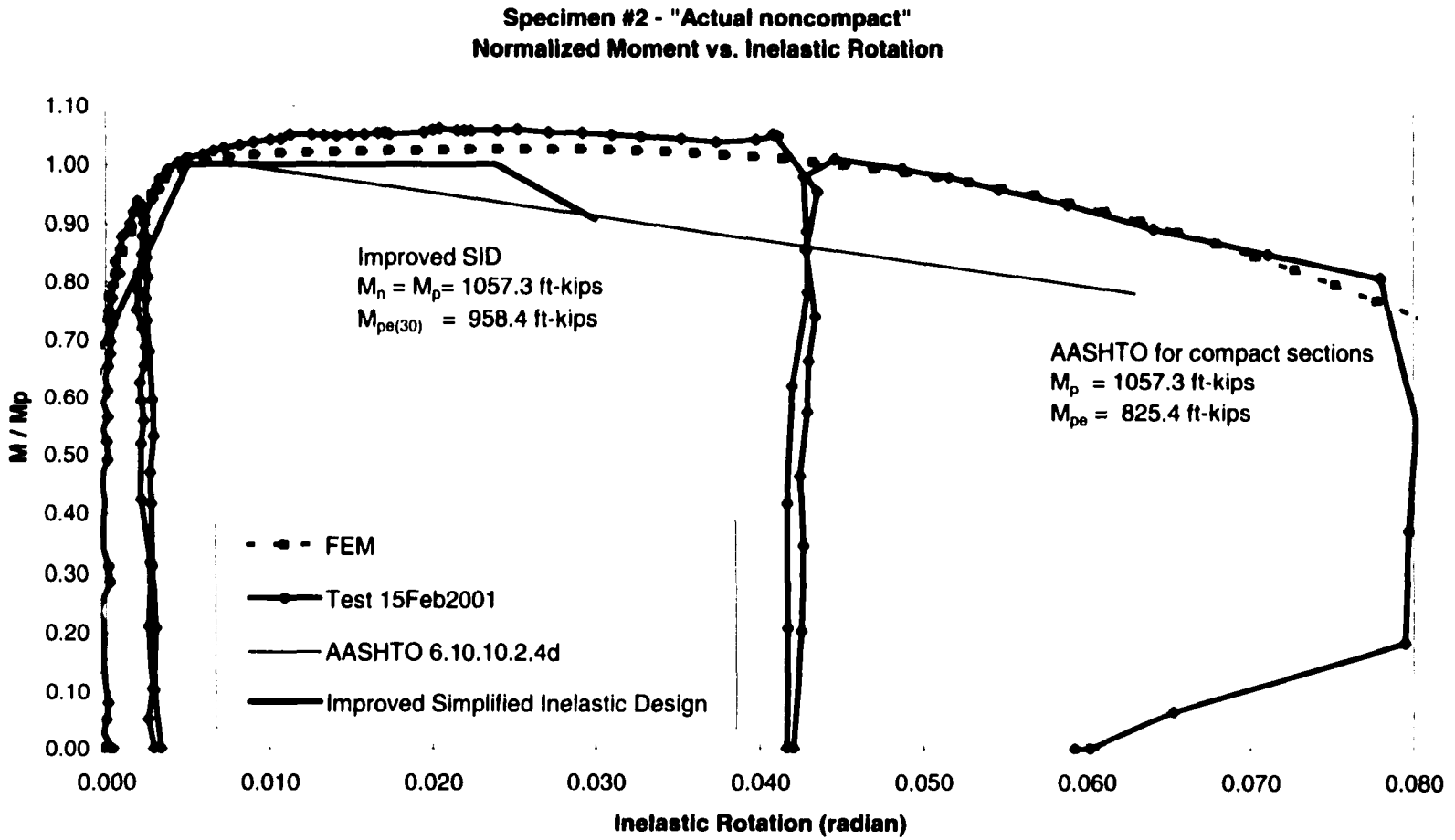

Figure 4.2.6 AASHTO predicted comparison for Specimen #2, actually

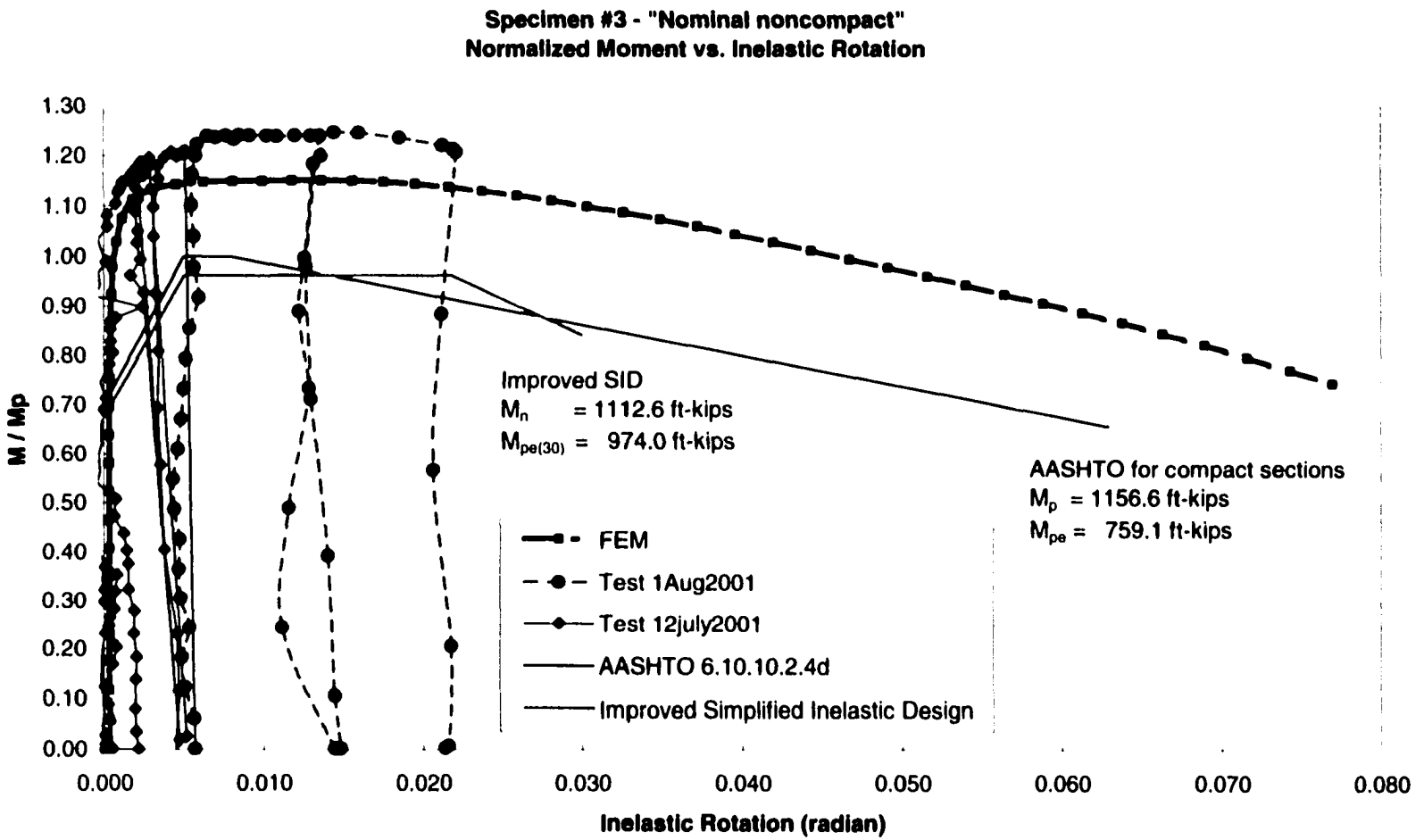

Figure 4.2.7 AASHTO predicted comparison for Specimen #3, nominally

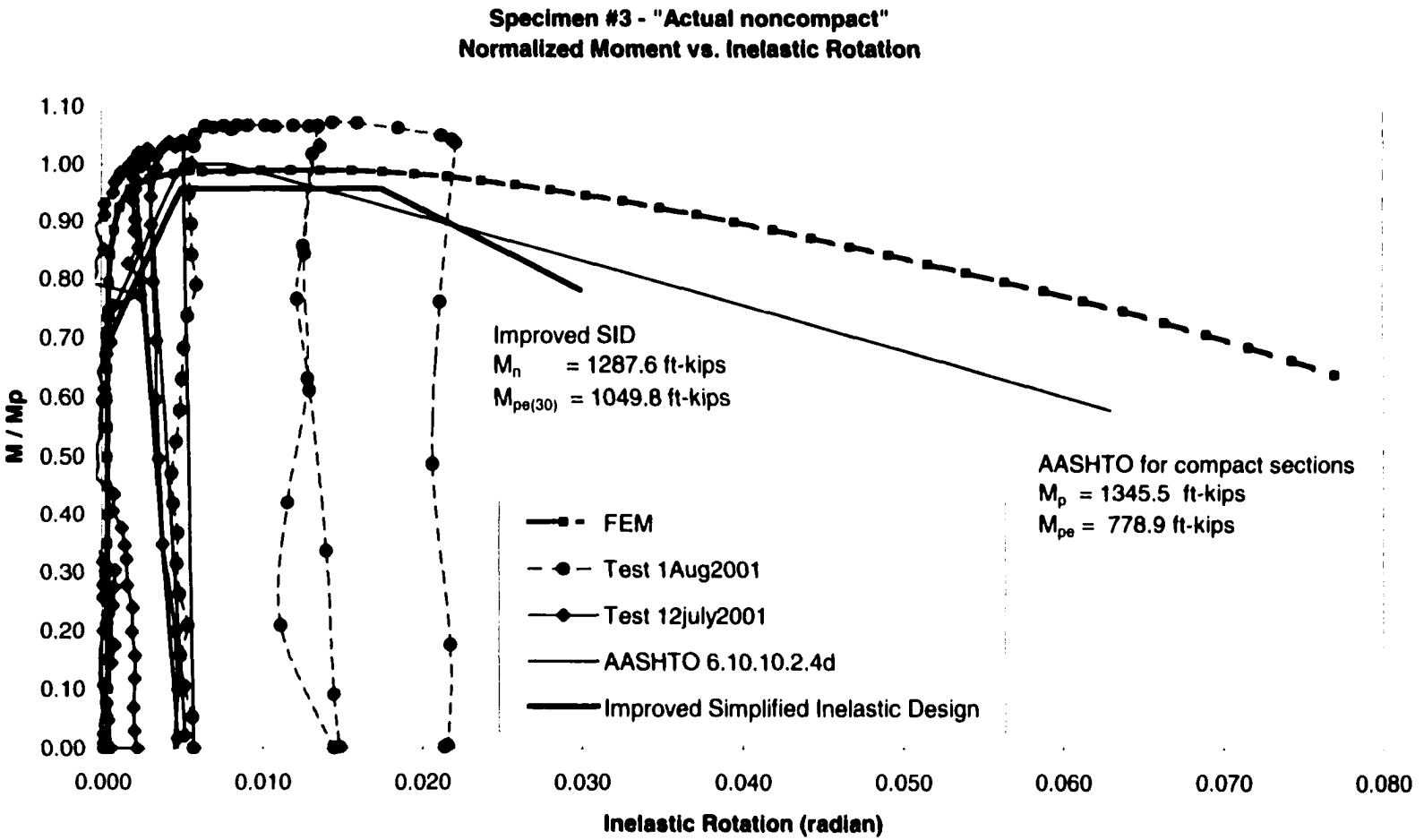

Figure 4.2.8 AASHTO predicted comparison for Specimen #3, actually

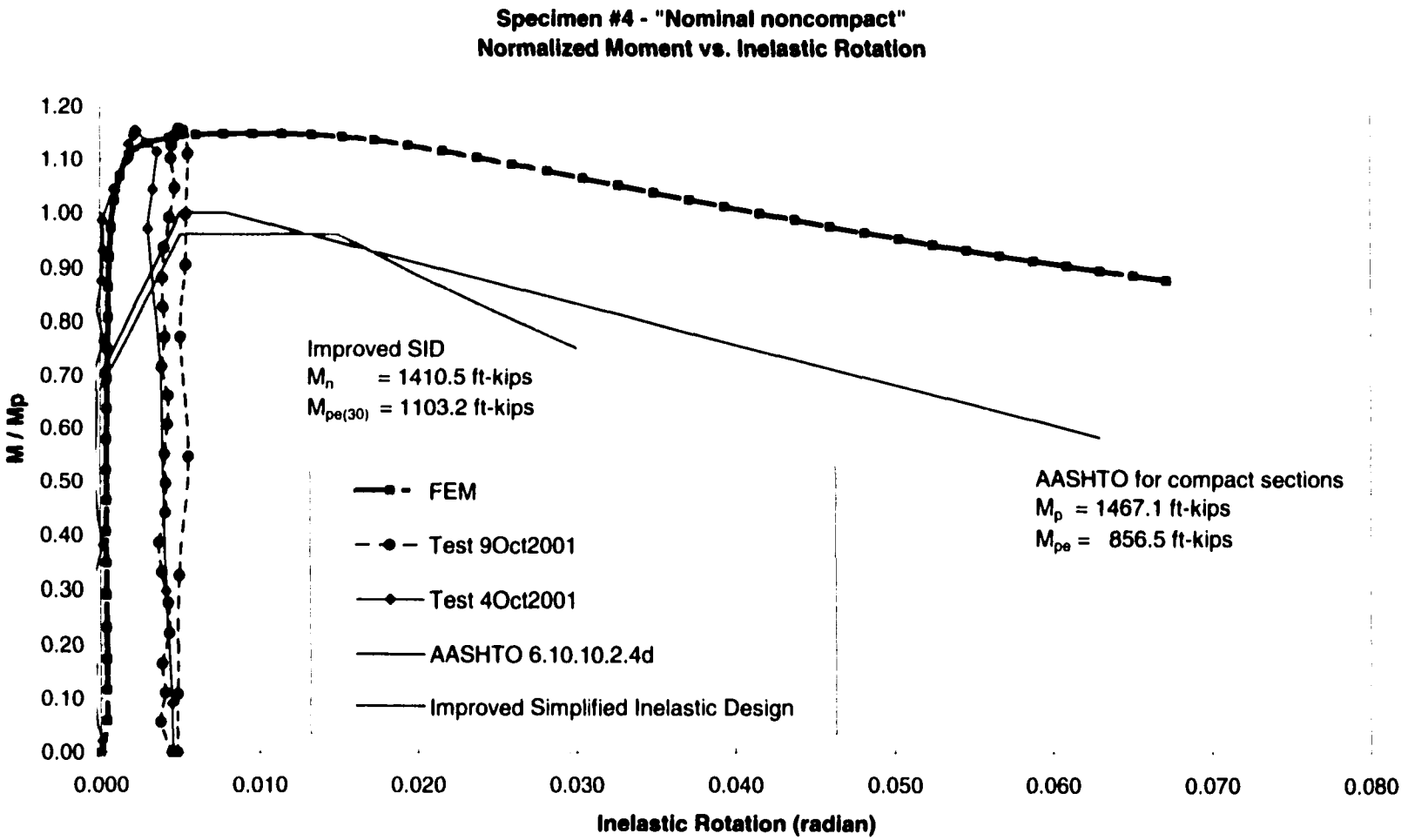

Figure 4.2.9 AASHTO predicted comparison for Specimen #4, nominally

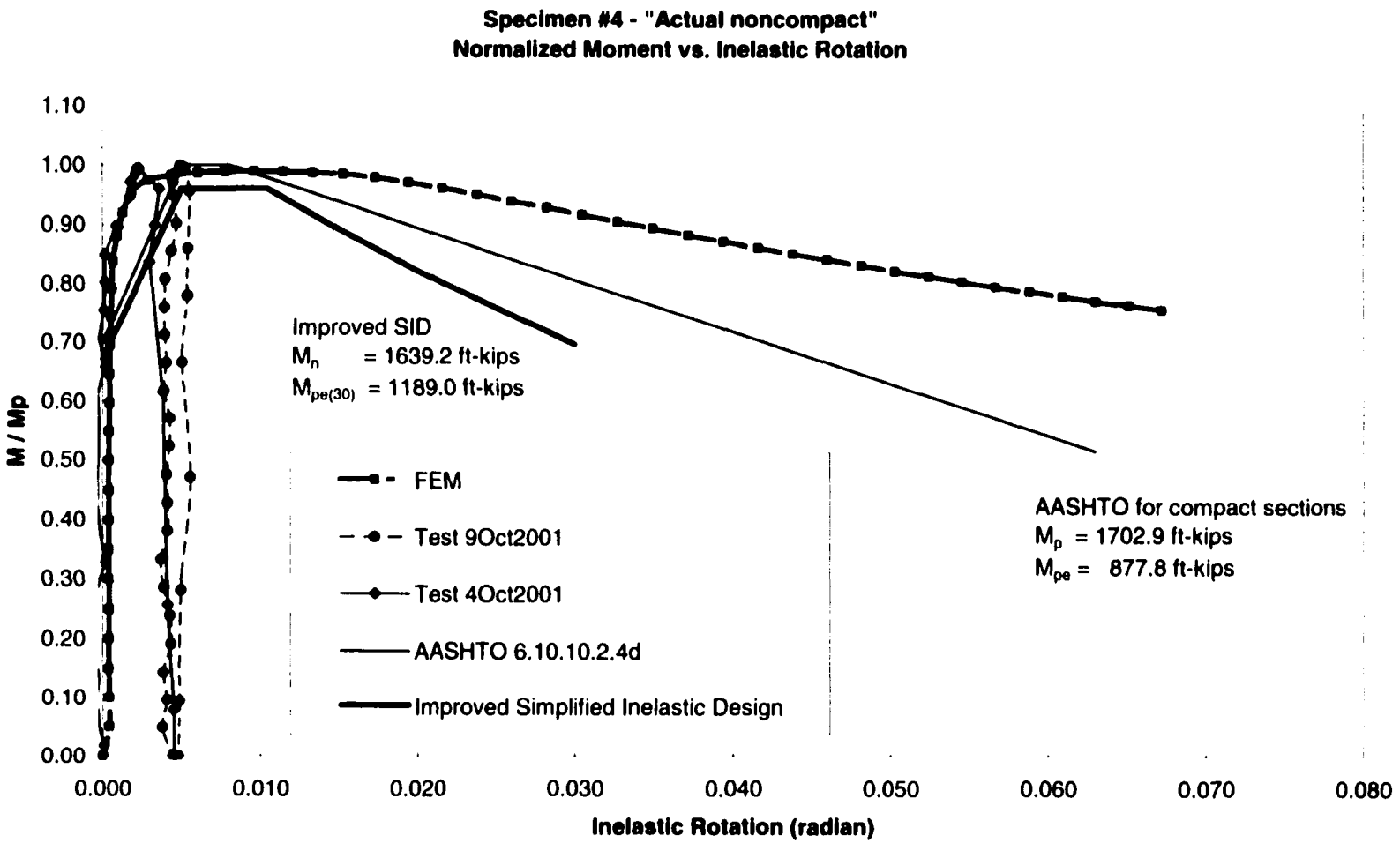

Figure 4.2.10 AASHTO predicted comparison for Specimen #4, actually

Nominally, the experimental and numerical results of inelastic moment-rotation relationship for both noncompact specimens, Specimens #3 and #4, exceed the current AASHTO specifications and the proposed improved simplified inelastic design predictions. Actually, the experimental inelastic moment-rotation curves for both specimens still exceed plastic moments, M_p. However, both numerical inelastic moment-rotation curves of the noncompact specimens do not reach the plastic moment, M_p, although they actually exceed the proposed design moment, M_n, and the proposed effective moment, $M_{pe(30)}$.

In summary, the differences in the plastic moments, M_p, and effective moments, M_{pe}, specified by AASHTO 6.10.10.1.2d (AASHTO, interim 2001) between the nominal and the average of the tested yield stresses are listed in Tables 4.2.1 and 4.2.2. Table 4.2.3 summarizes the AASHTO predicted comparisons for the four CSU girders. Additionally, the differences in the design moments, M_n, and the predicted effective moments, $M_{pe(30)}$, suggested at 30 mrads by the proposed Improved Simplified Inelastic Design (Improved-SID) (Barth, Hartnagel, White, and Barker, 2001) between the nominal and the average of the tested yield stresses are listed in Tables 4.2.4 and 4.2.5. Table 4.2.6 summarizes the proposed Improved-SID predicted comparisons for the four CSU girders.

Table 4.2.1 Nominal plastic moment, M_p, and AASHTO effective moment, M_{pe}

Specimen #	Nominal M_p (ft-kip)	F_{ye} Comp. Flange (ksi)	F_{ye} Tension Flange (ksi)	F_{ye} Web (ksi)	M_{pe} (ft-kip) (@ 63 mrads on plot)
1	786.2	68.07	55.14	26.51	651.6
2	909.3	68.07	68.07	26.51	806.1
3	1156.6	55.14	45.57	16.61	759.1
4	1467.1	45.57	45.57	15.31	856.5

Table 4.2.2 Actual plastic moment, M_p, and AASHTO effective moment, M_{pe}

Specimen #	Actual M_p (ft-kip)	F_{ye} Comp. Flange (ksi)	F_{ye} Tension Flange (ksi)	F_{ye} Web (ksi)	M_{pe} (ft-kip) (@ 63 mrads on plot)
1	917.4	70.68	57.25	20.10	667.9
2	1057.3	70.68	70.68	21.35	825.4
3	1345.5	57.25	47.32	12.75	778.9
4	1702.9	47.32	47.32	12.33	877.8

Table 4.2.3 Summary of AASHTO predicted comparisons for CSU girders

		Specimen #1 (nonsym.)	Specimen #2 (symmetric)	Specimen #3 (nonsym.)	Specimen #4 (symmetric)
D_{cp}/D	*Nominal*	0.594	0.5	0.571	0.5
	Actual	0.612	0.5	0.585	0.5
Classification	*Nominal*	Compact	Compact	Noncompact	Noncompact
	Actual	Noncompact	Noncompact	Noncompact	Noncompact
Experimental peak vs. M_p	*Nominal*	1.218	1.234	1.247	Exceed
	Actual	1.044	1.061	1.072	Exceed
Numerical peak vs. M_p	*Nominal*	1.190	1.192	1.151	1.148
	Actual	1.020	1.025	**0.990**	**0.989**
Experimental result vs. M_{pe}	*Nominal*	Exceed	Exceed	**No Data**	**No Data**
	Actual	Exceed	Exceed	**No Data**	**No Data**
Numerical result vs. M_{pe}	*Nominal*	Exceed	Exceed	Exceed	Exceed
	Actual	Exceed	Exceed	Exceed	Exceed

where:

D_{cp} = depth of web in compression, taken at the plastic moment (in.),

D = web depth inside flanges (in.),

M_p = plastic moment, and

M_{pe} = effective moment by AASHTO 6.10.10.1.2d (AASHTO, interim 2001).

Table 4.2.4 Nominal ISID design moment, M_n, and effective moment, $M_{pe(30)}$

Specimen #	Nominal M_p (ft-kip)	Nominal design moment M_n (ft-kip)	Improved-SID $M_{pe(30)}$ (ft-kip)
1	786.2	786.2	786.2
2	909.3	909.3	877.6
3	1156.6	1112.6	974.0
4	1467.1	1410.5	1103.2

Table 4.2.5 Actual ISID design moment, M_n, and effective moment, $M_{pe(30)}$

Specimen #	Actual M_p (ft-kip)	Nominal design moment M_n (ft-kip)	Improved-SID $M_{pe(30)}$ (ft-kip)
1	917.4	917.4	860.9
2	1057.3	1057.3	958.4
3	1345.5	1287.6	1049.8
4	1702.9	1634.3	1185.4

Table 4.2.6 Summary of ISID predicted comparisons for CSU girders

		Specimen #1 (nonsym.)	Specimen #2 (symmetric)	Specimen #3 (nonsym.)	Specimen #4 (symmetric)
D_{cp}/D	*Nominal*	0.594	0.5	0.571	0.5
	Actual	0.612	0.5	0.585	0.5
Classification	*Nominal*	Compact	Compact	Noncompact	Noncompact
	Actual	Noncompact	Noncompact	Noncompact	Noncompact
Experimental peak vs. M_n	*Nominal*	1.218	1.234	1.296	1.202
	Actual	1.044	1.061	1.120	1.042
Numerical peak vs. M_n	*Nominal*	1.190	1.192	1.197	1.195
	Actual	1.020	1.025	1.034	1.030
Experi. result vs. $M_{pe(30)}$	*Nominal*	1.218	1.264	**No Data**	**No Data**
	Actual	1.108	1.160	**No Data**	**No Data**
Nume. result vs. $M_{pe(30)}$	*Nominal*	1.190	1.235	1.306	1.420
	Actual	1.085	1.131	1.212	1.321

where:

D_{cp} = depth of web in compression, taken at the plastic moment (in.),

D = web depth inside flanges (in.),

M_n = improved simplified inelastic design (ISID) moment, and

$M_{pe(30)}$ = Improved-SID effective moment at inelastic rotation of 30 mrads.

4.3 Bracing Lengths: Numerical Effects For Specimens #3 and Experimental And Numerical Effects For Specimen #4

The effects of lateral bracing lengths on pier moment-rotation behavior of CSU's HPS70W I-shape noncompact girders, Specimen #3 and Specimen #4, will be studied from the response of the specimens with lateral compression-flange bracing classified in satisfying/dissatisfying the AASHTO requirements (AASHTO, 1998 and interim 2001) categories. Specimen #3 was experimentally tested with lateral compression-flange bracing configuration at midspan and the supports, which satisfies the AASHTO specifications for both categories of compact and noncompact sections (see Chapter 3, Section 3.3.4). Numerically, the finite element model for Specimen #3 was analyzed with four variations satisfying/dissatisfying the AASHTO specifications of lateral compression-flange bracing. Specimen #4 was experimentally tested and numerically analyzed with two variations satisfying/dissatisfying the AASHTO specifications of lateral compression-flange bracing.

As displayed in Figures 4.3.1 and 4.3.2, Specimen #3 with lateral compression-flange bracing satisfying AASHTO specifications experimentally presented the potential to exceed and maintain the plastic moment, M_p, of a noncompact girder. However, the four finite element models satisfying/dissatisfying the AASHTO specifications of lateral compression-flange bracing for the noncompact girder barely reach the plastic moment, M_p. The numerical models showed an insignificant effect of the studied unbraced lengths, only slightly on the plateau and the decreasing part, on the inelastic moment-rotation relationship for Specimen #3.

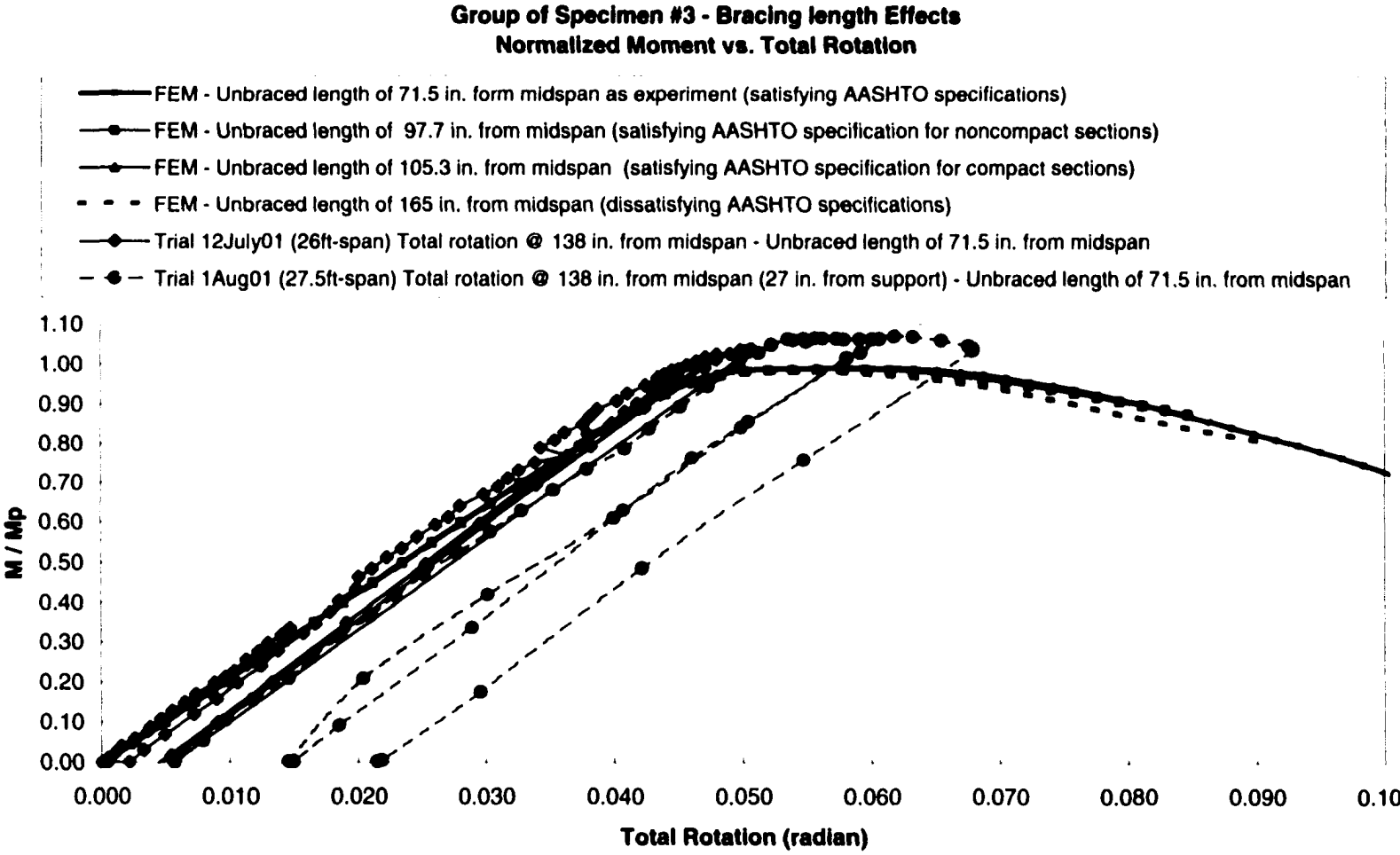

Figure 4.3.1 Numerical effects of bracing lengths on moment-total rotation relationship for Specimen #3

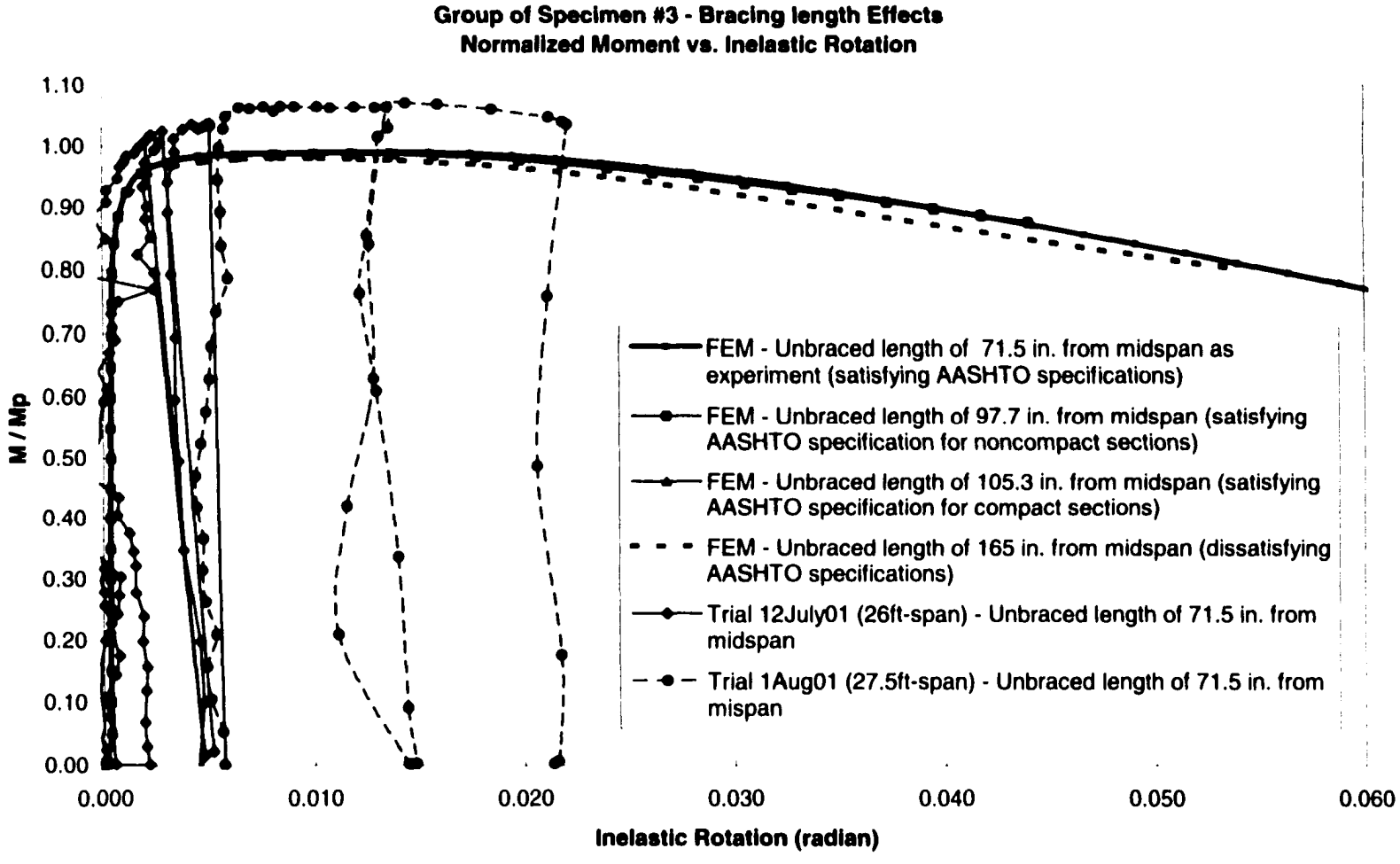

Figure 4.3.2 Numerical effects of bracing lengths on moment-inelastic rotation relationship for Specimen #3

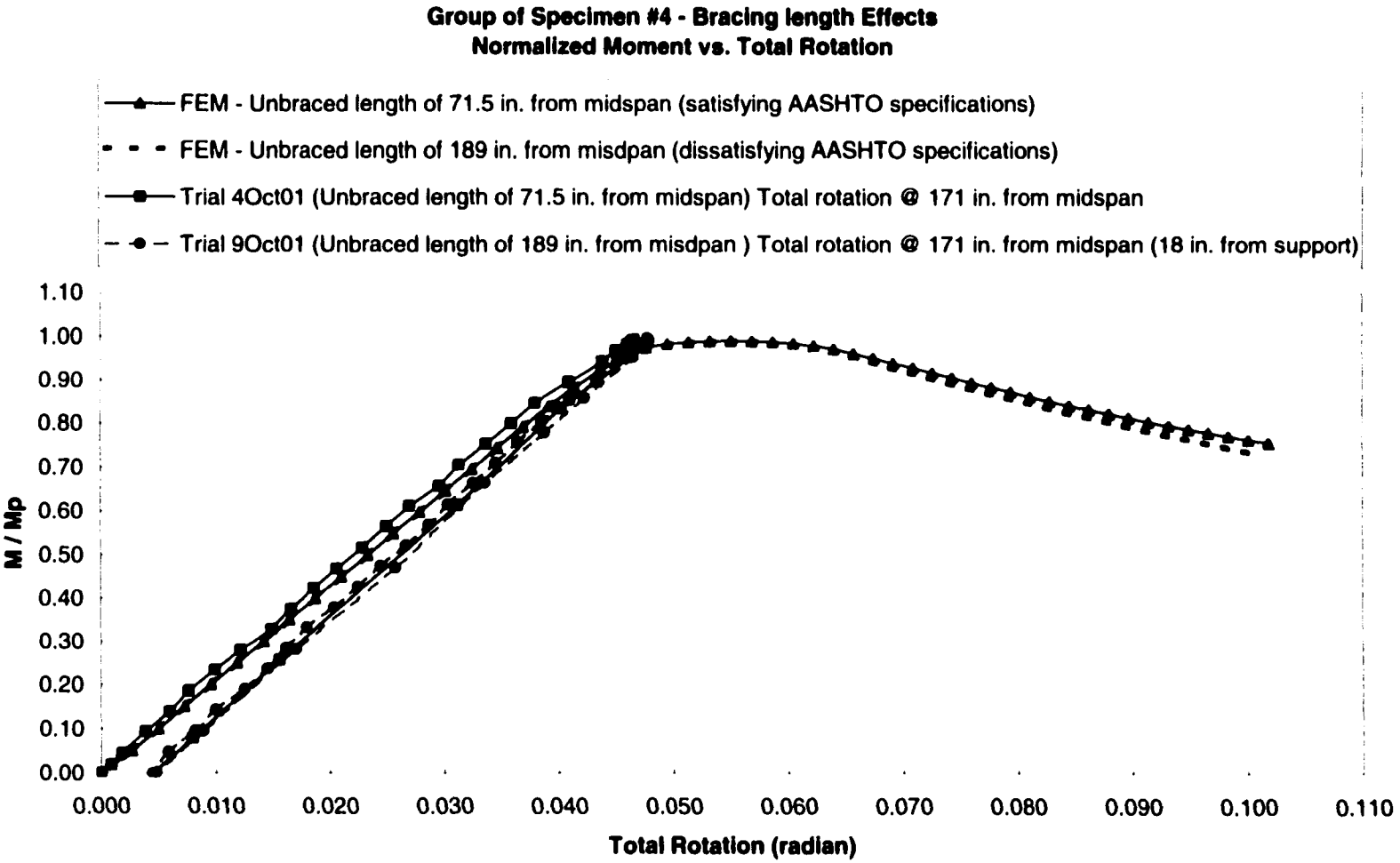

Figure 4.3.3 Experimental and numerical effects of bracing lengths on moment-total rotation for Specimen #4

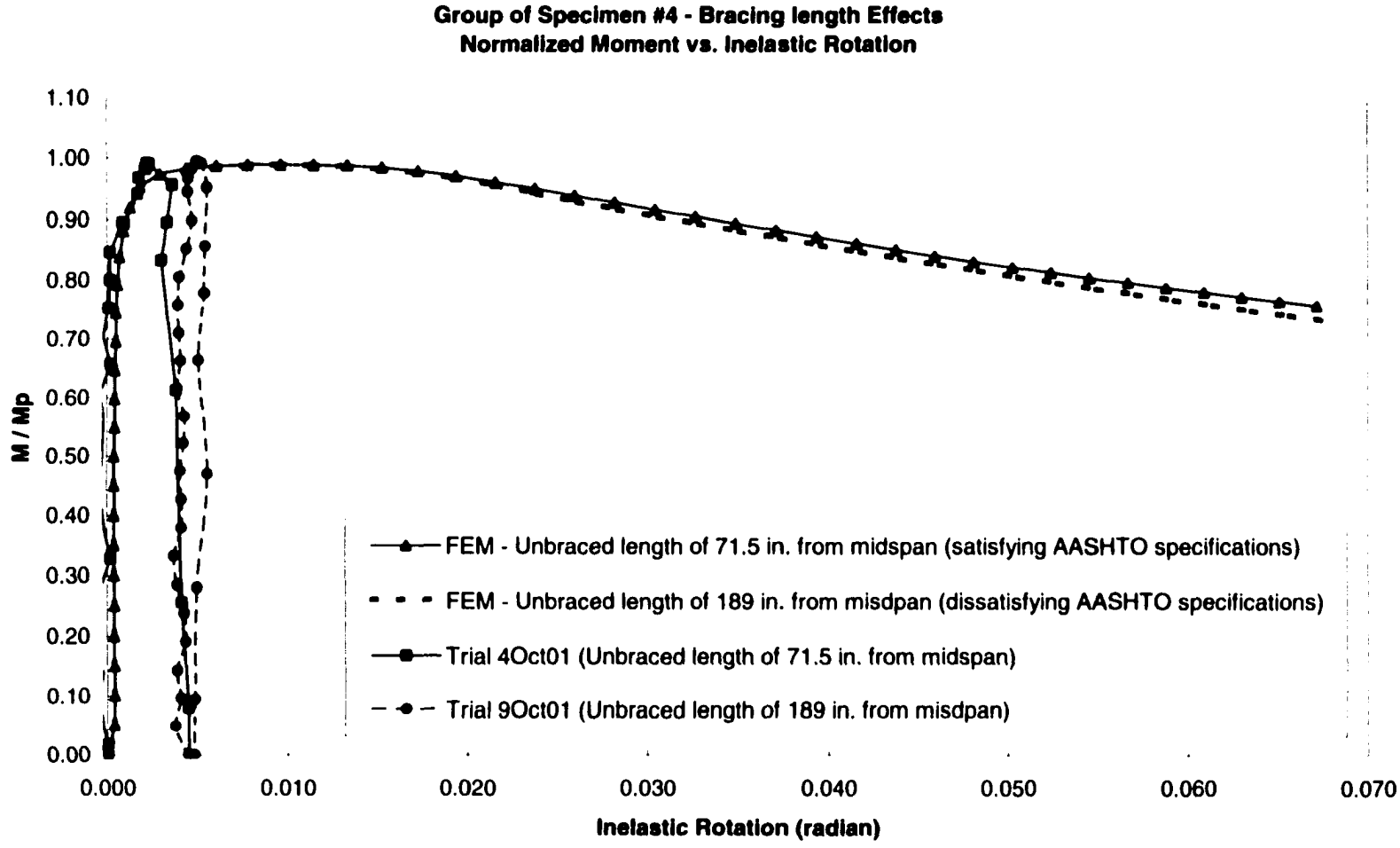

Figure 4.3.4 Experimental and numerical effects of bracing lengths on moment-inelastic rotation for Specimen #4

The corresponding numerical model of Specimen #4 was analyzed with two bracing configurations as experiments. As shown in Figures 4.3.3 and 4.3.4, the experimental lateral compression-flange bracing configurations had no effects on the ascending part and the plateau of the moment-rotation relationship for the noncompact girder Specimen #4. However, the numerical models displayed an insignificant effect of the studied unbraced lengths, only slightly on the decreasing part, on the inelastic moment-rotation relationship for Specimen #4.

4.4 Numerical Moment-Rotation Behaviors of FEM Models For Composite/Noncomposite HPS70W Girders

For each numerical run of composite girder analysis, the same ABAQUS post peak procedures, modified Rik's method for displacement-control, and nonlinear option are applied. For the I-shape steel portion, the same ABAQUS-S4R-shell elements are assigned across each flange and through the web, using the same material inputs (see Section 3.3.2) and accounting for initial imperfections and residual stresses (see Section 3.3.3) as for the noncomposite models. In addition, a tensile concrete deck (see Section 3.4.3) with steel rebars inside is appended to the tensile flange, using ABAQUS C3D8 solid (continuum) elements. At the interface of the concrete deck and the I-shape steel, continuum elements and shell elements will be assigned to have same nodes since AASHTO requires fully composite action if the composite action is used in bridge girders. Assuming all concrete cracks and fully plastic action of entire composite section, the equivalent transformed modulus of elasticity, E_{trans}, based on the pseudo-transformed area from steel rebars to concrete area with the pseudo-modular ratio,

$n = \frac{E_{rebars}}{E_{concrete}} \approx \frac{A_{concrete}}{A_{rebars}}$, is employed in ABAQUS runs to surpass the lack of compatibility of the numerical models when concrete deck cracks are large. Eventually, the pseudo-transformed area of the steel rebars, not the unknown modulus of elasticity of the cracked reinforced concrete deck, will contribute to the plastic moment in inelastic behavior.

First, Figures 4.4.1 presents the effects of composite/noncomposite on the moment-total rotation behavior of the FEM-models corresponding to Specimen #1 (nominal compact, nonsymmetric I-section). The ascending portion of the entire composite section (solid round marker) has steeper slope than those of the noncomposite sections since the composite section is stiffer as expected. Due to the strain hardening and section compactness, all FEM models provided peak moment exceeding the fictitious plastic moment, M_p, of the fictitious symmetric I-section (see Section 3.4.3). As expected, the noncomposite nonsymmetric-I model (blank diamond marker) that, as experiment, does not include the weight of concrete deck, and the composite fictitious-symmetric-I model (solid round marker) provided moment plateaus above that of the noncomposite fictitious-symmetric-I model including the weight of 1/3-scale concrete deck (triangle marker). Due to the fact that the composite model has more web in compression because of the neutral axis shifted closer to the tension flange, the post-plateau portion of the composite model descends faster with steeper slope than that of the noncomposite fictitious symmetric I-section.

Figure 4.4.2 presents the effects of composite/noncomposite on the moment-inelastic rotation behavior of the FEM-models corresponding to Specimen #1. Using average material tested data, all numerical moment-inelastic rotation relationships exceed

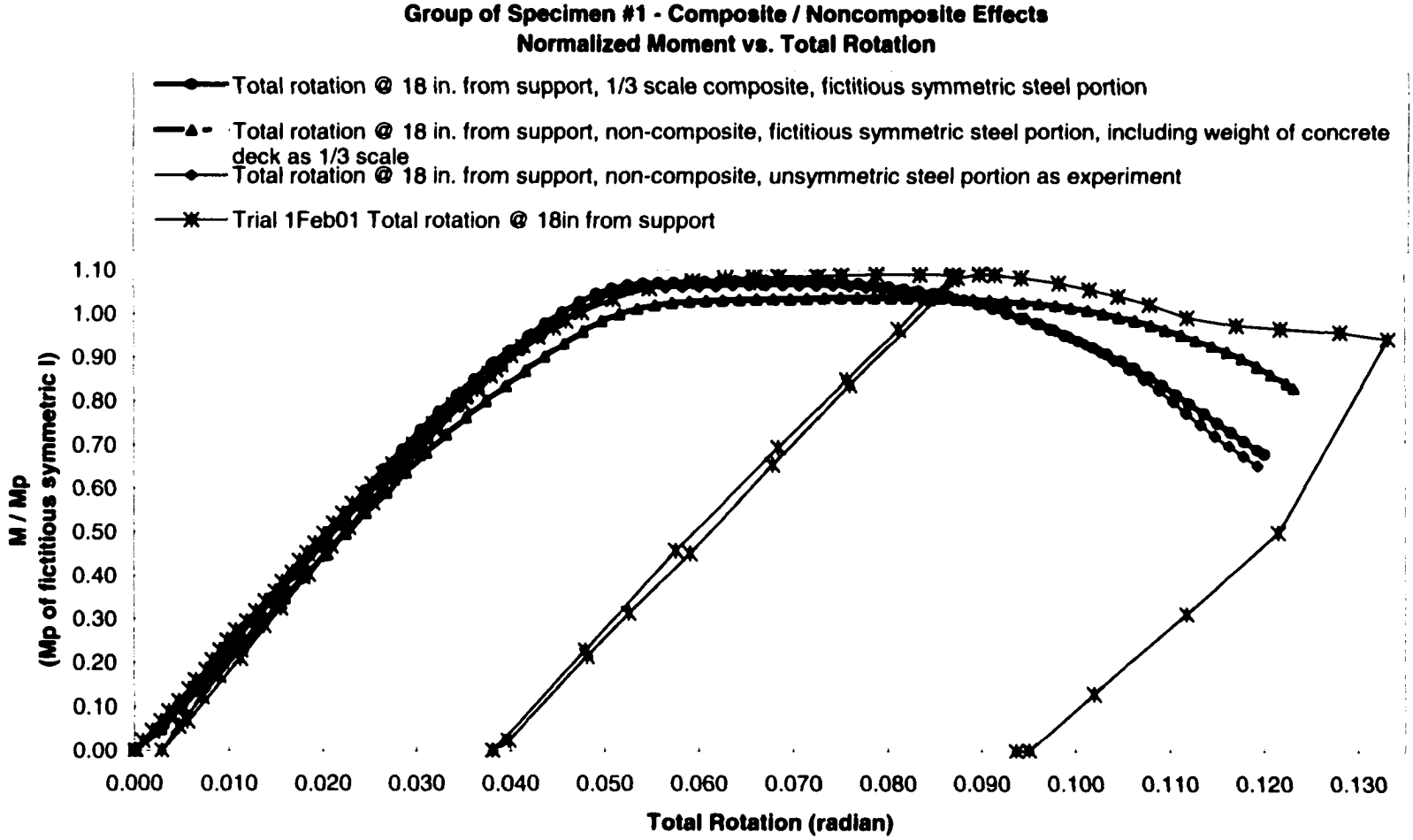

Figure 4.4.1 Composite/noncomposite moment-total rotation comparison for Specimen #1 (nominal compact, nonsymmetric I-section)

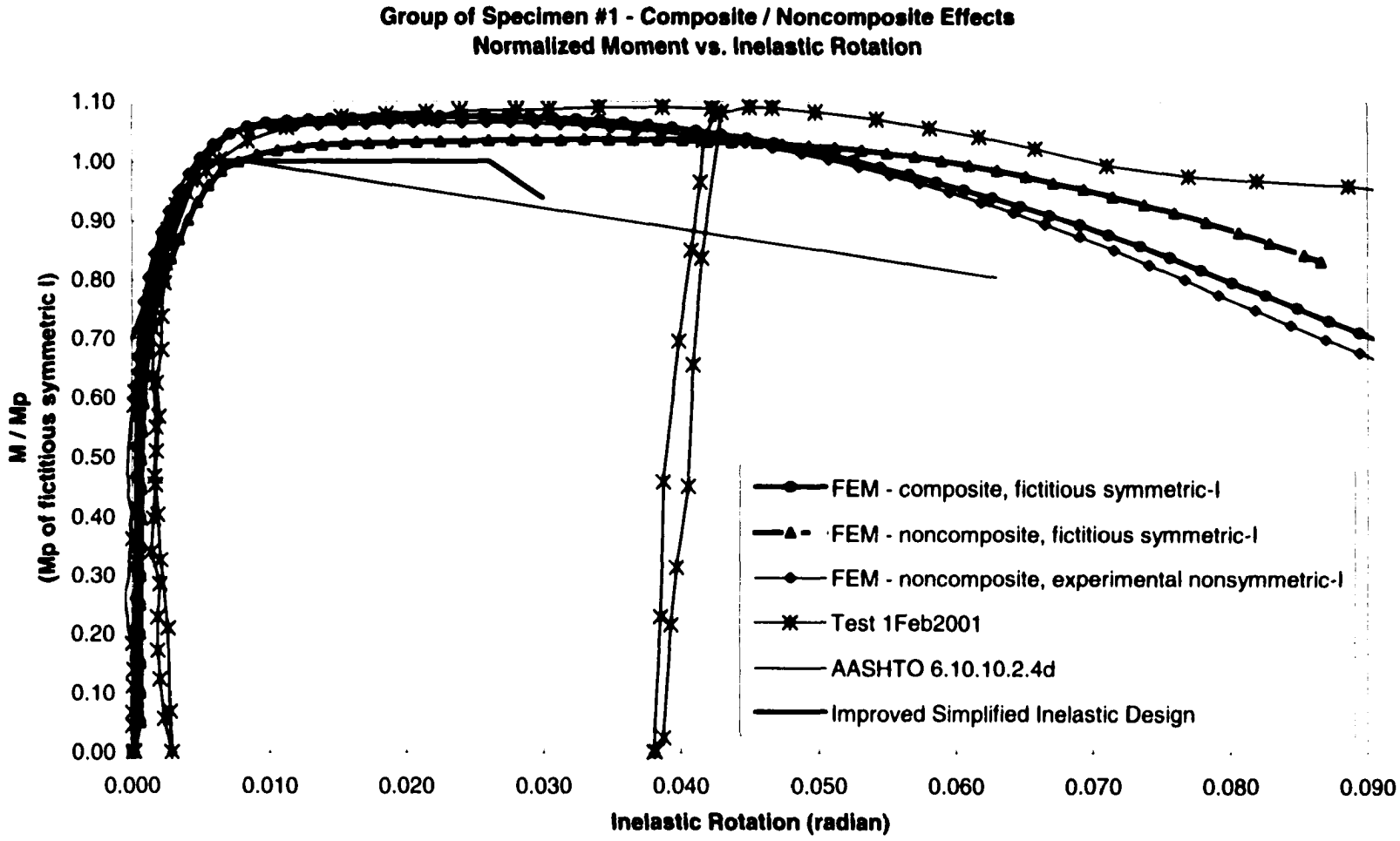

Figure 4.4.2 Composite/noncomposite moment-inelastic rotation comparison for Specimen #1 (nominal compact, nonsymmetric I-section)

the current AASHTO specifications (AASHTO, interim 2001) and the proposed improved simplified inelastic design predictions (Barth, Hartnagel, White, and Barker, 2001). In addition, the moment-inelastic rotation curves of the composite section and the noncomposite nonsymmetric-I model (as experiment) are almost coincident and above the curve of the noncomposite fictitious symmetric-I model (triangle marker) up to an inelastic rotation of 46 mrads. This value exceeds the maximum rotation of 30 mrads now thought necessary for redistribution of moments in bridges (Schilling, 1986; Barth, Hartnagel, White, and Barker, 2001). Hence, the composite model is more conservative than the noncomposite fictitious symmetric-I model is for the descending-portion behavior, and the noncomposite nonsymmetric experimental girder can be presumed sufficient to simulate the moment-inelastic rotation of composite section.

Second, similar effects of composite/noncomposite on the moment-total rotation behavior of the FEM-models corresponding to Specimens #2, (nominal compact, symmetric I-section) are presented in Figure 4.4.3. The ascending portion of the entire composite section has steepest slope since the composite section is stiffest as expected. Due to the strain hardening and section compactness, all FEM models provided peak moment exceeding the plastic moment, M_p, of the experimental symmetric I-section. In addition, the composite model (solid round marker) provided moment plateaus above that of the noncomposite models including the weight of 1/3-scale concrete deck (triangle marker) or not (blank diamond marker) as experiment. As expected, the post-plateau portion of the composite model descends faster with steeper slope since the composite model has more web in compression.

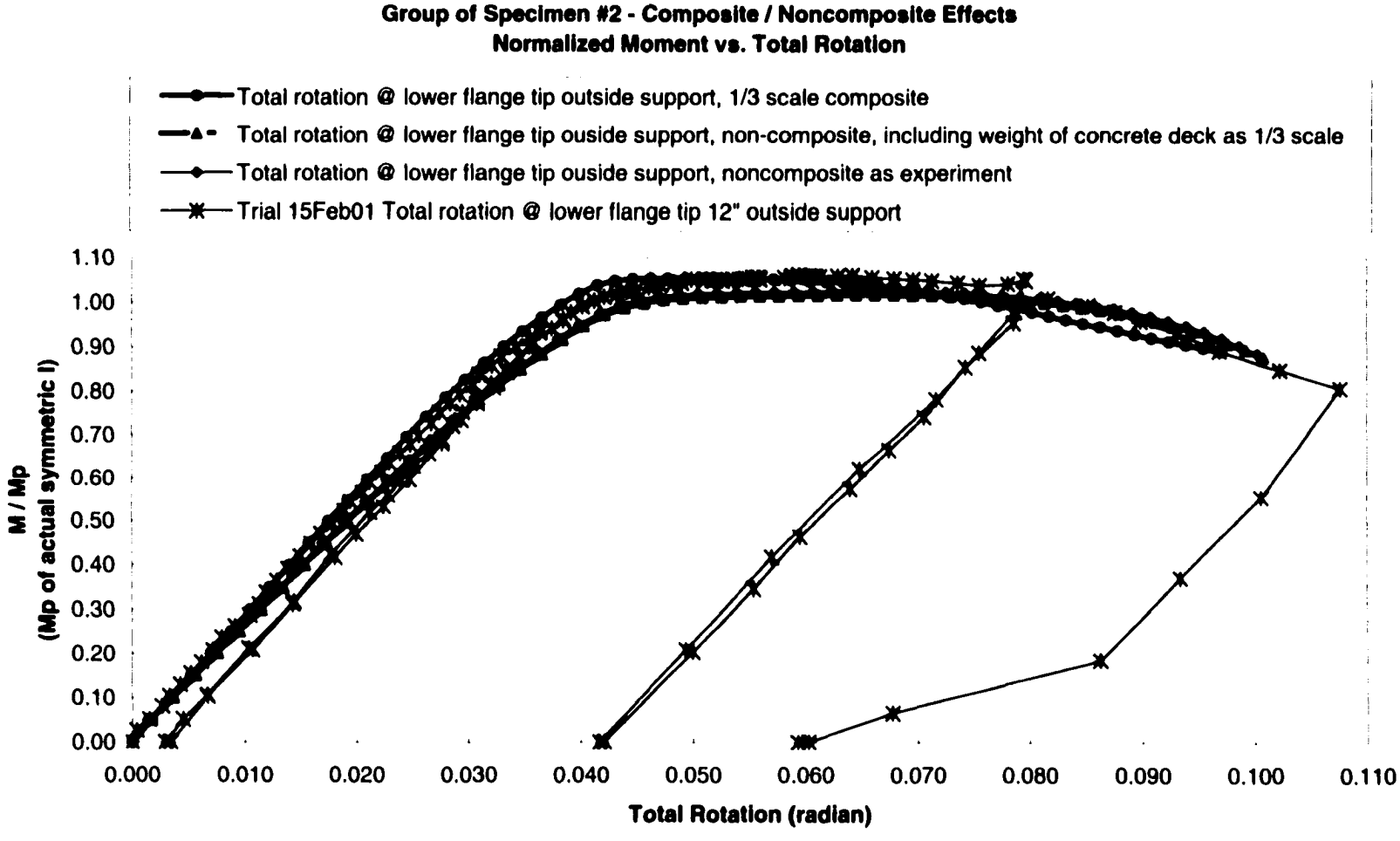

Figure 4.4.3 Composite/noncomposite moment-total rotation comparison for Specimen #2 (nominal compact, symmetric I-section)

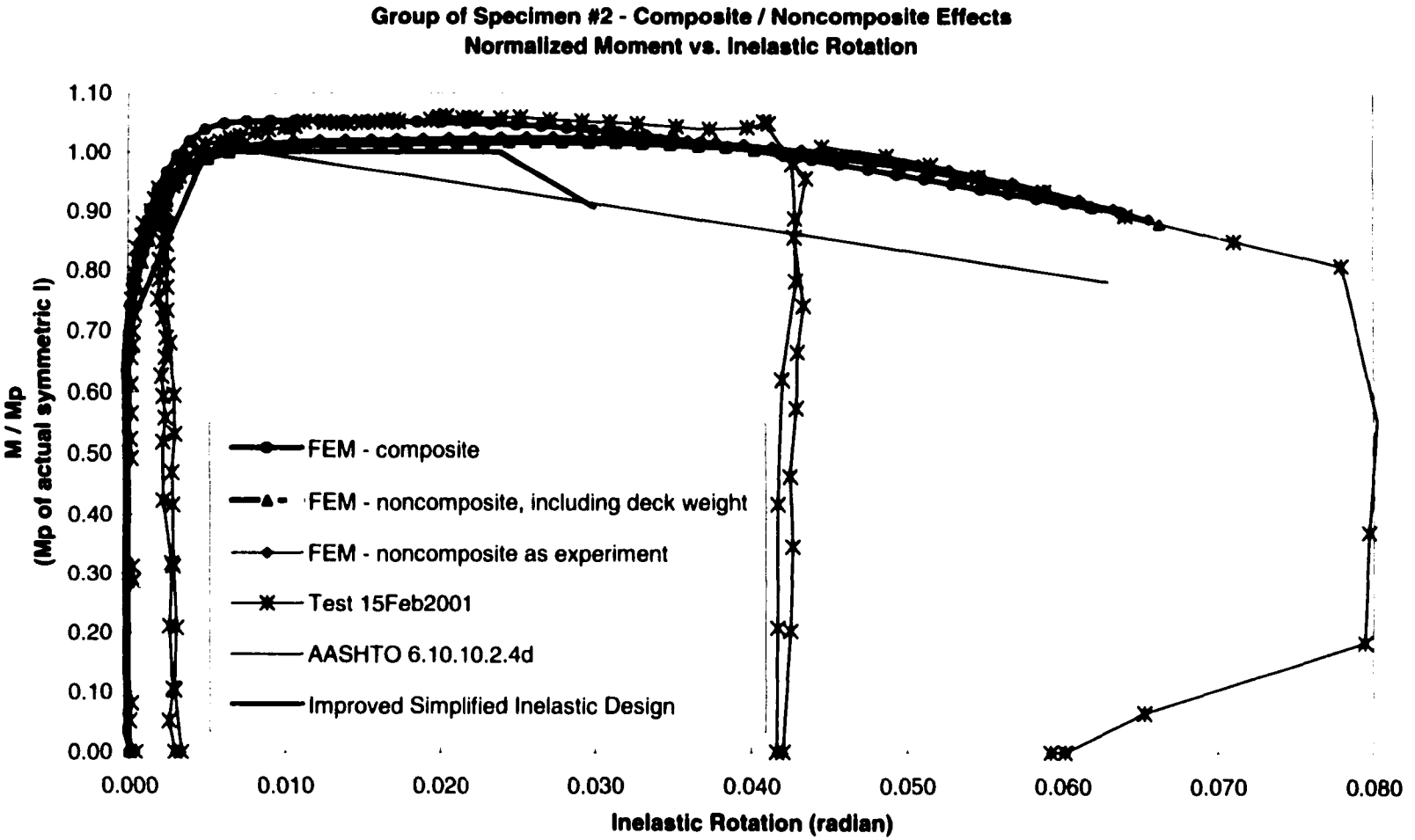

Figure 4.4.4 Composite/noncomposite moment-inelastic rotation comparison for Specimen #2 (nominal compact, symmetric I-section)

Figure 4.4.4 presents the effects of composite/noncomposite on the moment-inelastic rotation behavior of the FEM-models corresponding to Specimen #2. Using average material tested data, all numerical inelastic moment-rotation relationships exceed the current AASHTO specifications (AASHTO, interim 2001) and the proposed improved simplified inelastic design predictions (Barth, Hartnagel, White, and Barker, 2001). Additionally, the moment resistance of the composite section exceeds those of the noncomposite models, one as experiment and one including the deck weight, up to an inelastic rotation of 37 mrads that is greater than the critical value of 30 mrads (Schilling, 1986; Barth, Hartnagel, White, and Barker, 2001). As expected, the composite model is more conservative for the descending-portion behavior of the compact girder.

Third, the effects of composite/noncomposite on the moment-total rotation and moment-inelastic rotation behavior of the FEM-models corresponding to the noncompact girders, Specimens #3 and #4, are presented in Figures 4.4.5, 4.4.6, 4.4.7, and 4.4.8, respectively. The ascending portion of the entire composite section has steepest slope since the composite section is stiffest as expected. Although the composite noncompact model (solid round marker) can reach the plastic moment, M_p, the noncomposite noncompact section that includes the weight of 1/3-scale concrete deck (triangle marker) cannot because the sections are noncompact. Using average material tested data in Section 3.3.2, the composite noncompact models satisfy both the current AASHTO specifications and the proposed improved simplified inelastic design predictions. However, the noncomposite noncompact sections that include the deck weight (triangle marker) corresponding to Specimens #3 and #4 satisfy the proposed improved simplified inelastic design predictions but not the current AASHTO specifications.

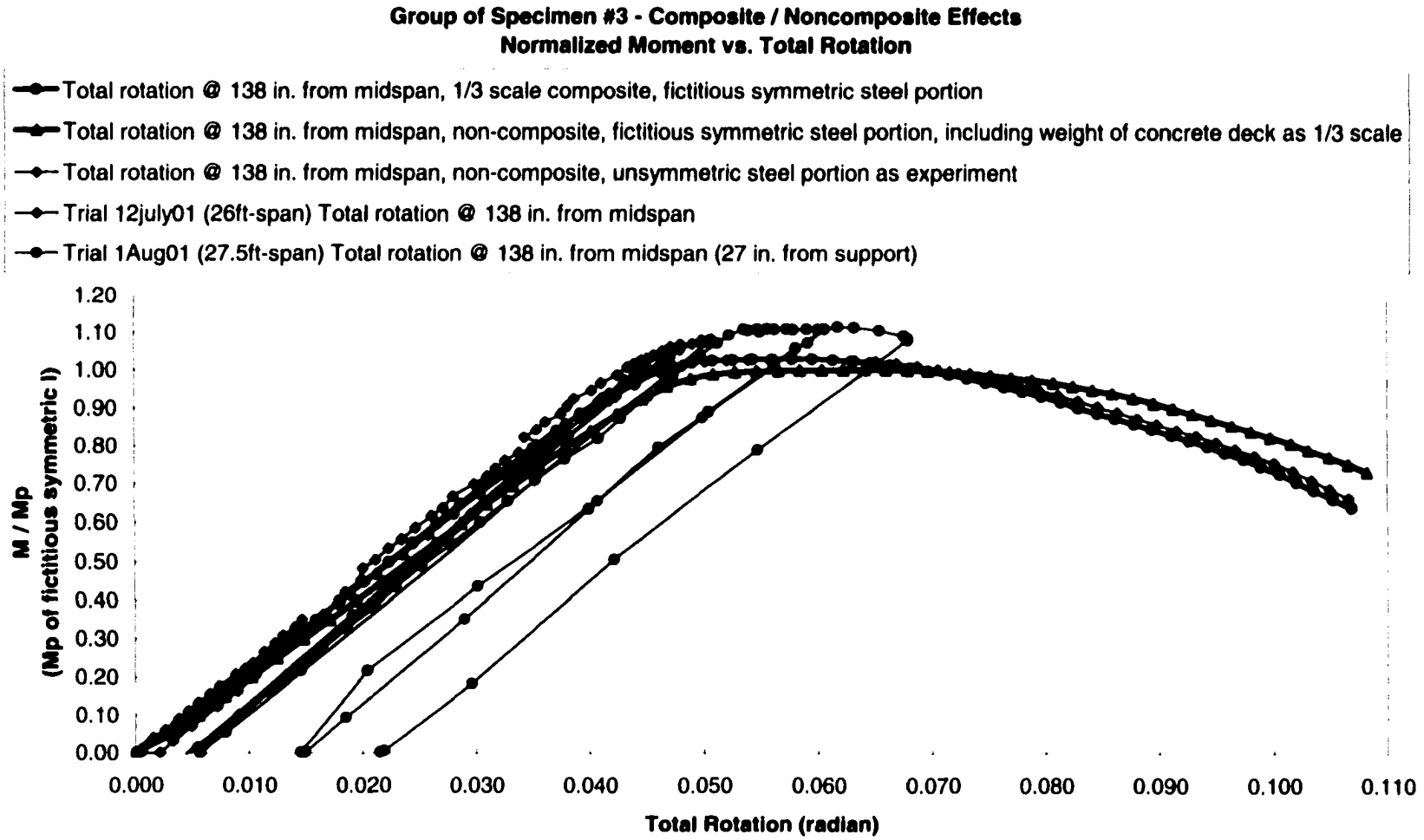

Figure 4.4.5 Composite/noncomposite moment-total rotation comparison for Specimen #3 (noncompact, nonsymmetric I-section)

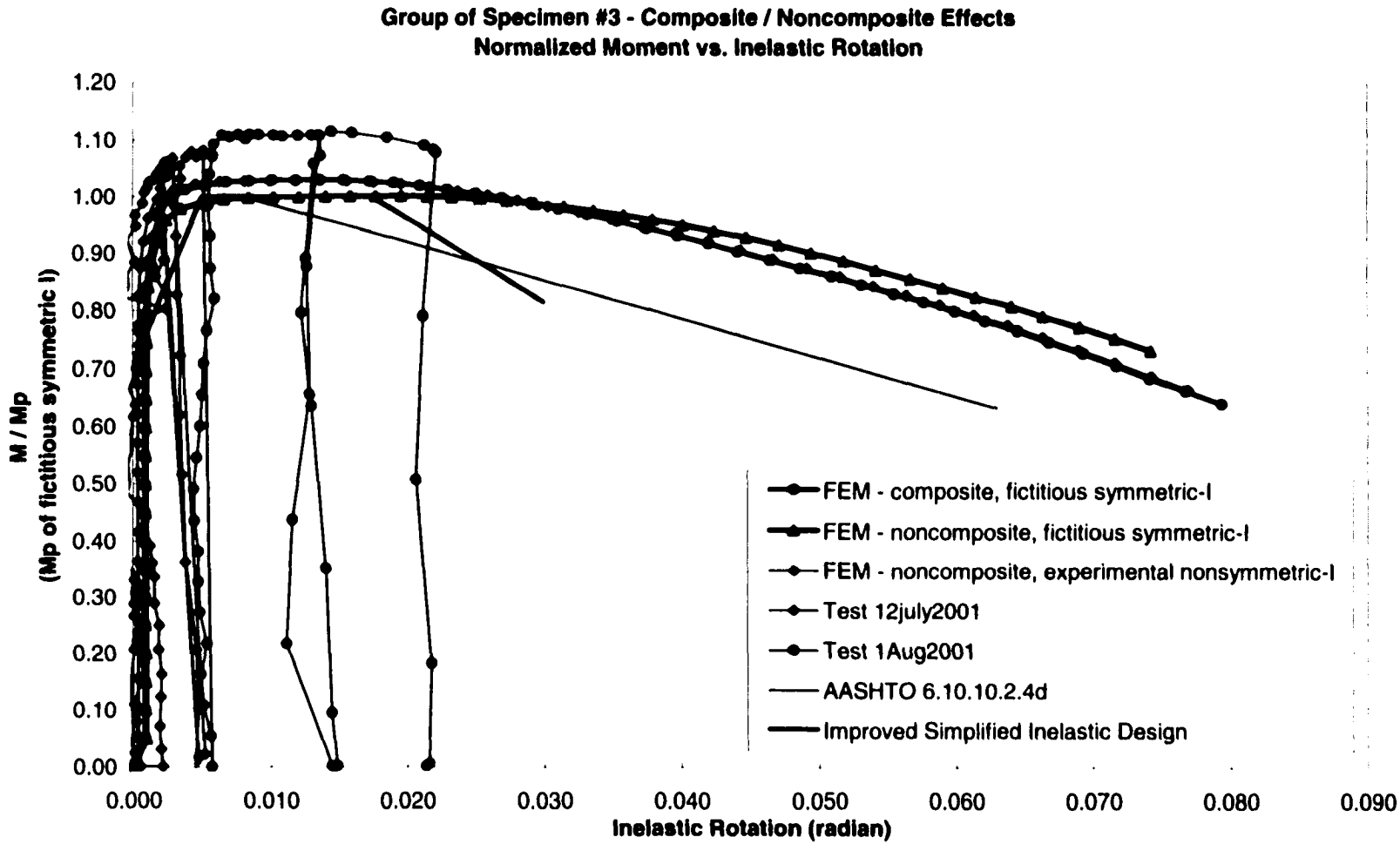

Figure 4.4.6 Composite/noncomposite moment-inelastic rotation comparison for Specimen #3 (noncompact, nonsymmetric I-section)

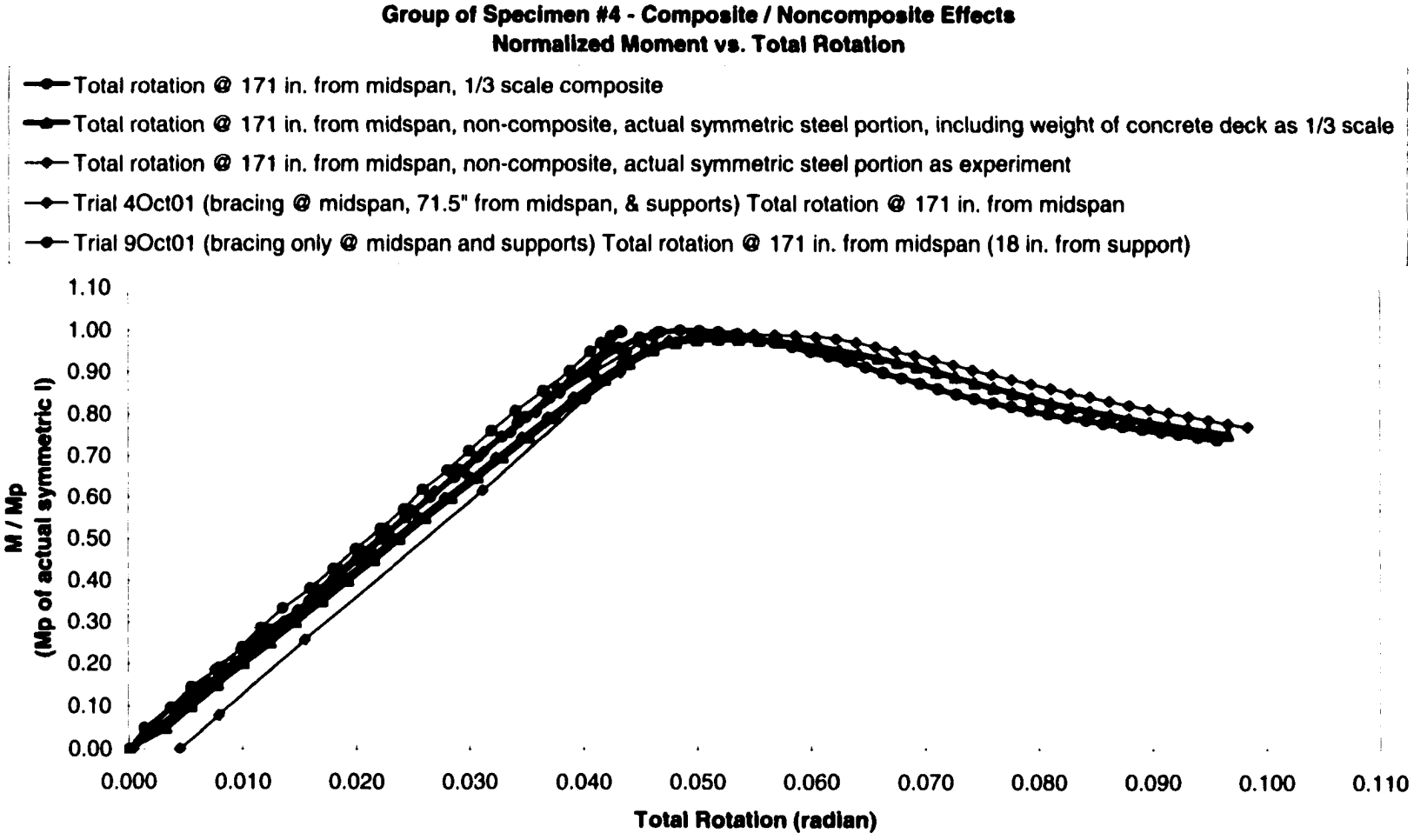

Figure 4.4.7 Composite/noncomposite moment-total rotation comparison for Specimen #4 (noncompact, symmetric I-section)

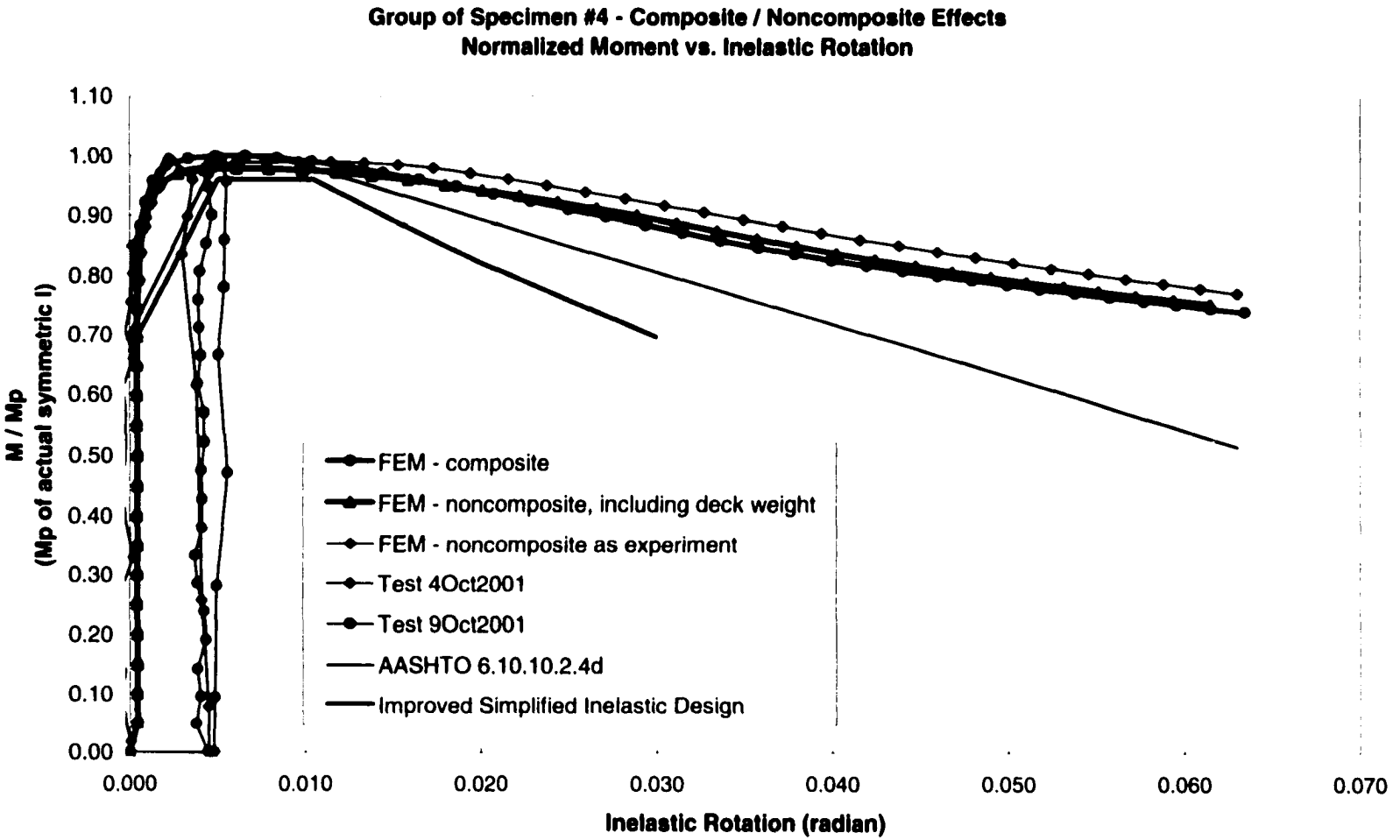

Figure 4.4.8 Composite/noncomposite moment-inelastic rotation comparison for Specimen #4 (noncompact, symmetric I-section)

Moreover, the moment-inelastic rotation curves of the composite section and the noncomposite nonsymmetric-I model for Specimen #3 are almost coincident and above the curve of the noncomposite fictitious symmetric-I model (triangle marker) up to an inelastic rotation of 31 mrads, which barely exceeds the critical value of 30 mrads (Schilling, 1986; Barth, Hartnagel, White, and Barker, 2001). Hence, the composite model is more conservative than the noncomposite fictitious symmetric-I model is for the descending-portion behavior, and the noncomposite nonsymmetric experimental girder can be presumed sufficient to simulate the moment-inelastic rotation of composite section.

Finally, the moment resistance of the composite section corresponding to Specimen #4 exceeds those of the noncomposite models, one as experiment and one including the deck weight, up to an inelastic rotation of 11 and 16 mrads, respectively. These values exceed the suggested plastic rotation at the onset of unloading, θ_{RL}, (Barth, Hartnagel, White, and Barker, 2001) that is calculated as 10 mrads for this noncompact section using average material tested data (see Section 3.3.2). As expected, the composite model is more conservative for the descending-portion behavior of the noncompact girder.

CHAPTER 5

SUMMARY AND CONCLUSION

5.1 Introduction

Inelastic analysis and design offers the potential for significant cost savings since it accounts for the reserve strength inherent in continuous-span steel girder bridges. Inelastic procedures allow for the yielding of entire steel cross sections to occur at the interior supports and permit moment-redistribution from negative pier moments to positive moment regions. Since the moment-redistribution causes slight inelastic rotation at the pier regions, small permanent deflection, and some residual moments, the bridge is still serviceable. After an initial overload, deformations stabilize, the structure achieves shakedown, and future loads will be resisted elastically.

A project to study the pier moment-rotation behavior of compact and noncompact high performance steel HPS70W I-girders was conducted at Colorado State University in the context of examining two restrictions for inelastic design of steel bridge girders in the current edition of the AASHTO LRFD bridge code (AASHTO interim 2001). The first restriction is that inelastic design involving the moment-rotation relationship of steel girders with a yield strength exceeding 50 ksi is prohibited. Though, bridge designers are currently allowed to go to plastic moment for I-girders having a yield strength of 70 ksi. The second restriction is that the AASHTO LRFD inelastic design methods cannot be

used on girders that do not meet the compactness requirements stated in the provisions. To determine whether or not these restrictions should be modified, examination of the pier moment-rotation behavior of HPS70W I-shape girders was undertaken through experimental testing and numerical modeling. Large-scale laboratory experiments were performed for noncomposite girders. Finite element models of the tested specimens were then analyzed based on the material inputs obtained from experimental examination of the stress-strain relationships for HPS70W. The inelastic moment-rotation behavior of HPS70W girders was determined both experimentally and numerically.

In addition, the inelastic pier moment-rotation post peak behaviors for noncomposite and composite I-girder sections are generally thought to be nearly the same. To be simplified and unified, a current focus is to have only one procedure that encompasses compact and noncompact cross-sectional girders as well as composite and noncomposite cross-sectional girders. In this study, from the noncomposite numerical models that were validated by experiment, finite element models were developed for composite girders and were examined.

5.2 Pier Moment-Rotation Behavior of HPS70W I-Girders

The pier moment-rotation behavior of HPS70W I-shape girders were synthetically developed from the response of specimens classified in compact/noncompact and composite/noncomposite categories. For the CSU "nominal compact/noncompact" noncomposite HPS70W girders, the experimental results obtained from girder testing and the numerical outcomes acquired from ABAQUS analyses are very close and verify each other. For each of the four CSU's HPS70W girders, the comparisons with AASHTO

specifications (AASHTO, interim 2001) consist of a division for "nominal compact/noncompact", in which the nominal yield stress, F_y = 70 ksi, is applied and another portion for "actual noncompact" (see Section 3.2), in which average tested yield strengths, F_{yw} = 69.83 ksi for the web and F_{yf} = 83.35 ksi for the flanges, are utilized in the predicted equations.

In addition, a number of experimental curves and numerical moment-total rotation and moment-inelastic rotation relationships at different locations were compared. At different locations near the supports, the moment-inelastic rotation relationships are numerically almost identical although the moment-total rotation relationships are different.

5.2.1 Effect of compact/noncompact steel section

For both compact girders, Specimen #1 and Specimen #2, the experimental and numerical results of inelastic moment-rotation relationship exceed the current AASHTO specifications and the proposed improved simplified inelastic design predictions (Barth, Hartnagel, White, and Barker, 2001), nominally and actually. Their moment-rotation responses actually developed a moment resistance greater than their plastic moment capacities until their inelastic rotations approximately reached 40 mrads and 44 mrads, respectively. These values are much greater than the maximum rotation of 30 mrads now thought necessary for redistribution of moments in bridges (Schilling, 1986).

For both noncompact specimens, Specimens #3 and #4, the experimental and numerical results of inelastic moment-rotation relationship nominally exceed the current AASHTO specifications and the proposed improved simplified inelastic design

predictions. Actually, the experimental inelastic moment-rotation curves for both specimens still exceed plastic moments, M_p. However, both numerical inelastic moment-rotation curves of the noncompact specimens do not reach the plastic moment, M_p, although they actually exceed the design moment, M_n, and the effective moment, $M_{pe(30)}$, predicted by the proposed improved simplified inelastic design.

5.2.2 Effect of bracing length

The effects of lateral bracing lengths on pier moment-rotation behavior of CSU's HPS70W I-shape noncompact girders, Specimen #3 and Specimen #4, were studied from the response of the specimens with lateral compression-flange bracing classified in categories of satisfying or dissatisfying the AASHTO requirements (AASHTO, interim 2001). Specimen #3 with lateral compression-flange bracing satisfying AASHTO specifications experimentally presented the potential to exceed and maintain the plastic moment, M_p, of a noncompact girder. In addition, the numerical models showed an insignificant effect of the studied unbraced lengths, slightly affecting the plateau and the decreasing part, on the inelastic moment-rotation relationship for Specimen #3.

The corresponding numerical model of Specimen #4 was analyzed with two bracing configurations as experiments. The experimental lateral compression-flange bracing configurations had no effects on the ascending part and the plateau of the moment-rotation relationship for the noncompact girder Specimen #4. However, the numerical models displayed an insignificant effect of the studied unbraced lengths, slightly affecting the decreasing part, on the inelastic moment-rotation relationship for Specimen #4.

5.2.3 Effect of composite section

For each numerical run of composite girder analysis, the same ABAQUS post peak procedures, modified Rik's method for displacement-control, and nonlinear option are applied as for noncomposite girders. In addition to the I-shape steel portion, a tensile concrete deck with steel rebars inside is appended to the tensile flange. Assuming all concrete cracks and fully plastic action of entire composite section, the equivalent transformed modulus of elasticity based on the pseudo-transformed area from steel rebars to concrete area with the pseudo-modular ratio (see Section 3.4.2) is employed in ABAQUS runs to surpass the lack of compatibility of the numerical models when concrete deck cracks are large. Eventually, the pseudo-transformed area of the steel rebars, not the unknown modulus of elasticity of the cracked reinforced concrete deck, will contribute to the plastic moment in inelastic behavior.

5.2.3.1 Effects on the moment-total rotation behavior

For the FEM-models corresponding to the compact/noncompact girders, the ascending portion of the entire composite section has steeper slope than those of the noncomposite sections since the composite section is stiffer as expected. For the compact girders, all FEM models provided peak moment exceeding the corresponding plastic moment, M_p, due to the strain hardening and section compactness. For the noncompact girders, although the composite model can reach the plastic moment, M_p, the noncomposite section that includes the weight of 1/3-scale concrete deck cannot because the sections are noncompact. Using average material tested data, the composite noncompact models satisfy both the current AASHTO specifications (AASHTO, 1998

and interim 2001) and the proposed improved simplified inelastic design predictions (Barth, Hartnagel, White, and Barker, 2001). However, the noncomposite noncompact sections that include the deck weight satisfy the proposed improved simplified inelastic design predictions but not the current AASHTO specifications. As expected for all compact/noncompact girders, the post-plateau portion of the composite model descends faster with steeper slope due to the fact that the composite model has more web in compression because of the neutral axis shifted closer to the tension flange.

5.2.3.2 Effects on the moment-inelastic rotation behavior

Using average material tested data, all numerical moment-inelastic rotation relationships corresponding to Specimen #1 (nominal compact, nonsymmetric I-section) exceed the current AASHTO specifications and the proposed improved simplified inelastic design predictions. In addition, the moment-inelastic rotation curves of the composite section and the noncomposite nonsymmetric-I model (as experiment) are almost coincident and above the curve of the noncomposite fictitious symmetric-I model up to an inelastic rotation of 46 mrads. This value exceeds the maximum rotation of 30 mrads now thought necessary for redistribution of moments in bridges (Schilling, 1986; Barth, Hartnagel, White, and Barker, 2001). Hence, the composite model is more conservative than the noncomposite fictitious symmetric-I model is for the descending-portion behavior, and the noncomposite nonsymmetric experimental girder can be presumed sufficient to simulate the moment-inelastic rotation of composite section.

Using average material tested data, all numerical inelastic moment-rotation relationships corresponding to Specimen #2 (nominal compact, symmetric I-section)

exceed the current AASHTO specifications and the proposed improved simplified inelastic design predictions. Additionally, the moment resistance of the composite section exceeds those of the noncomposite models, one as experiment and one including the deck weight, up to an inelastic rotation of 37 mrads that is greater the critical value of 30 mrads. As expected, the composite model is more conservative for the descending-portion behavior of the compact girder.

Corresponding to Specimen #3 (noncompact, nonsymmetric I-section), the moment-inelastic rotation curves of the composite section and the noncomposite nonsymmetric-I model (as experiment) are almost coincident and above the curve of the noncomposite fictitious symmetric-I model up to an inelastic rotation of 31 mrads, which barely exceeds the critical value of 30 mrads. Hence, the composite model is more conservative than the noncomposite fictitious symmetric-I model is for the descending-portion behavior, and the noncomposite nonsymmetric experimental girder can be presumed sufficient to simulate the moment-inelastic rotation of composite section.

Corresponding to Specimen #4 (noncompact, symmetric I-section), the moment resistance of the composite section exceeds those of the noncomposite models, one as experiment and one including the deck weight, up to an inelastic rotation of 11 and 16 mrads, respectively. These values exceed the suggested plastic rotation at the onset of unloading, θ_{RL}, (Barth, Hartnagel, White, and Barker, 2001) that is calculated as 10 mrads for this noncompact section using average material tested data. As expected, the composite model is more conservative for the descending-portion behavior of the noncompact girder.

5.2.4 Effect of initial residual stress and initial geometric imperfection

The effects of initial residual stresses and imperfections on the numerical outcomes are in agreement with previous studies of Yakel, Mans, and Azizinamini, 1999 and Zubeck, 2000. The effect of residual stresses in the moment-rotation diagram was "rounding off" the curve as the girder yields even though the magnitude of residual stresses has no effect on the ultimate moment capacity. In addition, what type or how much imperfection introduced into the model does not influence the results significantly, and thus one does not have to exactly recreate the imperfections found in the real girder. As expected, more imperfection introduced into the model makes the post-plateau portion of the moment-rotation curve to descend with steeper slopes although the influence was not significant.

In this research, the residual stresses are introduced as a constant value over each element. The piecewise-negative residual stress is applied as recommended by Yakel, Mans, and Azizinamini, 1999 and Zubeck, 2000 for the flanges and web. On the other hand, the maximum-positive residual stress is modified for going from ramp distribution to block distribution. Additionally, the piecewise residual stress distributions for the flange and the web were also adjusted to account for the tendency of a deeper web that has lower residual stresses at the web-flange junction. Furthermore, if the maximum residual stress of +16.5 ksi for welded shape (AISC, 1998) is applied, the entire distribution over web and flanges will be proportioned from the applied maximum value to the corresponding peak of +16.5 ksi.

The imperfection input for numerical analyses was modeled similarly to the study of Yakel, Mans, and Azizinamini, 1999, in which the resulting first-eigenvector from the

buckling analysis was scaled down such that the maximum displacement was 0.1 inch, and these scaled displacements were superimposed on the original geometry thus generating a distorted mesh. In this research, an arbitrary combination of eigenvectors, which are weighted descending from the first-eigenvector down to the fourth (Hibbitt, Karlsson & Sorensen, Inc., 1999), was scaled down such that the maximum combined displacement is from 0.1 to 0.2 inch and then applied as an initial imperfection.

5.3 Contribution of the Research

This study extends the knowledge base on inelastic moment-rotation behavior of high performance steel HPS70W compact and noncompact I-girders. Such behavior is restricted by current AASHTO specifications (AASHTO, 1998 and interim 2001). The results of this dissertation can be utilized to develop new design provisions, which in turn, can be employed to produce a more consistent, reliable, and economical bridge inventory.

The experimental and numerical responses agree well and thus validate the numerical model. These results also show that compact/noncompact and composite/noncomposite HPS70W I-girders have the strength and ductility suitable for the application of inelastic analysis and design. For the "nominal compact – actual noncompact" HPS girders (Specimen #1 and Specimen #2), the fact that material failure occurs before geometric failure is also demonstrated. In addition, the effects of the spacing arrangements of the lateral braces were studied for noncompact girders. Spacing arrangements were examined that both did and did not satisfy the AASHTO specifications. The results of the experiments on the lateral compression-flange bracing

configurations demonstrate that it is possible to reach the plastic moment, M_p, of the noncompact girder. Furthermore, the need for a unified procedure that encompasses compact and noncompact girders as well as composite and noncomposite girders is evident because some states allow composite construction over the interior support regions while others do not. The numerical results confirm that pier moment-rotation behavior is similar for composite and noncomposite cross sections.

5.4 Summary

This research provides experimental and numerical evidence of the pier moment-rotation behavior of compact and noncompact I-shape HPS70W bridge girders. Since HPS70W girders have adequate strength and ductility for inelastic design, it is suggested that the two restrictions for inelastic design of steel bridge girders in the current AASHTO LRFD bridge code (AASHTO, 1998 and interim 2001) should not apply for such girders. The results of the study also conclude that proposed improved simplified inelastic design (ISID) procedures (Barth, Hartnagel, White, and Barker, 2001) are suitable for high performance steel HPS70W compact and noncompact I-girders.

Nonetheless, this dissertation work is not intended to be a determining factor in the development of inelastic bridge design procedures. The results herein are intended to be an objective blind test for the ISID procedures. It is understood that the conclusions herein are based on a limited number of large-scale experiments and numerical models. Future work in large-scale testing on composite HPS70W I-girders is recommended in order to validate the finite element approach for application to the pier moment-rotation behavior of composite sections.

REFERENCES

American Association of State Highway Transportation Officials (1998 and interims 1999, 2000, & 2001). AASHTO LRFD Bridge Design Specifications, 2nd Edition.

American Institute of Steel Construction (1998). AISC Load & Resistance Factor Design, 2nd Edition.

American Society of Civil Engineers (1971). Plastic Design in Steel – A Guide and Commentary, ASCE Manuals and Report on Engineering Practice No. 41, 2nd Edition.

ASCE-AASHO (1968). "Design of Hybrid Steel Beams," by the Joint ASCE - AASHO (predecessor to AASHTO) Subcommittee on Hybrid Beams and Girders, C. G. Schilling, Chmn., Journal of the Structural Division, ASCE, Vol. 94, No. ST6, June.

Ansourian, P. (1982). "Plastic Rotation of Composite Beams." Journal of the Structural Division, ASCE, Vol. 108, No. ST3, March.

Barker, Michael G. (June 1990). The Shakedown Limit State of Slab-on-Girder Bridges, Ph.D. dissertation, University of Minnesota, Minneapolis, MN.

Barker, M. G., Galambos, T. V. (1992). "Shakedown Limit State of Compact Steel Girder Bridges," Journal of Structural Engineering, ASCE, Vol. 118, No. 4, April.

Barker, Michael G. (1995). "Inelastic Design of Steel Girder Bridges," Engineering Journal, AISC, Vol. 32, No. 1, First Quarter.

Barker, Michael G., Hartnagel, Bryan A., Schilling, Charles G., Dishongh, Burl E. (April 1997). Inelastic Design and Experimental Testing of Compact and Noncompact Steel Girder Bridges, Final Report No. 93-1 to Missouri Department of Transportation, Federal Highway Administration, University of Missouri-Columbia.

Barker, M. G., Hartnagel, B. A., Schilling, C. G., and Dishongh, B. E. (2000). "Simplified Inelastic Design of Steel Girder Bridges." Journal of Bridge Engineering, ASCE, 5(1), 58-66.

Barth, Karl E., White, Donald W. (1998). "Finite Element Evaluation of Pier Moment-Rotation Characteristics in Continuous-span Steel I Girders," Engineering Structures, 20(8) 761-788.

Barth, K. E., White, D. W., and Bobb, B. M. (2000). "Negative Bending Resistance of HPS70W Girders." Journal of Construction Steel Research, Elsevier, 53(1), 1-31.

Barth, Karl E., Hartnagel, Bryan A., White, Donald W., Barker, Michael G. (December 2001). "Improved Simplified Inelastic Design of Steel I Girder Bridges." Journal of Bridge Engineering, ASCE, under review.

Beedle, L. S. (1958). Plastic Design of Steel Frames, John Wiley and Sons, New York, NY.

Bethlehem Lukens Plate, Inc. (1999). High Performance Steels for Bridges: HPS70W - A Technical Overview, 008-HPS-70W Brochure.

Budynas, Richard G. (1999). Advanced Strength and Applied Stress Analysis, 2nd Edition.

Carskaddan, P.S. (1991). Concrete Cracking in the Autostress Method, Memo, AISC Marketing, Pittsburgh, PA, Oct.2.

Dally, James W., Rilley, William F. (1991). Experimental Stress Analysis, 3rd Edition.

Dishongh, B. E. (Jan. 1990). Residual Damage Analysis: A Method for the Inelastic Rating of Steel Girder Bridges, Ph.D. dissertation, University of Minnesota, Minneapolis, MN.

Dishongh, B. E. (Nov. 1992). Residual Deformation Analysis for Bridges, Louisiana Department of Transportation and Development, Baton Rouge, LA.

Dishongh, B. E., Galambos, T. V. (1992). "Residual Deflection Analysis for Inelastic Bridge Rating," Journal of Structural Engineering, ASCE, Vol. 118, No. 6, June.

Eyre, D. G., Galambos, T. V. (1969). Variable Repeated Loading – A Literature Survey, Bulletin No. 142, Welding Research Council, July.

Eyre, D. G., Galambos, T. V. (1970). "Shakedown Tests on Steel Bars and Beams," Journal of the Structural Division, ASCE, Vol. 96, No. ST7, July.

Eyre, D. G., Galambos, T. V. (1973). "Shakedown of Grids," Journal of the Structural Division, ASCE, Vol. 99, No. ST10, Oct.

Fahnestock, Larry A., Sause, Richard (May 1998). Flexural Strength and Ductility of HPS100W Steel I-girders, ATLSS Report No. 98-05, Lehigh University, Bethlehem, PA.

Frost, R. W., Schilling, C. G. (1964). "Behavior of Hybrid Beams Subjected to Static Loads," Journal of the Structural Division, ASCE, Vol. 90, No. ST3, June.

Fukumoto, Y., Yoshida, H. (1969). "Deflection Stability of Beams Under Repeated Loads," Journal of the Structural Division, ASCE, Vol. 95, No. ST7, July.

Galambos, T. V., et al., (1993). Inelastic Rating Procedures for Steel Beam and Girder Bridges, National Cooperative Highway Research Program, NCHRP Report 352.

Griffeth, Michael (March 2001). Experimental Moment-Rotation Tests of HPS70W Steel Girders, Master of Science Thesis, Colorado State University.

Grubb, M.A. (1985). Design Example: A Two-Span Continuous Highway Bridge Designed by the Autostress Method, Report on Project 188, AISI, May 10.

Grundy, P., (1976). "Bridge Design Criteria," Nov. 25 to 26, 1976, Australian Metal Structures Conference held in Adelaide, Australia.

Grundy, P., (1983). "The Application of Shakedown Theory to the Design of Steel Structures," Instability and Plastic Collapse of Steel Structures, L. J. Morris (Edition), Granada Publishing, London, UK.

Gurley, C. R. (1981). "Plastic Design of Two-Way Structures and Elements," Journal of Constructional Steel Research, Vol. 1, No. 3, May.

Gurley, C. R. (1982). "Plastic Analysis of Advanced Grillage and Plate Problems with Nodal Forces," Journal of Constructional Steel Research, Vol. 2, No. 1, Jan.

Haaijer G., Carskaddan, P.S. (1970). "Autostress Design of Continuous Steel Bridge Members," Proceedings of the Canadian Structural Engineering Conference, held at Montreal, Canada.

Haaijer, G. (1993). Objectives and Early Research of Autostress Design, Transportation Research Record 1380, Transportation Research Board.

Haaijer G., Carskaddan, P.S., Grubb, M.A. (1987). Suggested Autostress Procedures for Load Factor Design of Steel Beam Bridges, Bulletin No. 29, AISC, April.

Hartnagel, Bryan A. (August 1997). Inelastic Design and Experimental Testing of Compact and Noncompact Steel Girder Bridges, Ph.D. dissertation, University of Missouri-Columbia.

Hartnagel, Bryan A. and Barker, Michael G. (2000). "Inelastic Design and Testing of Steel Bridges Comprising Noncompact Sections." AISC Engrg. J., 37(1), 3-12.

Hewlett Packard, Inc. (June 1986). HP 3852A Data Acquisition/Control Unit - Strain Gage Accessory Configuration and Programming Manual.

Hewlett Packard, Inc. (June 1986). HP 3852A Data Acquisition/Control Unit – Main Frame Accessory Configuration and Programming Manual.

Hewlett Packard, Inc. (February 1987). HP 3852A Data Acquisition/Control Unit – Getting Started Guide, 1st Edition.

Hibbitt, Karlsson & Sorensen, Inc. (1997). ABAQUS/Standard – User's Manual, Version 5.7, Vol. I, II, & III.

Hibbitt, Karlsson & Sorensen, Inc. (1997). ABAQUS/Post Manual, Version 5.7.

Hibbitt, Karlsson & Sorensen, Inc. (1997). ABAQUS/Theory Manual, Version 5.7.

Hibbitt, Karlsson & Sorensen, Inc. (1999). Buckling, Postbuckling, and Collapse Analysis with ABAQUS.

Highway Research Board (1962a). The AASHTO Road Test, Proceedings of the May 16-18, 1962, Conference held in St. Louis, MO, HRB Special Report 73, National Research Council, Washington, DC.

Highway Research Board (1962b). The AASHTO Road Test, Report 4, Bridge Research, HRB Special Report 61D, National Research Council, Washington, DC.

Ho, H. S. (1972). "Shakedown in Elastic-Plastic System Under Dynamic Loading," Journal of Applied Mechanics, Vol. 39.

Hodge, Philip G., Jr. (1959). Plastic Analysis of Structures, McGraw-Hill Book Company, Inc., New York, NY.

Measurements Group, Inc. (1988). Strain Gage Based Transducers.

Measurements Group, Inc. (1996-2000). Strain Gage Technology - Product and Technical Reference Binder.

MTS System Corporation (June 1997). Model 407 Controller – Product Manual, Version 5.0.

National Instruments Corporation (January 1998). LabVIEW™ User Manual.

National Instruments Corporation (February 1999). LabVIEW™ QuikStart Guide.

Neal, B. G. (1956). The Plastic Methods of Structural Analysis, John Willey and Sons, New York, NY.

Rotter, J. M., Ansourian, P. (1979). "Cross-Section Behavior and Ductility in Composite Beams." Proceedings of the Institution of Civil Engineers, London, England, Part 2, Vol. 67, June.

Schaevitz™ Sensors, Inc. (2001). "Schaevitz LVDT Technology," internet file on www.schaevitz.com website.

Schilling, Charles G. (Jan. 1984). Highway Structures Design Handbook (Chapter I/6 – Fatigue, Section III – Fatigue Behavior), United States Steel Corporation, Pittsburgh, PA.

Schilling, Charles G. (July 1986). Exploratory Autostress Girder Designs, Report on Project 188, American Iron and Steel Institute.

Schilling, Charles G. (May 1989). Chapter Two – Safety and Serviceability Criteria for Highway Bridges, Bridges Overstress Criteria , Interim Report of FHWA Project, Dept. of Civil Engineering, City College of New York, NY.

Schilling, Charles G. (1991). "Unified Autostress Method," Engineering Journal, AISC, Vol. 28, No. 4, Fourth Quarter.

Schilling, Charles G. (1993). Unified Autostress Method, Transportation Research Record 1380, Transportation Research Board, Washington, DC.

Schilling, Charles G., Barker, Michael G., Dishongh, Burl E., Hartnagel, Bryan A. (January 1997). Inelastic Design Procedures and Specifications, Final Report submitted to the American Iron Steel Institute, University of Missouri-Columbia.

Schilling, Charles G., Morcos, Sherif S. (July 1988). Moment-Rotation Tests of Steel Girders With Ultracompact Flanges, American Iron and Steel Institute.

Toridis, T. G., Wen, R. K. (1966). "Inelastic Response of Beams to Moving Loads," Journal of the Engineering Mechanics Division, ASCE, Vol. 92, No. EM6, Dec.

Weber, D. C. (August 1994). Experimental Verification of Inelastic Load and Resistance Factor Design Limits, Master of Science Thesis, University of Missouri-Columbia.

White, Donald W. (February 1994). Analysis of the Inelastic Moment-Rotation Behavior of Non-Compact Steel Bridge Girders, Report CE-STR-94-1 to American Iron and Steel Institute, Purdue University, West Lafayette, IN.

White, Donald W., Barth, Karl E. (1998). "Strength and Ductility of Continuous Span Steel I-Girders in Negative Bending," Journal of Construction Steel Research, 45(3) 241-280.

White, Donald W., Barth, Karl E., Bobb, Betsy M. (December 1998). Strength and Ductility of HPS70W Girders, Final Report to American Iron and Steel Institute, School of Civil and Environmental Engineering, Georgia Institute of Technology.

Yakel, A. J., Mans, P., Azizinamini, A. (November 1999). Flexural Capacity of HPS70W Bridge Girders, National Bridge Research Organization, University of Nebraska-Lincoln.

Zubeck, Michael W. (May 2000). Nonlinear Analysis of Intermediate Support Regions of Continuous Span Steel Girders, Ph.D. dissertation, University of Missouri-Columbia.

GLOSSARY

Abutment: An end support for a bridge superstructure.

Actual Rotation Capacity: The plastic rotation corresponding to the plastic moment, or to an effective plastic moment, on the plastic-rotation curve for the section; the plastic-rotation curve is above this plastic moment, or effective plastic moment, for a plastic rotation equal to the actual rotation capacity.

Alternating Plasticity: Yielding in both directions when a section is subjected to large reversals of moments.

Automoment: Moment that develops as a result of local yielding at one or more locations in a continuous-span member and remains after all loading has been removed; this is also called redistribution moment.

Beam: A member whose primary purpose is to support loads applied perpendicular to its length; this term usually refers to rolled shapes.

Beam-Line Method: A method of calculating the redistribution moments and plastic rotation due to yielding at section by plotting on a single graph the plastic-rotation curve for the section and a straight line defining the angular discontinuity at the section as a function of moment; this is a special case of the unified autostress and residual-deformation methods.

Bending Strength: The maximum bending moment that can be applied to a section without violating applicable specification requirements.

Classical Plastic-Design Assumptions: Assumptions normally made in the plastic design of buildings; the main ones are that plastic rotations concentrated at single cross section so that the rest of the structure is elastic and that the total rotation curve for all sections is linear to the plastic moment and thereafter remains at the plastic moment for a sufficient rotation to form a mechanism.

Compact Compression Flange: A compression flange that can sustain sufficient strains so that the entire cross section can be assumed to be at the yield stress when calculating its bending strength; the flange must satisfy specified slenderness and bracing-spacing requirements to qualify as compact.

Compact Section: A section that has a compact web and compression flange; the bending strength of the section is equal to its plastic-moment capacity.

Compact Web: A web that can sustain sufficient bending strains so that the entire cross section can be assumed to be at the yield stress when calculating the bending strength; the web must satisfy a specified slenderness limit to qualify as compact.

Composite Beam or Girder: A steel beam or girder connected to a concrete slab so that the steel element and the slab, and/or the longitudinal rebars within the slab, respond to the bending loads as a unit; in positive-bending region, both the slab and rebars participate in this unit, but in negative-bending regions only the rebars participate.

Compression-Flange Bracing Spacing: Distance between supports resisting lateral deflection of the compression flange.

Conjugate Beam: A conceptual beam used to represent a real bending member when calculating member distortions.

Continuity Relationship: A relationship between the moment at all pier locations in a continuous-span member and the plastic rotations at all yield locations; this relationship is based on the fact that the member must be continuous with all plastic rotations in place and involves the variation of stiffness along the member.

Cracked Section: A composite section in which the slab is assumed to carry no stress because of tensile cracking.

Cross Frame: A transverse truss framework connecting adjacent longitudinal bending members.

Deflection Stability: Stabilization of permanent deflection after progressive increases due to sequential loading; this is also called shakedown.

Deflection-Stability Loading: The highest sequential loading that results in deflection stability; this is also call shakedown loading.

Design: Proportioning and detailing the components and connections of a bridge to satisfy the requirements of specifications.

Design Lane: A width of bridge assumed to carry the full specified truck or lane loading; the width of the design lane may differ from that of the traffic lane.

Diaphragm: A transversal bending member connecting adjacent longitudinal bending members.

Dummy-Load Method: A method of deflection analysis in which the work done by a unit dummy (conceptual) load as a structure deforms due to the actual loading is equated

to the internal energy generated by the dummy-load moments to get the deflection at the dummy-load location.

Dynamic Yield Stress or Strain: The yield stress or strain for a given or assumed strain rate; the dynamic yield stress or strain is higher than the yield stress or strain.

Dynamic Yielding: The time dependence of yielding in a steel member; after any increment of load or deflection imposed in the inelastic range, a short time (usually a few minutes) is required for the resulting deflections and loads to stabilize.

Effective Plastic Moment: The moment corresponding to a specified required rotation on the plastic-rotation curve for the section; the plastic-rotation curve is above this moment for a plastic rotation equal to the required value.

Elastic Analysis: An analysis in which the moments and/or deflections caused by applied loads are calculated without considering yielding.

Elastic Design: Design based on an elastic analysis; in such design, the elastic moments are sometimes limited to values above the yield moment even though this implies that yielding will occur.

Elastic Moment: Moment from an elastic analysis.

Elastic Moment Envelope: A plot of the maximum positive and negative elastic moments that can occur at all locations along a member as a result of a given sequential loading; this plot is made by successively placing specified live loads at the positions that cause the highest moments at each location and combining these moments with concurrent dead load moments.

Elastic Rotation: An elastic change in slope over a length of a member.

Engineer: The engineer directly responsible for the design of the bridge.

Factored Loading: The service live load and/or the nominal dead load times a load factor specified for various load combinations.

Finite-Element Method: A method of analysis in which the structure is discretized into elements connected at nodes, the shape of the element displacement field is assumed, and partial or complete compatibility is maintained among the element interfaces, and nodal displacements are determined by using energy variational principles or equilibrium methods.

Flange Slenderness: One half the width of a flange divided by its thickness.

Girder: A member whose primary purpose is to support loads applied perpendicular to its length; this term usually refers to fabricated members.

Grillage Method: A method of analysis in which all or part of the superstructure is discretized into orthotropic components that represent the characteristics of the structure.

Hybrid Girder: A fabricated steel girder with a web that has a lower specified minimum yield stress than one or both flanges.

Initial Geometric Imperfection: Initial out-of-plumpness, out-of-straightness, cross-section distortions, and connection eccentricities that affect the strength and stability of large-long bridge girders.

Incremental Collapse: A progressive increase without limit of permanent deflection due to sequential loading.

Indeterminate Analysis: An analysis that utilizes stiffness properties to calculate moments that cannot be determined by statics.

Inelastic Analysis: An analysis in which the moments and/or deflections caused by applied loads are calculated by considering yielding.

Inelastic Design: Design based on an inelastic analysis.

Inelastic Lateral Redistribution of Moments: A redistribution of elastic moments among the individual girders in a multigirder bridge due to local yielding at one or more locations in the girders.

Inelastic Redistribution of Moments: A change in the elastic moment in a continuous-span beam or girder due to local yielding at one or more location: usually the negative moments at piers are reduced and the positive moments elsewhere are increased.

Inelastic Region: The phase of an analysis that involves yielding.

Lateral Bracing: A truss placed in a vertical plane between two main members to resist lateral loads and deflections.

Lateral Buckling: Buckling of the compression flange of a bending member by lateral deflection and twist.

Limit State: A design limit related to the usefulness of a structure.

Mechanism: A system of member segments and real and/or plastic hinges that offers no resistance to deformation.

Mechanism Method: A method of calculating the ultimate strength of a beam, girder, or frame in which the loading required to cause each possible mechanism is determined: the lowest loading is the ultimate strength.

Negative-Bending Region: Any length in which the member is subjected to negative moment under the loading condition being considered.

Negative-Bending Section: Any section that is subjected to negative moment under the loading condition being considered; this section may be a positive-bending section under a different loading condition.

Negative Moment: Moment producing tension at the top edge of the member.

Noncompact Compression Flange: A compression flange that does not qualify as compact, but can reach the yield stress without local or lateral buckling; the flange must satisfy specified slenderness and bracing requirements to qualify as noncompact.

Noncompact Section: A section that has a noncompact compression flange and web; the bending strength of this section is usually equal to its yield-moment capacity.

Noncompact Web: A web that does not qualify as compact, but can sustain sufficient bending strain so that the stress in the compression flange can reach the yield stress; the web must satisfy a specified slenderness requirement to qualify as noncompact.

Permanent Deflection: Deflection that remains in a member after all the loading has been removed.

Pier: An interior support for a bridge superstructure.

Plastic Design: A design based on an inelastic analysis; this term usually refers to the classical inelastic procedures used in building design.

Plastic Hinge: A yield location at which the moment is assumed to remain constant at the plastic moment, or the effective plastic moment, while plastic rotation occurs.

Plastic Moment: A moment calculated by assuming that the entire cross section is at the yield stress in either tension or compression; this moment approximates the bending strength of a compact section.

Plastic Rotation: A permanent change in slope that occurs over a length of a member due to yielding; usually, the yielding occurs over a short length and is assumed to be concentrated in an angular discontinuity at a single cross section for plastic-design calculations.

Positive-Bending Region: Any length in which the member is subjected to positive moment under the loading condition being considered.

Positive-Bending Section: Any section that is subjected to positive moment under the loading condition being considered; this section may be a negative-bending section under a different loading condition.

Positive Moment: Moment producing tension at the bottom edge of the member.

Proportional Loading: A set of individual concentrated and/or distributed loads applied in specified directions at specified locations and interrelated by specified ratios; the magnitude of the proportional loading is defined by a single factor that applied to all individual loads.

Redistribution Moment: Moment that develops as a result of local yielding at one or more locations in a continuous-span member and remains after all loading has been removed; this is also called automoment.

Reliability Index: A measure of safety equal to the difference between the mean resistance, or strength, and a corresponding mean load effect divided by the combined standard deviation; values of the reliability index correspond to the probabilities of failure as listed below:

Reliability Index	Probability of Failure
0	0.50
1	0.159
2	0.0228
3	0.00135
4	0.0000317

Required Rotation Capacity: The amount of plastic rotation required at a plastic-hinge location to permit formation of a mechanism involving that hinge; no plastic rotation is required at the last hinge to form.

Residual-Deformation Method: An inelastic method of calculating the redistribution moments and permanent deflections by satisfying continuity and rotation relationship at yield locations; the unified autostress method utilizes these same relationships, but different computational procedures.

Residual Stress: Internal stress created during the manufacture, fabrication, or subsequent loading of a member; such stresses are in equilibrium at each cross section.

Rotation Curve: A plot of applied moment vs. the plastic, elastic, or total rotation over a length of a member.

Rotation Relationship: A relationship between the total moment (elastic moment plus redistribution moment) and plastic rotation at a section; this is the plastic-rotation curve for the section.

Sequential Loading: A series of proportional loadings applied sequentially in any order including repeats of some or all of the individual loadings; the magnitude of the sequential loading is defined by a single factor that applies to all individual loads.

Shakedown: Stabilization of permanent deflection after progressive increases due to sequential loading; this is also called deflection stability.

Shakedown Loading: The highest sequential loading that results in shakedown; this is also called deflection-stability loading.

Shape Factor: Ratio of the plastic moment to the yield moment.

Slab: The concrete deck of a bridge superstructure.

Slope-Deflection Method: A method of deflection analysis in which equations that interrelate the slopes and moments at the ends of a beam segment are used to calculated deflections and angular discontinuities.

Static Yield Stress or Strain: The yield stress or strain corresponding to a zero strain rate; the quantities are determined form a tensile stress by stopping the imposed deformation several time within the inelastic range and allowing the stress and deformation to stabilize after each stop.

Statical Method: A method of calculating the strength of a mechanism by treating the portion of the member within the mechanism as a simple span, applying the known plastic moments at both ends, and varying the applied loads and corresponding moment diagram to make the combined moments equal to the plastic moment at the critical location within the span.

Stress Range: The algebraic difference between the extreme values in a stress cycle.

Three-Moment Equation: An equation that interrelates the moment and slopes at three adjacent supports of a continuous-span member and can be used in indeterminate analysis.

Total Rotation: The sum of elastic and plastic rotations that occur over a length of member.

Traffic Lane: A width of bridge designated to carry one lane of traffic and marked on the bridge.

Ultimate Strength: The highest proportional loading that can be carried by a member.

Uncracked Section: A composite section in which the slab is assumed to be fully effective because no tensile cracking has occurred.

Unified Autostress Method: An inelastic method of calculating the redistribution moments and permanent deflections due to a given stationary or sequential loading by satisfying continuity and rotation relationships at yield locations; the residual-

deformation method utilizes the same relationships, but different computational procedures.

Validate: To confirm that the results of a numerical code calculation agree with the results from a corresponding experiment.

Verify: To confirm that the results of a numerical code calculation agree with the results of a theoretical prediction for a corresponding problem.

Web Slenderness: Twice the depth of the web in compression divided by the web thickness.

Yield Moment: The lowest moment that causes yielding in a section if residual stresses are ignored; for composite sections, it is the sum of moments applied before and after the slab has hardened to cause yielding in a steel flange.

Yield Strain: The strain corresponding to the yield stress.

Yield Stress or Strain: The lowest stress or strain at which yielding occurs if residual stresses are ignored.

NOTATION

The following symbols are used in this research:

$A_{concrete}$ = area of the concrete slab;

a_r = ratio of web compression area to flange compression area, taken at the plastic moment;

A_{rebars} = area of reinforcing steel;

b_f, b_{fc} = width of compression flange;

b_t = width of each projecting stiffener element;

D = total web depth;

D_c = depth of web in compression for elastic section;

D_{cp} = depth of web in compression at theoretical plastic-moment capacity;

E = elastic modulus;

f_c, f_{cf} = elastic flange stress caused by factored loads;

f_{rd} = elastic flange stress caused by inelastic redistribution moment;

F_L = nominal compression flange stress at first yielding accounting for residual stress and hybrid web effects;

F_r = nominal compression flange stress at the onset of significant inelastic effects associated with flange local buckling;

F_u = ultimate strength;

F_y = yield stress;

F_{yc} = yield stress of compression flange;

F_{yf} = yield stress of flange being considered;

F_{ys} = yield stress of reinforcing steel;

F_{yt} = yield stress of tension flange;

F_{yw} = yield stress of web;

I = moment of inertia;

k_c = flange buckling coefficient;

L = span length;

L_b = laterally unsupported length between brace points;

L_p = maximum unbraced length;

L_{pd} = maximum laterally unsupported length permitted for inelastic design;

M = internal bending moment;

$M_{(c)}$ = composite section moment;

M_c = internal moment, calculated using elastic envelopes;

M_h = larger of moments at ends of unbraced segment;

M_l = smaller of moments at ends of unbraced segment;

M_{mc} = maximum potential flexural resistance associated with the compression flange, attainable if the flange is compact and the member is adequately braced;

M_{mt} = maximum potential flexural resistance associated with the tension flange and the reinforcing steel;

$M_{(nc)}$ = noncomposite section moment;

M_n = nominal moment capacity;

M_p = cross-section plastic-moment capacity;

M_{pe} = effective plastic moment;

$M_{pe(9)}$ = effective plastic moment corresponding to 9 mrads of plastic rotation;

$M_{pe(30)}$ = effective plastic moment corresponding to 30 mrads of plastic rotation;

M_{pf} = flange plastic moment capacity component;

M_{pw} = web plastic moment capacity component;

M_{rd} = inelastic redistribution moment;

M_{rwc} = moment capacity associated with the compression flange for a braced girder with a compact flange and the web at the noncompact limit;

M_{rwt} = moment capacity associated with the tension flange for a braced girder with a compact flange and the web at the noncompact slenderness limit;

M_y = nominal yield moment capacity;

M_{yc} = compression flange yield moment capacity;

R = rotation capacity;

R_b = web bend buckling reduction factor;

R_f = flange local buckling reduction factor;

R_h = web hybrid reduction factor;

R_w = web local buckling reduction factor;

r_t = radius of gyration about the weak bending axis of the area of the compression flange plus 1/3 area of the web in compression;

r_y = radius of gyration about the weak bending axis of whole section;

S_x = generic elastic section modululs;

S_{xc} = compression flange elastic section modulus;

$S_{x(c)}$ = generic composite-section elastic section modulus;

$S_{x(nc)}$ = generic noncomposite-section elastic section modulus;

S_{xs} = elastic section modulus associated with the reinforcing steel, for a composite member in negative bending;

S_{xt} = tension flange elastic section modulus;

t_{fc} = compression flange thickness;

t_h = thickness of the concrete haunch above the top flange;

t_p = thickness of stiffener;

t_s = thickness of the concrete slab;

t_w = web thickness;

V = internal shear force;

V_n = nominal web shear capacity;

YR = F_y/F_u = yield ratio;

α = fraction of yield moment allowed;

$\varepsilon_{st}/\varepsilon_y$ = ratio of strain at which strain-hardening begins, ε_{st}, to yield strain, ε_y;

λ_{pf} = compression flange compactness limit;

λ_{pw} = new compact web slenderness limit;

λ_{rf} = noncompact flange slenderness limit;

λ_{rw} = noncompact web slenderness limit;

λ_{uct} = ultracompact flange slenderness limit;

λ_{ucw} = ultracompact web slenderness limit;

ϕ = resistance factor;

ϕ_{sd} = shakedown resistance factor;

θ_p = plastic rotation;

θ_{RL} = plastic rotation at which pier-section flexural resistance theoretically will start to decrease with increasing rotations;

θ_u = the rotation at which the moment capacity returns to M_p after exceeding M_p and deforming past θ_p.

APPENDIX

APPENDIX CONTENTS

A.1 Hartnagel, 1997 – Figures of Test Setup

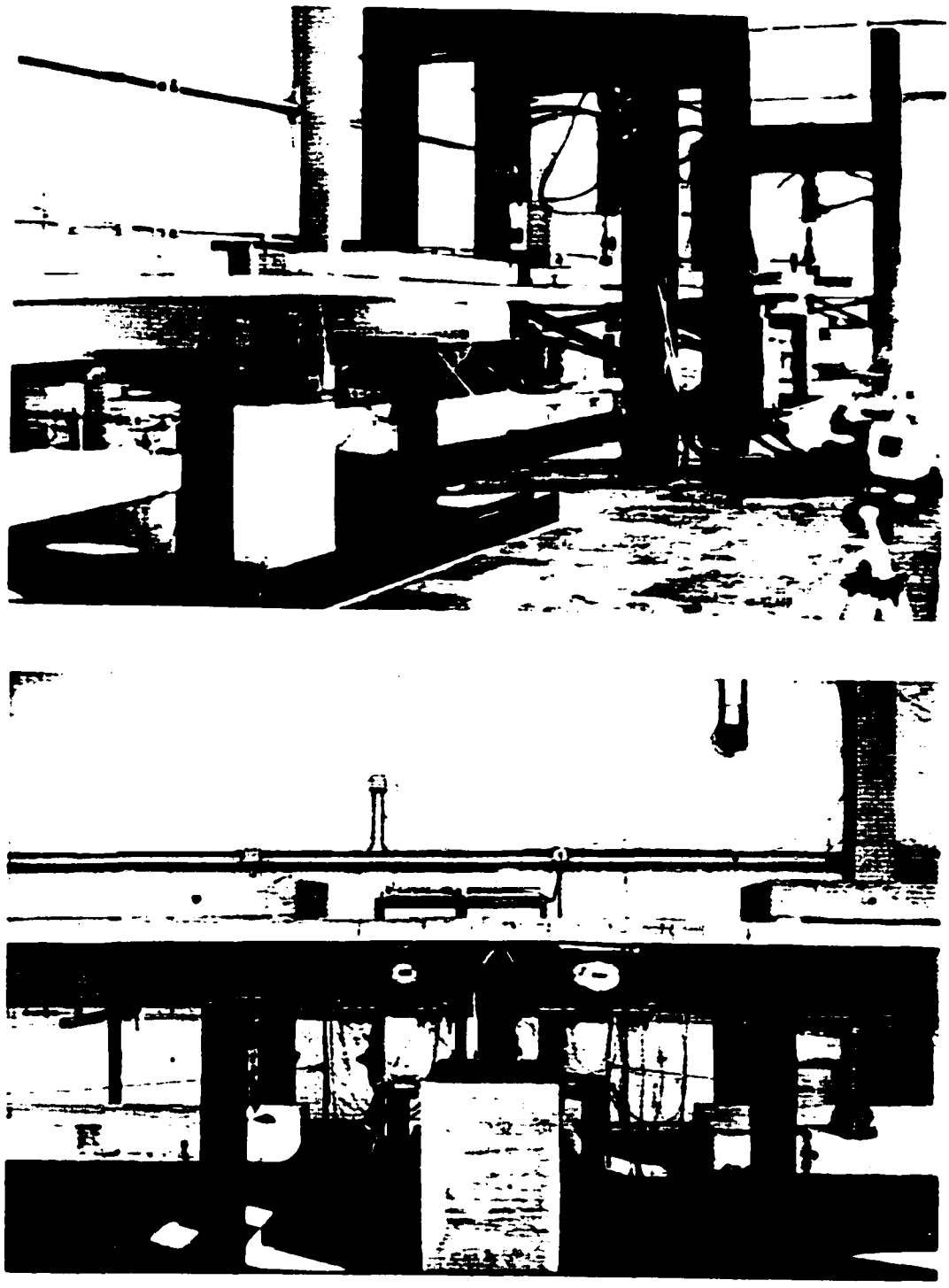

Figure 3.8 Compact Girder Photos

(Source: Hartnagel's dissertation, 1997)

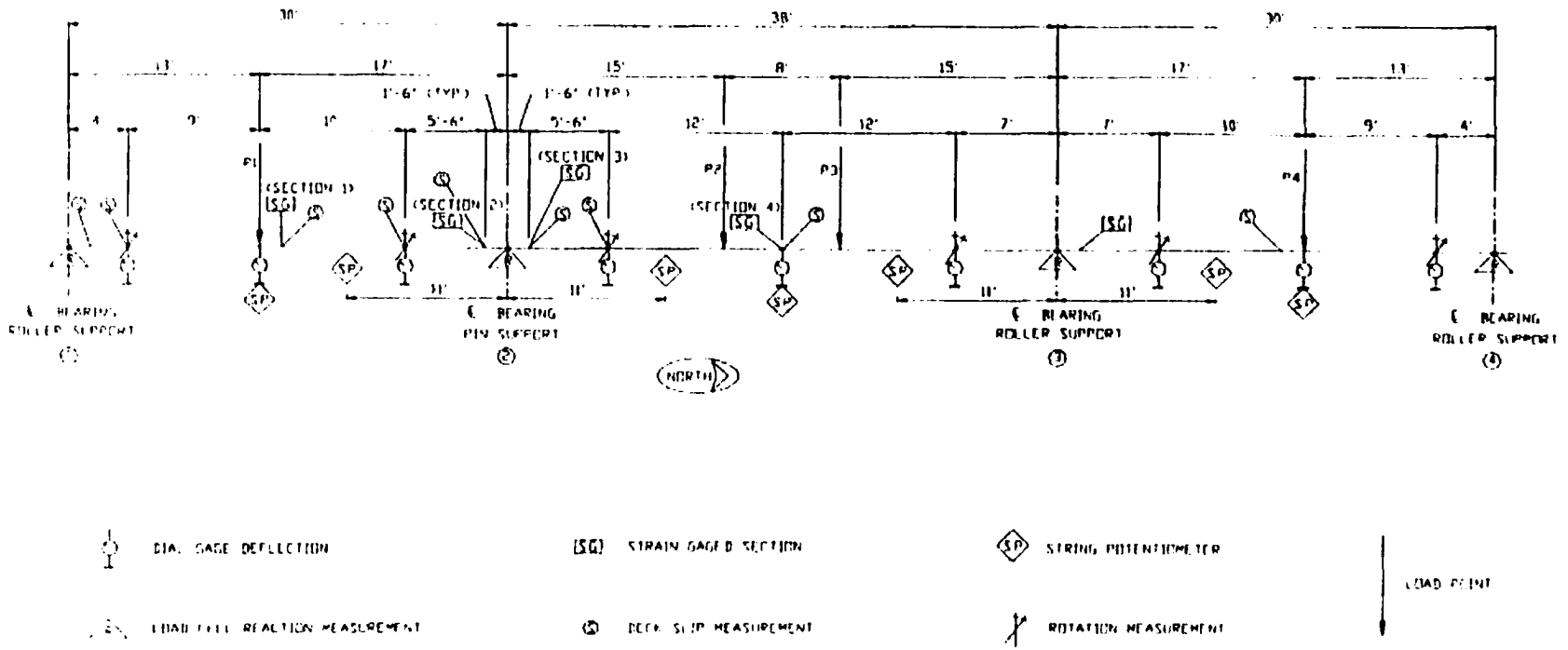

Figure 3.7 Test Measurement Layout

(Source: Hartnagel's dissertation, 1997)

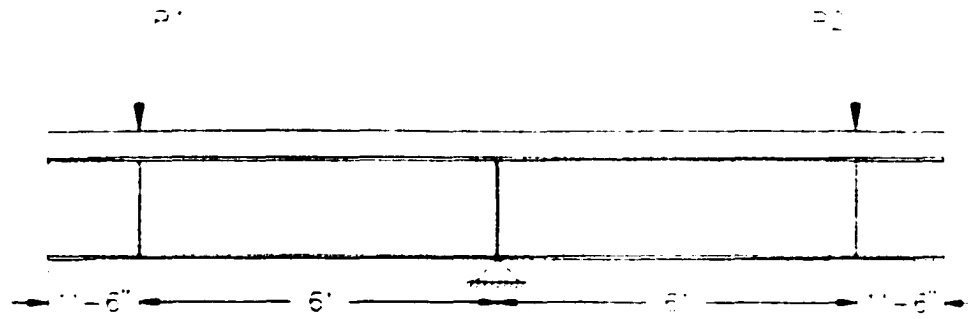

Figure 3.17 Component A, B and C Test Layout

(Source: Hartnagel's dissertation, 1997)

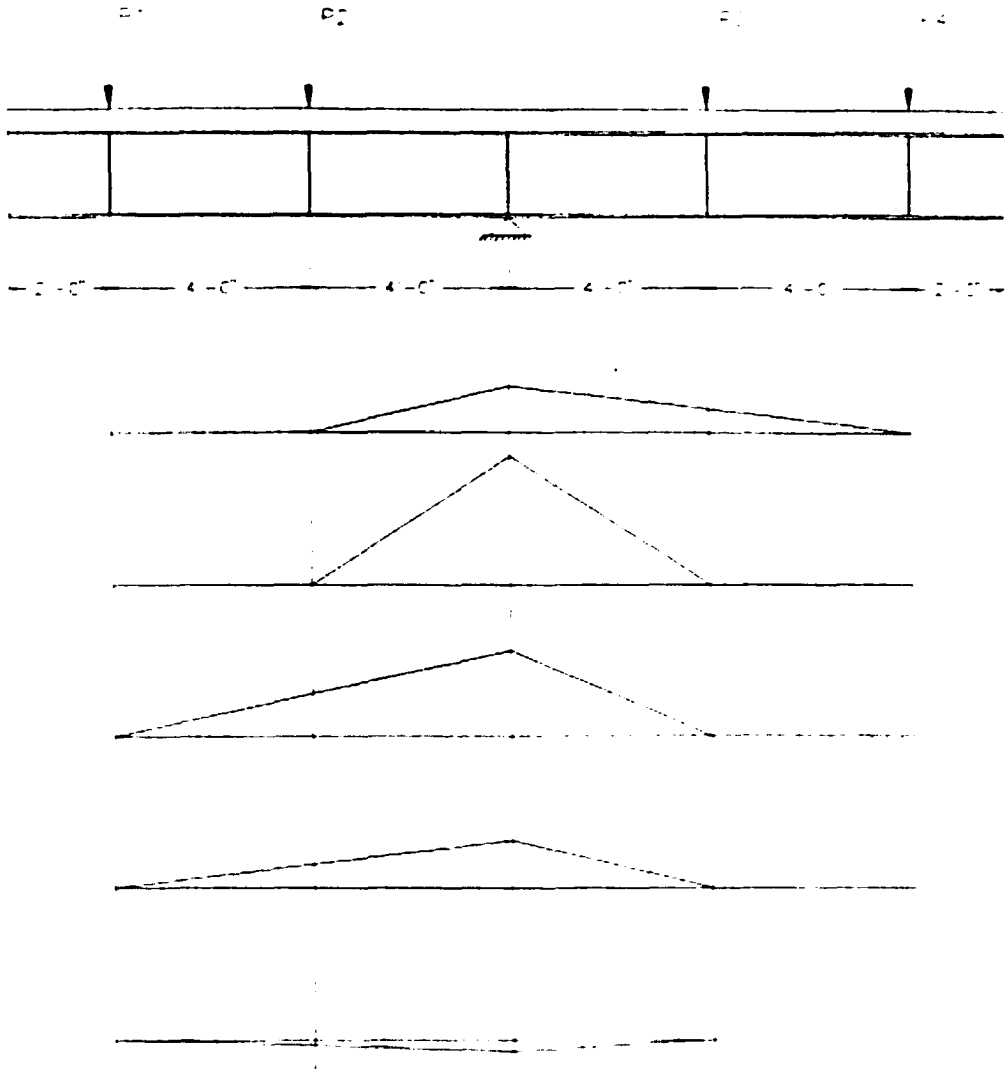

Figure 3.18 Component D Test Layout and Moving Load Moment Diagrams

(Source: Hartnagel's dissertation, 1997)

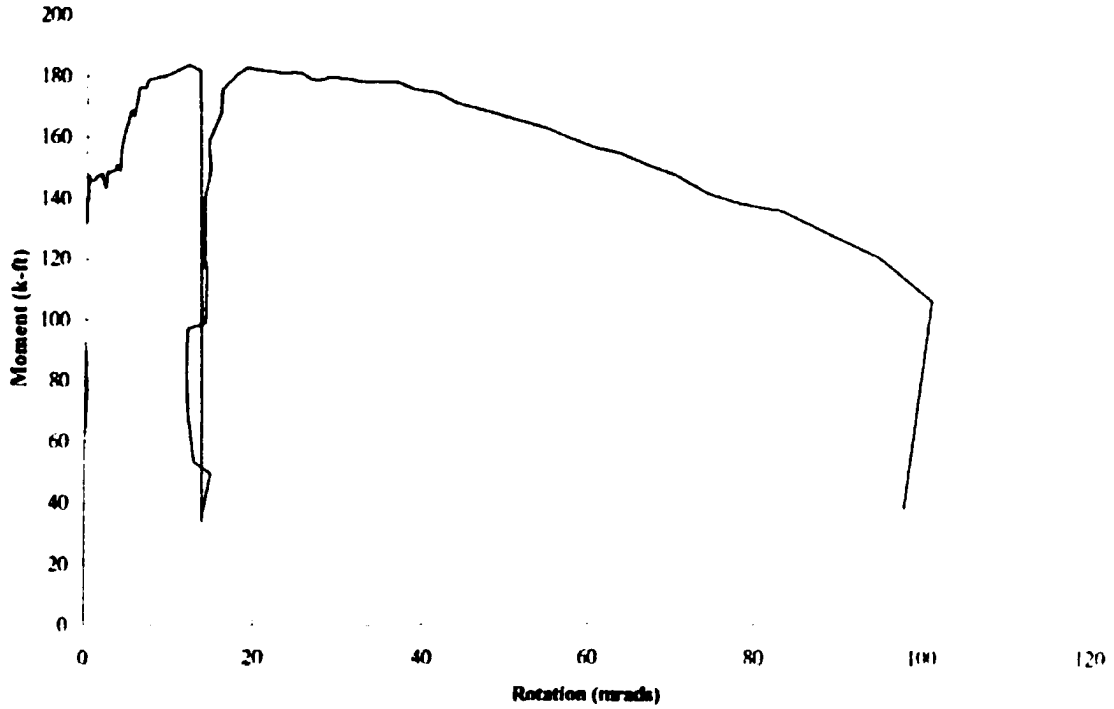

Figure 3.12 Moment vs Inelastic-Rotation for the Interior Support

(Source: Hartnagel's dissertation, 1997)

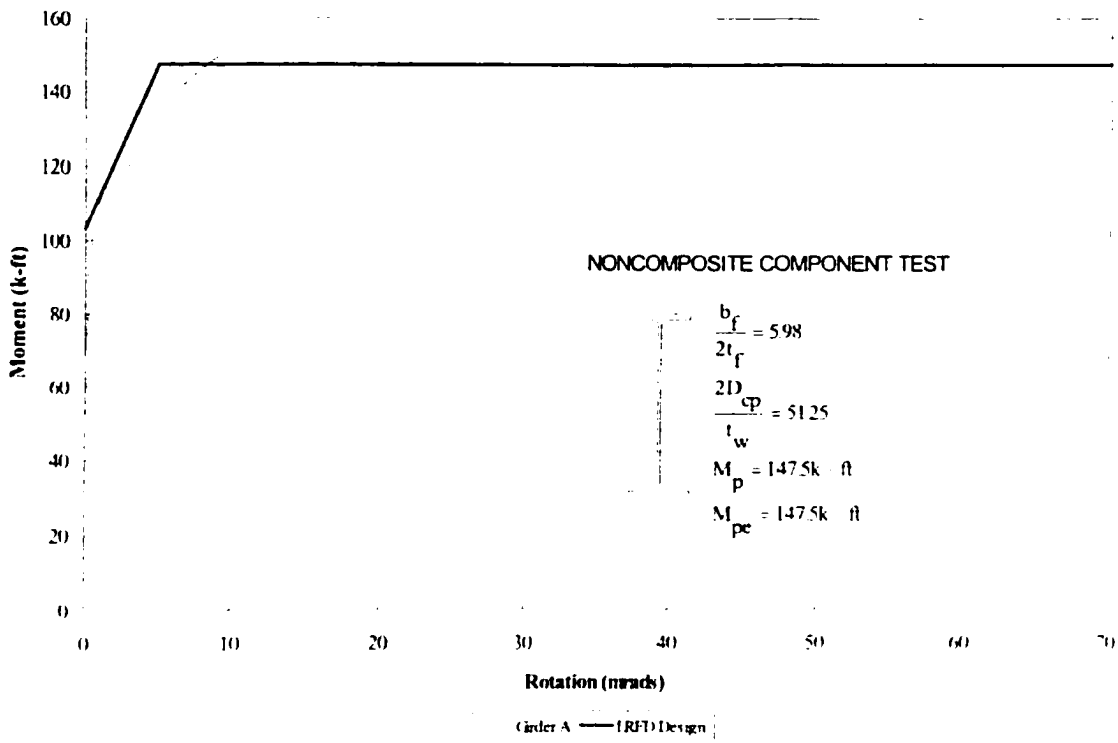

Figure 3.19 Moment vs Inelastic-Rotation for Girder A

(Source: Hartnagel's dissertation, 1997)

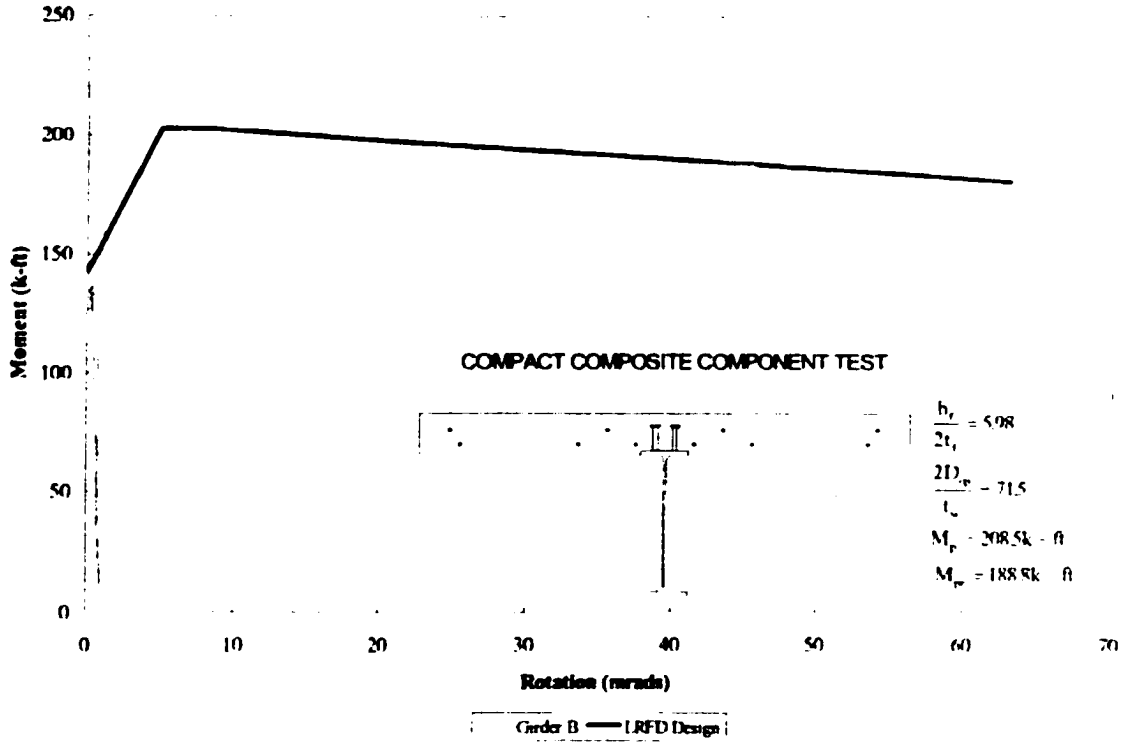

Figure 3.20 Moment vs Inelastic-Rotation for Girder B

(Source: Hartnagel's dissertation, 1997)

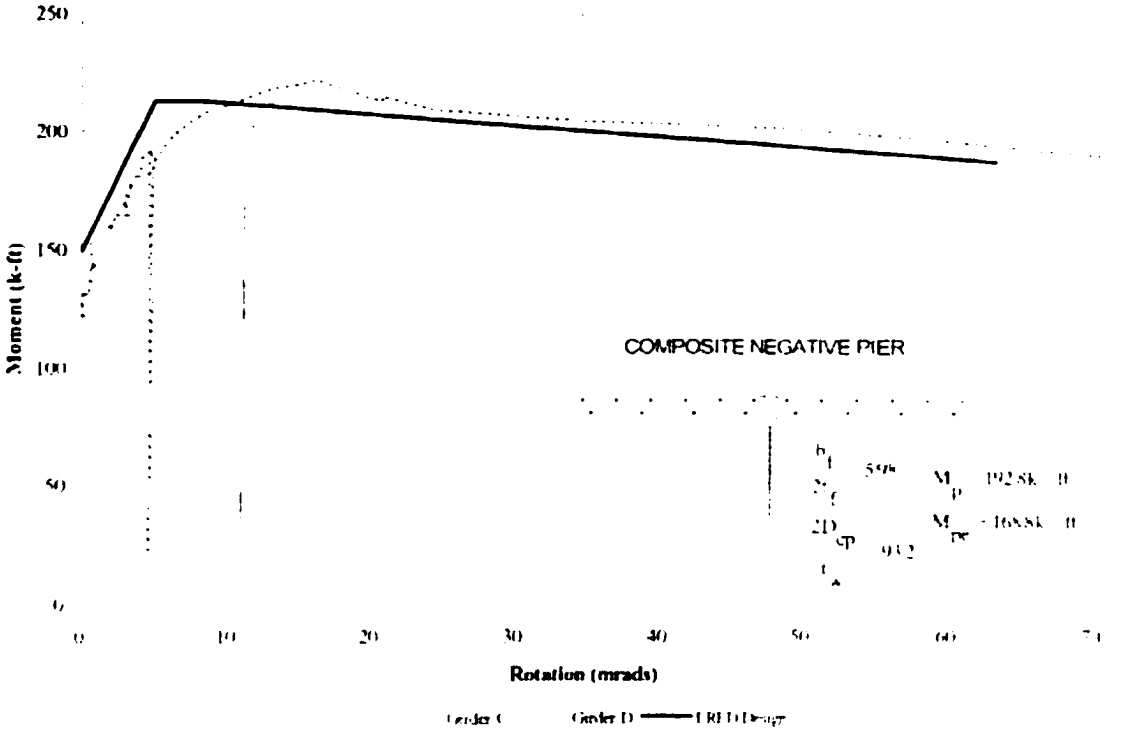

Figure 3.21 Moment vs Inelastic-Rotation for Girder C and Girder D

(Source: Hartnagel's dissertation, 1997)

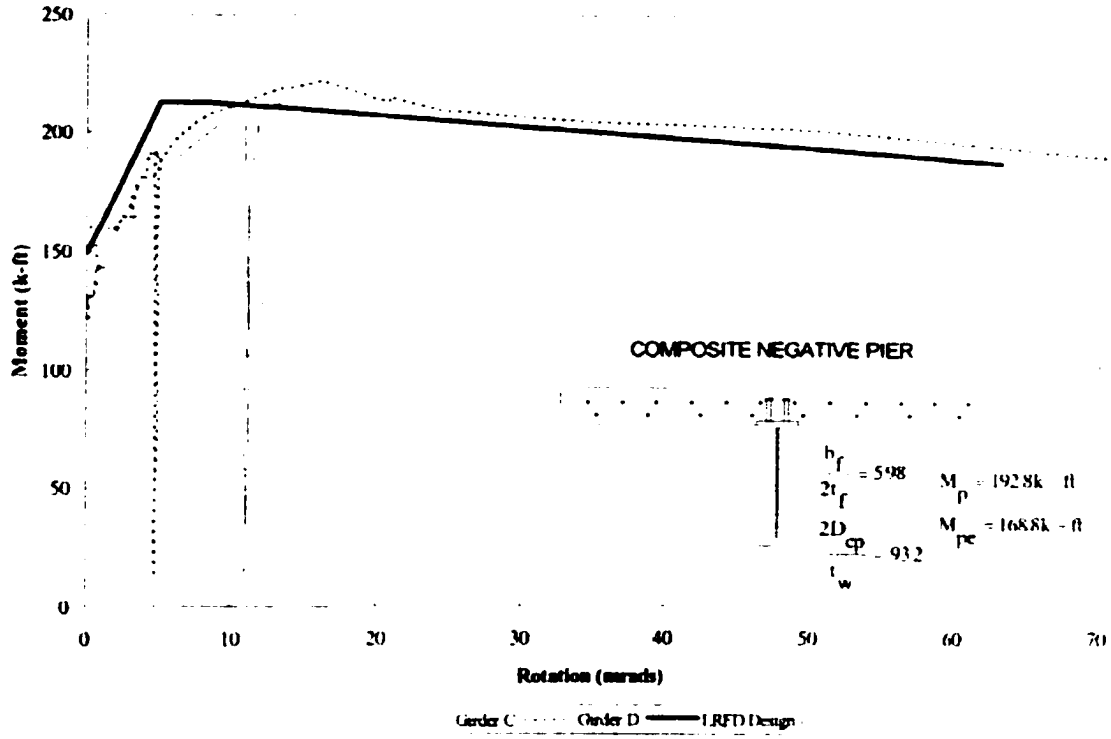

Figure 3.21 Moment vs Inelastic-Rotation for Girder C and Girder D

(Source: Hartnagel's dissertation, 1997)

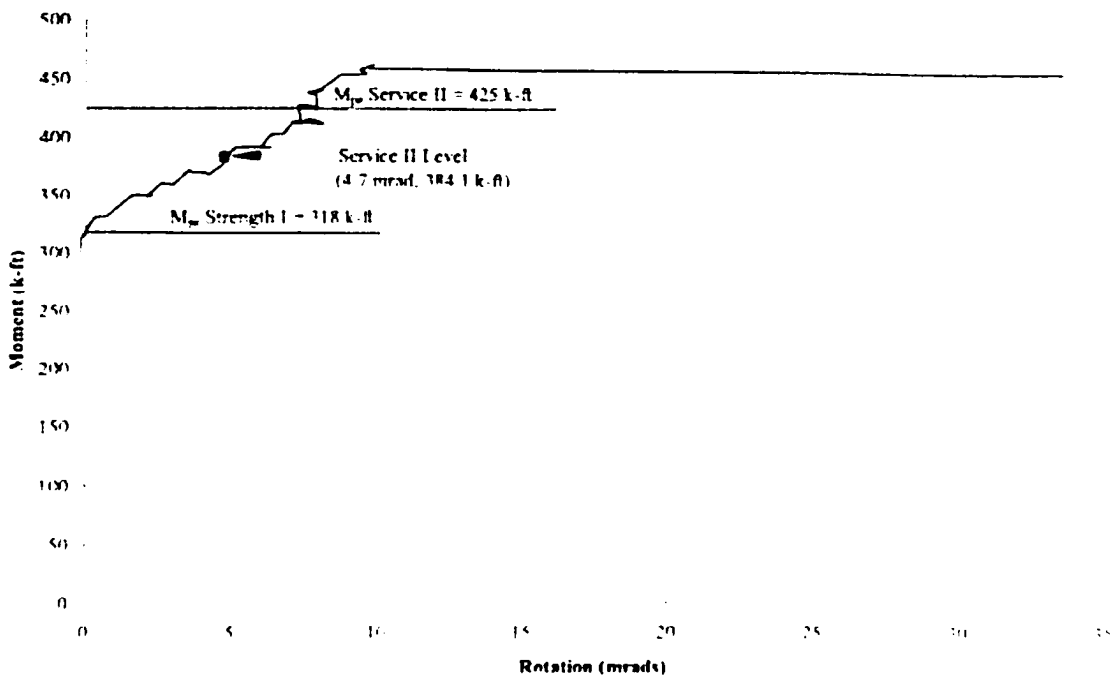

Figure 4.14 Moment vs Inelastic Rotation for the Interior Support

(Source: Hartnagel's dissertation, 1997)

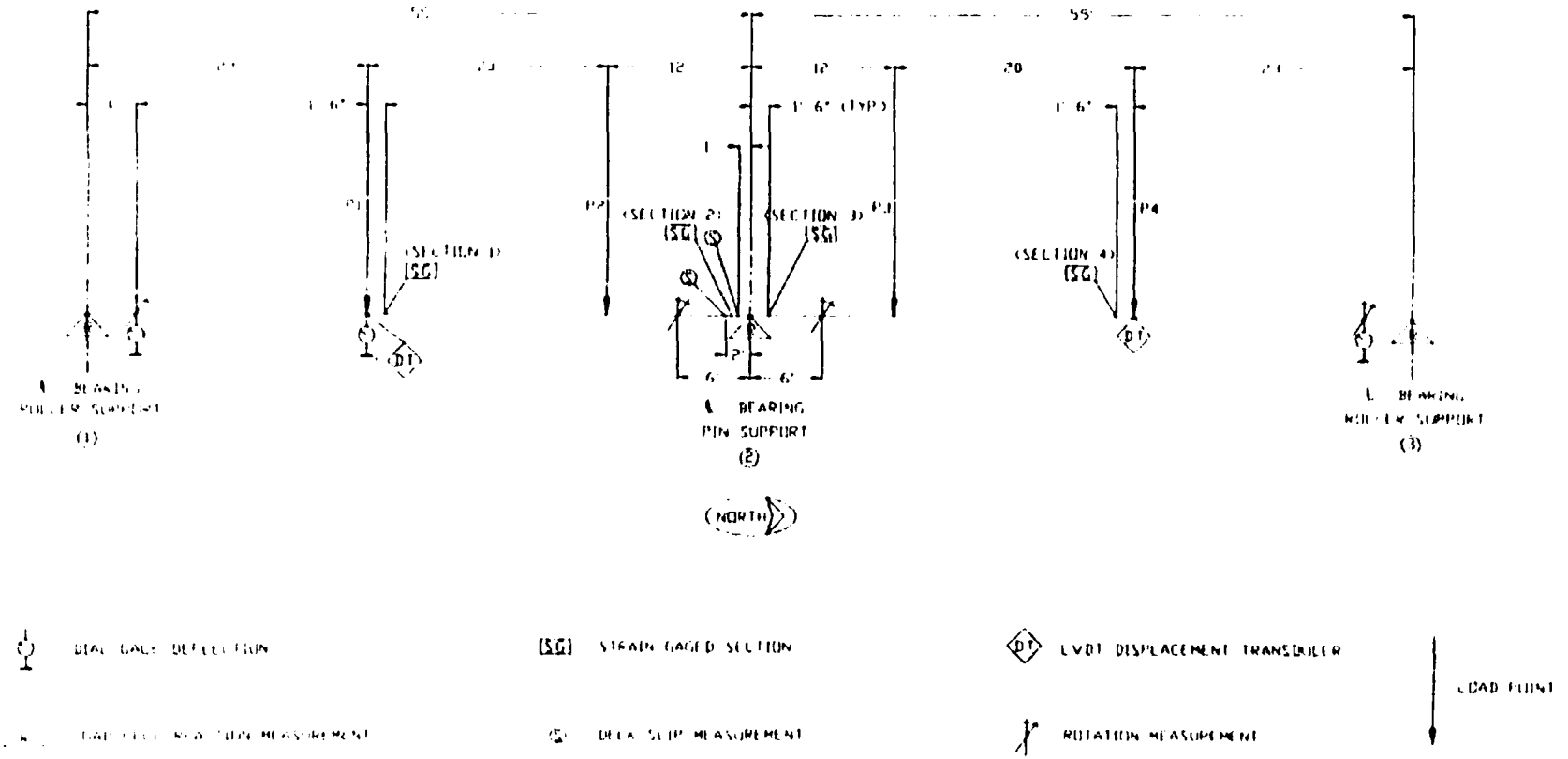

Figure 4.11 Test Measurement Layout

(Source: Hartnagel's dissertation, 1997)

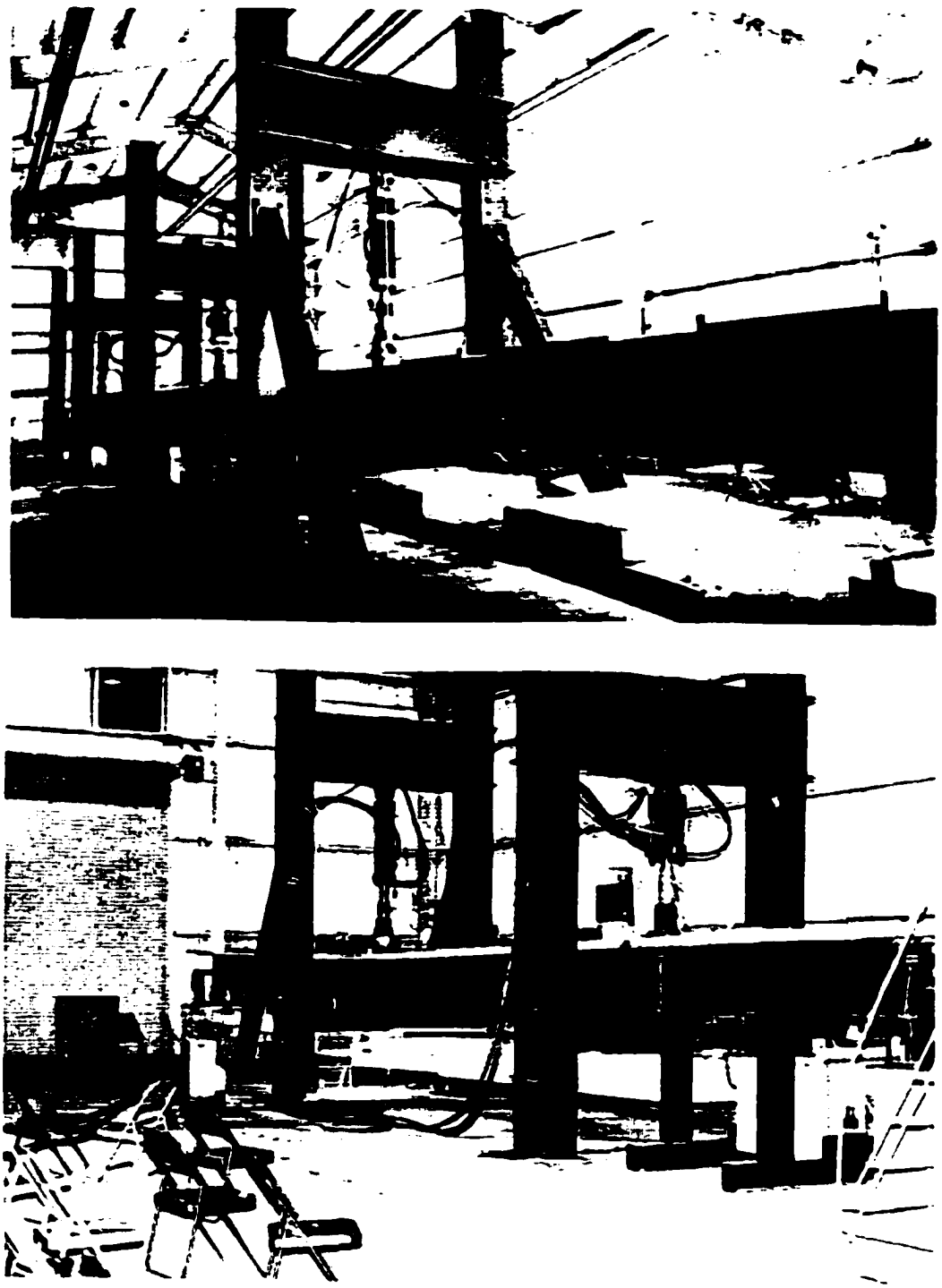

Figure 4.12 Noncompact Girder Photos

(Source: Hartnagel's dissertation, 1997)

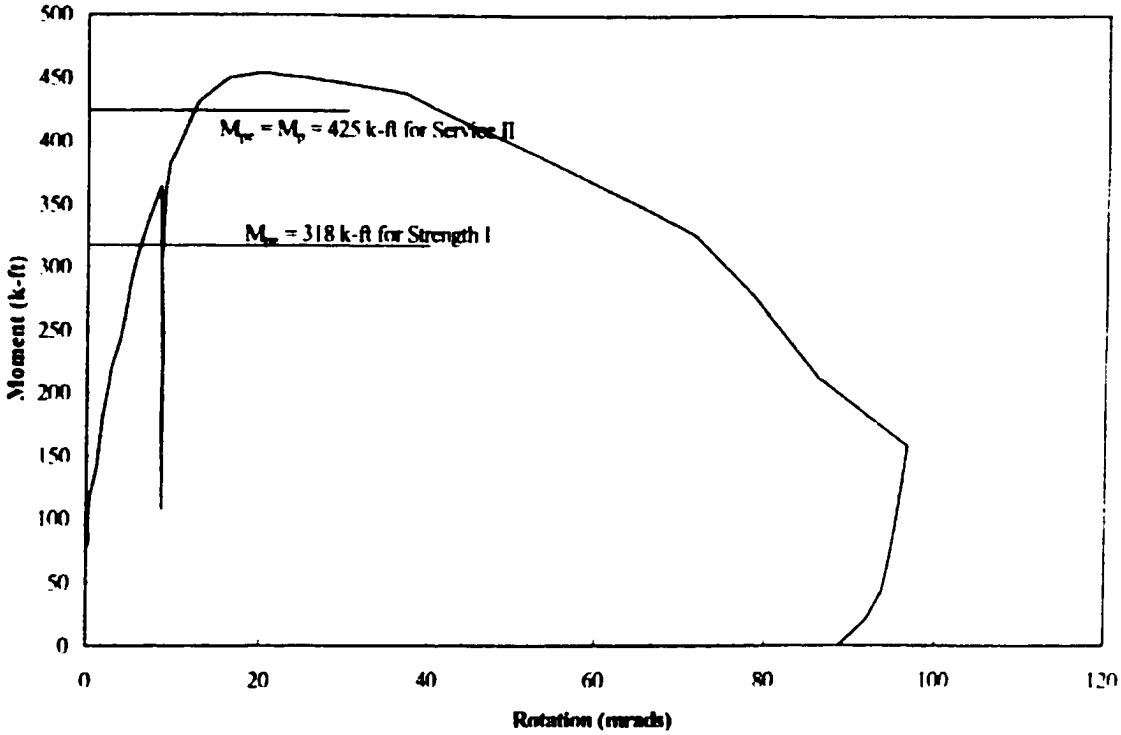

Figure 4.20 Moment vs Inelastic-Rotation for the Composite Component
(Source: Hartnagel's dissertation, 1997)

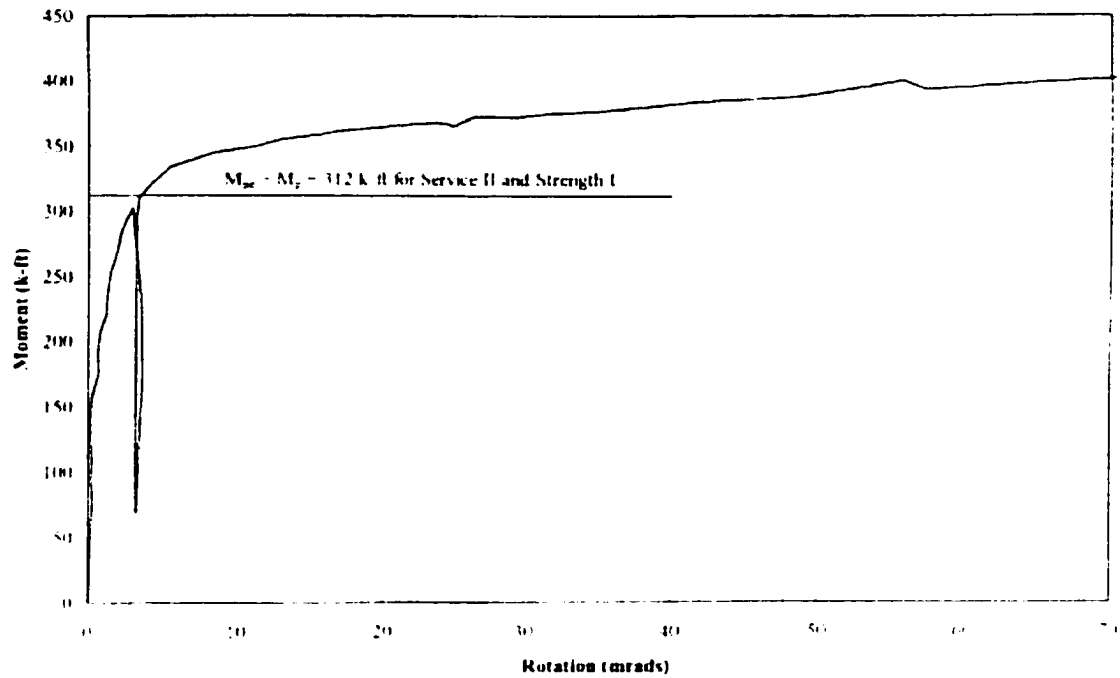

Figure 4.21 Moment vs Inelastic-Rotation for the Noncomposite Component
(Source: Hartnagel's dissertation, 1997)

A.2 Fahnestock & Sause, 1998 – Figures of Test Setup

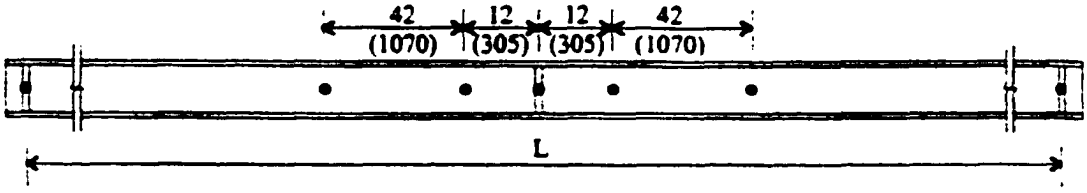

Figure 3.10 Location of Rotation Meters

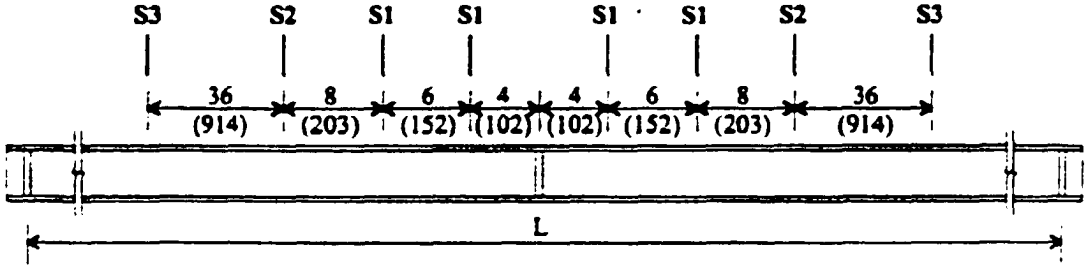

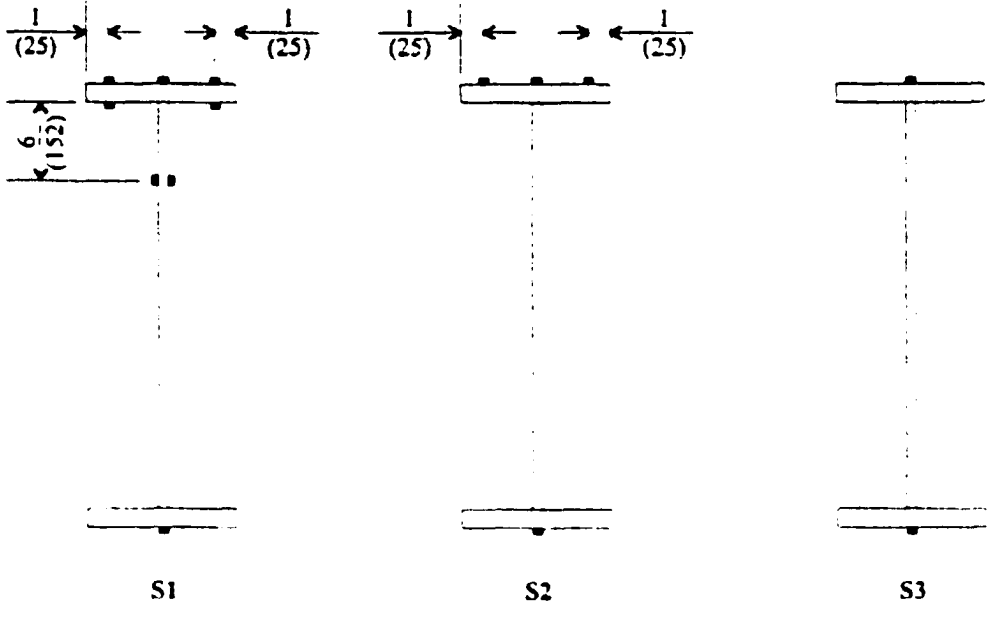

Note: Primary dimensions in inches; secondary dimensions in millimeters.

Figure 3.11 Location of Strain Gages

(Source: Fahnestock & Sause's report, 1998)

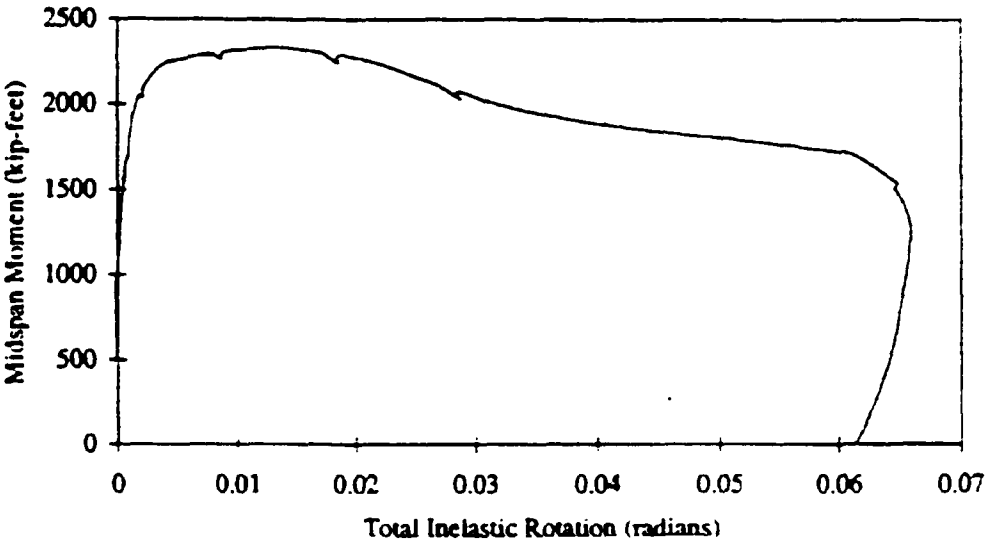

Figure 4.18 Midspan Moment versus Total Inelastic Rotation

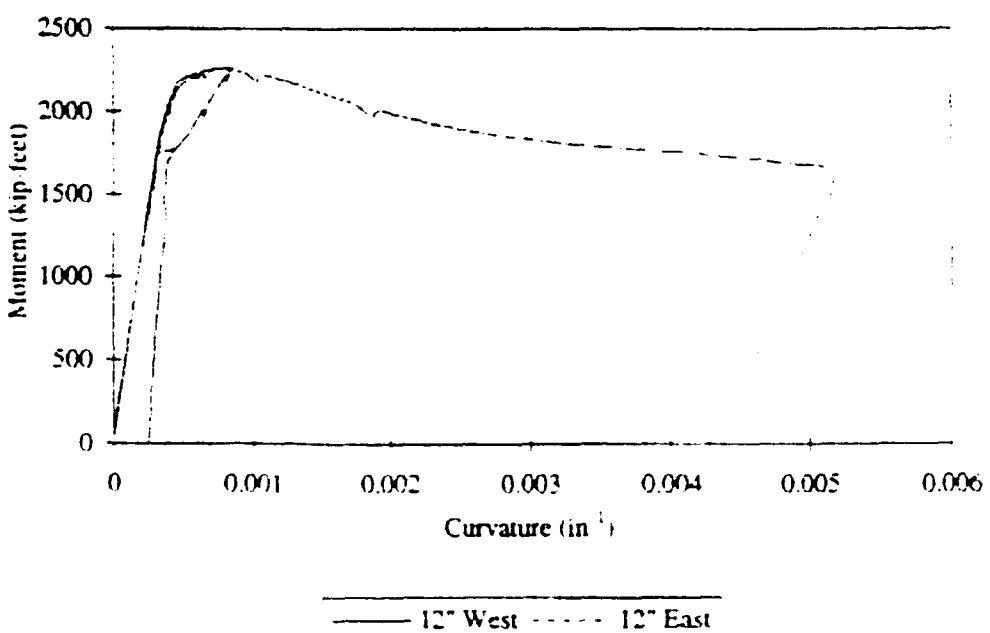

Figure 4.19 Average Moment versus Curvature in Section 12 in. (305 mm) on Either Side of Midspan

(Source: Fahnestock & Sause's report, 1998)

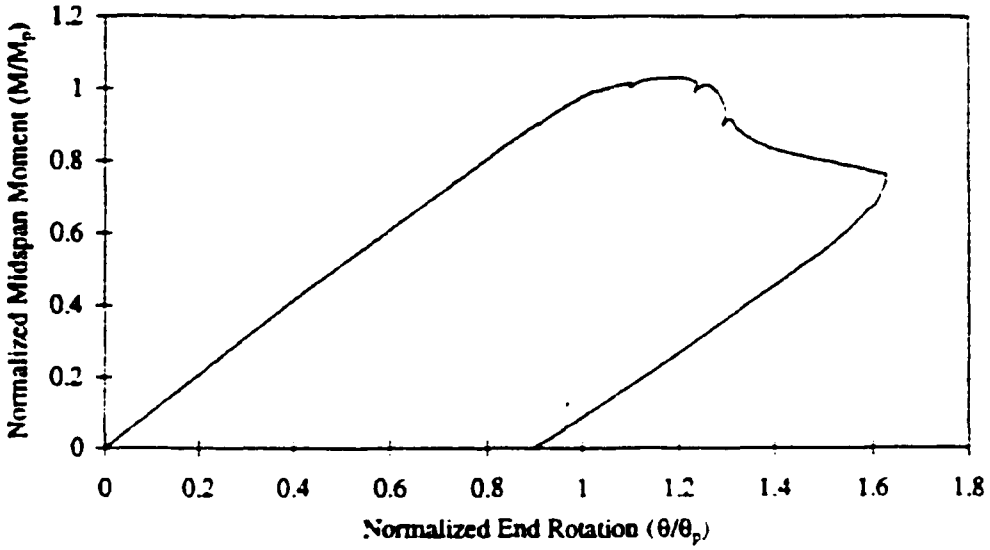

Figure 4.20 Normalized Midspan Moment versus Normalized End Rotation

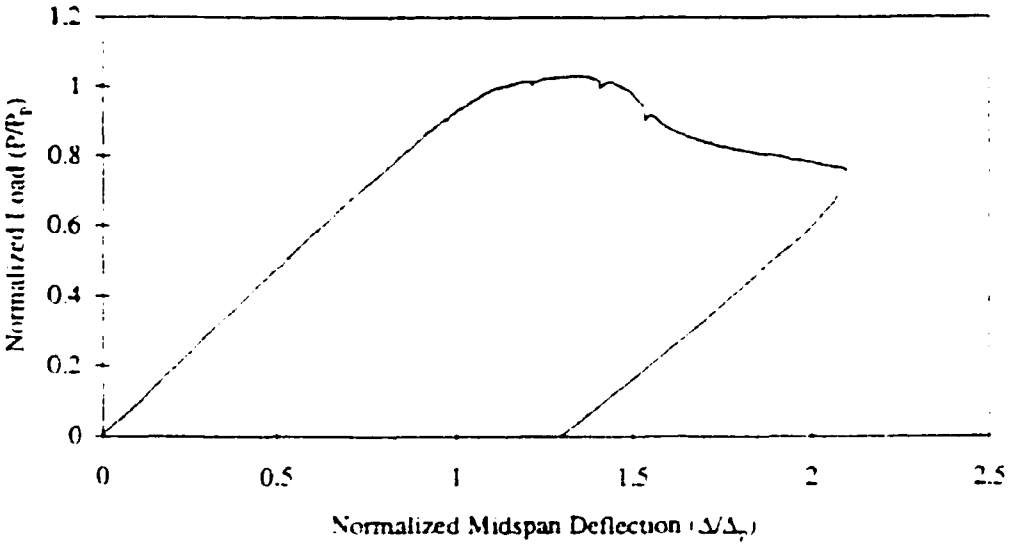

Figure 4.21 Normalized Load versus Normalized Midspan Displacement

(Source: Fahnestock & Sause's report, 1998)

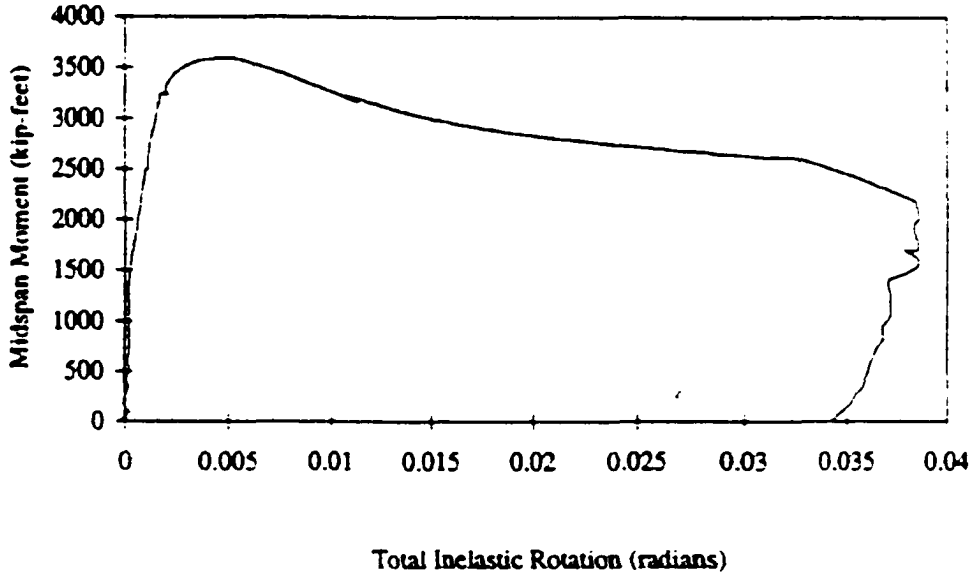

Figure 5.19 Midspan Moment versus Total Inelastic Rotation

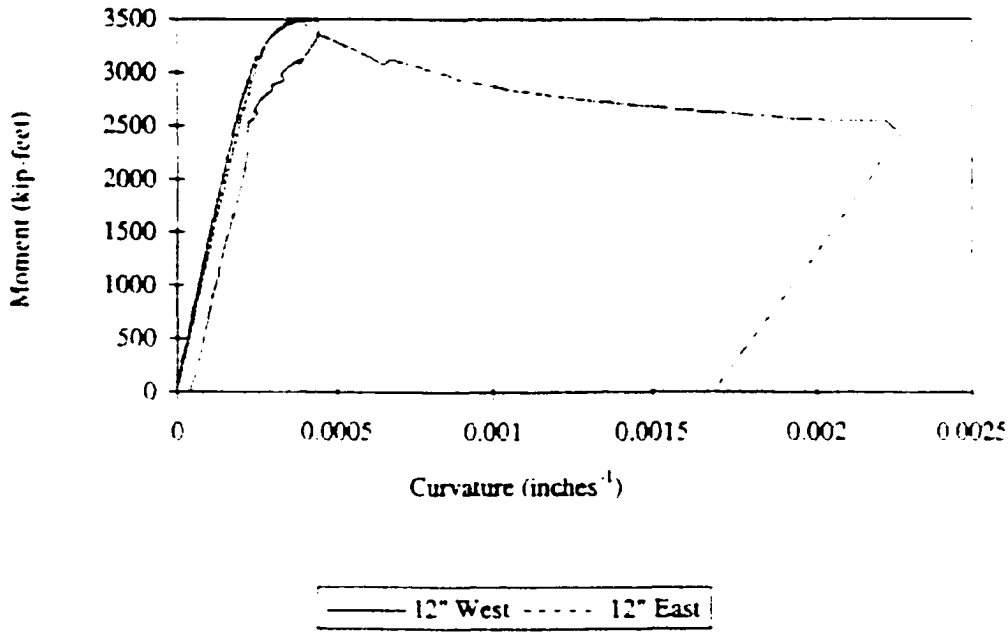

Figure 5.20 Average Moment versus Curvature in Section 12 in. (305 mm) on Either Side of Midspan

(Source: Fahnestock & Sause's report, 1998)

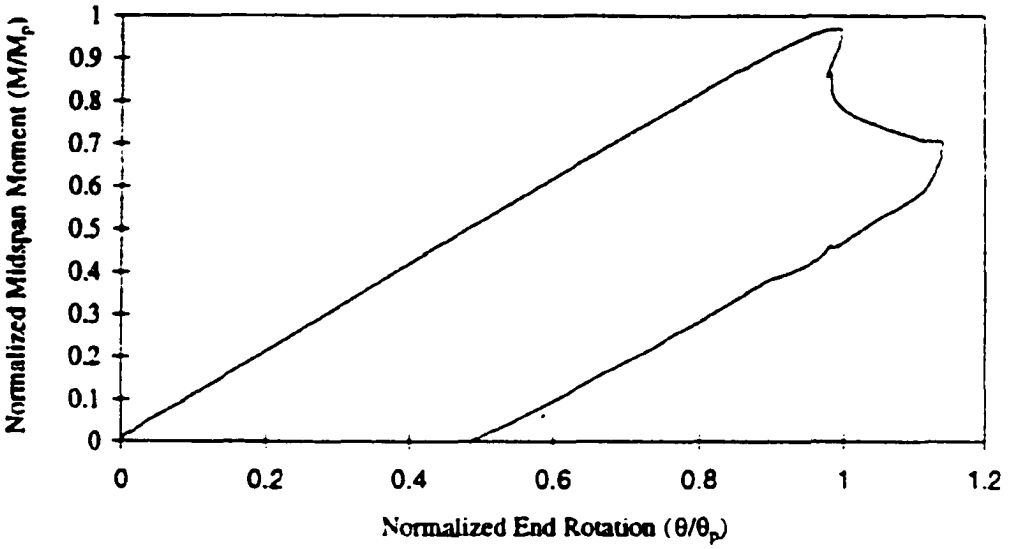

Figure 5.21 Normalized Midspan Moment versus Normalized End Rotation

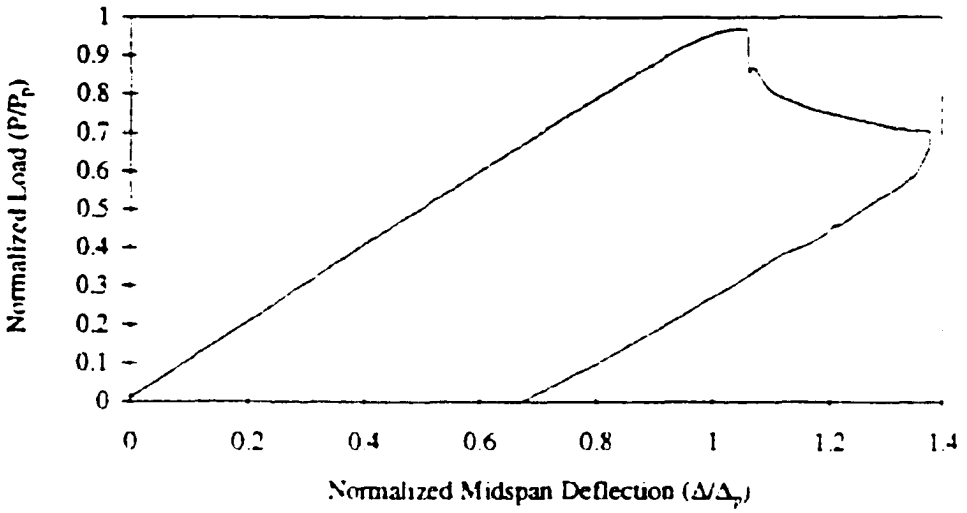

Figure 5.22 Normalized Load versus Normalized Midspan Deflection

(Source: Fahnestock & Sause's report, 1998)

A.3 Yakel, Mans, & Azzinamini, 1999 - Figures of Test Setup

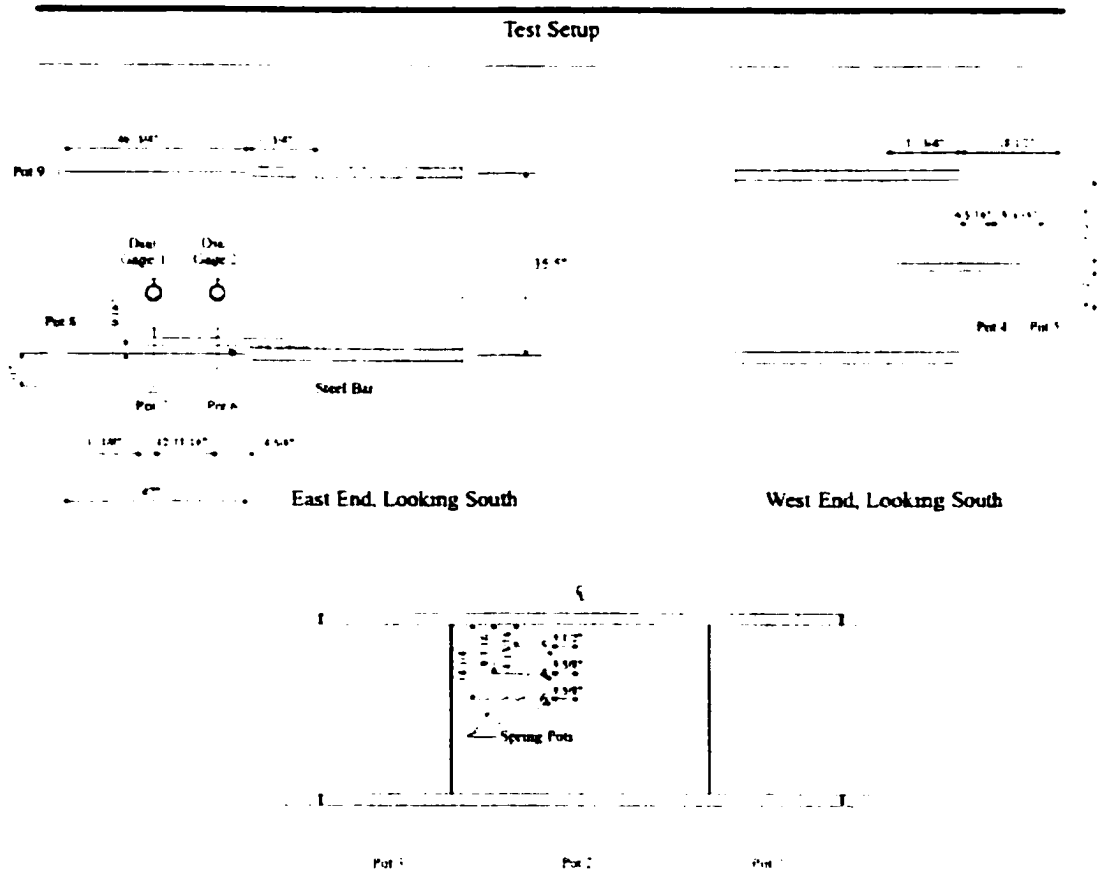

Figure 2-13. Potentiometer Locations for Test Girder A before Adjusting Loading System

(Source: Yakel, Mans, & Azizinamini's report, 1999)

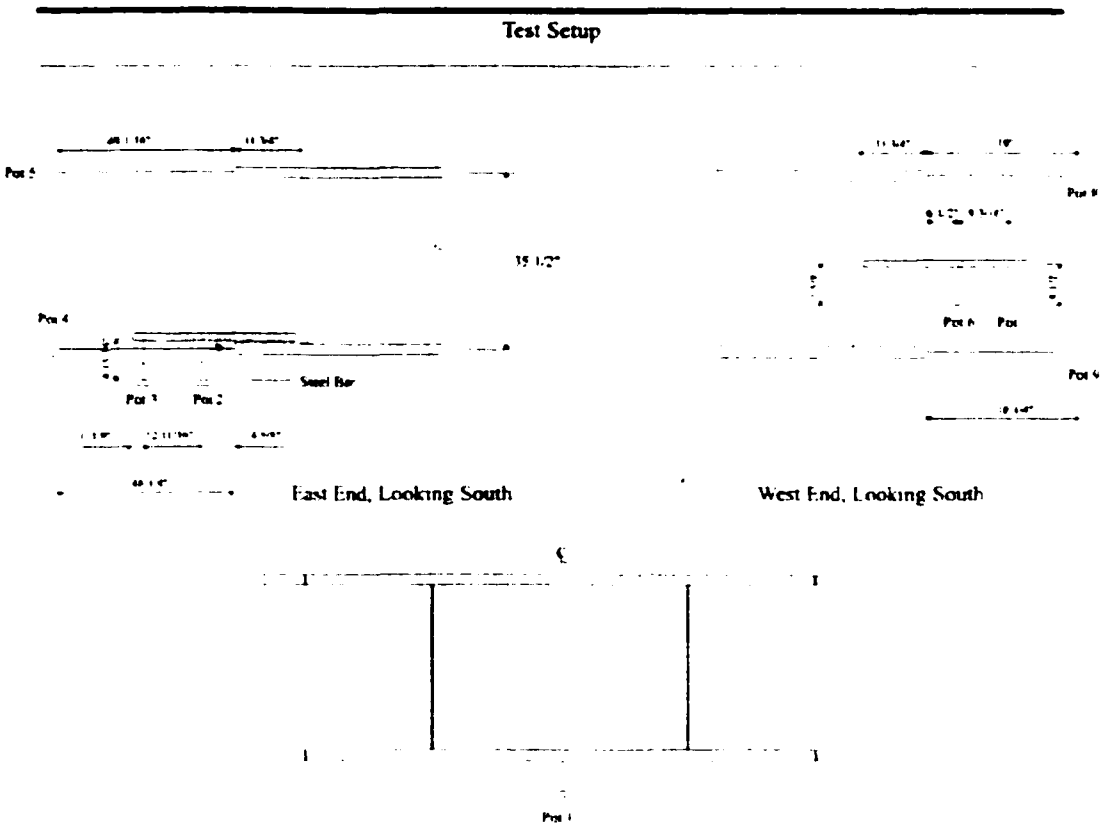

Figure 2-14. Potentiometer Locations for Test Girder A after Adjusting Loading System

(Source: Yakel, Mans, & Azizinamini's report, 1999)

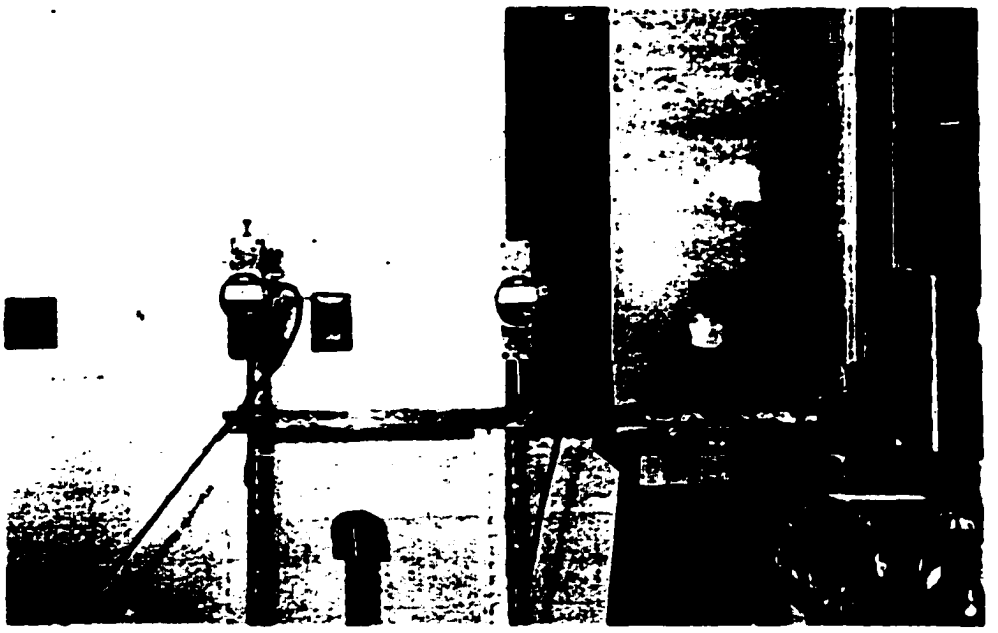

Figure 2-15. Digital Dial Gages to determine Rotation at East End of Test Girder A

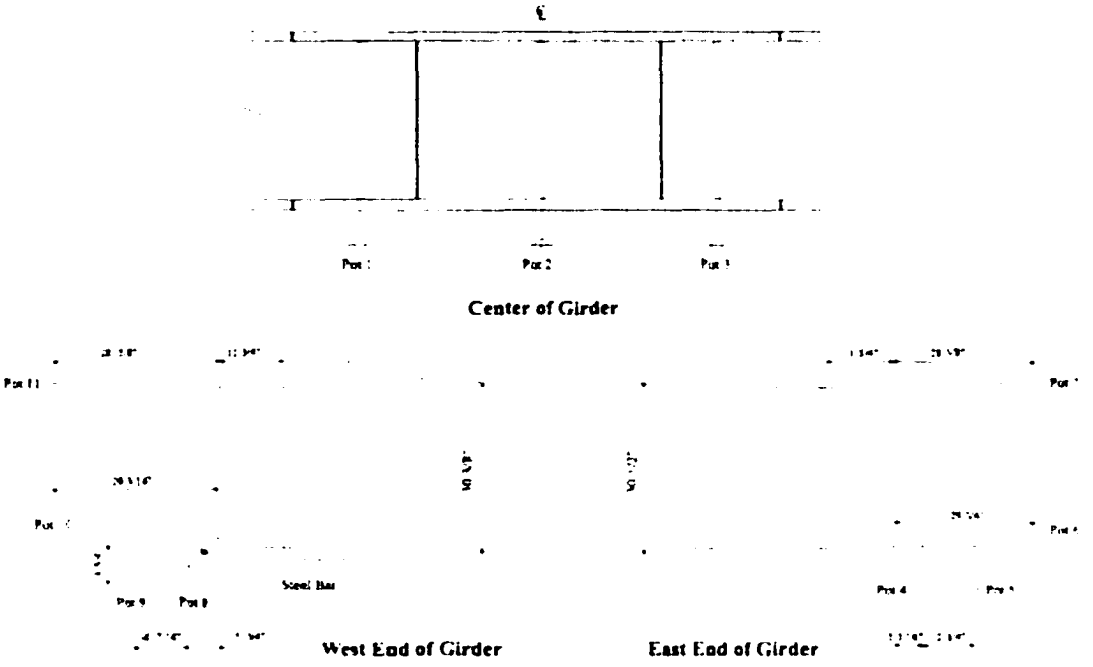

Figure 2-16. Potentiometer Locations for Test Girder D

(Source: Yakel, Mans, & Azizinamini's report, 1999)

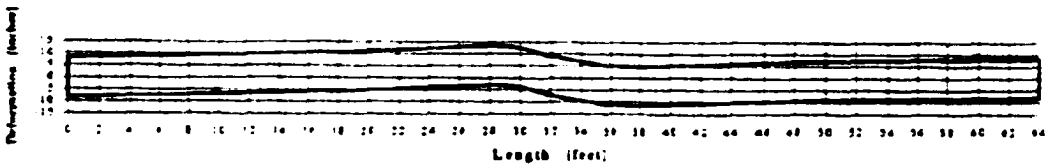

Figure 2-24. Deformed Shape of Top Flange of Test Girder A

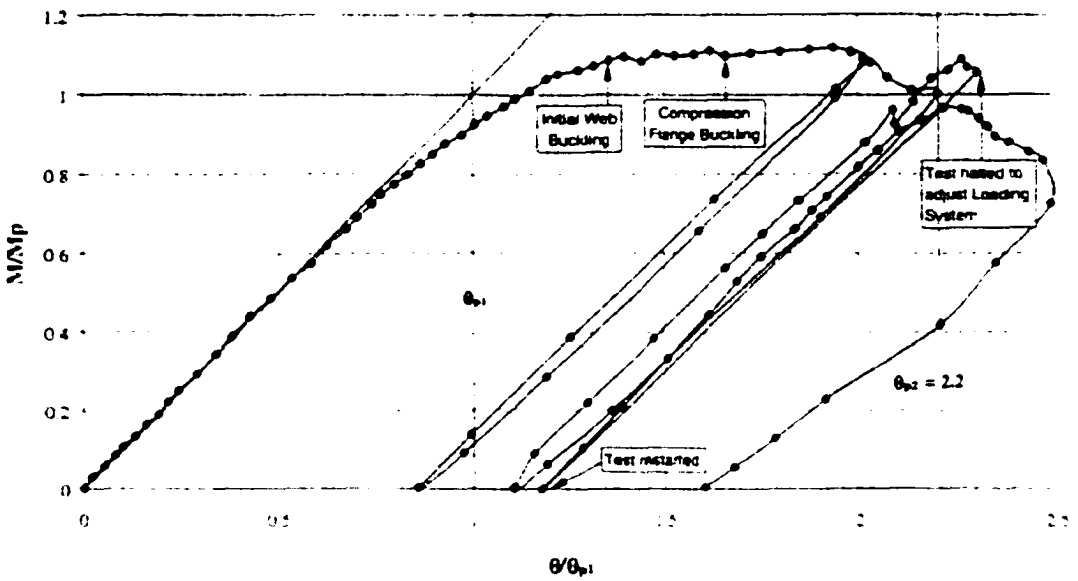

Figure 2-25. Normalized Moment versus Rotation Curve for Test Girder A

(Source: Yakel, Mans, & Azizinamini's report, 1999)

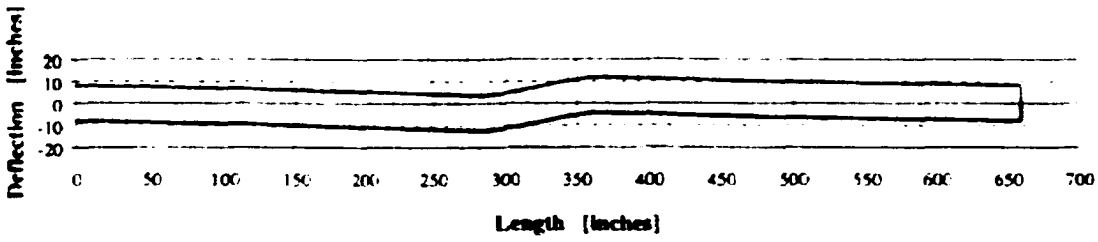

Figure 2-37. Deformed Shape of Top Flange of Test Girder D

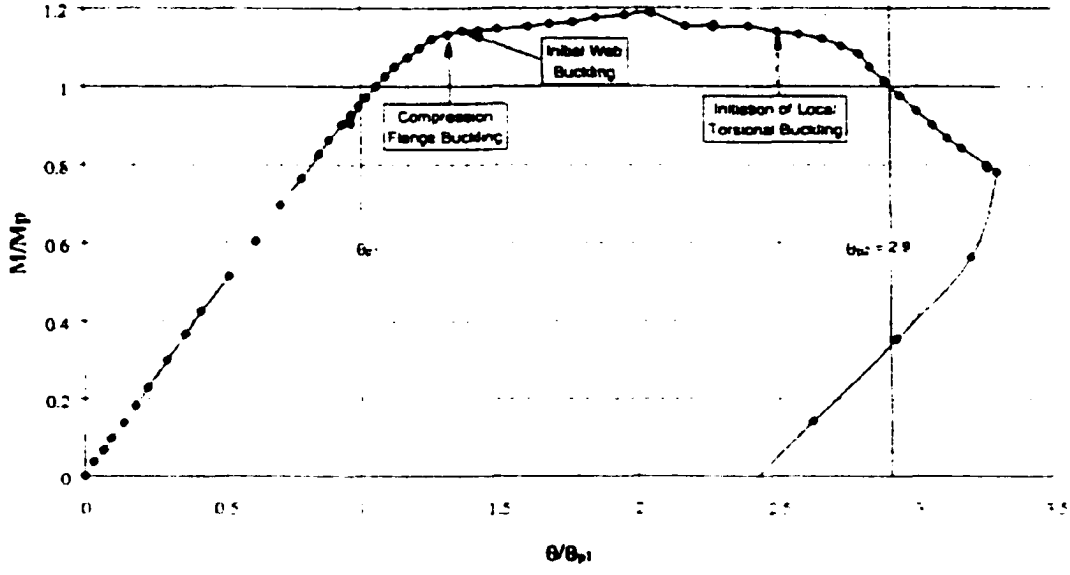

Figure 2-38. Normalized Moment versus Rotation Response of Test Girder D

(Source: Yakel, Mans, & Azizinamini's report, 1999)

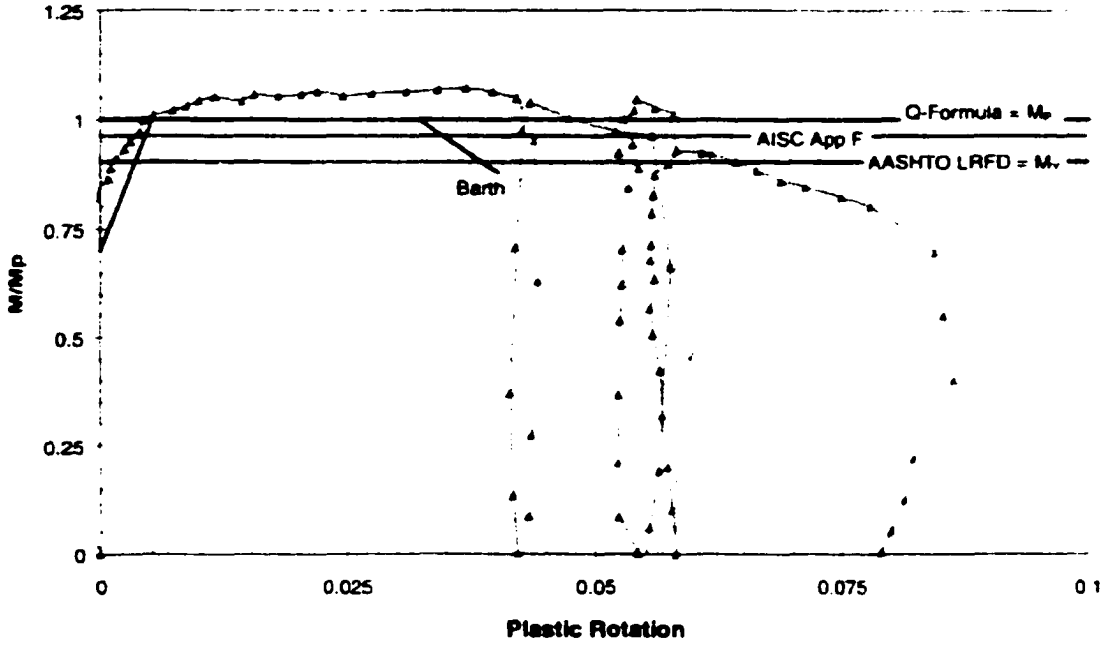

Figure 2-46. Moment Capacity of Test Girder A using Several Methods

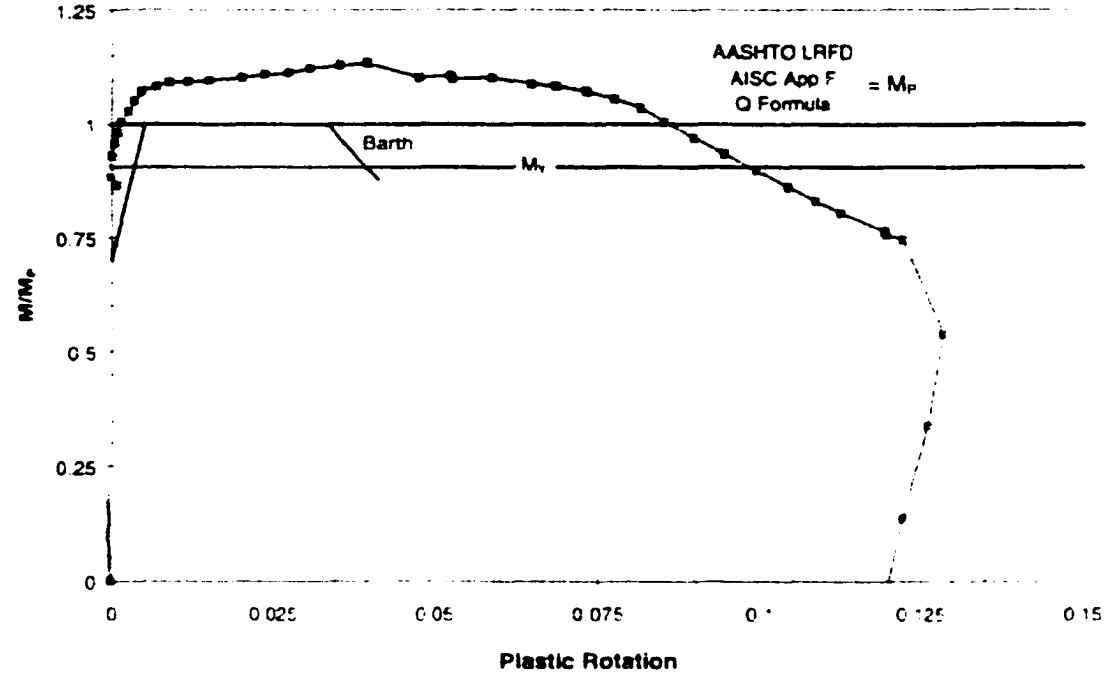

Figure 2-47. Moment Capacity of Test Girder D using Several Methods

(Source: Yakel, Mans, & Azizinamini's report, 1999)

A.4 Barth, Hartnagel, White, and Barker, 2001 - Improved Simplified Inelastic Design : Calculation of the Nominal Moment Resistance

Calculation of the Flexural Capacity M_n

At present, work is underway by a task committee under the auspices of AASHTO T-14, to simplify and unify the LRFD provisions for I girder design. Potential resistance equations would predict strengths greater than the yield moment capacity M_y for some geometries, and would provide a continuous definition of the strength between that of braced compact sections, which have a nominal capacity of M_p, and other sections, which have smaller maximum strengths due to stability considerations. This section presents a subset of potential equations that are applicable for general unstiffened and transversely-stiffened I girders with a compact compression flange and which satisfy $L_b \leq L_{pd}$. The expressions may be summarized as follows:

1. If these types of girders have compact webs, $M_n = M_p$.
2. If they have slender webs,

$$M_n = R_b R_h \min(F_{yc}S_{xc}, F_{yt}S_{xt}, F_{ys}S_{xs}) \quad (7)$$

where R_b and R_h are web load shedding (due to bend buckling) and hybrid reduction factors similar to those in the current AASHTO LRFD (2001) provisions (with R_h simplified by using the compression flange yield strength F_{yc} instead of the applied stress f_c, and R_h determined based on the portion of the cross-section that experiences first yielding, i.e., the compression flange, the tension flange or the reinforcing steel), S_{xc}, S_{xt} and S_{xs} are elastic section moduli associated with the compression flange, tension flange and reinforcing steel respectively, accounting for noncomposite and composite loading conditions (see below), and F_{yt} and F_{ys} are the yield strengths of the girder tension flange

and of the reinforcing steel. Equation (7) is written in a form applicable to general noncomposite unstiffened and transversely stiffened I girders as well as to composite I girders in negative bending. Composite I girder sections in positive bending are handled separately. Longitudinally-stiffened I girders are not addressed here, since test data on the inelastic M-θ_p response of these types of girders is limited.

3. If they have noncompact webs (intermediate between compact and slender),

$$M_n = \min(M_{mc}, M_{mt}) \tag{8a}$$

where M_{mc} and M_{mt} are the maximum potential flexural resistances associated with the compression flange and the tension flange or reinforcing steel respectively (attainable if the compression flange is compact and the member is adequately braced, as is the case in this discussion). The capacity M_{mc} is expressed as

$$M_{mc} = \left[1 - \left(1 - \frac{M_{rwc}}{M_p}\right)\left(\frac{2D_c/t_w - \lambda_{pw}}{\lambda_{rw} - \lambda_{pw}}\right)\right] M_p \tag{8b}$$

where

$$M_{rwc} = R_h F_{yc} S_{xc} \tag{8c}$$

is the strength obtained from the compression flange check in Eq. (7) when $2D_c/t_w = \lambda_{rw}$. The term

$$\lambda_{rw} = 5.70\sqrt{E/F_{yc}} \tag{8d}$$

is the noncompact web slenderness limit, simplified from the (AASHTO 2001) provisions, and

$$\lambda_{pw} = \frac{D_c}{D_{cp}} \frac{\sqrt{E/F_{yc}}}{(0.54M_p/M_y - 0.1)^2} \tag{8e}$$

(Source: Barth, Hartnagel, White, and Barker, 2001) 222

is a new, modified compact web slenderness limit. For homogeneous doubly-symmetric I girder sections with $M_p / M_y \cong 1.14$, Eq. (8e), multiplied by the ratio D_{cp}/D_c, gives approximately the same requirement on $2D_{cp}/t_w$ as the current AISC (1999) and base AASHTO (2001) compact web slenderness limits. However, Eq. (8e) accounts for the observed behavior in experimental tests and in finite element studies that the web needs to be stockier for the section to be able to develop the plastic moment when M_p/M_y is large, due to nonsymmetry of the cross-section for example (see (White and Barth 1998)). Also, the ratio D_c/D_{cp} in Eq. (8e) converts from the appropriate measure for the compact web limit ($2D_{cp}/t_w$) to the appropriate measure for the noncompact web limit ($2D_c/t_w$). This makes the terms consistent within the last inside parentheses of Eq. (8b). Equation (8b) simply provides a linear transition between $M_{mc} = M_p$ at $2D_c/t_w = \lambda_{pw}$ and $M_{mc} = M_{rwc}$ at $2D_c/t_w = \lambda_{rw}$; nevertheless, comparisons to experimental data indicate excellent accuracy. The term M_y in Eq. (8e) is defined as

$$M_y = \min(R_h F_{yc} S_{xc}, R_h F_{yt} S_{xt}, R_h F_{ys} S_{xs}) \tag{8e}$$

Similarly, the maximum capacity associated with the tension flange, or the tension flange or the reinforcing steel in composite I girders in negative bending, is expressed as

$$M_{mt} = \left[1 - \left(1 - \frac{M_{rwt}}{M_p}\right)\left(\frac{2D_c / t_w - \lambda_{pw}}{\lambda_{rw} - \lambda_{pw}}\right)\right] M_p \tag{8f}$$

where

$$M_{rwt} = \min(R_h F_{yt} S_{xt}, R_h F_{ys} S_{xs}) \tag{8g}$$

It should be noted that in a majority of design situations, in which nominal first yielding occurs at the compression flange, the compression flange check controls the strength and

thus the tension flange and reinforcing steel checks in the above equations are not required. Also, in unshored composite construction, yielding of the reinforcing steel within the negative moment region is particularly unlikely.

For noncomposite I sections, the elastic section moduli S_{xc} and S_{xt} in Eqs. (7) and (8) are calculated based on ordinary strength of materials concepts. For unshored composite I sections in negative bending, S_{xc}, S_{xt} and S_{xs} are calculated as follows. The fundamental formula for the elastic stress due to combined noncomposite and composite loading is

$$f = \frac{M_{(nc)}}{S_{x(nc)}} + \frac{M_{(c)}}{S_{x(c)}} = \frac{(M_{(nc)} + M_{(c)})}{S_x} \tag{9a}$$

where the subscripts (nc) and (c) indicate noncomposite and composite quantities, and S_x represents either S_{xc}, S_{xt} or S_{xs}. The cracked composite section is utilized for calculation of the $S_{x(nc)}$ values. A general equation for the elastic section moduli in the above formulas is obtained by solving this equation for S_x, i.e.,

$$S_x = \frac{\left(\frac{M_{(nc)}}{M_{(c)}} + 1\right)}{\left(\frac{M_{(nc)}}{M_{(c)} S_{x(nc)}} + \frac{1}{S_{x(c)}}\right)} \tag{9b}$$

Also, for unshored composite construction,

$$S_{xs} = S_{xs(c)}\left(\frac{M_{(nc)}}{M_{(c)}} + 1\right) \tag{9c}$$

since the reinforcing steel is stressed only due to the composite loading. As noted above, the strength is typically not governed by the tension flange and reinforcing steel checks.

(Source: Barth, Hartnagel, White, and Barker, 2001) 224

The reader should note that although there are a number of equations in the above procedure, the calculation of the pier section maximum flexural capacity based on the above equations is quite simple in concept and in application.

Handling of Sections with Noncompact Flanges

Some of the experimental tests considered subsequently slightly violate the flange compactness limit. In these cases, the compression flange based strength is calculated as

$$M_n = \left[1 - \left(1 - \frac{R_b F_r S_{xc}}{M_{mc}}\right)\left(\frac{b_{fc}/2t_{fc} - \lambda_{pf}}{\lambda_{rf} - \lambda_{pf}}\right)\right] M_{mc} \tag{10a}$$

where $M_{mc} = M_p$ if the web is compact, $M_{mc} = R_b R_h F_{yc} S_{xc}$ if the web is slender, and M_{mc} is given by Eq. (8b) if the web is noncompact. Also, λ_{pf} is specified in Eq. (4),

$$F_r = \min\left(F_L, R_h F_{yt}\frac{S_{xt}}{S_{xc}}, R_h F_{ys}\frac{S_{xs}}{S_{xc}}\right) \tag{10b}$$

is the nominal compression flange stress at the onset of significant inelastic effects, where F_L is defined by (F_{yc} – 69 MPa) for rolled shapes and by min(F_{yc} – 114 MPa, F_{yw}) in welded shapes, and

$$\lambda_{rf} = 0.95\sqrt{\frac{k_c E}{F_r}} \tag{10c}$$

is the flange slenderness at the theoretical transition between elastic and inelastic local flange buckling. The term k_c in Eq. (10c) is the flange local buckling coefficient, taken equal to 0.763 for rolled shapes, and given by

$$k_c = \max\left[0.4, \min\left(0.763, \frac{4}{\sqrt{2D_c/t_w}}\right)\right] \tag{10d}$$

(Source: Barth, Hartnagel, White, and Barker, 2001) 225

for welded shapes. One should note that for typical bridge I girders (i.e., for $2D_c/t_w \geq 100$), k_c as expressed by Eq. (10d) is always equal to 0.4. Equations (10) give an excellent fit to Johnson's (1985) test data, as well as other experimental and analytical results. Similar to Eqs. (8b) and (8f), Eq. (10a) provides a simple linear transition between $M_n = M_{mc}$ at $b_{fc}/2t_{fc} = \lambda_{pf}$ and $M_n = R_b F_r S_{xc}$ at $b_{fc}/2t_{fc} = \lambda_{rf}$.

The above equations constitute a set of potential unified I girder flexural strength equations, for cases in which adequate lateral support is provided such that lateral-torsional buckling limit states do not control. These equations are being proposed in efforts to unify and simplify the AASHTO LRFD provisions. White and Jung (2002) and White et al. (2002a, b and c) present the complete set of these equations, including consideration of the lateral torsional buckling limit state for general I beams and girders, design of longitudinally stiffened I girders, and extensive comparisons to experimental test data.

Effective Plastic Moment Equations

Although the moment-rotation model shown in Fig. 1, combined with the equations presented in the previous two subsections, could be used directly in traditional autostress procedures, effective plastic moments M_{pc} are needed for the simplified inelastic design method developed by Schilling et al. (1997). The following simple equations for M_{pc} can be derived from Eqs. (1), (2) and (6) by first approximating the quadratic term in Eq. (1) by substituting either (0.03 – 0.005 = 0.025) or (0.009 – 0.005 = 0.004) for $(\theta_p - \theta_{RL})$, then substituting either 0.03 or 0.009 for θ_p in the linear term of this equation.

For I sections satisfying $b_{fc}/2t_{fc} \leq \lambda_{pf}$ (Eq. (4)), $L_b \leq L_{pd}$ (Eq. (3)), $D/b_{fc} \leq 4.25$, $D_{cp}/D \leq 0.75$ and $V \leq 0.6V_n$, we can write

$$\frac{M_{pe}(30)}{M_n} = 2.63 - 2.3\frac{b_{fc}}{t_{fc}}\sqrt{\frac{F_{yc}}{E}} - 0.35\frac{D}{b_{fc}} + 0.39\frac{b_{fc}}{t_{fc}}\sqrt{\frac{F_{yc}}{E}}\frac{D}{b_{fc}} \leq 1 \qquad (11a)$$

$$\frac{M_{pe}(9)}{M_n} = 2.90 - 2.3\frac{b_{fc}}{t_{fc}}\sqrt{\frac{F_{yc}}{E}} - 0.35\frac{D}{b_{fc}} + 0.39\frac{b_{fc}}{t_{fc}}\sqrt{\frac{F_{yc}}{E}}\frac{D}{b_{fc}} \leq 1 \qquad (11b)$$

where $M_{pe}(30)$ and $M_{pe}(9)$ are the effective plastic moments corresponding to 30 and 9 mrads of plastic rotation at the pier section respectively.

For I sections satisfying the above limits, and also with either ultra-compact webs (i.e., satisfying Eq. (5)), or general I girders with transverse stiffeners spaced at $d_o \leq D/2$ on each side of the pier section over a distance $\geq D/2$, and with the other web panels within the unbraced lengths adjacent to the piers designed such that $V \leq 0.6V_n$, we obtain

$$\frac{M_{pe}(30)}{M_n} = 2.78 - 2.3\frac{b_{fc}}{t_{fc}}\sqrt{\frac{F_{yc}}{E}} - 0.35\frac{D}{b_{fc}} + 0.39\frac{b_{fc}}{t_{fc}}\sqrt{\frac{F_{yc}}{E}}\frac{D}{b_{fc}} \leq 1 \qquad (11c)$$

$$M_{pe}(9) = M_n \qquad (11d)$$

The reader may note that the web slenderness $2D_{cp}/t_w$ does not appear within Eqs. (11). Barth and White (1998) and White and Barth (1998) observed in their studies that the web slenderness tends to influence the maximum flexural capacity significantly (when the web is noncompact or slender), but that otherwise, it does not have a significant effect on the inelastic $M\text{-}\theta_p$ response. They found that the $M\text{-}\theta_p$ characteristics, for girders satisfying the specified limits, are influenced most significantly by the compression flange slenderness $b_{fc}/2t_{fc}$ and the aspect ratio of the cross-section D/b_{fc}.

(Source: Barth, Hartnagel, White, and Barker, 2001) 227

A.5 Plastic Moments, M_p, for Specimens #1, #2, #3, and #4

1) Plastic moment & load, M_p & P, of Specimen #1, 19.5 ft-span, simply supported

a) If using $F_{yf} = F_{yw} = 70$ ksi

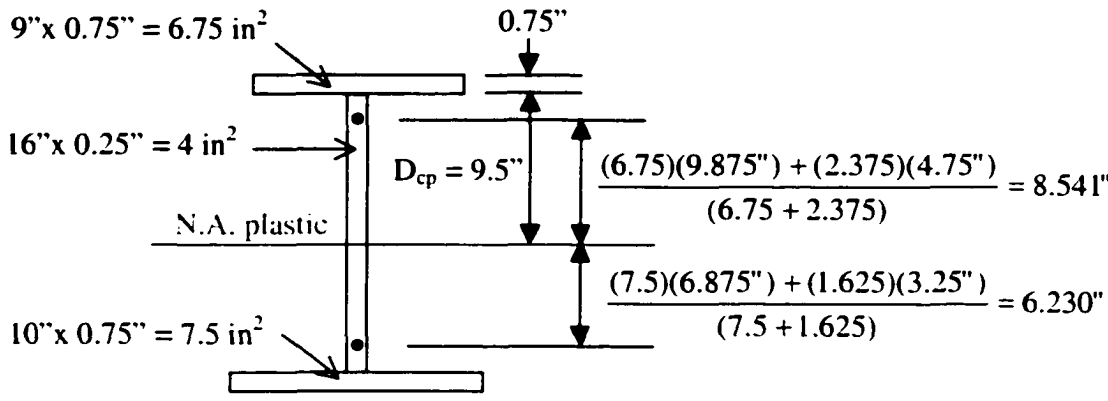

N.A. of plastic section: $A_C = A_T$

$$6.75\ in^2 + 0.25D_{cp} = 7.5\ in^2 + (16 - D_{cp})(0.25\ in)$$

$$0.5\ D_{cp} = 4.75$$

$$D_{cp} = \underline{9.5\ in}$$

$F_y = \sigma_y.A = (70\ ksi)(9.125\ in^2) = 638.75\ K$

$M_p = F.la = (638.75\ K)(8.541" + 6.230") = 9,434.7\ K\text{-}in = \underline{786.23\ K\text{-}ft}$

$$P = \frac{4M_p}{L} = \frac{4(786.23\ Kft)}{19.5\,ft} = \underline{161.278\ K}$$

For half beam & 16 segments $\Rightarrow$ $\dfrac{161.278\,lb}{(2)(16)} = \underline{5,039.94\ lb}$

Nodal loads for FEM:

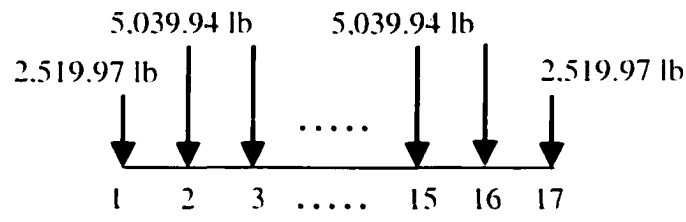

b) If using $F_{yf} = 83.35$ ksi and $F_{yw} = 69.83$ ksi

Total area = 6.75 +7.5 +4 = 18.25 in^2

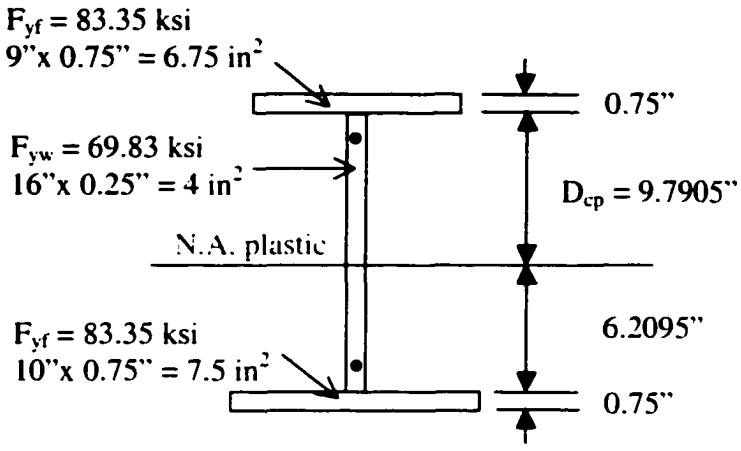

N.A. of plastic section: $F_C = F_T$

$$F_C = (83.35 \text{ ksi})(6.75 \text{ in}^2) + (69.83 \text{ ksi})(0.25\ D_{cp})$$

$$F_T = (69.83 \text{ ksi})(16 - D_{cp})(0.25 \text{ in}) + (83.35 \text{ ksi})(7.5 \text{ in}^2)$$

$$D_{cp} = \underline{9.7905 \text{ in}}$$

$M_p = \Sigma(F.la)$

$$= \left\{ \begin{array}{l} (83.35 \text{ ksi})(6.75 \text{ in}^2)(9.7905" + 0.75"/2) \\ + (69.83 \text{ ksi})(2.4476 \text{ in}^2)(9.7905"/2) \\ + (69.83 \text{ ksi})(1.5524 \text{ in}^2)(6.2095"/2) \\ + (83.35 \text{ ksi})(7.5 \text{ in}^2)(6.2095" + 0.75"/2) \end{array} \right\} = 11{,}009.1 \text{ K-in} = \underline{917.4 \text{ K-ft}}$$

$$P = \frac{4M_p}{L} = \frac{4(917.4 \text{ Kft})}{19.5 \text{ ft}} = \underline{188.19 \text{ K}}$$

For half beam & 16 segments $\Rightarrow \dfrac{188{,}190.5 \text{ lb}}{(2)(16)} = \underline{5{,}881 \text{ lb}}$

Nodal loads for FEM:

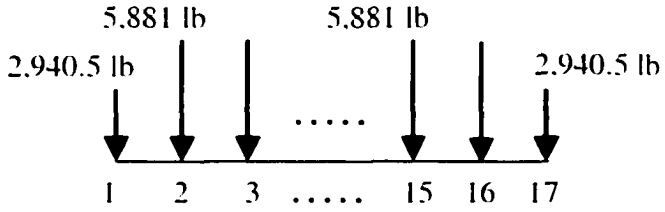

2) Plastic moment & load, M_p & P, of Specimen #2, 22.0 ft-span, simply supported

a) If using $F_{yf} = F_{yw} = 70$ ksi

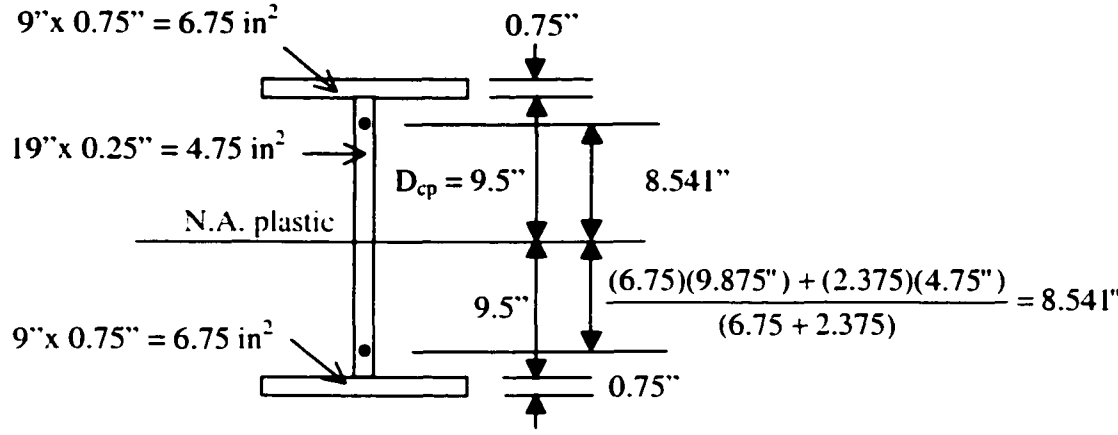

$F_y = \sigma_y.A = (70 \text{ ksi})(6.75 \text{ in}^2 + 2.375 \text{ in}^2) = 638.75 \text{ K}$

$M_p = F.la = (638.75 \text{ K})(8.541" + 8.541") = 10,911 \text{ K-in} = \underline{909.27 \text{ K-ft}}$

$$P = \frac{4M_p}{L} = \frac{4(909.27 \text{ Kft})}{22 \text{ ft}} = \underline{165.322 \text{ K}}$$

For half beam & 16 segments $\Rightarrow \dfrac{165.322 \text{ lb}}{(2)(16)} = \underline{5,166.3 \text{ lb}}$

Nodal loads for FEM:

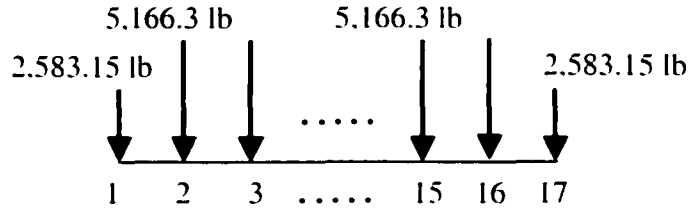

b) If using $F_{yf} = 83.35$ ksi and $F_{yw} = 69.83$ ksi

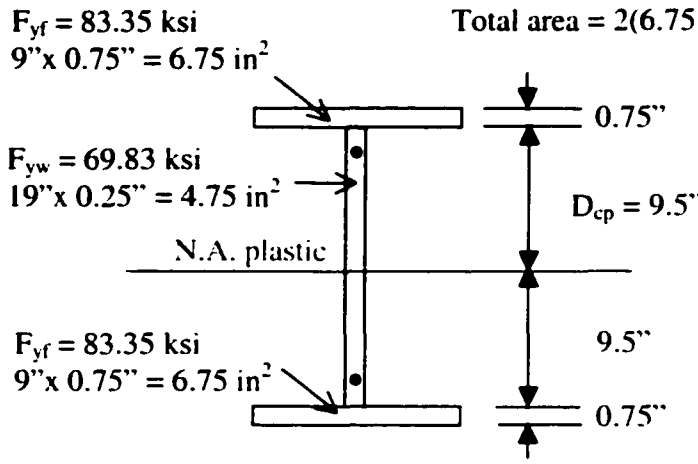

$$M_p = \Sigma(F.la)$$

$$= 2\left\{\begin{array}{l}(83.35\text{ ksi})(6.75\text{ in}^2)(9.5" + 0.75"/2) \\ +(69.83\text{ ksi})(2.375\text{ in}^2)(4.75")\end{array}\right\} = 12{,}687.7\text{ K-in}$$

$$= \underline{1{,}057.3\text{ K-ft}}$$

$$P = \frac{4M_p}{L} = \frac{4(1{,}057.3\text{ Kft})}{22\text{ ft}} = \underline{192.2\text{ K}}$$

For half beam & 16 segments $\Rightarrow$ $\dfrac{192{,}238\text{ lb}}{(2)(16)} = \underline{6{,}007.4\text{ lb}}$

Nodal loads for FEM:

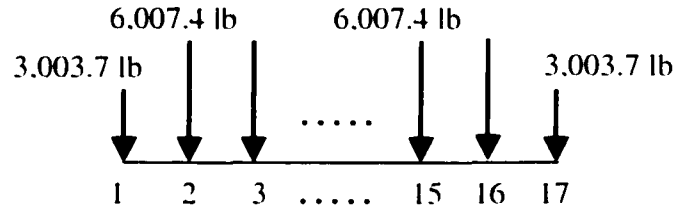

3) Plastic moment & load, M_p & P, of Specimen #3, 26.0 ft-span (7/12/01 test) and 27.5 ft-span (8/1/01 test), simply supported

a) If using $F_{yf} = F_{yw} = 70$ ksi

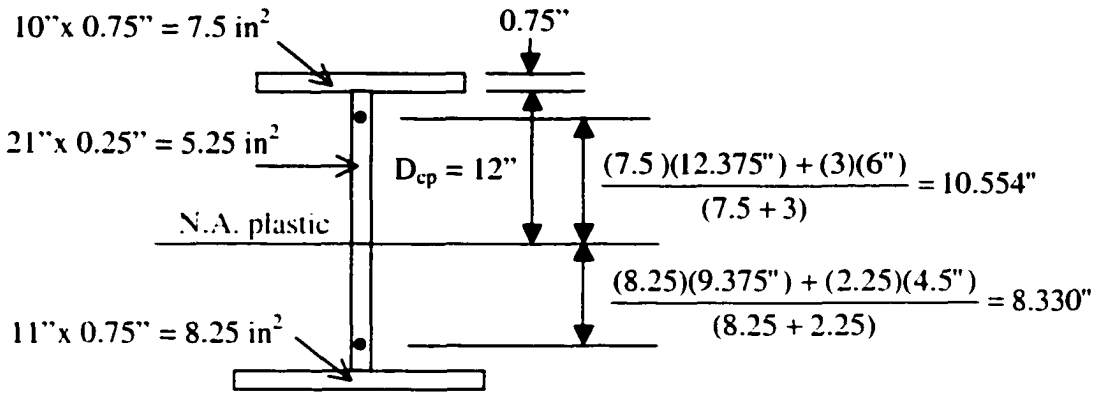

N.A. of plastic section: $A_C = A_T$

$$7.5\ in^2 + 0.25D_{cp} = 8.25\ in^2 + (21 - D_{cp})(0.25\ in)$$

$$0.5\ D_{cp} = 6\ in.$$

$$D_{cp} = \underline{12\ in}$$

$F_y = \sigma_y.A = (70\ ksi)(10.5\ in^2) = 735\ K$

$M_p = F.la = (735\ K)(10.554" + 8.330") = 13{,}879.7\ K\text{-}in = \underline{1{,}156.64\ K\text{-}ft}$

- If L = 26 ft: $P = \dfrac{4M_p}{L} = \dfrac{4(1{,}156.64\ Kft)}{26\ ft} = \underline{177.945\ K}$

- If L = 27.5 ft: $P = \dfrac{4M_p}{L} = \dfrac{4(1{,}156.64\ Kft)}{27.5\ ft} = \underline{168.24\ K}$

For half beam & 16 segments $\Rightarrow \dfrac{168{,}238.6\ lb}{(2)(16)} = \underline{5{,}257.45\ lb}$

Nodal loads for FEM:

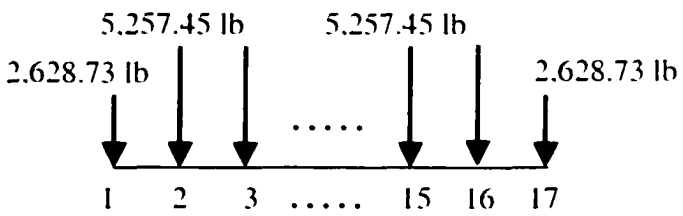

b) If using $F_{yf} = 83.35$ ksi and $F_{yw} = 69.83$ ksi

Total area = 7.5 +8.25 +5.25 = 21 in^2

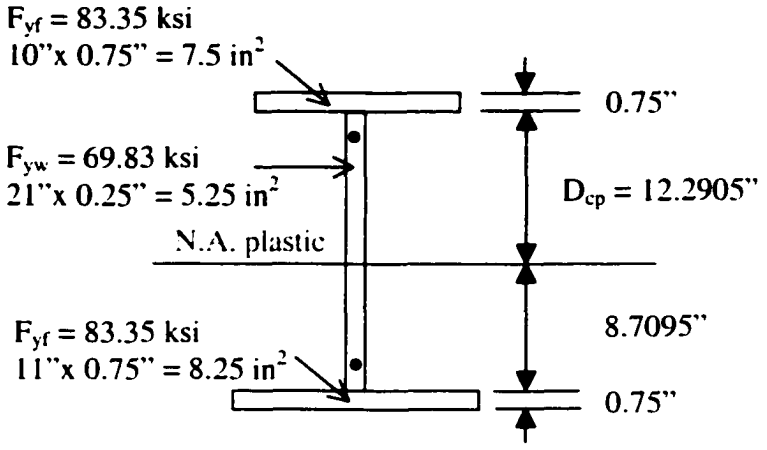

N.A. of plastic section: $F_C = F_T$

$$F_C = (83.35 \text{ ksi})(7.5 \text{ in}^2) + (69.83 \text{ ksi})(0.25\ D_{cp})$$

$$F_T = (69.83 \text{ ksi})(21 - D_{cp})(0.25 \text{ in}) + (83.35 \text{ ksi})(8.25 \text{ in}^2)$$

$$D_{cp} = \underline{12.2905 \text{ in}}$$

$M_p = \Sigma(F.la)$

$$= \left\{ \begin{array}{l} (83.35 \text{ ksi})(7.5 \text{ in}^2)(12.2905" + 0.75"/2) \\ + (69.83 \text{ ksi})(3.0726 \text{ in}^2)(12.2905"/2) \\ + (69.83 \text{ ksi})(2.1774 \text{ in}^2)(8.7095"/2) \\ + (83.35 \text{ ksi})(8.25 \text{ in}^2)(8.7095" + 0.75"/2) \end{array} \right\} \begin{array}{l} = 16{,}145.8 \text{ K-in} \\ = 1{,}345.5 \text{ K-ft} \end{array}$$

- If L = 26 ft: $P = \dfrac{4M_p}{L} = \dfrac{4(1{,}345.5 \text{ Kft})}{26 \text{ ft}} = \underline{207.0 \text{ K}}$

- If L = 27.5 ft: $P = \dfrac{4M_p}{L} = \dfrac{4(1{,}345.5 \text{ Kft})}{27.5 \text{ ft}} = \underline{195.7 \text{ K}}$

For half beam & 16 segments $\Rightarrow \dfrac{195{,}706.4 \text{ lb}}{(2)(16)} = \underline{6{,}115.8 \text{ lb}}$

Nodal loads for FEM:

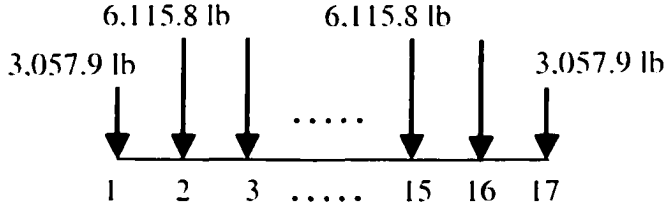

4) Plastic moment & load, M_p & P, of Specimen #4, 31.5 ft-span, simply supported

a) If using $F_{yf} = F_{yw} = 70$ ksi

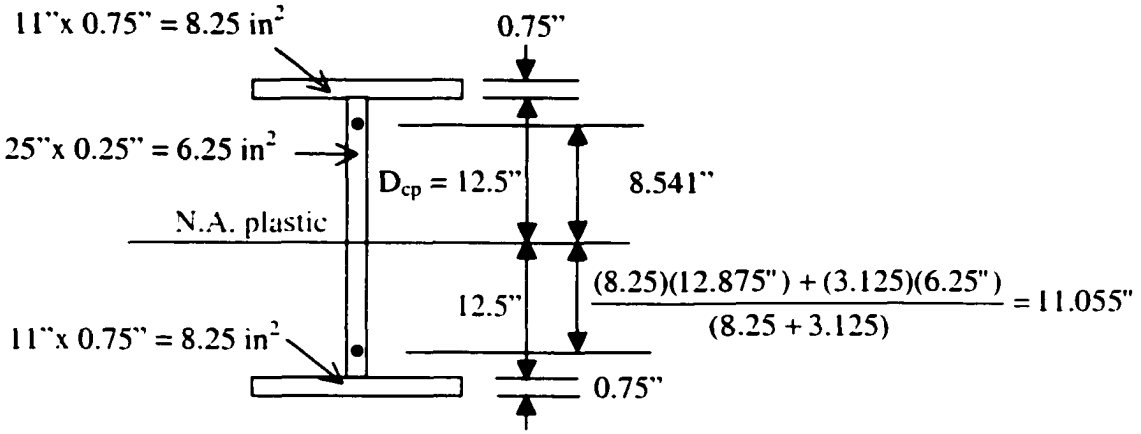

$F_y = \sigma_y.A = (70 \text{ ksi})(8.25 \text{ in}^2 + 3.125 \text{ in}^2) = 796.25 \text{ K}$

$M_p = F.la = (796.25 \text{ K})(11.055" + 11.055") = 17.605.0 \text{ K-in} = \underline{1.467.08 \text{ K-ft}}$

$$P = \frac{4M_p}{L} = \frac{4(1.467.08 \text{ Kft})}{31.5 \text{ ft}} = \underline{186.30 \text{ K}}$$

For half beam & 16 segments $\Rightarrow \dfrac{186.296 \text{ lb}}{(2)(16)} = \underline{5.821.75 \text{ lb}}$

Nodal loads for FEM:

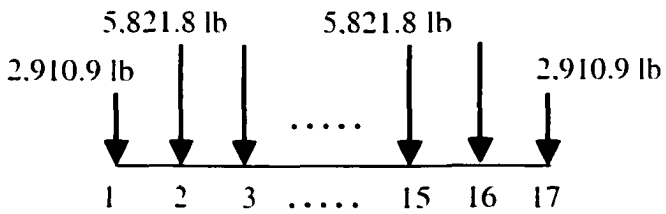

b) If using $F_{yf} = 83.35$ ksi and $F_{yw} = 69.83$ ksi

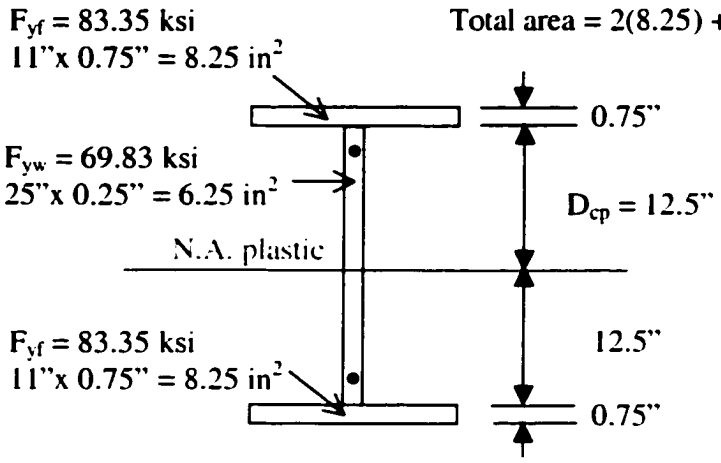

$$M_p = \Sigma(F.la)$$

$$= 2\left\{\begin{array}{l}(83.35\text{ ksi})(8.25\text{ in}^2)(12.5" + 0.75"/2) \\ +(69.83\text{ ksi})(3.125\text{ in}^2)(6.25")\end{array}\right\} = 20{,}435.34\text{ K-in}$$

$$= \underline{1{,}702.9\text{ K-ft}}$$

$$P = \frac{4M_p}{L} = \frac{4(1{,}702.9\text{ Kft})}{31.5\text{ ft}} = \underline{216.25\text{ K}}$$

For half beam & 16 segments $\Rightarrow$ $\dfrac{216.247\text{ lb}}{(2)(16)} = \underline{6{,}757.72\text{ lb}}$

Nodal loads for FEM:

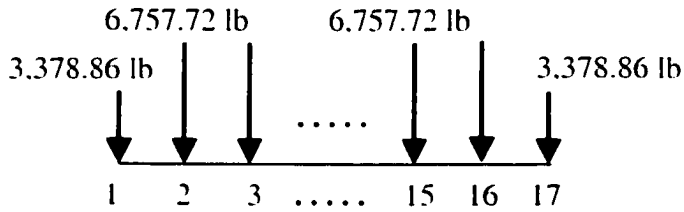

A.6 Fictitious Plastic Moments, M_p, of the Fictitious Symmetric Steel Used In Composite/Noncomposite Comparisons

1) Plastic moment & load, M_p & P, of fictitious symmetric-I corresponding to Specimen #1, 19.5 ft-span, simply supported

If using F_{yf} = 83.35 ksi and F_{yw} = 69.83 ksi

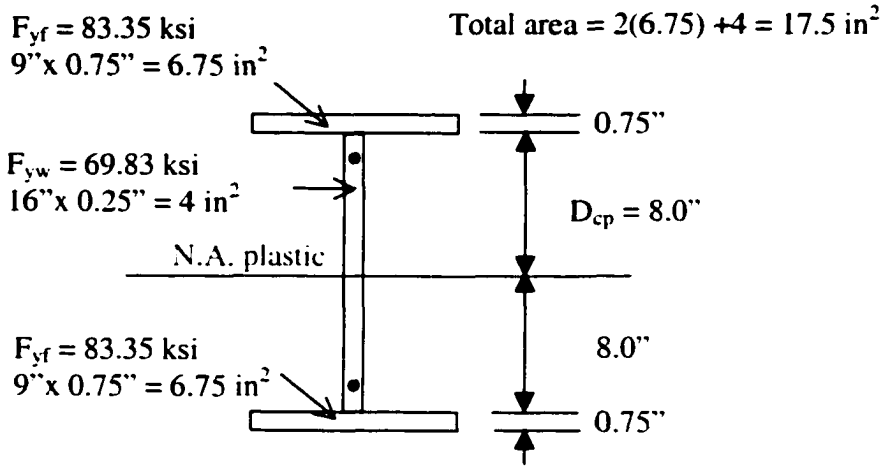

$$M_p = \Sigma(F.la)$$

$$= 2\left\{\begin{array}{l}(83.35\text{ ksi})(6.75\text{ in}^2)(8.0" + 0.75"/2) \\ +(69.83\text{ ksi})(2.0\text{ in}^2)(4.0")\end{array}\right\} = 10{,}541.54\text{ K-in}$$

$$= \underline{878.5\text{ K-ft}}$$

$$P = \frac{4M_p}{L} = \frac{4(878.5\text{ Kft})}{19.5\text{ft}} = \underline{180.2\text{ K}}$$

For half beam & 16 segments $\Rightarrow \dfrac{180.197\text{ lb}}{(2)(16)} = \underline{5.631.2\text{ lb}}$

Nodal loads for FEM:

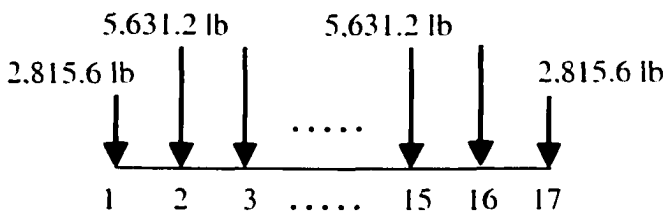

2) Plastic moment & load, M_p & P, of fictitious symmetric-I corresponding to Specimen #3, 26.0 ft-span (7/12/01 test) and 27.5 ft-span (8/1/01 test), simply supported

If using F_{yf} = 83.35 ksi and F_{yw} = 69.83 ksi

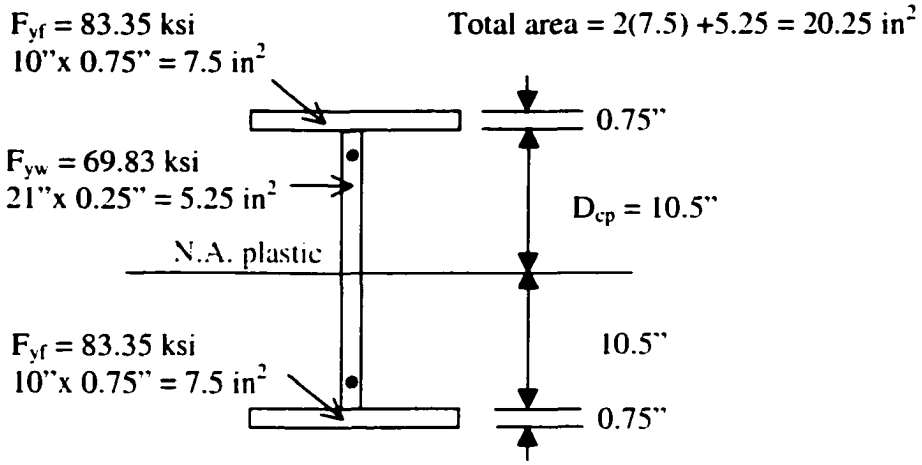

$$M_p = \Sigma(F.la)$$

$$= 2\left\{\begin{array}{l}(83.35\text{ ksi})(7.5\text{ in}^2)(10.5" + 0.75"/2) \\ +(69.83\text{ ksi})(2.625\text{ in}^2)(5.25")\end{array}\right\} = 15.521.9\text{ K-in}$$

$$= \underline{1,293.5\text{ K-ft}}$$

$$P = \frac{4M_p}{L} = \frac{4(1,293.5\text{ Kft})}{27.5\text{ ft}} = \underline{188.1\text{ K}}$$

For half beam & 16 segments $\Rightarrow$ $\dfrac{188.144\text{ lb}}{(2)(16)} = \underline{5,879.5\text{ lb}}$

Nodal loads for FEM:

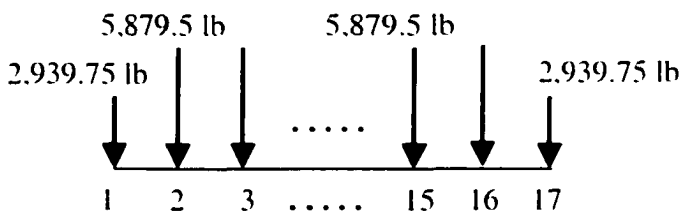

A.7 Stress-strain relationships of HPS70W flange and web coupons at CSU

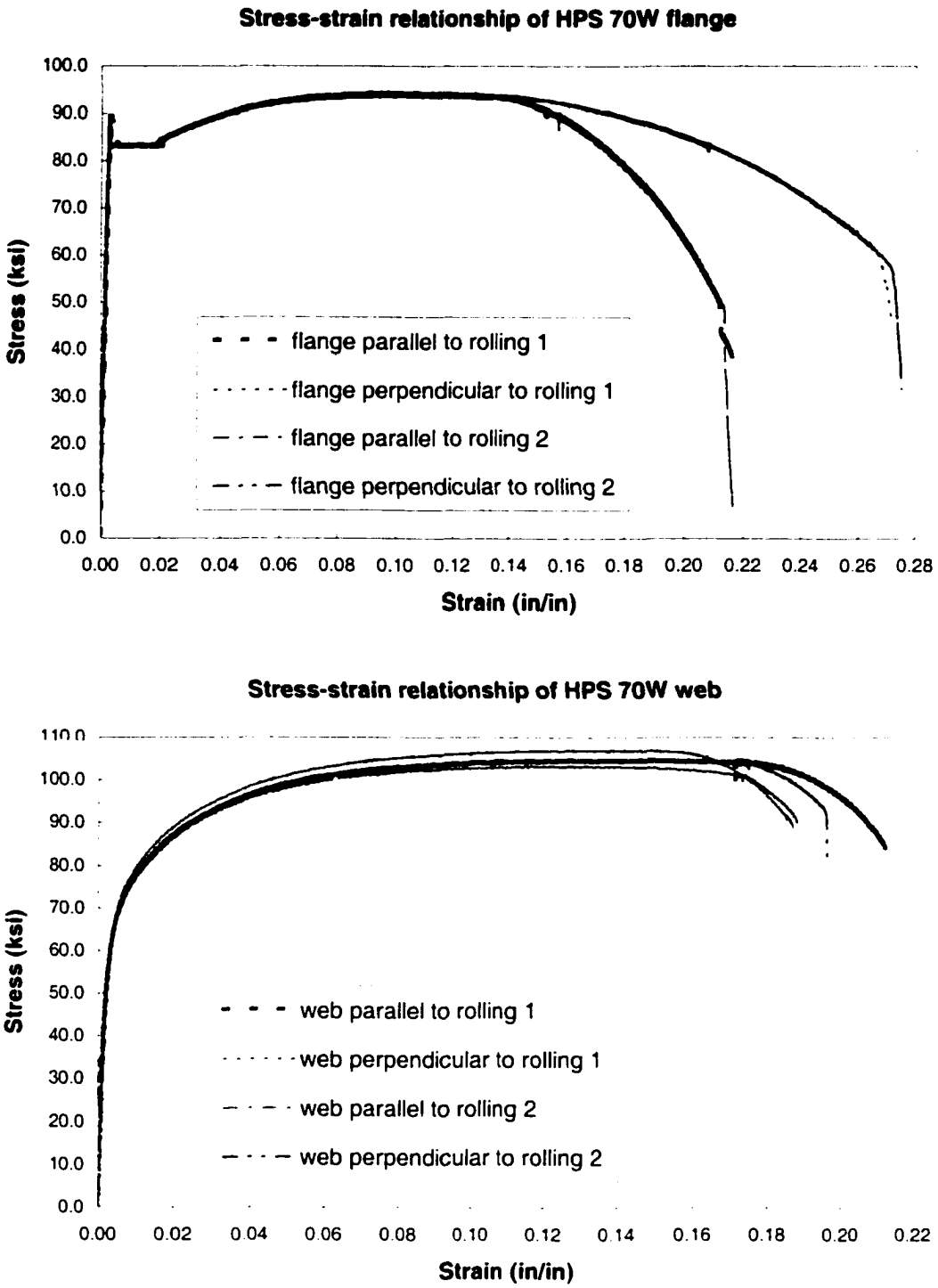

Figure A.7.1 Engineering stress-strain curves until failure of HPS70W flange and web coupons at CSU